ABSTRACT

Title of dissertation: FUNDAMENTAL UNDERSTANDING OF ROTOR AEROMECHANICS AT HIGH ADVANCE RATIO THROUGH WIND TUNNEL TESTING

Benjamin Berry, Doctor of Philosophy, 2016

Dissertation directed by: Professor Inderjit Chopra
Department of Aerospace Engineering

The purpose of this research is to further the understanding of rotor aeromechanics at advance ratios (μ) beyond the maximum of 0.5 (ratio of forward airspeed to rotor tip speed) for conventional helicopters. High advance ratio (μ) rotors have applications in high speed compound helicopters. In addition to one or more conventional main rotors, these aircraft employ either thrust compounding (propellers), lift compounding (fixed-wings), or both.

An articulated 4-bladed model rotor was constructed, instrumented, and tested up to a maximum advance ratio of μ = 1.6 in the Glenn L. Martin Wind Tunnel at the University of Maryland. The data set includes steady and unsteady rotor hub forces and moments, blade structural loads, blade flapping angles, swashplate control angles, and unsteady blade pressures.

A collective-thrust control reversal—where increasing collective pitch results in lower rotor thrust—was observed and is a unique phenomenon to the high advance ratio flight regime. The thrust reversal is explained in a physical manner as well

as through an analytical formulation. The requirements for the occurrence of the thrust reversal are enumerated. The effects of rotor geometry design on the thrust reversal onset are explored through the formulation and compared to the measured data.

Reverse-flow dynamic stall was observed to extend the the lifting capability of the edgewise rotor well beyond the expected static stall behavior of the airfoil sections. Through embedded unsteady blade surface pressure transducers, the normal force, pitching moment, and shed dynamic stall vortex time histories at a blade section in strong reverse flow were analyzed. Favorable comparisons with published 2-D pitching airfoil reverse flow dynamic stall data indicate that the 3-D stall environment can likely be predicted using models developed from such 2-D experiments.

Vibratory hub loads were observed to increase with advance ratio. Maximum amplitude was observed near $\mu = 1$, with a reduction in vibratory loads at higher advance ratios. Blade load 4/rev harmonics dominated due to operation near a 4/rev fanplot crossing of the 2nd flap bending mode natural frequency. Oscillatory loads sharply increase in the presence of retreating blade reverse flow dynamic stall, and are evident in blade torsion, pitch link, and hub load measurements. The blades exhibited torsion moment vibrations at the frequency of the 1st torsion mode in response to the reverse flow pitching moment loading.

FUNDAMENTAL UNDERSTANDING OF ROTOR AEROMECHANICS AT HIGH ADVANCE RATIO THROUGH WIND TUNNEL TESTING

by

Benjamin Berry

Dissertation submitted to the Faculty of the Graduate School of the
University of Maryland, College Park in partial fulfillment
of the requirements for the degree of
Doctor of Philosophy
2016

Advisory Committee:
Professor Inderjit Chopra, Chair/Advisor
Professor James Baeder
Professor Anya Jones
Professor Anubhav Datta
Professor Michael Coplan, Dean's Representative

Table of Contents

List of Tables

List of Figures

List of Abbreviations

a	Airfoil section lift-curve slope, rad^{-1}
a_X	Acceleration in x-direction
A	Rotor disk area, πR^2
A_b	Rotor blade planform area, σA
c	Blade chord
c_c	Section chord force coefficient
c_d	Section drag coefficient
c_l	Section lift coefficient
$c_{m,c/4}$	Section moment coefficient about the quarter chord
$c_{m,3c/4}$	Section moment coefficient about the three-quarter chord
c_n	Section normal force coefficient
C_D	Drag coefficient, $\frac{D}{\rho A(\Omega R)^2}$
$C_{D,E}$	Equivalent drag, $C_P/\mu + C_D$
C_{FM}	Flap bending moment coefficient, $\frac{M_F}{\rho A(\Omega R)^2 R}$
C_H	H-force coefficient, $\frac{H}{\rho A(\Omega R)^2}$
C_L	Lift coefficient, $\frac{L}{\rho A(\Omega R)^2}$
C_{MX}	Roll moment coefficient, $\frac{M_X}{\rho A(\Omega R)^2 R}$
C_{MY}	Pitch moment coefficient, $\frac{M_Y}{\rho A(\Omega R)^2 R}$
C_P	Power coefficient (shaft), $\frac{P}{\rho A(\Omega R)^3}$
C_p	Pressure coefficient, $\frac{p_s - p_\infty}{\frac{1}{2}\rho V^2}$
C_T	Thrust coefficient, $\frac{T}{\rho A(\Omega R)^2}$
C_{TM}	Torsion moment coefficient, $\frac{M_T}{\rho A(\Omega R)^2 R}$
C_Y	Side force coefficient, $\frac{Y}{\rho A(\Omega R)^2}$
f	Frequency, Hz
k	Reduced frequency, $\omega c/2V$
k_Ω	Reduced frequency based on 1P, $\frac{\Omega c}{2u_T}$
k_{rev}	Reduced freq based on T_{rev}, $\frac{\pi c}{T_{rev} u_T}$
M	Mach number
N_b	Number of blades
P, /rev	Frequency in per revolution, i.e. $2\pi f/\Omega$
p_s	Static pressure
p_∞	Freestream pressure
r	Rotor blade spanwise location, non-dim, y/R
R	Rotor radius
T_{rev}	Period of reverse flow region, sec
u_T	Blade section in-plane velocity
u_P	Blade section out-of-plane velocity
U_∞	Free-stream velocity
X	Rotor longitudinal axis, parallel to disk, positive aft
Y	Rotor lateral axis, parallel to disk, positive starboard
Z	Rotor vertical axis, normal to disk, positive up

α	Angle of attack
α_s	Rotor shaft tilt, disk angle of attack, positive aft
β	Blade flapping angle
β_{1c}	Longitudinal flapping angle, $\cos\psi$
β_{1s}	Lateral flapping angle, $\sin\psi$
λ	Inflow velocity, $v/\Omega R$
λ_i	Inflow velocity, induced component
μ	Advance ratio, $U_\infty \cos\alpha_s/(\Omega R)$
ω	Frequency, rad/s
Ω	Rotor rotation speed, rad/s
ψ	Rotor blade azimuth
ρ	Air density
σ	Rotor solidity, A_b/A
θ	Blade pitch angle
θ_0	Rotor collective pitch angle, at root
θ_{1c}	Rotor lateral cyclic pitch angle, $\cos\psi$
θ_{1s}	Rotor longitudinal cyclic pitch angle, $\sin\psi$

BET	Blade element theory
DFT	Discrete Fourier transform
FFT	Fast Fourier transform
RCAS	Rotorcraft Comprehensive Analysis System
UMD	University of Maryland
UMARC	University of Maryland Advanced Rotorcraft Code

Chapter 1: Introduction

1.1 Background and Motivation

The purpose of this research is to further the understanding of rotor behavior at advance ratios beyond 0.5 (ratio of forward airspeed to rotor tip speed). High advance ratios take place in high-speed compound helicopters that use edgewise rotors. In addition to one or more conventional main rotors, these aircraft employ either thrust compounding (propellers), lift compounding (fixed-wings), or both. Recent examples of such aircraft are the Sikorsky X2 (coaxial main rotors with thrust compounding) and the Eurocopter X^3 (single main rotor with thrust and lift compounding)—both demonstrator aircraft—shown in fig. 1.1. These stand in contrast to non-edgewise compound helicopters such as tilt-rotors (fig. 1.2), which operate in forward flight with prop-rotors in a propeller mode, and have different rotor aerodynamics. To understand the reason for interest in edgewise compound helicopters, the limitations of conventional helicopters must first be expounded upon.

Helicopters and other rotorcraft are primarily distinguished from other aircraft for the ability to takeoff and land vertically, as well as hover. This capability is necessary for operation without a runway, and for transporting people and cargo from constrained areas or unprepared surfaces. Helicopters, however, are not capable of

efficient forward flight at high airspeeds, relative to fixed-wing aircraft. Conventional helicopters—as opposed to tilt-rotor aircraft—with a single main rotor are limited in forward airspeed due to compressibility effects on the advancing side and high angle of attack flow including dynamic stall on the retreating side. This stall develops as increasing forward airspeed reduces the relative airspeed of the retreating rotor blade (fig. 1.3), which requires increasing pitch angles to maintain moment equilibrium (trim) with the advancing blade. Eventually the angle of attack of the retreating blade exceeds the stall angle, which prevents further increases in rotor thrust, and thus, aircraft airspeed. Coaxial helicopters can avoid this issue by primarily producing thrust on the advancing blade, and offloading the retreating blade, thus leaving each rotor unbalanced in moments. This is known as operating in lift-offset mode, since the lateral rotor lift generation is not balanced in the center, but offset to the advancing side of the rotor disk. The moment imbalance from each rotor cancels the other, and leaves the rotor system in a net balanced condition (fig. 1.4). Sikorsky Aircraft utilized this method of operation, known as an Advancing Blade Concept, on both the XH-59/S-69 and the X2 coaxial demonstrator aircraft [1]. A coaxial helicopter has other design challenges related to high-speed flight, namely increased hub/shaft drag (relative to a single rotor), and advancing blade compressibility.

For both edgewise single and coaxial rotor aircraft, high forward flight speeds also have the impediment of compressibility on the advancing blade tip. Typical hover tip speeds of a helicopter are in the range of Mach 0.65, which means at a forward flight speed of Mach 0.35 (230 kts), the advancing blade tip is fully

(a) Eurocopter X3 [2]

(b) Sikorsky X2 [1]

Figure 1.1: Examples of compound helicopters.

(a) AW609 [3]

(b) V22 [4]

Figure 1.2: Examples of tilt-rotor aircraft.

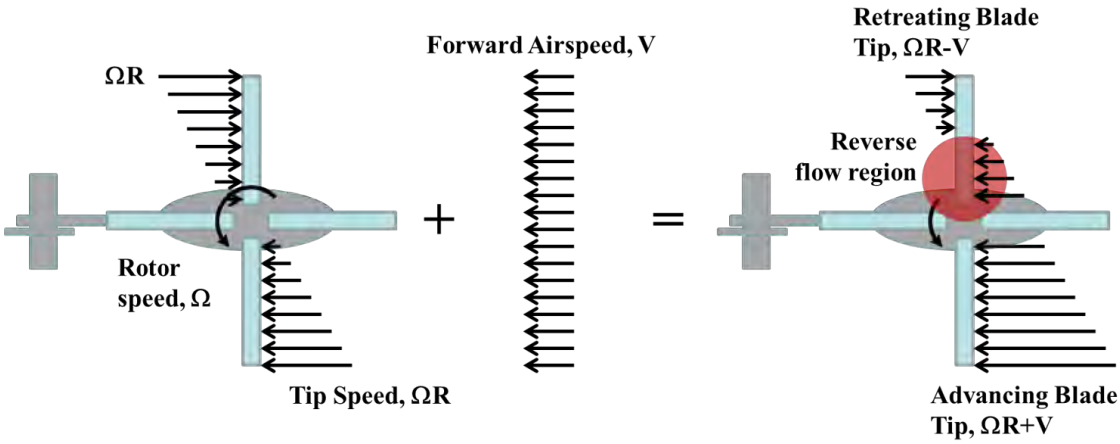

Figure 1.3: Effect of forward flight on retreating blade velocities.

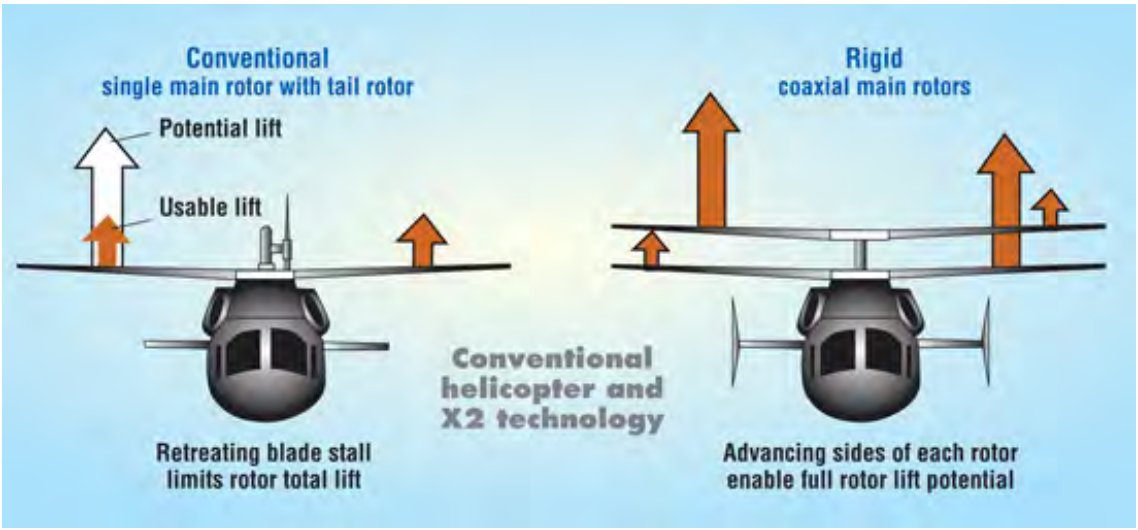

Figure 1.4: Coaxial counter-rotating rotors are able to maintain a lift asymmetry in each rotor during forward flight, with moments from each rotor cancelling. Retreating blade stall is alleviated by eliminating the need for retreating blade lift to balance rotor moments, as in a single-rotor vehicle (image left) [5].

supersonic. Even at lower flight speeds, roughly Mach 0.25 (170 kts), the tip would reach the drag divergent Mach number, where local shocks form and sectional drag increases sharply, typically between Mach 0.85–0.95 depending on the airfoil section properties [6]. This results in a large increase in drag, as well as a chordwise shift in the center of pressure further aft, causing large blade pitching moment impulses which manifest as strong vibrations.

One solution to the issue of compressibility is to reduce the rotor angular velocity as the forward flight speed increases to maintain a sub-critical advancing blade tip Mach number, and hence, reduce power penalties. Slowing the rotor mitigates compressibility issues but also reduces thrust capability. Thus, the impetus for slowed-rotor edgewise compound helicopters, which normally have additional propulsion (propeller or jet) and possibly additional lifting surfaces (fixed wings). Conceptually, the rotor is slowed at least enough to maintain subcritical tip speeds (or more to reduce drag and power consumption), while the propulsive thrust is mostly carried by the auxiliary propulsion system (axially propeller). The rotor can additionally be unloaded partially in lift, which is more efficiently produced by a fixed-wing.

Conventionally and historically, helicopter rotor RPM has been fixed for all flight conditions. Fixed RPM operation has origins in both powertrain, engine, and structural design challenges. Historically turboshaft engine output speed could not be reduced significantly without a significant loss in fuel efficiency (SFC). With a constant engine output speed, a multi-speed transmission could be utilized to vary rotor speed, but this would involve large increases in transmission cost/weight and

a potential decrease in reliability. The design of the rotor and airframe structure to avoid resonant conditions at two or more rotor frequencies also increases the risk and cost of such variable-RPM vehicle concepts.

Engineering advances have mitigated many of the concerns of variable rotor RPM operation. Turboshaft engines are now becoming available that can vary some output speed with a low impact on SFC. The V-22 Osprey, a production tilt-rotor aircraft, reduces rotor RPM via engine speed reduction by about 19% in high-speed forward flight [7]. The Sikorsky X2 and the Eurocopter X^3 also reduce rotor speed with engine speed reduction in flight by 20% and 22%, respectively [8, 9]. Two-stage transmissions have also been demonstrated in flight on rotorcraft in the last 10 years [8, 10]. Advances in computational modeling and testing capabilities in the past 3 decades have allowed designers to better tailor rotor blade and airframe structures to avoid multiple frequencies of variable rotor RPM concepts [8]. Thus, the design challenges for implementation of a slowed-rotor compound helicopter have receded to the point where workable demonstrator aircraft could conceivably be built and flown to high advance ratios, much beyond 0.8.

The remaining risk of such a slowed-rotor concept is the unknown (or rather, unverified) aero-mechanical behavior of edgewise rotors at such high advance ratios. Aeromechanics refers to the coupling of aerodynamic (fluid), elastic (structural), and kinematic (motions) behaviors. Analytical and numerical modeling techniques have been used to predict rotor behavior at high-advance ratios in slowed-rotor compounds (as will be outlined in the following section). However, there exists limited experimental data and no flight test data for powered rotors beyond advance

ratios of about 0.5. Therefore, the predictive tools and theory available to rotorcraft designers have not been extensively validated to the flight regimes necessary for high-speed. This leaves a critical gap in confidence that must then be overcome through repeated flight tests of prototypes and/or large safety factors for components (i.e. weight). Both scenarios result in increased program risk and cost, which can lead to program cancellation (military) or erosion of concept profitability (civilian).

As such, there is a strong need for high-quality experimental measurements on edgewise rotors at advance ratios from 0.5–2.5 or higher to cover the largest range of proposed concepts. This work addresses this major deficiency through high-advance ratio rotor testing in a wind tunnel. From this comprehensive dataset, physical insight into rotor behavior at these conditions can also be developed.

1.2 Summary of Previous Work

The following sections will detail literature reviews of the prior work relating to rotor aeromechanics at high advance ratio in two parts: 1) Experimental laboratory investigations, and 2) Analytical and numerical modeling studies that can be used as a benchmark for accuracy of modern design tools.

1.2.1 High Advance Ratio Experiments

1.2.1.1 Wheatley and Hood, 1934 (PCA-2)

Early high advance ratio rotor tests were conducted on rotors from autogiros, which were the earliest production rotorcraft. An isolated rotor from a Pitcairn

PCA-2 autogiro was tested in the Langley full-scale wind tunnel by the NACA in 1933 [11]. The purpose of the experiment was to further understanding of rotary-wing aircraft in general. The testing was for an un-powered rotor in autorotation, so the tip speed depended on a combination of the collective, the disk angle of attack, and the wind speed. Advance ratios from 0.1 to just above 0.7 were tested for the isolated rotor. Three collective pitch settings were tested, with the disk angle of attack being varied to achieve the target rotor speed for each wind speed. Rotor lift-to-drag ratios were measured, with the maximum value of about 7 being achieved at advance ratios between 0.35 and 0.4. Wheatley and Hood also recorded measurements of the downwash angle distribution around the rotor disk, but only reported the results for two advance ratios, 0.448 and 0.294, much lower than the advance ratios of interest in the present study.

1.2.1.2 Meyer and Falabella, 1953

Meyer and Falabellas experiments [12] on a 5-ft diameter model rotor focused on measurement of the aerodynamic loading (airloads) of the rotor blade. Their test covered an advance ratio range from 0.10 to 1.0. The model rotor had two high-stiffness blades with flap and lag articulation. They tested the rotor with zero hinge offset, as well as with a nominal 13 percent hinge offset. They also reported a configuration with cantilevered blade root.

Airload measurements were made using pressure port holes distributed along the blade surface, with internal tubing running down the blade and connecting to

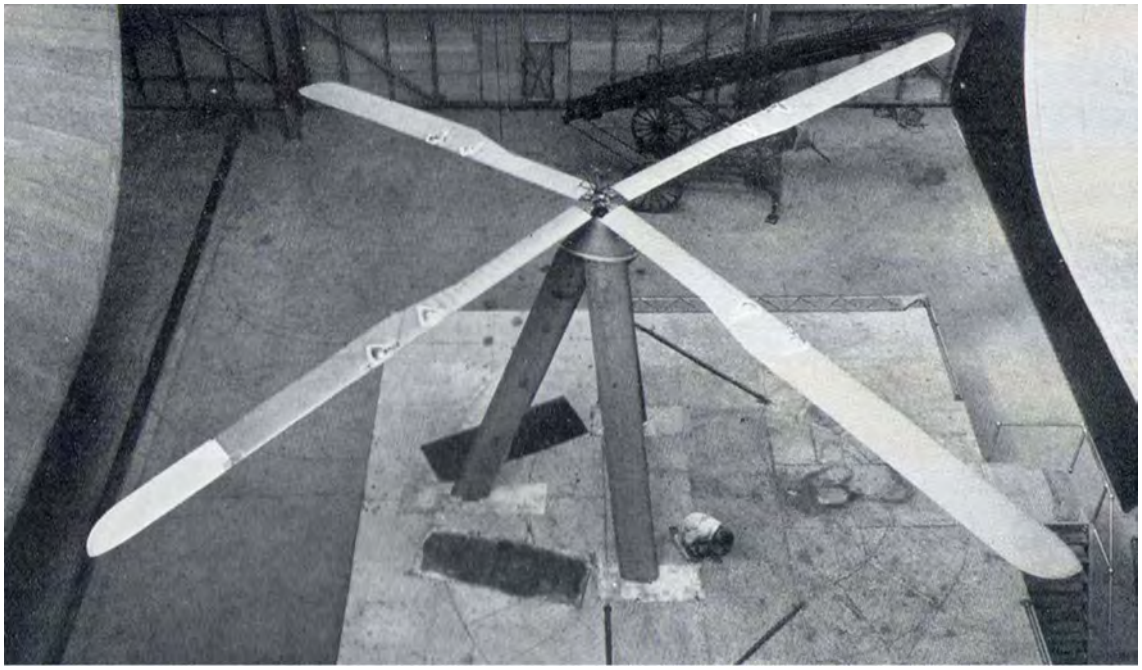

Figure 1.5: PCA-2 rotor test setup in the Langley Full Scale Wind Tunnel [11].

a pressure pickup unit located in the hub. This single transducer in the hub would measure a differential pressure between two ports on opposite surfaces (upper and lower) at a specific chord and span location. A switching mechanism would allow the selection of which pair of pressure ports were active. With this method, many measurements could be made with only a single pressure transducer. The drawback of such an approach is that the large length of tubing between the port and the transducer affects the frequency response. To correct the measurements, Meyer and Falabella conducted and applied a dynamic calibration to each port hole using a portable chamber that could apply sinusoidal pressure variations. The dynamic corrections, however, were not applied to the published airloads data, except for phase (azimuth) correction based on expected maximum amplitude location.

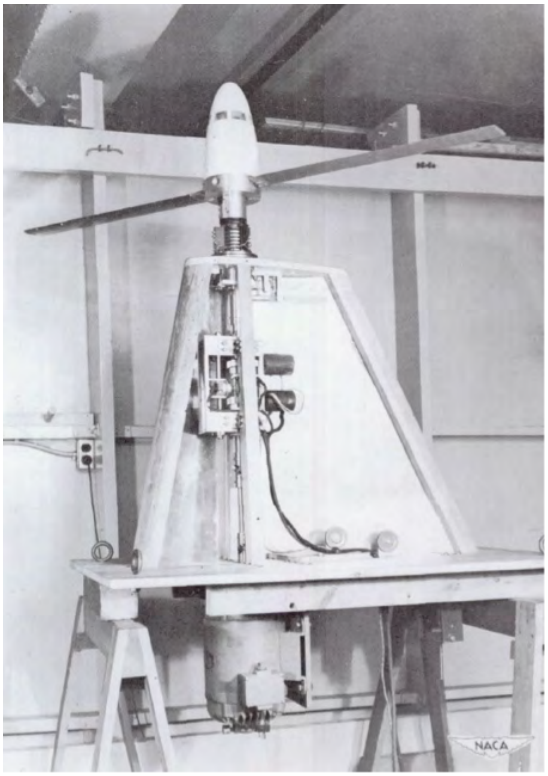

Figure 1.6: Meyer and Falabella wind tunnel test setup with cantilevered rotor configuration [12].

The collective pitch of the rotor blades was adjusted before each test run, but there was no mechanism for cyclic feathering. Therefore, the rotor blades were not trimmed to zero flapping or to zero moments. Rotor lift and shaft torque measurements were taken, but not reported in the published data.

1.2.1.3 Jenkins Model Rotor Testing, 1965

Jenkins tested a 15-ft diameter model rotor (fig. 1.9) over a range of advance ratios from 0.65 to 1.45 [13]. The test was conducted in the Langley full-scale tunnel and reported in 1965. The model rotor was a two-bladed teetering rotor, using

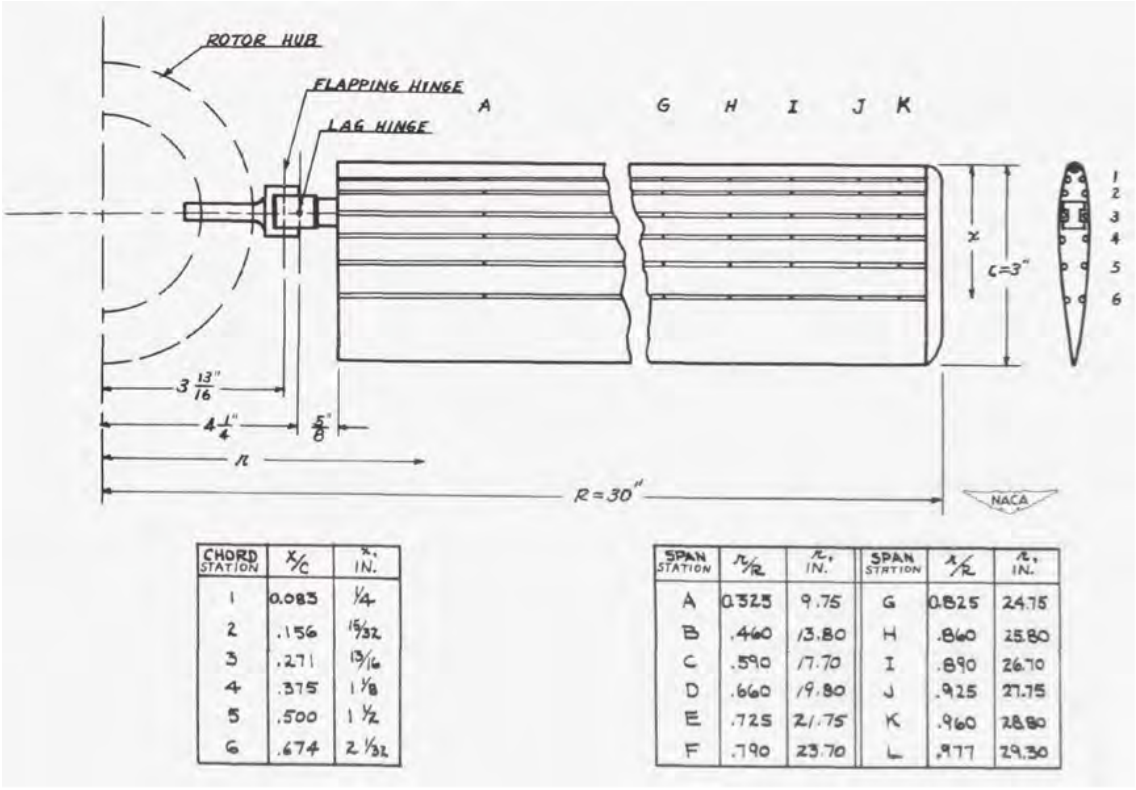

CHORD STATION	x/c	x, IN.
1	0.083	1/4
2	.156	15/32
3	.271	13/16
4	.375	1 1/8
5	.500	1 1/2
6	.674	2 1/32

SPAN STATION	r/R	r, IN.	SPAN STATION	r/R	r, IN.
A	0.325	9.75	G	0.825	24.75
B	.460	13.80	H	.860	25.80
C	.590	17.70	I	.890	26.70
D	.660	19.80	J	.925	27.75
E	.725	21.75	K	.960	28.80
F	.790	23.70	L	.977	29.30

Figure 1.7: Spanwise and chordwise locations of blade surface pressure ports [12].

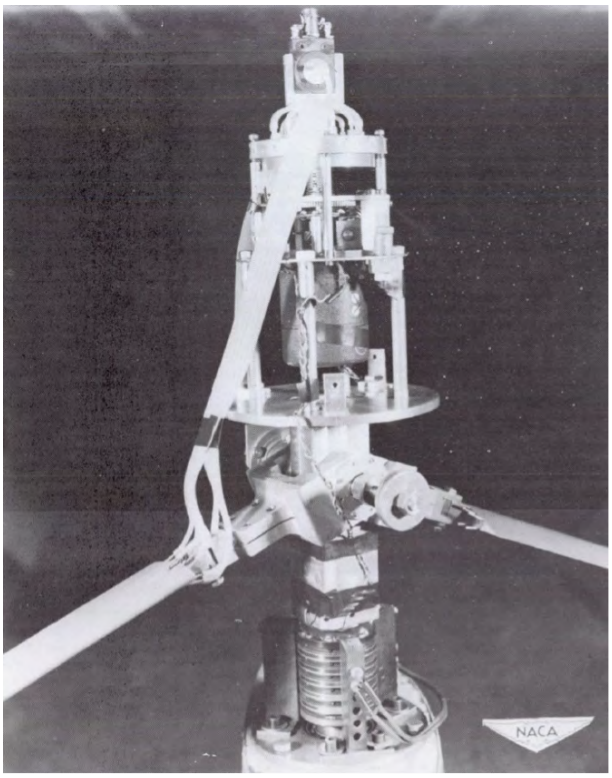

Figure 1.8: Hub assembly for the zero hinge offset rotor, showing pressure tubing from the blade connected to the pressure pickup inside the hub [12].

uniform blades with a NACA 0012 airfoil cross-section and no twist or chord taper. Blade stiffness and mass properties were not reported. Measured data included thrust, torque, H-force (drag), swashplate settings, and blade flapping motions. Longitudinal shaft tilt settings of 0.5 and 5.5 degrees aft were tested. Photographs of the retreating blade with tufts were taken to visualize local flow direction and extent of separation. This was the first work to experimentally observe the collective-thrust control reversal phenomenon, which is where a positive increment to collective results in a negative change in rotor thrust, for a rotor trimmed to zero flapping (fig. 1.10). Jenkins attributed this to the increased sensitivity of the rotor longitudinal flapping response with respect to collective pitch. More recent correlation of this dataset with comprehensive analysis will be covered in the next section.

1.2.1.4 McCloud, Biggers, and Stroub, 1968

Five full-scale rotor geometries were wind tunnel tested to high-advance ratio and reported by McCloud, Biggers, and Stroub in 1968 [14], with performance measurements taken up to a maximum advance ratio of 1.05 and advancing tip Mach numbers up to 1.0. Two of the rotors were articulated and 56 ft in diameter. The other three were two-bladed teetering rotors, with diameters of 48 ft and 34 ft. Blade geometric and mass properties were provided, but not blade stiffness. The rotors all used NACA 0012 airfoil profiles for the entire span, except for one rotor which had tapering thickness at the tip. The tests were conducted in the 40 ft by 80 ft wind tunnel at NASA Ames Research Center. Six-component forces and moments

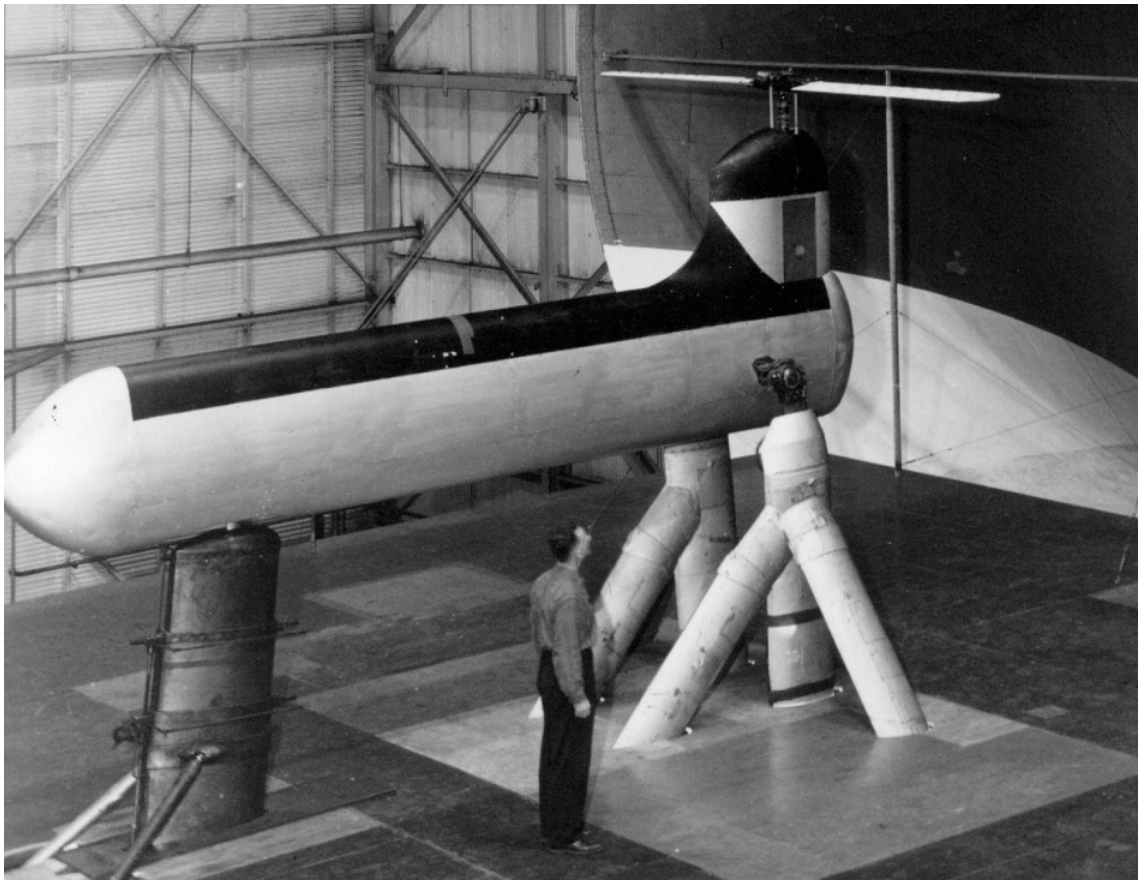

Figure 1.9: Test setup for Jenkins, 1965 in the Langley full-scale wind tunnel [13].

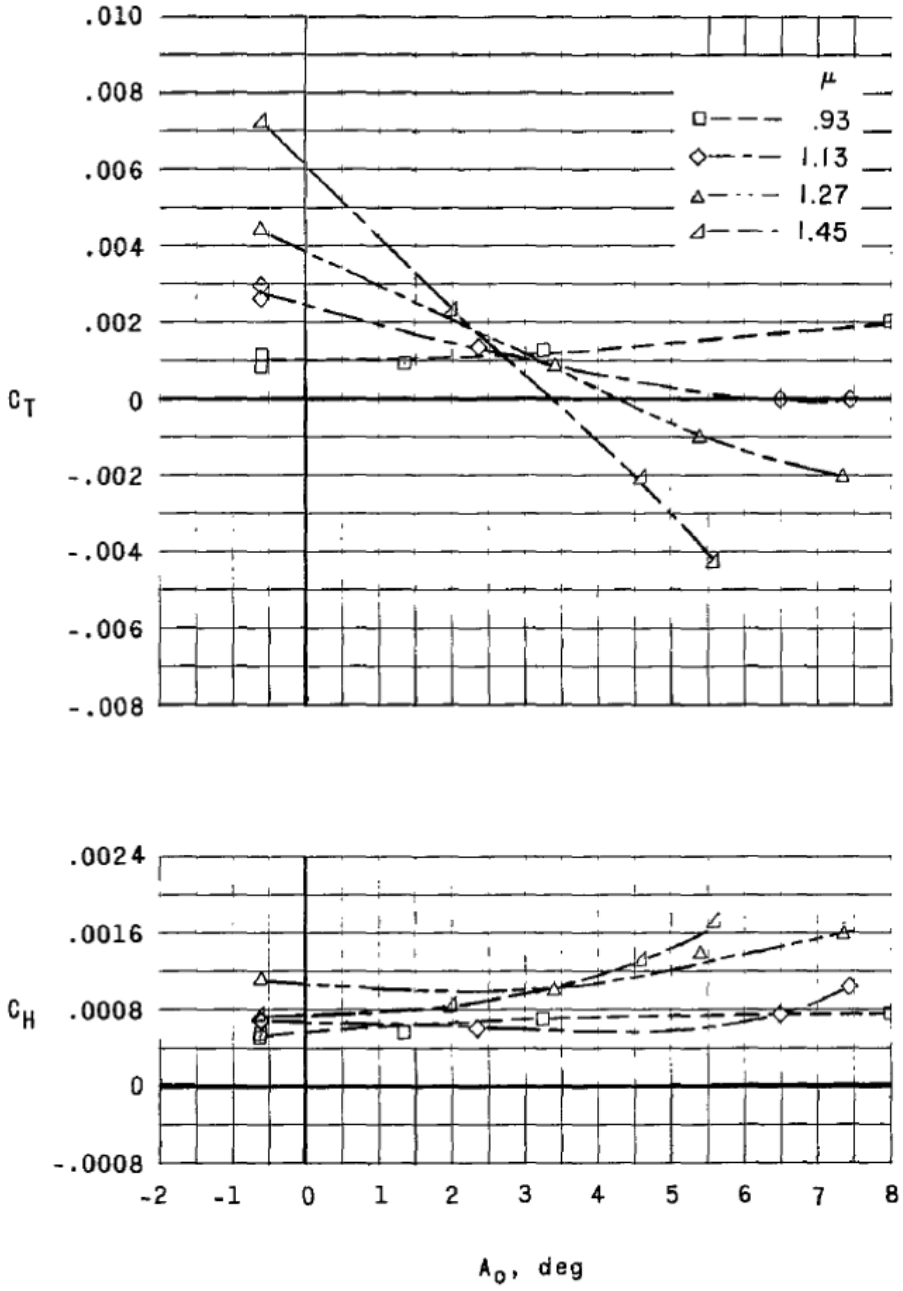

Figure 1.10: Rotor thrust and H-force coefficients vs collective pitch (A0) for high advance ratio, showing collective-thrust reversal [13].

were recorded and the trim targets were zero flapping.

1.2.1.5 Charles and Tanner, 1969

Charles and Tanner [15] reported test details and results from the same two full-scale teetering rotors as McCloud, et al., but with an expanded test envelope. The rotor of interest to this study is the 34-ft diameter rotor which was tested to advance ratios from 0.51 to 1.1. The second rotor with a tapered tip was used to investigate high tip-Mach number conditions, and reached an advance ratio of 0.52. Again, the rotor geometry was provided, but not the stiffness distribution. Blade structural loads were monitored with strain gages but the results were not reported.

The rotor was tested at a constant wind speed of 190 kts (the tunnel limit of the NASA Ames 40 x 80) and advance ratio was varied with rotor rotational speed. The rotor was trimmed to minimum first harmonic flapping with respect to the rotor shaft. The measurements were performance-based: rotor forces and moments, shaft torque, and control angles for trim. Their primary goal was to benchmark the state-of-the-art analyses at the time, which were not detailed. They concluded that propulsive force (drag) predictions were inadequate and optimistic with respect to the measured data above advance ratios of 0.5. The test data was further analyzed in 2008 by Frank Harris, which will be covered in the next section on analysis.

1.2.1.6 Ewans and Krauss, 1973

Ewans and Krauss reported an experiment conducted in 1972 by the Republic Division of the Fairchild Corporation under contract from the Naval Air Systems Command [16]. They tested an 8-foot diameter model rotor in the 12-ft pressurized wind tunnel (variable density) at NASA Ames Research Center up to an advance ratio of 2.46 and 350 kts, the highest experimental advance ratio reported in the literature. They were testing a one-seventh scale reverse velocity rotor system (RVR). This RVR concept was designed for slowed-rotor compound helicopter applications, and included double-ended reversible airfoils along the blade span (fig. 1.11). These airfoils were meant to improve performance of the retreating blade in reverse flow. Two-dimensional wind tunnel tests were undertaken to experimentally characterize the performance of these airfoil shapes in both forward and reverse orientations. A swashplate with the ability to control the cyclic pitch at two-per-rev frequencies was also developed for the concept (fig. 1.12), which they claimed would allow more control of the lift distribution around the azimuth. This higher-harmonic swashplate was built for the model but was not used in this set of experiments.

Measurements included steady balance data (six components), control positions, blade root motions (flap, lag, pitch), and selected blade strain. Flapwise bending stress was measured at 0.37, 0.51, and 0.71 radius. Axial load on the lag damper was measured as a proxy of chordwise blade stresses and to indicate stability. Axial load on the pitch link was measured for control system loads as well as to quantify blade torsion.

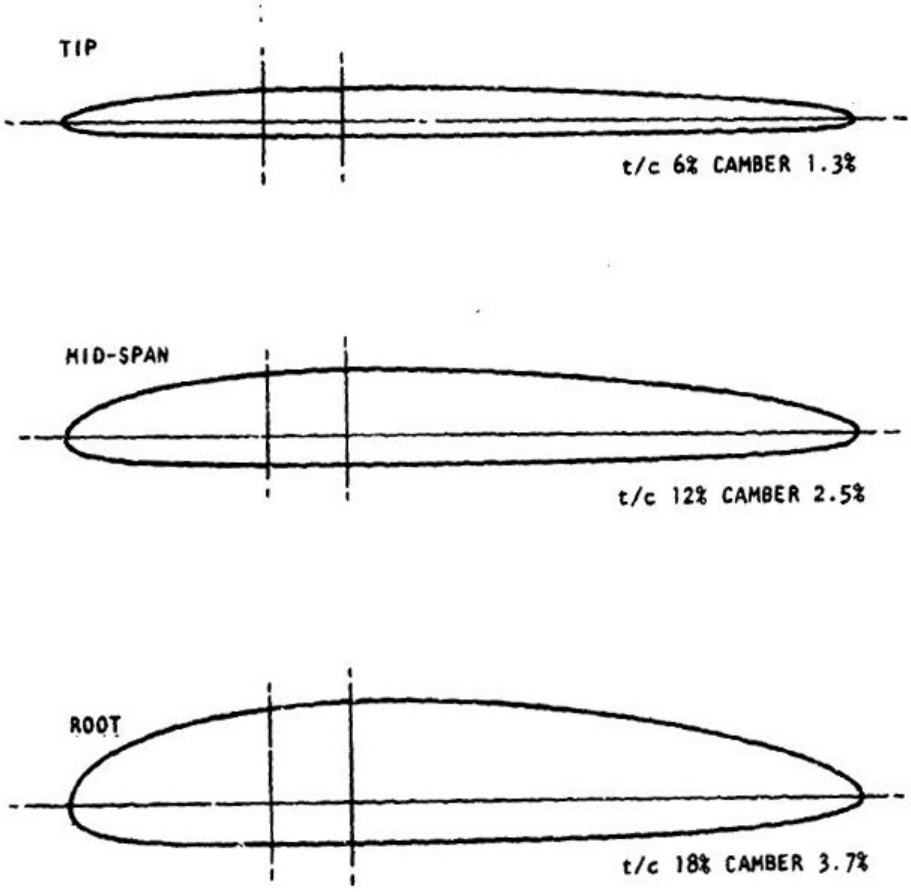

Figure 1.11: The "reversible" airfoil section profiles used in the Reverse Velocity Rotor wind tunnel model [16].

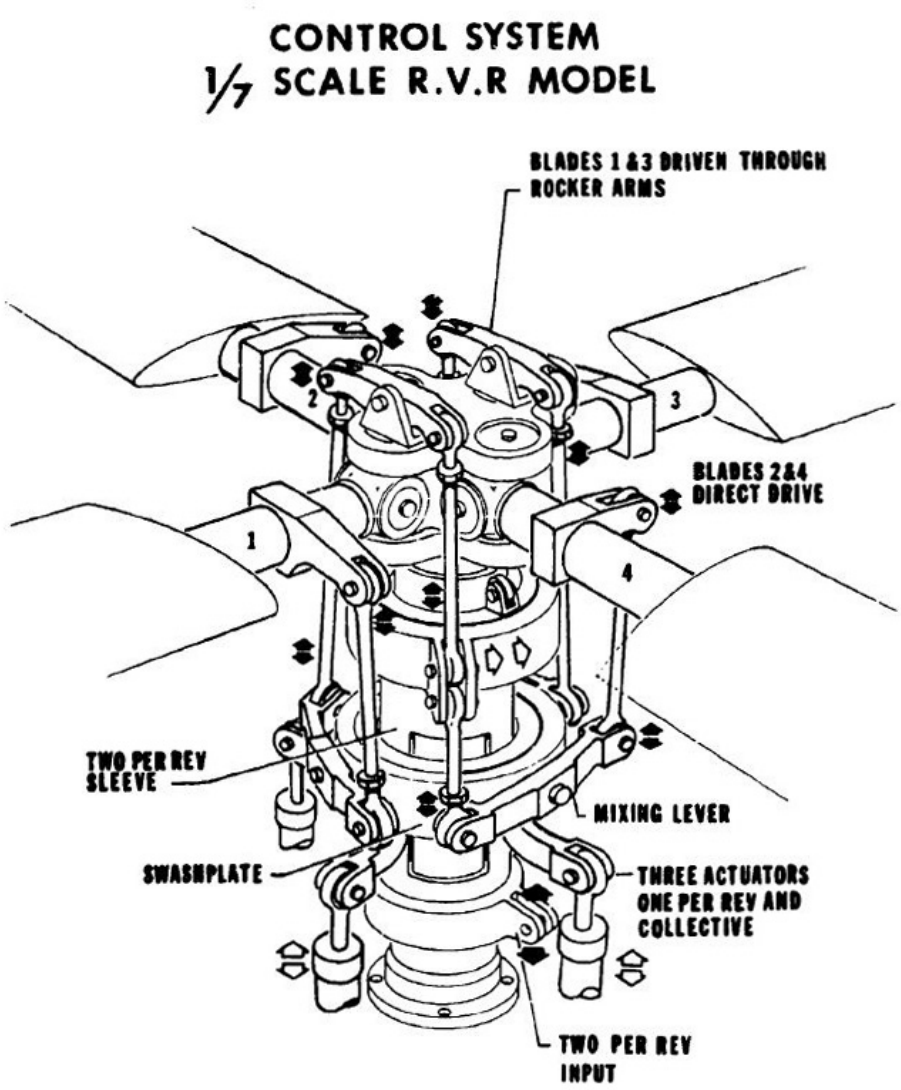

Figure 1.12: Two-per-rev swashplate developed for the Reverse Velocity Rotor wind tunnel model [16].

A key results from the experiments was that the rotor was free of any dynamic instability and could be controlled and trimmed throughout the entire flight envelope. Measured lift-to-drag ratios increased with advance ratio, with a dip at advance ratio of 0.8 (fig. 1.13). The collective-lift reversal was also observed and noted (fig. 1.14), with similar trends as that measured by Jenkins [13]. The authors deduced that collective could become a viable means of lift control at high advance ratio beyond 1.4, whereas around 0.9, collective pitch is not effective.

The authors also conducted analytical studies for correlation purposes. A prominent conclusion was that the Reynolds number difference between model and full scale had a large effect on airfoil properties, and therefore rotor performance. Going to full-scale and higher Reynolds numbers significantly increased the rotor performance (lower drag, higher lift). They also found that doubling the blade flapping inertia (lowering the Lock number) increased rotor L/D by about 8% at high advance ratio (1.7). That result was presented without further discussion. Their analytical studies also concluded that increased delta-3 pitch-flap coupling would improve flapping stability at high advance ratio.

1.2.1.7 UH-60A: Norman 2011 and Datta, Yeo, Norman 2013

The most recent high-advance ratio test was the full-scale UH-60A airloads rotor, tested in the U.S. Air Forces National Full-Scale Aerodynamics Complex (NFAC) facility at NASA Ames Research Center [17] (fig. 1.15). This test used the same rotor blades from a 1993 instrumented flight test of a UH-60A. The objectives

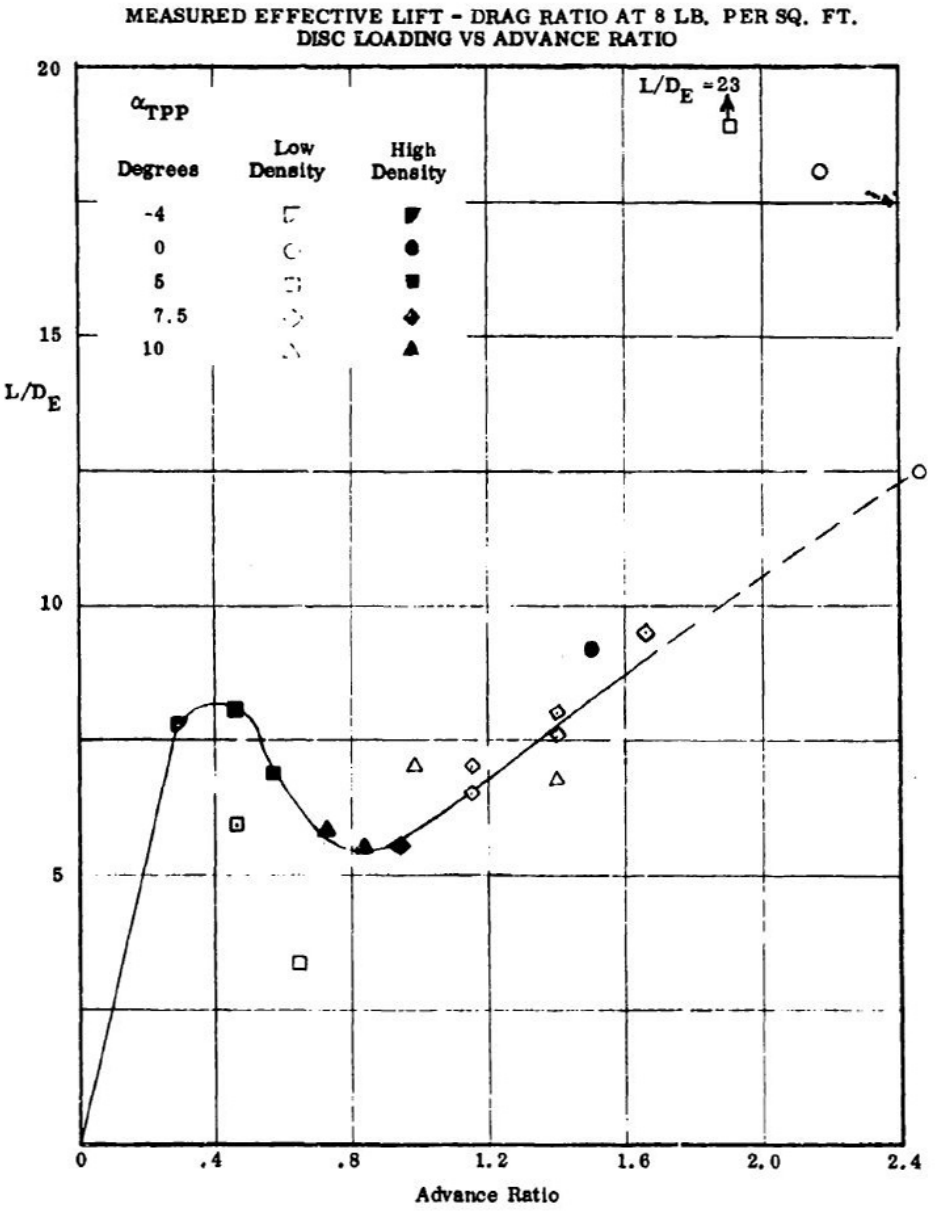

Figure 1.13: Measured effective rotor lift-to-drag ratio at constant disk loading for increasing advance ratio [16].

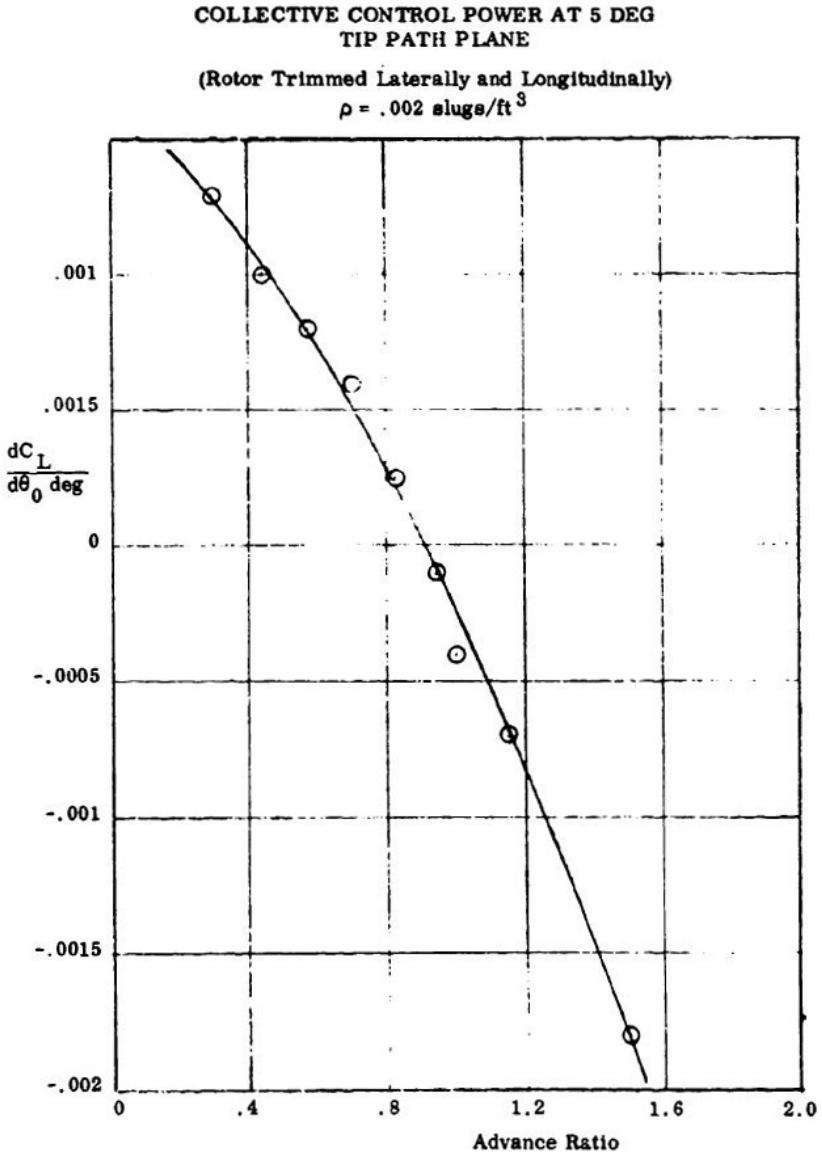

Figure 1.14: Change in lift sensitivity to collective versus advance ratio [16].

were to acquire a comprehensive set of quality data with which to challenge state-of-the-art modeling tools, and evaluate differences between the wind tunnel and flight testing environments.

Measurements were wide-ranging, and included rotor performance, blade pressures, blade loads, blade displacement (photogrammetry), and rotor wake particle image velocimetry. One rotor blade was instrumented with 235 pressure transducers (from the original flight test in 1993), in chord-wise arrays at 9 radial stations (fig. 1.16). Of those original 235 sensors, 160 functioned well for the entire wind tunnel entry. A separate rotor blade was instrumented with 28 strain-gage bridges for blade loads (flap bending, chord bending, and torsion).

The test plan encompassed much more than slowed-rotor, high-advance ratio cases, but those are not of primary interest to this review. Slowed-rotor conditions up to advance ratio of 1.0 were explored at 100%, 65%, and 40% of nominal rotor speed, with varying wind speed. Collective sweeps were conducted at three shaft angles: 0, 2, and 4 degrees (positive nose up).

Analysis of select data from this test were reported by Datta, Yeo, and Norman [18]. The authors published key results from the wind tunnel test including performance, vibratory loads, and blade pressures. The collective-thrust reversal trend with increasing advance ratio was evident, although there were few pitch angles measured at the highest advance ratios (fig. 1.17). The rotor lift-to-drag ratio was found to be quite poor at high advance ratios for zero shaft angle (fig. 1.18). The L/D was improved with rearward shaft angle (positive disk angle of attack), but was still significantly lower compared to lower advance ratios.

Figure 1.15: Instrumented UH-60A airloads rotor in the 40 x 80 ft NFAC wind tunnel at NASA Ames [17].

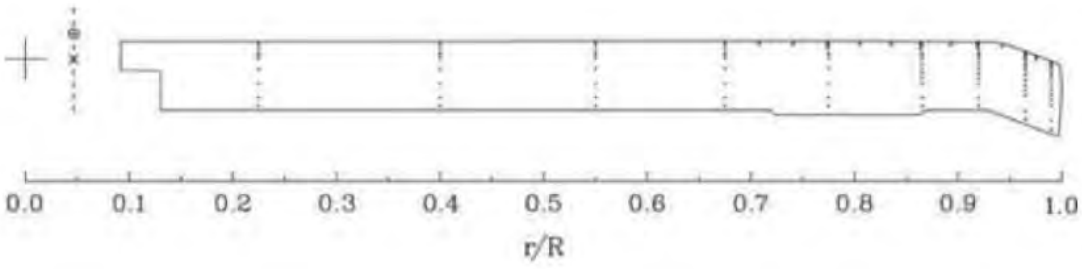

Figure 1.16: Distribution of pressure transducers on instrumented rotor blade [17]

Blade loads, particularly flap bending moment, were found to increase with advance ratio. The largest increases were observed in the 4 per rev harmonics of the bending moment. Torsion moment was generally seen to be equal or less at high advance ratio, however the magnitude on the retreating blade was sensitive to collective setting. Pitch link loads showed increases with advance ratio, which was partially ascribed to retreating blade impulse due to reverse flow.

Unsteady blade surface pressure measurements revealed complex flow patterns at high advance ratio on the retreating blade. Reverse flow due to high advance ratio resulting in apparent separation from the sharp trailing edge (aerodynamic leading edge in reverse flow), and a vortex forming and travelling chordwise from trailing edge to leading edge on the suction side of the airfoil (fig. 1.19). The authors dubbed this reverse-chord dynamic stall because of the similarities of the pressure readings with conventional dynamic stall. Integration of the pressure sensors gave the section pressure forces in the form of normal force, pitching moment, and chord force. Comparing the non-dimensional normal force and pitching moment, the authors concluded that the reverse-flow center of lift acts around 0.5c instead of the typically assumed 0.75c (reverse airfoil 0.25c) (fig. 1.20). For this reason it was concluded that the stall vortex would not be as detrimental to torsional loads as forward-flow dynamic stall, where the center of lift travels farther from 0.25c (the assumed blade structure shear center) towards the trailing edge. The authors also observed local supersonic flow near the advancing blade tip for slowed-rotor conditions, despite the tip Mach number being only 0.52, and the thrust and cyclic angles also being relatively small (fig. 1.21). They concluded that the blade must be experiencing

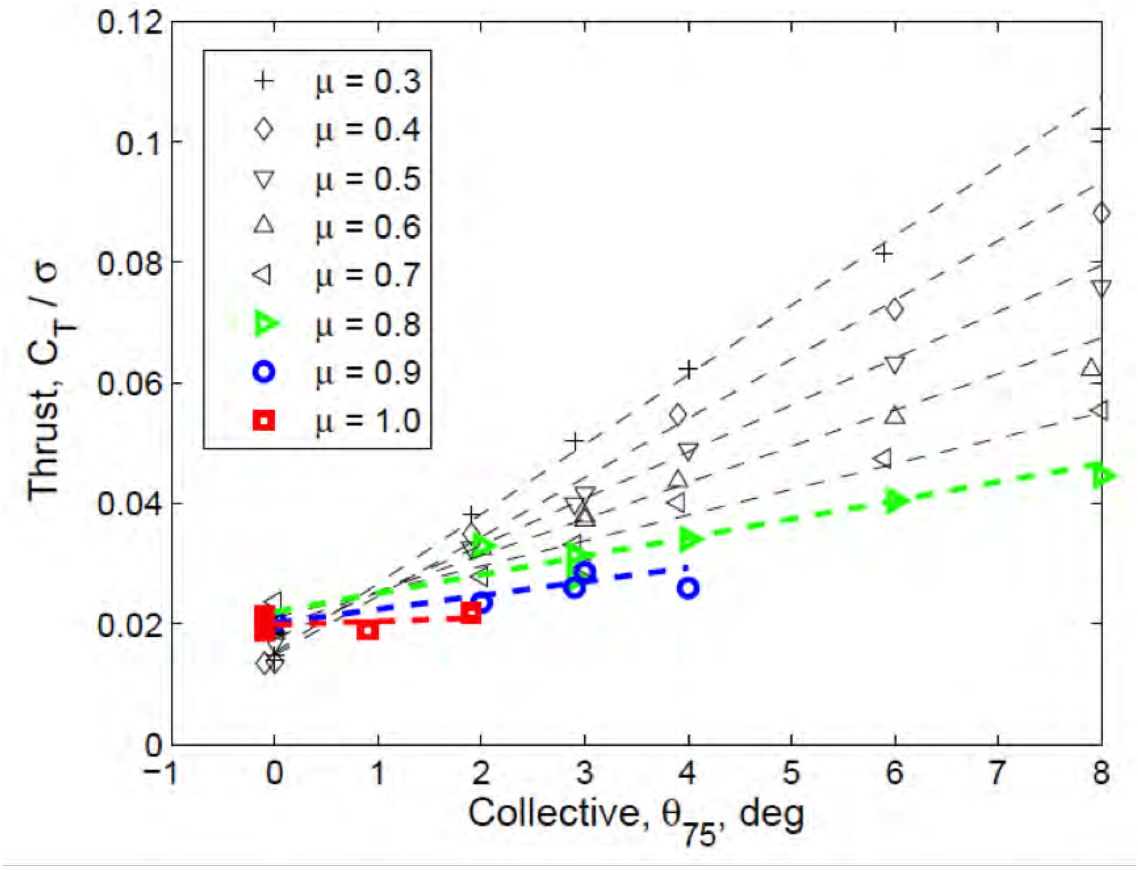

Figure 1.17: Collective thrust reversal trends evident in UH-60A slowed-rotor wind tunnel test [18].

significant elastic twist, resulting in large negative angle of attack in the outboard section, and therefore large suction peaks on the lower surface that accelerate the flow locally to supersonic conditions.

1.2.1.8 Quackenbush, Wachspress, McKillip, and Sibilia, 2011

Quackenbush et al tested a model rotor (4.33 ft, 1.32 m diameter) in the Glenn L. Martin Wind Tunnel at the University of Maryland (fig. 1.22) [19]. The tests

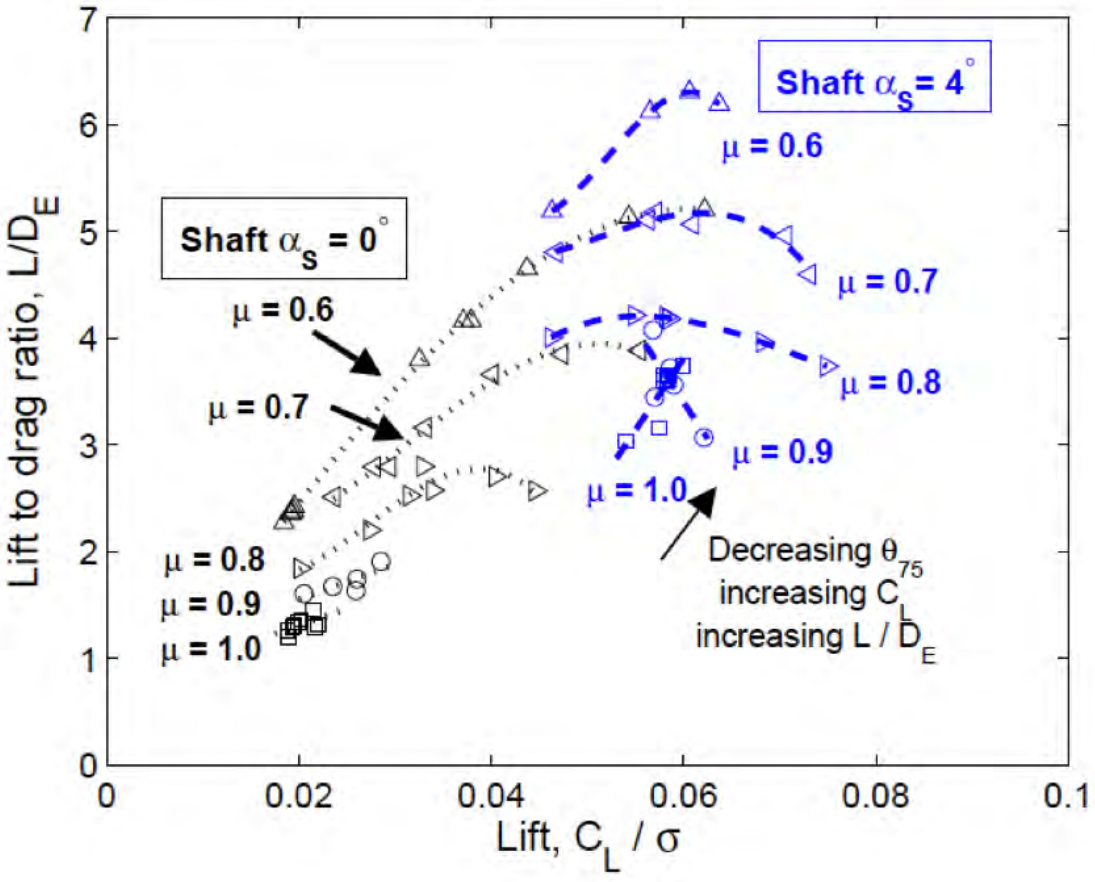

Figure 1.18: Lift to drag ratio versus lift for varying advance ratio. Zero and positive 4 deg shaft, 40% NR [18].

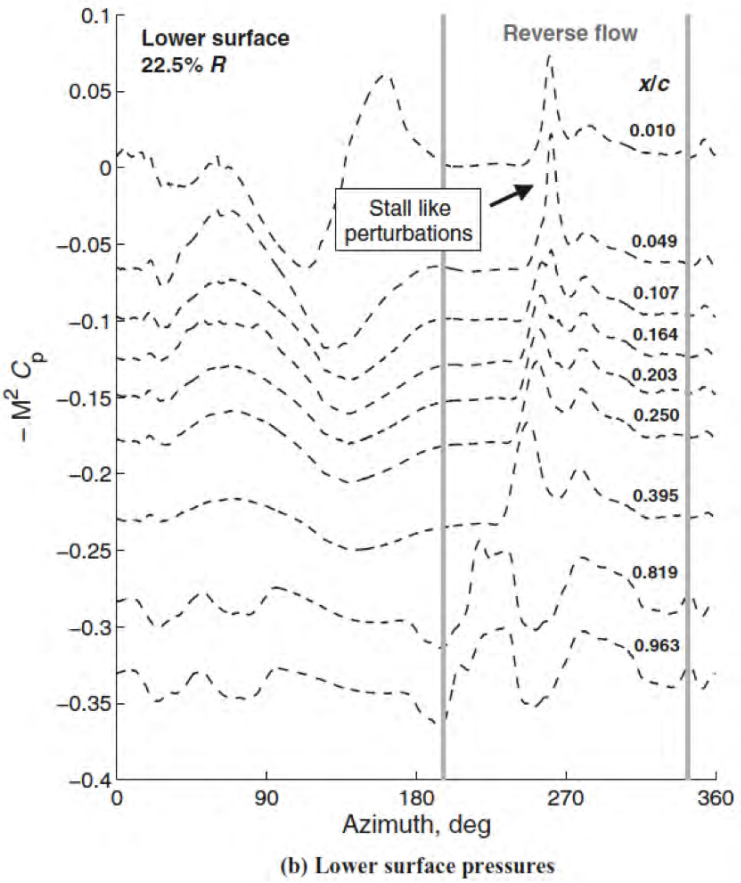

(b) Lower surface pressures

Figure 1.19: Chordwise pressure perturbations traveling from trailing edge to leading edge, indicating reverse-chord dynamic stall [18].

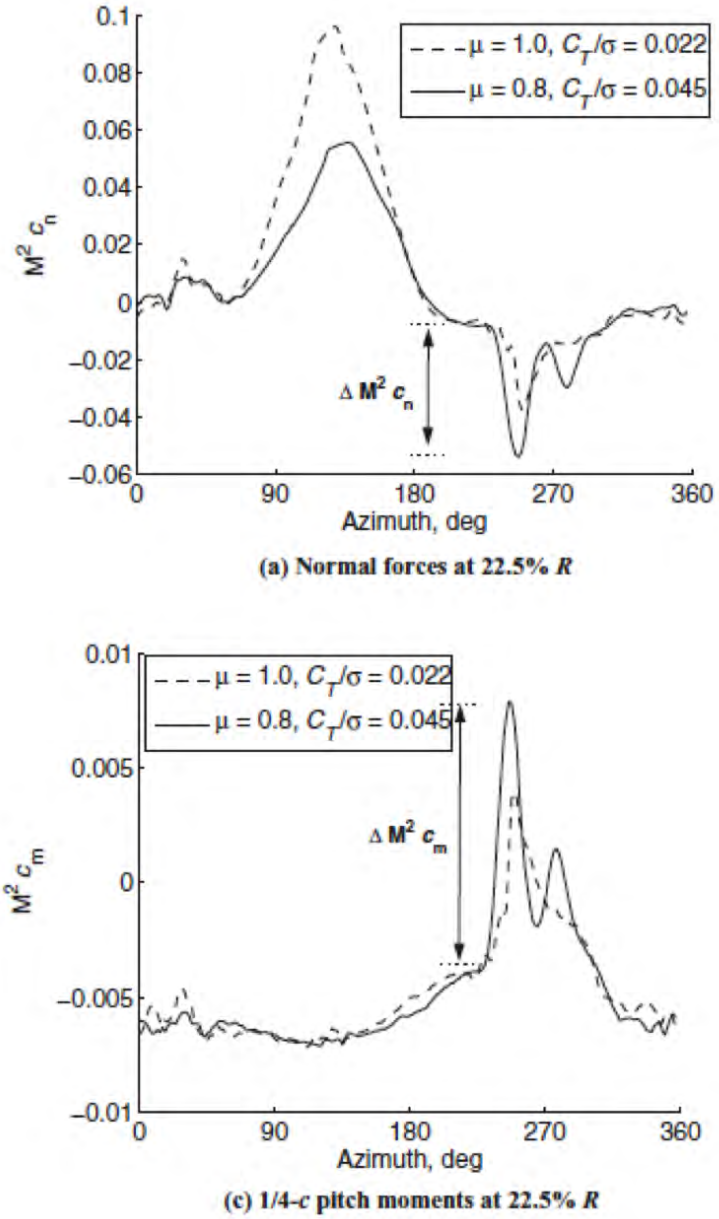

Figure 1.20: Section normal force and pitching moments from UH-60A test data showing retreating blade impulses [18].

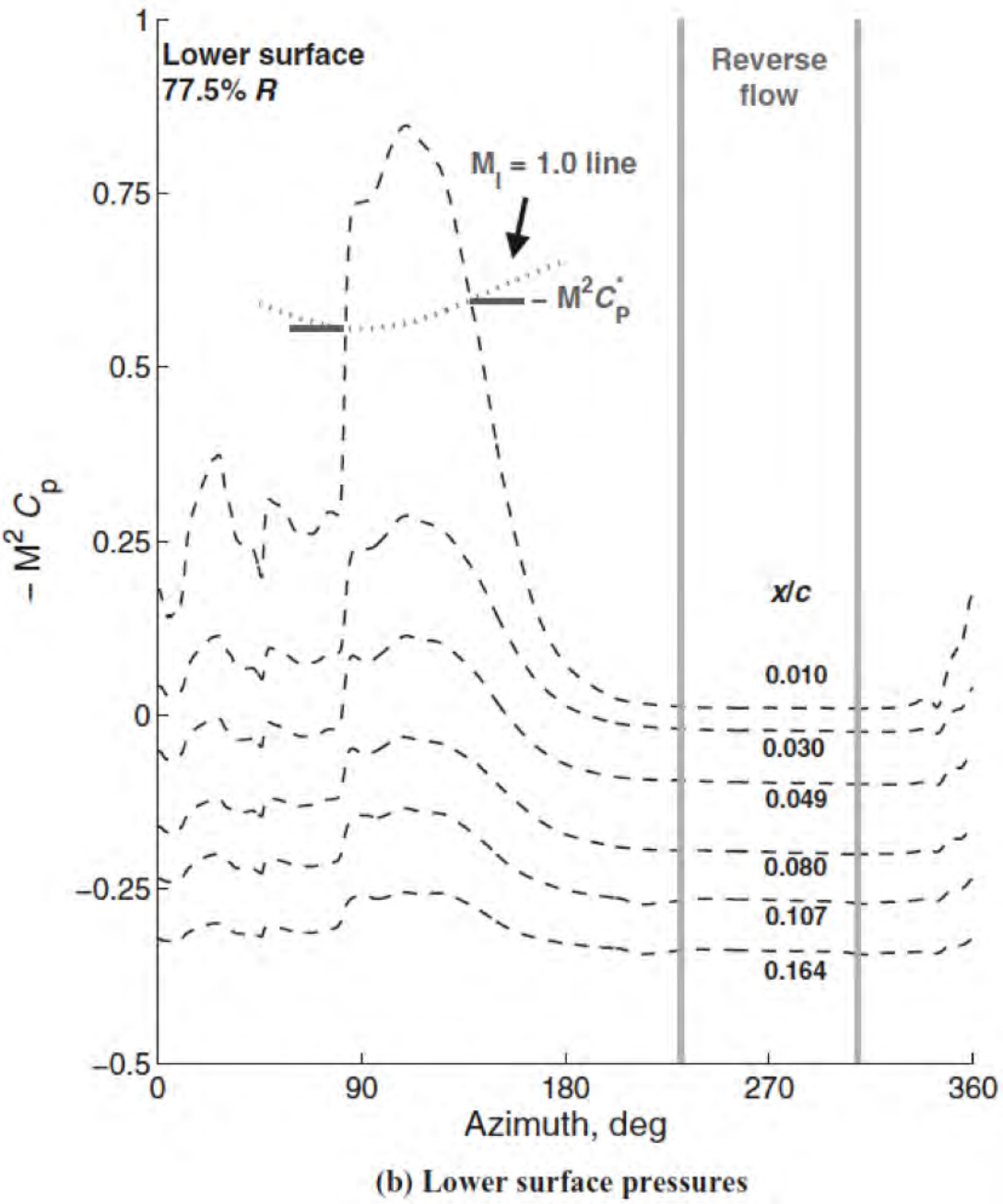

Figure 1.21: Pressure coefficients showing local supersonic velocities on the advancing blade [18].

were primarily with the rotor unpowered in autorotation, with measurements of rotor lift, rotor drag, and rotor speed. Unpowered operation was cited as being of interest for slowed-rotor compound helicopters. It also allowed comparison with existing gyrocopter data. Measured rotor lift and drag in autorotation showed similar trends as the full-scale autogyro rotor from Wheatley and Hoods PCA-2 tests (which went to an advance ratio of 0.7), but significantly extended the advance ratio range. This test reached a maximum rotor advance ratio of 2.0.

Some limited testing was conducted with the rotor powered, with rotor shaft torque being measured, up to advance ratio of 1.0. Shaft angle of attack, rotor blade flap angles, and blade root pitch angles were also measured. In-plane rotor force coefficient (CH) measurements were shown to be accurately predicted through analytical expressions when the mean rotor drag coefficient was set to 0.2, which was extracted from torque measurements in hover testing at zero-lift (fig. 1.23). The high drag coefficient was tentatively attributed to the low Reynolds number of the model blade sections.

Flow visualization was attempted using blade surface-mounted tufts, and an overhead camera and strobe light system. The rotor was at a shaft angle of attack of 2.8 degrees, with a collective pitch input of -1.1 degrees. Cyclic pitch was set to zero. The tufts revealed expected kinematic radial/yawed flow trends on the advancing portion of the rotor disk. The retreating blade in the third and fourth quadrants of the rotor disk showed more complex flow behavior at an advance ratio of 1.7 (fig. 1.24), that the authors attributed to vortical structures forming from flow separation starting at the sharp trailing edge (aerodynamic leading edge in reverse

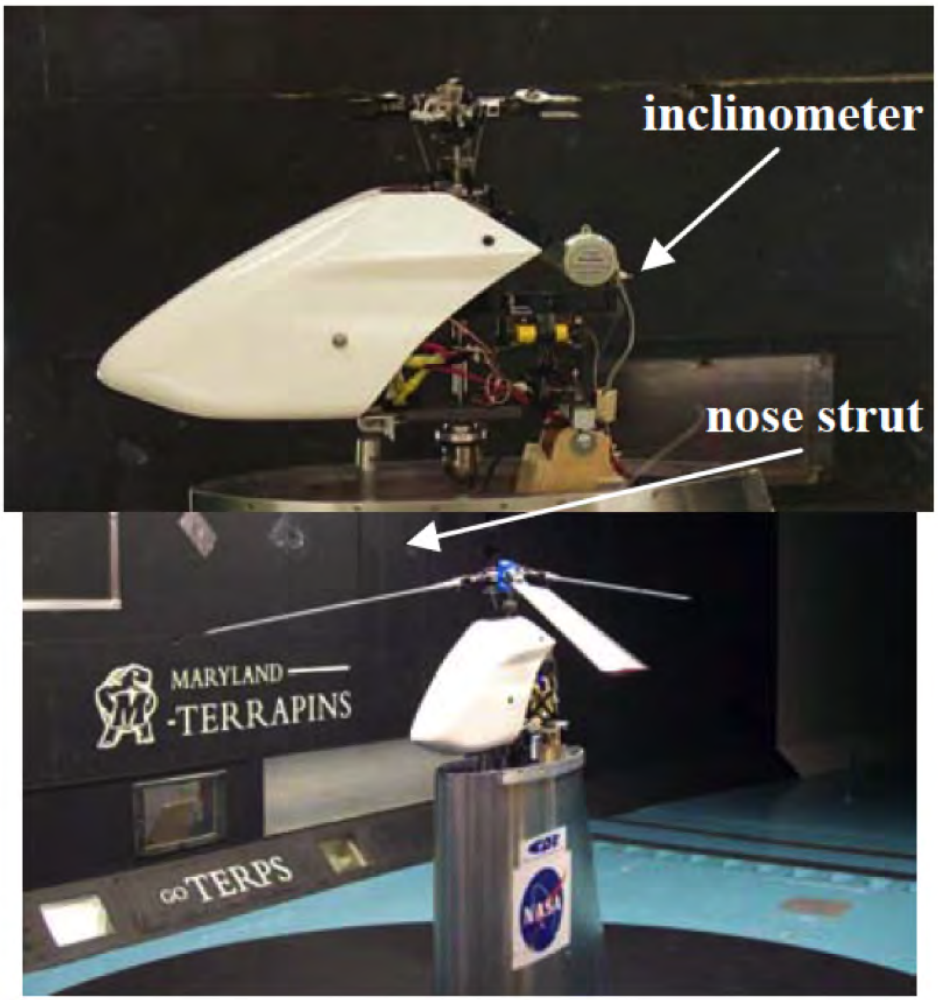

Figure 1.22: Wind tunnel test setup for Quackenbush, et al [19]

flow). However, at an advance ratio of 1.0, the retreating blade flow did follow the expected kinematic flow vectors.

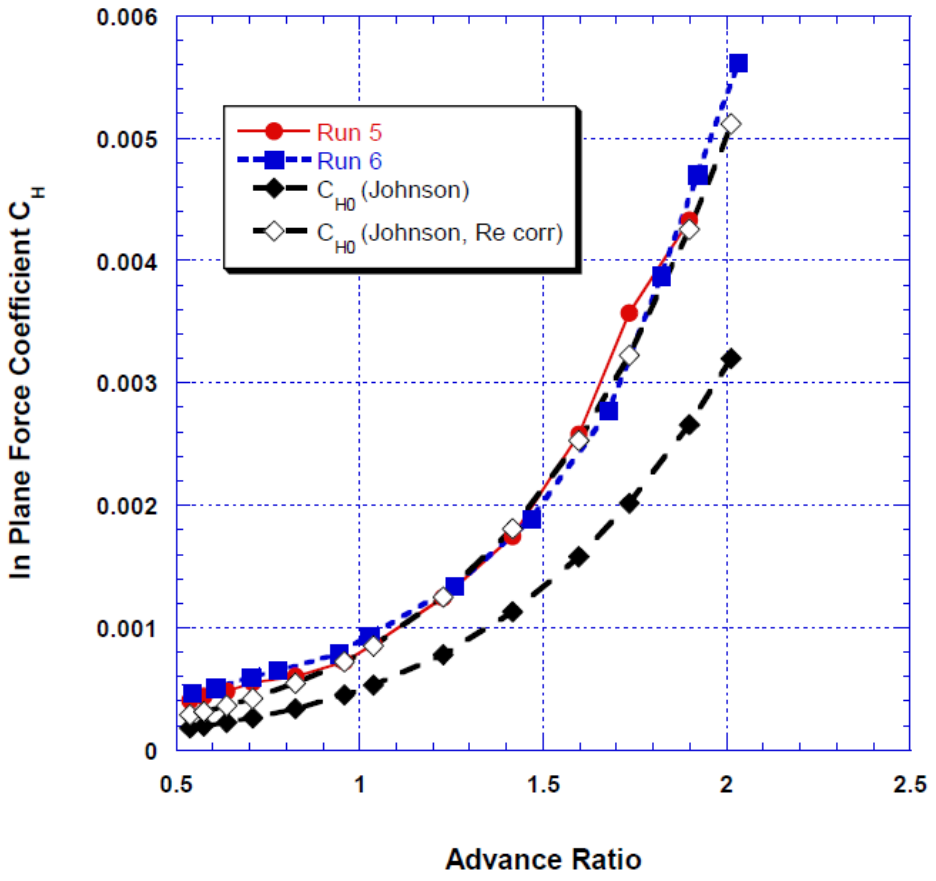

Figure 1.23: In-plane rotor force coefficient measured vs theory for adjusted mean airfoil drag coefficient [19].

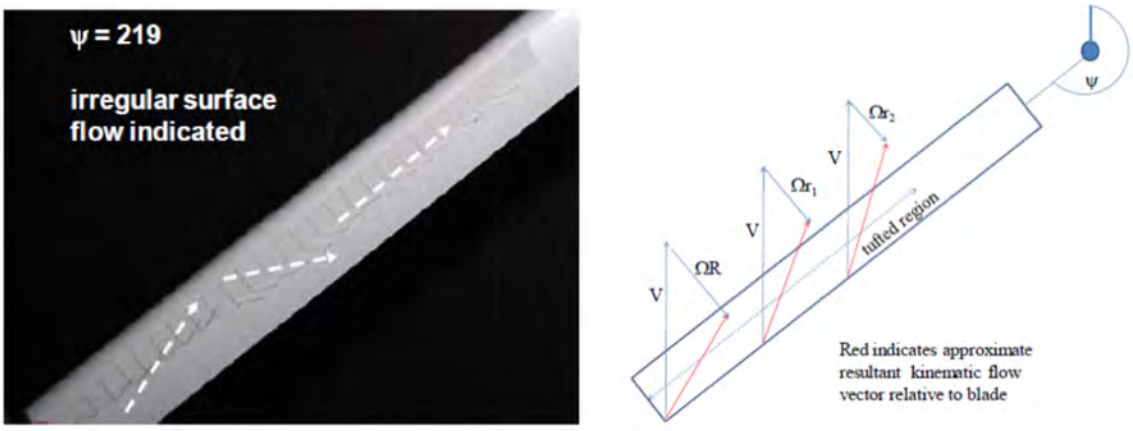

Figure 1.24: Flow visualization (surface-mounted tufts) results at advance ratio of 1.7 showing surface flows not following the resultant kinematic flow vectors [19].

1.2.2 High Advance Ratio Analysis and Correlation

1.2.2.1 Wheatley, PCA-2, 1934

An analysis method published by Wheatley was used for comparison with the PCA-2 autogiro test that was conducted by Wheatley [11]. The method was largely similar to the theories of Glauert and Lock, with the main extensions being the inclusion of blade twist, reverse-flow effects, and tip-losses. Aerodynamics due to blade flapping were neglected, and induced velocity was assumed to be uniform by a fixed-wing analogy. Flapping motion was considered up to the second harmonic of the Fourier series. For section aerodynamics, the linear region of lift was represented by a lift-curve slope.

1.2.2.2 Gessow and Crim, 1955

Alfred Gessow and Almer Crim published a 1955 NACA technical note detailing a method to predict the transient and steady-state behavior of flapping motion for articulated or teetering rotors [20]. The primary interest was to model the stability of flapping rotors at advance ratios above 1. The objective was to account for more complexities associated with high-advance ratio flight than were typically included in prior analyses, such as Wheatley. Specifically, the improved analysis would account for blade section stall, compressible flow, reversed-flow velocities, and non-small angles for section inflow and blade flapping. Rigid blades (no flexibility in bending or torsion) were still assumed. Blade stall, compressibility effects, and reverse-flow velocities were included by allowing for table look-up of actual airfoil properties at all angles of attack and Mach numbers.

The model essentially relies on solving the rotor blade equations of motion through numerical integration using a Runge-Kutta methods using digital computers. Gessow and Crim used the time-history of the integration convergence as an analog to the transient behavior of the rotor at a certain flight conditions and control inputs. Example simulations showed that higher Lock numbers (lighter rotor blades) resulted in a flapping instability of articulated rotors at a high advance ratio of 3.0 (fig. 1.25).

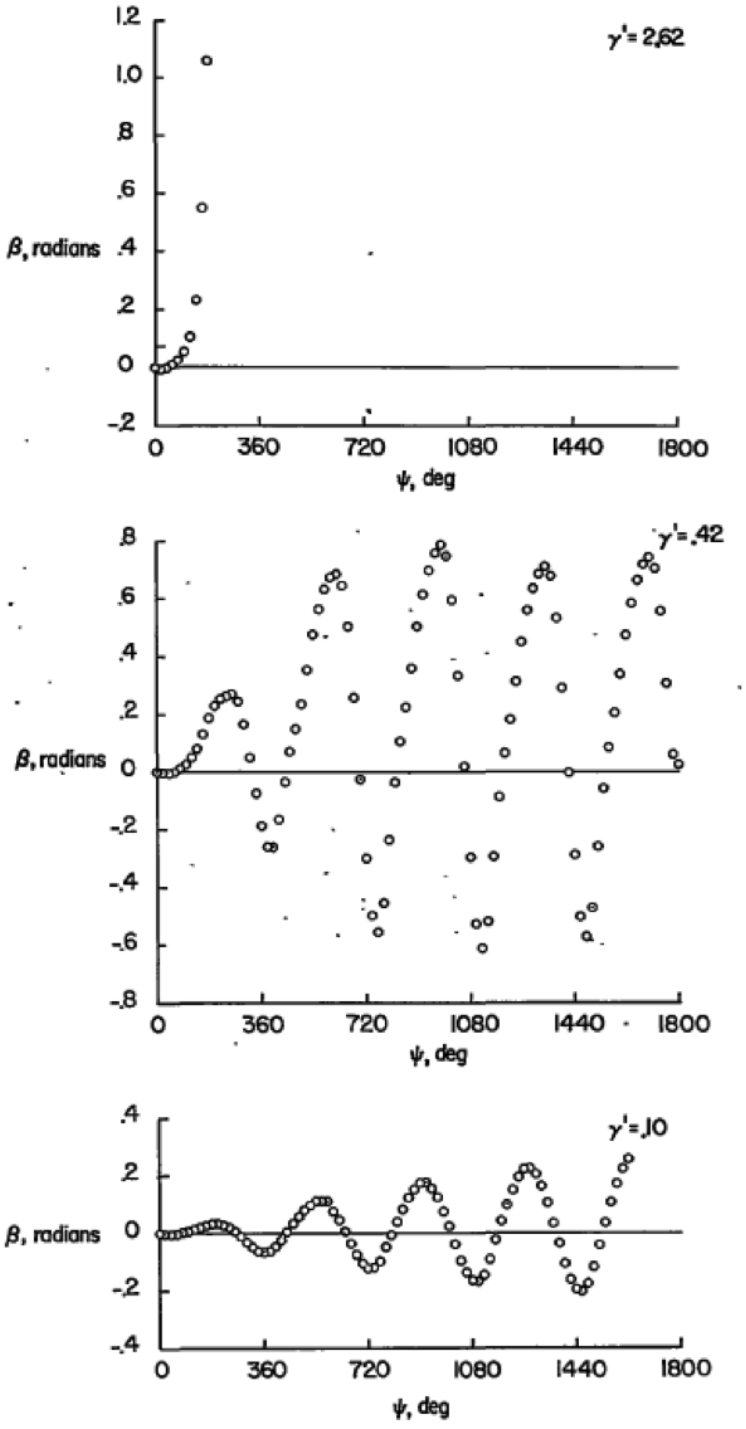

Figure 1.25: Predicted transient blade-flapping motion, $\mu = 3.0$, $\theta_{.75} = 2$ deg [20].

1.2.2.3 Harris, Theory versus Test, 2008

In 2008, Harris compiled a comprehensive report on the state-of-the-art of slowed-rotor, high advance ratio predictive capabilities [21]. The report focused primarily on the most commonly used modern comprehensive analysis codes (i.e. CAMRAD II, RCAS, and CHARM). Harris compared these results with the theory available in 1934 (Developed through the efforts of Wheatley, Bailey, Lock, and Glauert), and benchmarked both against available full-scale rotor test data. This report is extensive and cannot be fully covered in this dissertation, but pertinent conclusions will be summarized.

The results of the study for modern theory showed significant improvements in the prediction for rotor L/D. The 1934 theory in general over-predicted L/D. Harris still found deficits in the modern analysis codes beyond advance ratios of 0.62, particularly with respect to predictions of control positions and shaft angle of attack.

In the experimental data (H-34 rotor), there was non-zero lift measured at zero shaft angle and zero collective pitch (fig. 1.26). Harris concluded that this was due to elastic torsion caused by an unexpected non-zero pitching moment of the airfoil section at zero angle of attack.

The blade root-cutout drag was also found to be a major driver of rotor drag at high advance ratio, and therefore needs to be accounted properly for accurate L/D predictions. In this study, the H-34 rotor blade root-cutout was assigned a drag coefficient of approximately five-times that of the NACA0012 airfoil section to

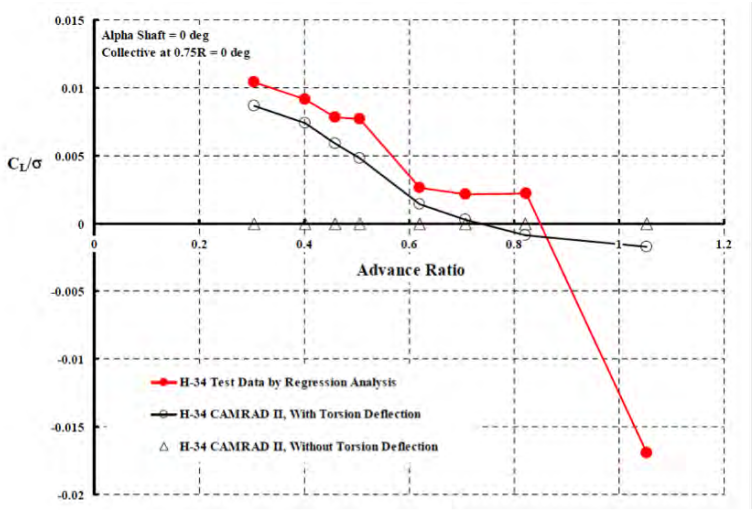

Figure 1.26: Predictions of rotor lift at zero shaft tilt and zero collective, with and without torsion elasticity modeled [21].

calibrate predictions with test data.

1.2.2.4 Floros and Johnson, 2009

Floros and Johnson [22] published a correlation study of CAMRAD II comprehensive analysis with the isolated rotor data set published by Jenkins [13]. The goal was to qualify the capabilities of CAMRAD II to predict rotor performance at high advance ratio, and then use it to analyze a generic compound helicopter design. The authors showed excellent agreement with the rotor thrust trends for collective sweeps over a range of advance ratios (fig. 1.27(a)). They observed an offset in the absolute values for the test data, where there was not zero thrust for the zero collective case (which they surmised would be expected for a symmetric airfoil rotor at zero shaft tilt). Assuming a testing measurement error, they therefore applied a

bias offset to the test data in pitch and thrust coefficient (fixed for all test cases). The predictions extended to higher positive collective settings than were present in the test data, and a flattening of the thrust trends was observed. The authors hypothesized that this was an indication of the airfoils stalling in reverse flow. Floros and Johnson stated that the advance ratio where thrust reversal occurs depends on the airfoil and the blade twist, but detailed explorations of those sensitivities were beyond the scope of their paper. For this rotor, the critical advance ratio was between 0.9 and 1.0.

Rotor torque coefficient and in-plane force coefficient predictions by the analysis showed correct trends but with slope and magnitude errors (fig. 1.27(b), fig. 1.27(c)). These errors were explained by the difficulty of predicting drag forces vs. lift forces, and by the likelihood of load-cell measurement error due to the low dimensional magnitude of the applied loads during the test.

1.2.2.5 Bowen-Davies and Chopra, 2014–2015

Bowen-Davies and Chopra correlated the UMARC (University of Maryland Advanced Rotor Code) comprehensive analysis tool with the slowed-rotor UH-60A data set [23–25]. Rotor thrust correlation was found to deteriorate above an advance ratio of about 0.7 (fig. 1.28). Rotor drag force was significantly under-predicted if rotor root drag was ignored (fig. 1.29). A fixed correction factor (not varying with pitch) to the drag coefficient of the root shank did not correct the drag correlation at all collective pitch angles (fig. 1.30). The authors obtained much-improved drag

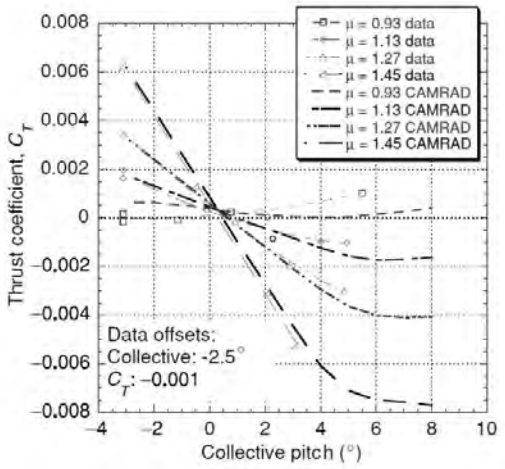

(a) Thrust

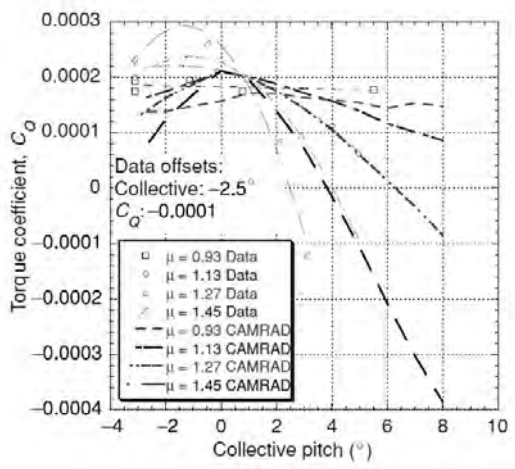

(b) Torque

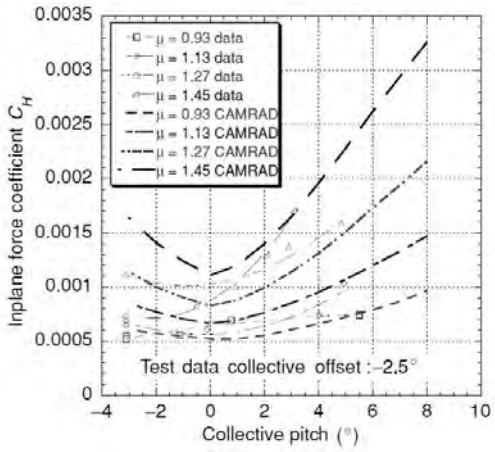

(c) In-Plane Force

Figure 1.27: CAMRAD thrust, torque, and in-plane force correlation with test data [22].

correlation when the impact of the fuselage was approximately modeled as an upwash (fig. 1.31). Cyclic pitch angle prediction also degraded at high advance ratios (beyond 0.7).

Oscillatory (1/rev and above) and vibratory (3–5/rev) blade flap bending moments at 50% span were well-captured by UMARC for all advance ratios in both magnitude and phase. Vibratory blade torsional moments at 50% span not well-predicted in magnitude above advance ratio of 0.5. At an advance ratio of 0.9, the peak vibratory torsional moment is under-predicted in magnitude by 70%, and the phase also shows poor alignment. However, at this same condition, the peak-to-peak oscillatory torsional moment is only under-predicted by about 25%, which indicates a cancelling of errors for the first 5 harmonics.

Airloads, particularly sectional normal force, were calculated in UMARC and compared to the UH-60A experiment, which had pressure sensors embedded throughout one rotor blade. The magnitude and phase of the normal force oscillations at an outboard section, 92%R, were well-captured for all advance ratios. It was found that modeling a second trailing vortex (from the root) significantly improved correlation around zero azimuth, where the root vortex interacts with outboard sections of the blade (fig. 1.32).

1.2.2.6 Ormiston, 2004–2012

Ormiston [26–28] used RCAS comprehensive modeling tool with a rigid blade assumption to correlate with the UH-1 and H-34 rotor tests detailed previously in

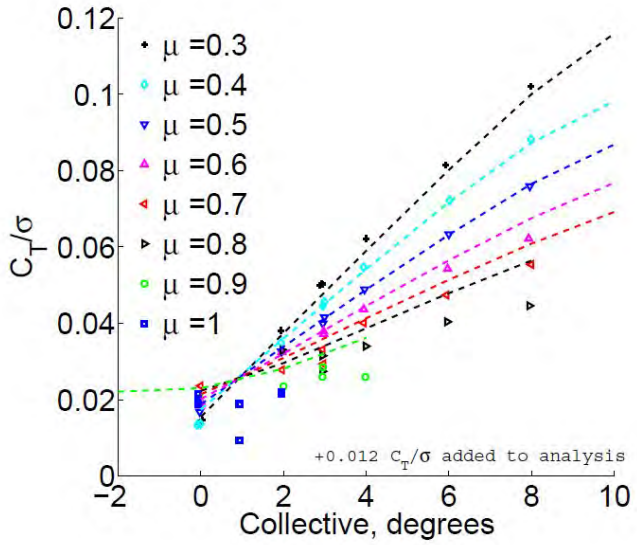

Figure 1.28: UMARC correlation with UH-60A test data for thrust variation with collective [23].

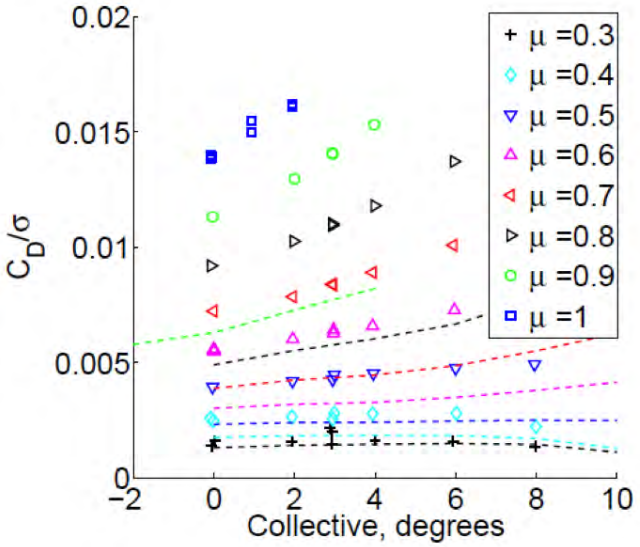

Figure 1.29: UMARC rotor drag correlation with no root shank corrections [23].

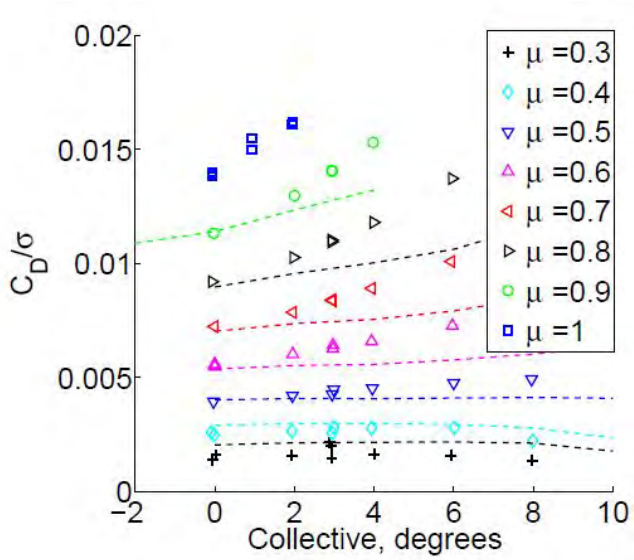

Figure 1.30: UMARC rotor drag correlation with a fixed root shank drag coefficient assumption [23].

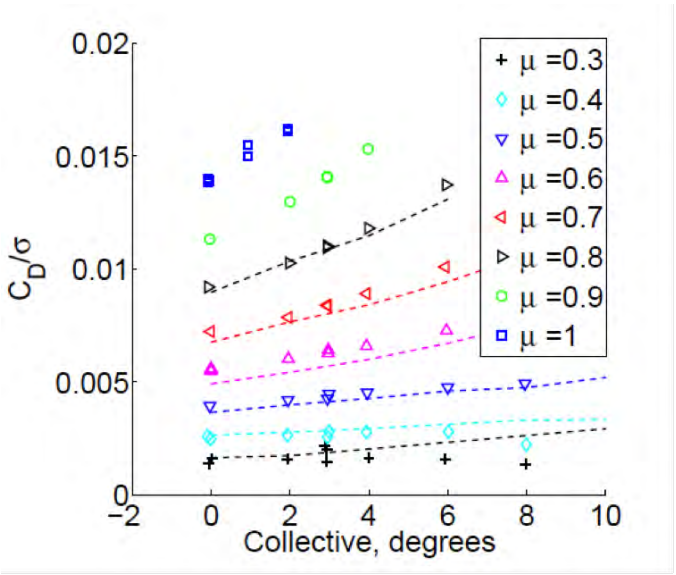

Figure 1.31: UMARC rotor drag correlation with root shank drag coefficient and a fuselage upwash model [23].

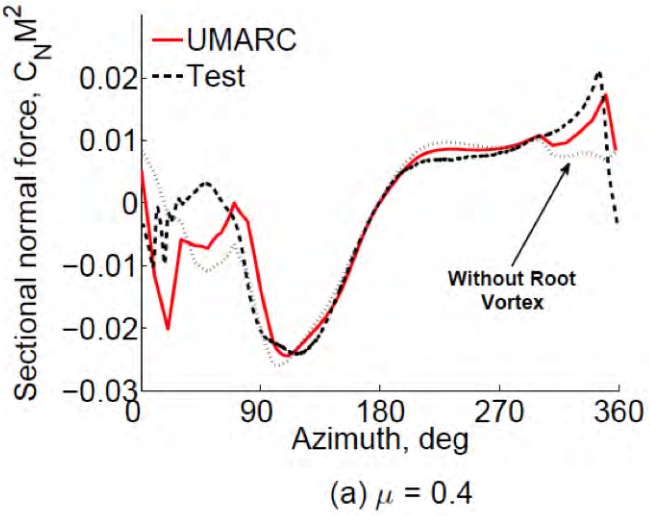

Figure 1.32: Section normal force correlation with the effects of including a root vortex model in UMARC [23].

this dissertation. He also used RCAS with elastic blade modeling to correlate with the UH-60A slowed-rotor tests. In both cases, Peters-He dynamic inflow was used to model induced velocity. Rotor lift (thrust) vs. collective correlations for the UH-60A test using RCAS simulation is shown in fig. 1.33.

Ormiston investigated the induced power trends in a rotor at high advance ratio using an analytical formulation. Non-uniform inflow modeling shows that the induced power trends given by Glauerts classical momentum theory (uniform inflow) are not accurate above advance ratio of about 0.4 (fig. 1.34). Induced power does not asymptote to zero but instead increases significantly between 0.4 and 1.0 advance ratio.

Ormiston developed an induced power model, based on linear aerodynamic theory and using an analytical formulation to provide insights that can sometimes

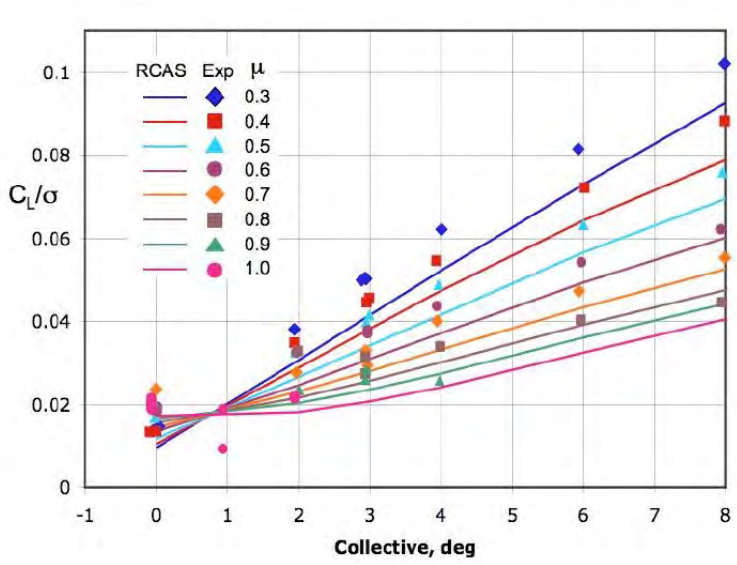

Figure 1.33: RCAS correlation with UH-60A [28].

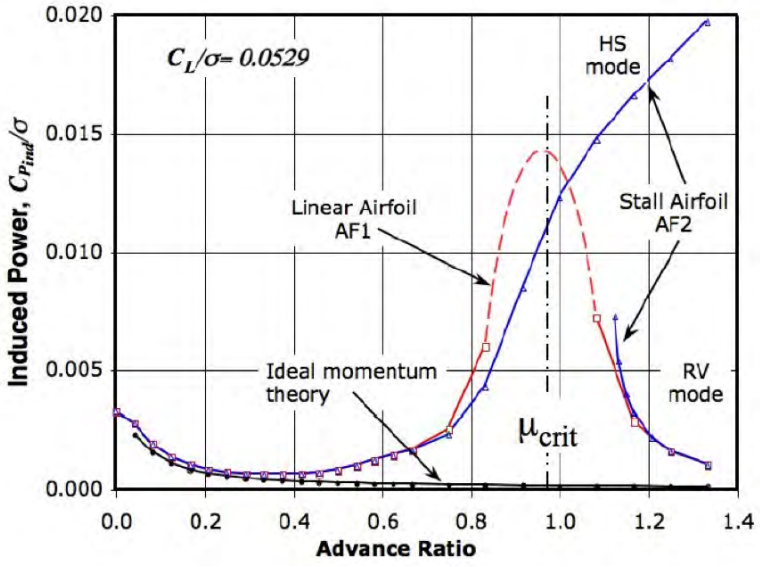

Figure 1.34: Induced power trends for various analytical models and airfoil representations [28].

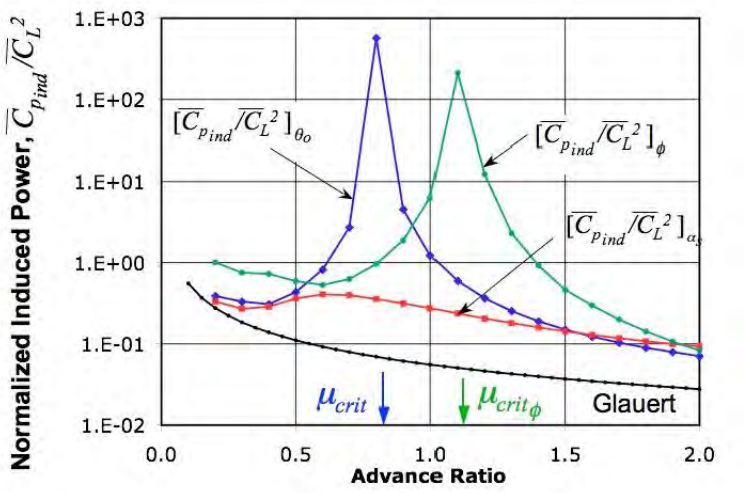

Figure 1.35: Effect on induced power for the three modes to control rotor lift: collective θ_0, shaft angle α_s, and blade twist ϕ [28].

be opaque using numerical vortex wake methods. The model neglects profile drag, and uses sectional airloads (no stall) and induced velocities integrated over the blade span and azimuth to calculate induced power. The resulting power constants were solved using RCAS computations with a non-uniform dynamic inflow model. Through this exercise, Ormiston could easily show sensitivities of rotor induced power to three modes of controlling rotor lift: collective pitch, disk angle of attack (shaft tilt), and blade twist rate (fig. 1.35). The trim condition for all three modes was zero hub moments (roll and pitch equilibrium). Disk angle of attack was shown to be the more efficient (lower induced power) mode for the lifting rotor. Collective pitch and twist rate both experience singularities at critical advance ratios where there is no lift sensitivity.

By adding a simple formulation for profile power, Ormiston calculated the

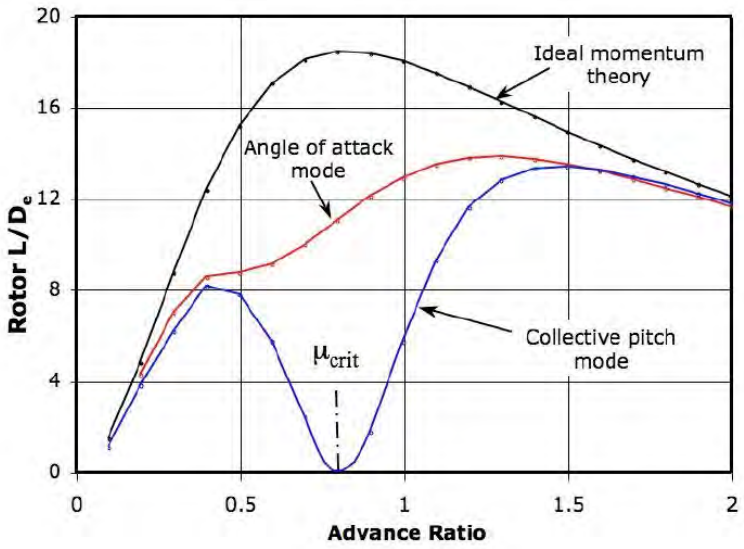

Figure 1.36: Rotor L/D_E for two control modes for hypothetical rotor [28].

L/D_E of the rotor for a fixed lift coefficient over a range of advance ratios (fig. 1.36). The takeaway result was that the angle of attack mode of rotor lift was more efficient than using collective pitch. The study also revealed a fundamental speed limit of a conventional single main rotor helicopter that is independent of blade stall or compressibility effects, and instead is a consequence of increases in induced power due to severe non-uniformity of inflow.

Ormiston hypothesized that the critical advance ratio (onset of collective thrust reversal) would be sensitive to root cutout, since the inboard airfoils in reverse flow were responsible for negative lift with increased collective pitch. Therefore, increasing blade root cutout should delay the critical advance ratio.

1.2.2.7 Montaudouin, Reveles, and Smith, 2014

Montaudouin, Reveles, and Smith [29] conducted a computational study on rotor aeromechanics at high advance ratios, using the aforementioned 2011 experiment by Continuum Dynamics [19] as a benchmark for correlation. The simulation used a loose-coupled CFD-CSD (Computational fluid dynamics with computational structural dynamics) strategy, with Overflow as the fluid solver and Dymore as the structural solver. Two trim targets were implemented, experimental thrust and zero torque (the experiment was in autorotation).

The authors observed blade-vortex interactions in the aft quadrants of the rotor disk, with the max severity of the interactions occurring at advance ratios of 1.0 (fig. 1.37). At higher advance ratios, the wake structure did not have a severe interaction, but this could change depending on the specific rotor geometry (i.e., number of blades).

1.2.2.8 UH-60A: Potsdam, Yeo, and Ormiston, 2013

Potsdam, Yeo, and Ormiston [30] conducted analysis correlations with the UH-60A slowed-rotor wind tunnel test database. Both comprehensive analyses (CAMRAD II and RCAS) and CFD-CSD (Helios) [31] were performed. All three analyses correctly predicted the trends of the steady loads and trimmed control angles, with varying levels of absolute agreement. In general, thrust was well predicted for all analyses (fig. 1.38). However, rotor drag and torque correlations were not satisfactory for any of the three tools (fig. 1.39). Modeling of the root shank drag was shown

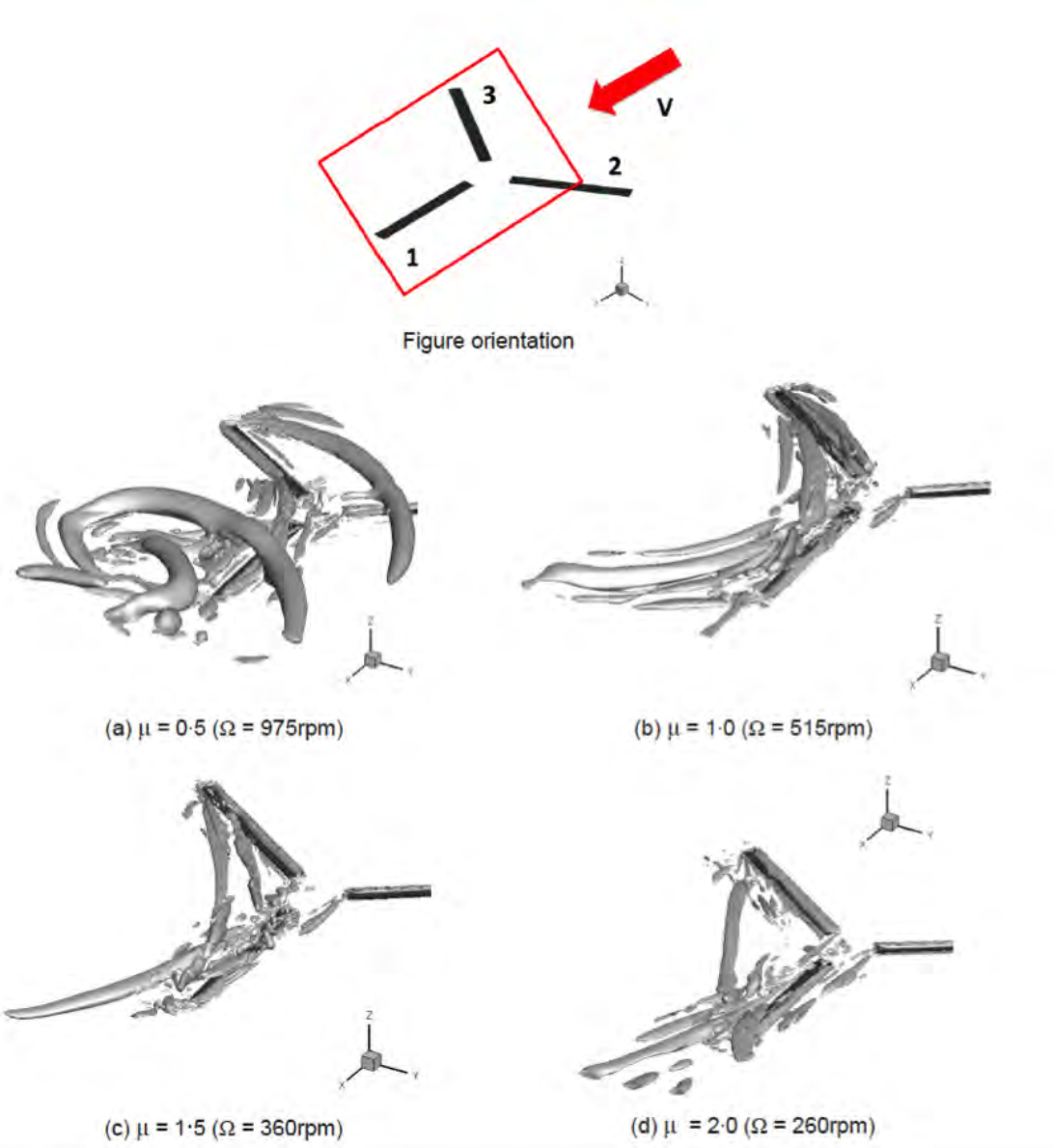

Figure 1.37: Blade-vortex interaction visualizations from CFD for varying advance ratio [29].

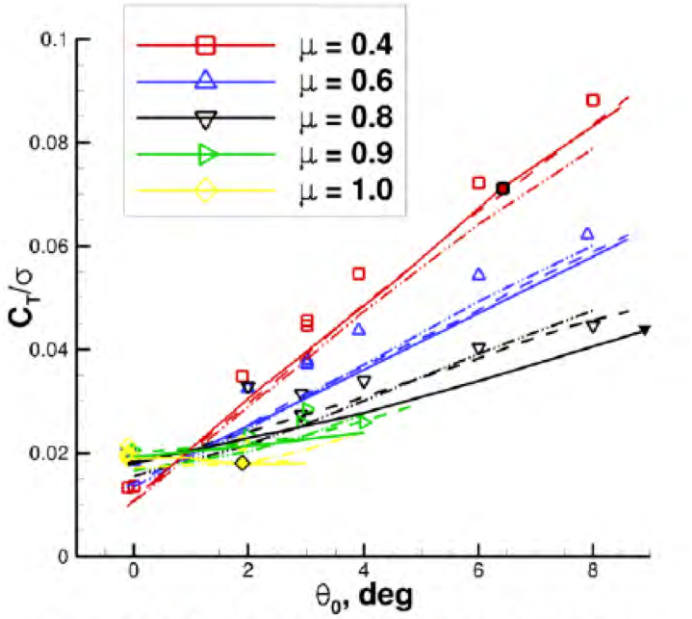

Figure 8 Thrust coefficient vs. collective:
symbols – test, —— Helios, – – – CAMRAD, –··– RCAS

Figure 1.38: Thrust coefficient vs collective correlation for various predictive tools [30].

to be important for performance predictions but did not affect airloads significantly. The comprehensive tools had to rely on empirical corrections for shank drag, while CFD could model the effects of the geometry directly. Blade vibratory loads were well-predicted by all analysis tools, for both flap and torsion moments at high advance ratio (fig. 1.40, fig. 1.41). Pitch link unsteady loads were also well-captured for CFD-CSD.

1.2.3 Summary of the State-of-the-Art

Predictive capabilities of modern rotor analyses for rotor aeromechanics at high advance ratios were assessed by several authors.

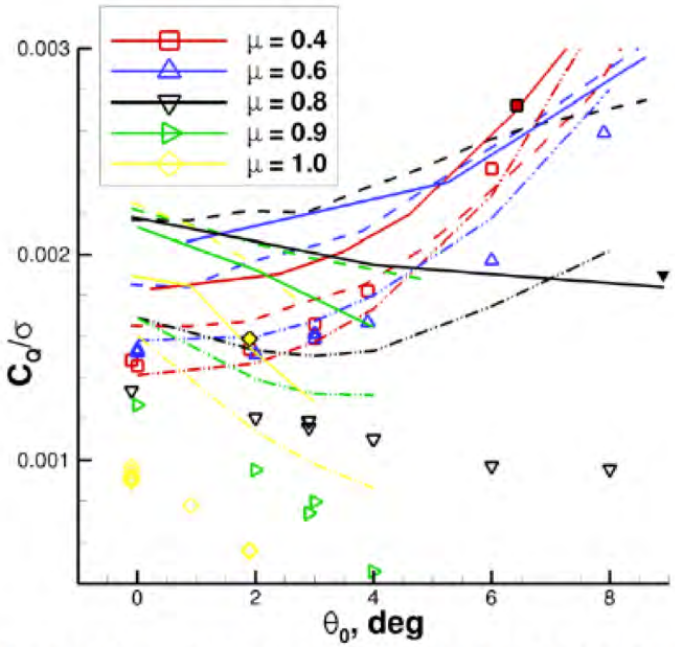

Figure 10 Rotor torque coefficient vs. collective: symbols – test, —— Helios, – – – CAMRAD, –··– RCAS

Figure 1.39: Rotor torque correlation for CFD and comprehensive analyses [30].

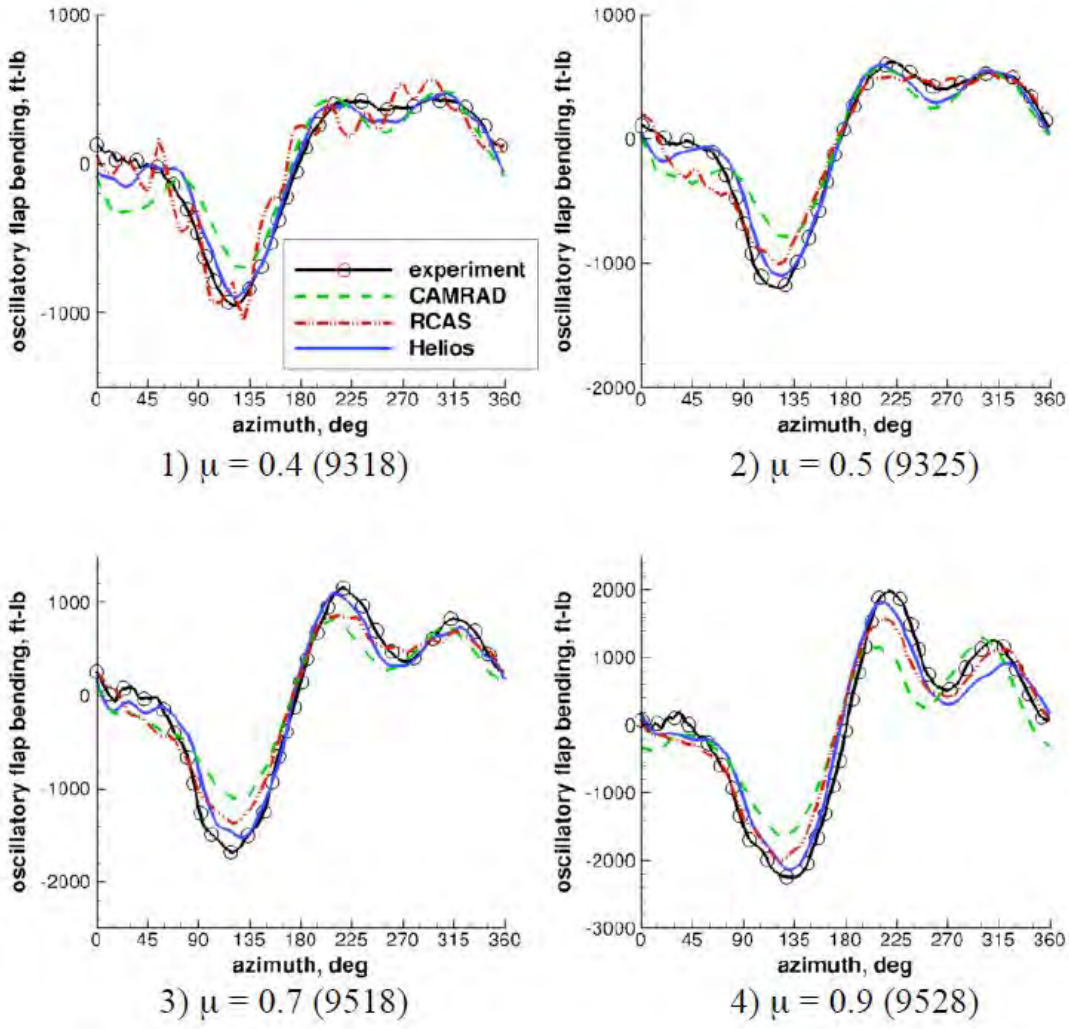

Figure 1.40: Oscillatory blade flap bending moment, $\alpha_s = 4$ deg, $C_T/\sigma = 0.063$, r/R = 0.50 [30].

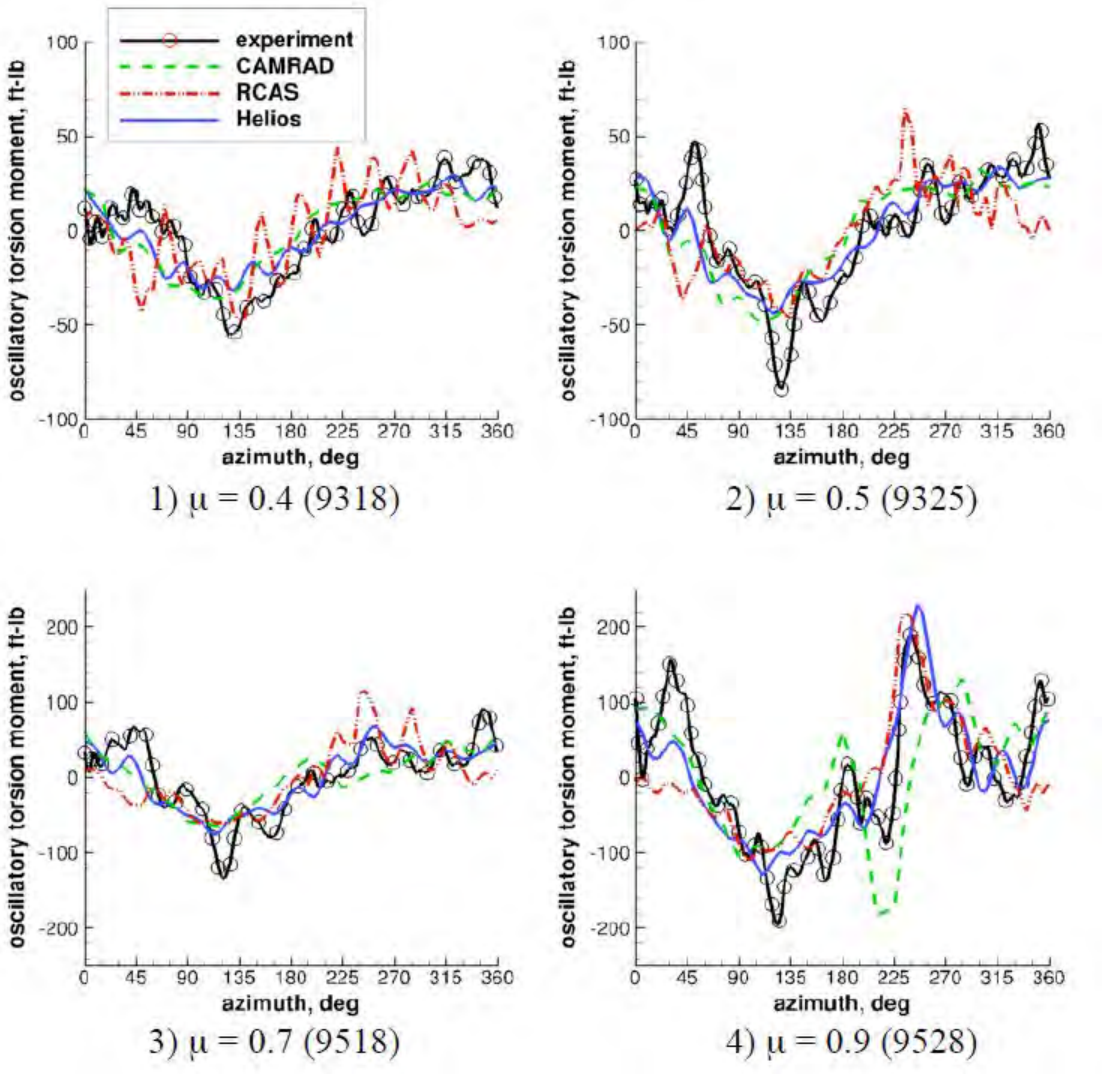

Figure 1.41: Oscillatory blade torsional moment, $\alpha_s = 4$ deg, $C_T/\sigma = 0.063$, r/R = 0.50 [30].

General conclusions from the studies are as follows:

1. Rotor Performance

   (a) Rotor performance—meaning rotor thrust, drag, and torque—was measured in almost all of the experiments.

   (b) Rotor thrust can be adequately predicted by modern comprehensive analysis methods for all testing advance ratios. There is scatter amongst specific tests, and specific analysis programs, but generally the correlation is acceptable for design purposes.

   (c) Rotor H-force, and therefore rotor drag, are not predicted satisfactorily at high advance ratio. Typically, the blade root (shank) region begins to drive the rotor drag, and is generally only captured in comprehensive analyses using empirical correction factors. CFD can more accurately predict this drag if the correct geometry is included in the model. Significant under-prediction of drag can result if this component is ignored.

   (d) Rotor torque for the UH-60A correlations was shown to be over-predicted by both CFD and comprehensive analysis.

   (e) The errors due to rotor drag prediction filter into rotor L/D, which is sufficiently predicted for conceptual design studies.

2. Rotor Vibratory Loads

   (a) Vibratory blade loads were only measured in two experiments, and only the UH-60A test had a wide range of measurements useful for analytical

validation studies. Vibratory hub loads were measured in the UH-60A tests, but issues with the dynamic calibration has delayed publication of comprehensive results as of the writing of this work.

(b) Flapwise blade bending moment loads were well-predicted (within 10%) by comprehensive analysis for both phase and magnitude, reflecting the correlations obtained from section normal forces. ([23, 25]).

(c) Blade oscillatory torsion moments were not well-captured by comprehensive analysis above advance ratios of 0.5. This again correlates with the poor predictions of sectional pitching moments made by analysis.

(d) CFD/CSD analysis generally performed better than comprehensive analysis at capturing 1–5/rev harmonic magnitudes of blade flap bending and torsional moments at high advance ratio, but at much higher computational cost.

These correlation studies were focused primarily on four full-scale rotor experimental data sets and two model-scale experiments. These six experiments represent nearly all of the available data for edgewise rotors operating above advance ratios of about 0.7. The conclusions stated above regarding analysis correlations of loads were all from the UH-60A slowed-rotor dataset, a single experiment that went to a maximum advance ratio of 1.0. There is a clear need for more controlled rotor experiments at high advance ratio that measure performance, vibratory loads, and airloads. Additional experiments should also investigate a variety of rotor geometries, and increase the advance ratio envelope. A summary of the existing experi-

			Performance																					
				Steady hub loads					Vib hub loads					Blade Loads						Advance Ratio				
Test	Full-Scale	Trimmed	Torque	Thrust	Drag	Side Force	Pitch Moment	Roll Moment	Thrust	Drag	Side Force	Pitch Moment	Roll Moment	Blade bending	Blade Torsion	Blade lag bending	Pitch link loads	Airloads	PIV Flow Meas.	μ > 0.5	μ =1.0	μ >1.0	μ > 1.5	μ > 2.0
Berry 2014		X	X	X	X	X	X	X	X	X	X	X	X	X	X		X	X		X	X	X	X	
Meyer 1953																		X		X	X			
Ewans 1973		X	X	X	X		X	X						X						X	X	X	X	X
Jenkins 1965		X	X	X	X															X	X	X		
Wheatley 1934	X	X	X	X	X															X				
McCloud 1968	X	X	X	X	X	X	X	X												X	X			
Charles 1968	X	X	X	X	X															X	X			
UH-60A 2010	X	X	X	X	X	X	X	X	X					X	X	X	X	X	X	X	X			

Figure 1.42: Summary of High Advance Ratio Experimental Data Sets

mental high advance ratio datasets to date are given in fig. 1.42. This table reveals the gaps in existing data sets, which are needed for validation of analysis. Only two experiments, Jenkins [13] and Ewans [16], measured rotor data much above an advance ratio of 1.0. Only the UH-60A tests gathered comprehensive blade loads and airloads data. Meyers focused on airloads at the exclusion of almost everything else, including trimming the rotor. None of the experiments published vibratory hub loads, with the exception of limited data from the UH-60A test. The present work, highlighted in the table, therefore was focused on filling in these important gaps, and complementing existing data.

1.3 Scope of Present Research

The focus of the present research is two-fold. First, to address the need for experimental data on rotor performance and loads at high-advance ratio. Second, to

explore and analyze the fundamental science of physical phenomenon experienced by edgewise rotors in this unique flight regime. This exploration is made possible with extensive instrumentation from the testing phase of this work, as well as re-examination of experiments, modeling, and hypotheses of prior authors.

The experimental portion of the research involved five separate wind tunnel test entries (1–2 weeks each) over a period of about 6 years, with an advance ratio range of 0–1.61. Two different rotor geometries were tested, with the primary geometry being a simple rectangular rotor, with no pre-twist, and a symmetric NACA0012 airfoil. The second geometry was rectangular, but had a built-in negative pre-twist, and used a cambered SC1095 airfoil. The rotors were 5.6 ft and 6.0 ft in diameter, respectively. These simple geometries with widely available 2D airfoil data were chosen because a primary goal was to create a publicly available dataset that is useful for validating analyses or modeling tools. They were not chosen or designed as simple rotors for validations in high advance ratio edgewise flight.

The nominal angular velocity was set to match the tip Mach numbers of typical full-scale helicopters (Mach-scaled). The rotor and hub were 4-bladed and fully articulated, with a coincident flap and lag hinge. Measurements included steady and vibratory hub loads for 3 forces and 2 moments, shaft torque, pitch link loads, blade hinge motions, swashplate settings (collective and cyclics), blade root pitch, blade bending and torsion moments, and blade surface pressures. Rotor longitudinal shaft tilt could be adjusted between runs. Wind speed and rotor RPM were set to achieve the desired advance ratio, and collective (thrust) sweeps were performed. The rotor was trimmed to zero flapping (tip-path plane perpendicular to the shaft)

for each case.

The first round of high μ testing at UMD in 2009 reached advance ratios of 0.66 while investigating the effect of variable RPM on performance and loads [32]. The second round of testing in 2011 achieved advance ratios up to 1.2 and focused on conditions for compound helicopters, such as rearward shaft tilt [33]. These two tests were conducted with the twisted blade geometry. Testing was then conducted in 2012 up to advance ratio of 1.0 on a different rotor geometry (untwisted) and compared results with previous testing for performance and vibratory loading trends [34]. Continued testing on the same rotor geometry in 2013 reached advance ratios of 1.41, with points beyond 1.04 set to zero collective pitch [35]. The 2013 test was also the first to incorporate pressure transducers within the blade surface, capable of measuring unsteady pressures. However, nearly all of the pressure sensors aft of the $0.25c$ position failed early in testing, which eliminated the possibility of integrating sectional airloads, or even the observation of possible trailing edge suction peaks in reverse flow.

In 2014, the final wind tunnel test that will be discussed in this work was performed [36], and addressed many of the issues encountered in the previous tests. In this test, advance ratios up to 1.61 were achieved, and blade surface pressures were successfully measured with minimal sensor failures. The 2014 test results contributed the most useful and interesting results, and will be the focus of this dissertation.

1.4 Contributions of Present Research

The present research contributed the following to the state-of-the-art:

1. Experimental wind tunnel test data of two Mach-scale rotor geometries to advance ratios up to 1.61. Key contributions that were missing or rare in prior work include vibratory hub loads, blade loads, and blade surface pressures.

2. Significant data set expansion of the collective range at advance ratios of 1.0 and 1.2, showing collective-thrust control reversal and stall. Hypotheses of reverse-flow blade stall were confirmed to be responsible for the collective-thrust trends at high collective pitch.

3. Analytical derivations and simple numerical formulations of the blade element formulation to determine the impact of various rotor blade design parameters (lift-curve slope, twist, taper, shaft tilt, and root cutout) on the critical advance ratio where collective-thrust reversal occurs.

4. Blade pressure data (airloads) demonstrating dynamic stall due to reverse flow at high advance ratio. Data set of reverse-flow dynamics stall data at several advance ratios and pitch settings.

5. Correlation of reverse-flow dynamic stall with 2D reverse-flow dynamic stall measurements from the literature. The correlation revealed that 3D reverse-flow dynamic stall can likely be accurately predicted using models developed from the 2D data.

1.5 Organization of the Dissertation

This dissertation describes the test setup and blade construction in detail, followed by a description of the test procedures that were followed and lessons learned. Selected experimental results will then be presented, along with a discussion of particular features of the high-advance ratio regime. The discussion will be interspersed with the experimental results. Recommendations for future work will then be given.

Chapter 2: Test Equipment, Instrumentation, and Calibration

2.1 Rotor Test Stand

The rotor test stand at the Alfred Gessow Rotorcraft Center (AGRC) was used for the present study. This test stand typically supports rotors up to about 6 ft (1.8 m) diameter, and can be used on the AGRC hover tower (fig. 2.1) or be transferred into the Glenn L. Martin Wind Tunnel for forward flight experimentation.

The rotor hub used for the present study was a fully-articulated hub with coincident flap and lag hinges (fig. 2.2). Blade feathering was allowed through a tension-torsion bar, which consisted of steel wire windings encased in an elastomer. Rotor power was supplied by a 75 hp (56 kW) electric motor driving a hydraulic pump with a 2:1 reduction belt drive system capable of a maximum 2500 RPM. The rotor pulley is connected to the rotor shaft through a splined gear. The rotor shaft is connected to the rotor hub through a shear disk. This disk, as well as the shaft itself, was instrumented to give rotating shaft torque. The splined gear provides a vertically floating attachment to the entire rotor hub, which is supported by the fixed-frame rotor balance. The fixed-frame rotor balance load cell provides static and dynamic signals of six-components (3 forces, 3 moments). The balance also supports the non-rotating swashplate actuators, which are low-bandwidth electric

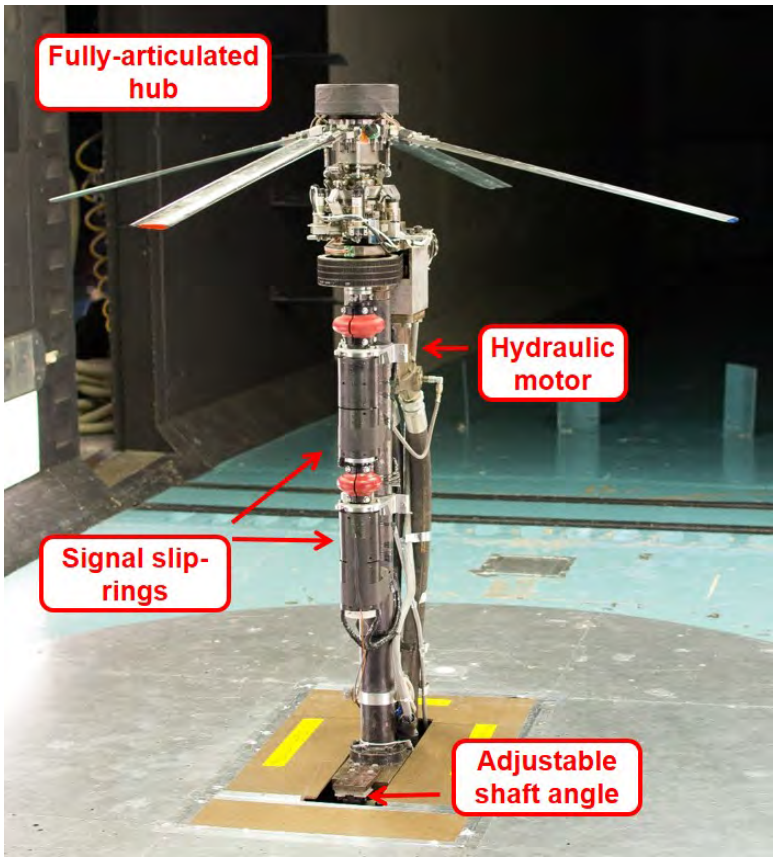

Figure 2.1: Rotor test stand mounted in the Glenn L. Martin Wind Tunnel.

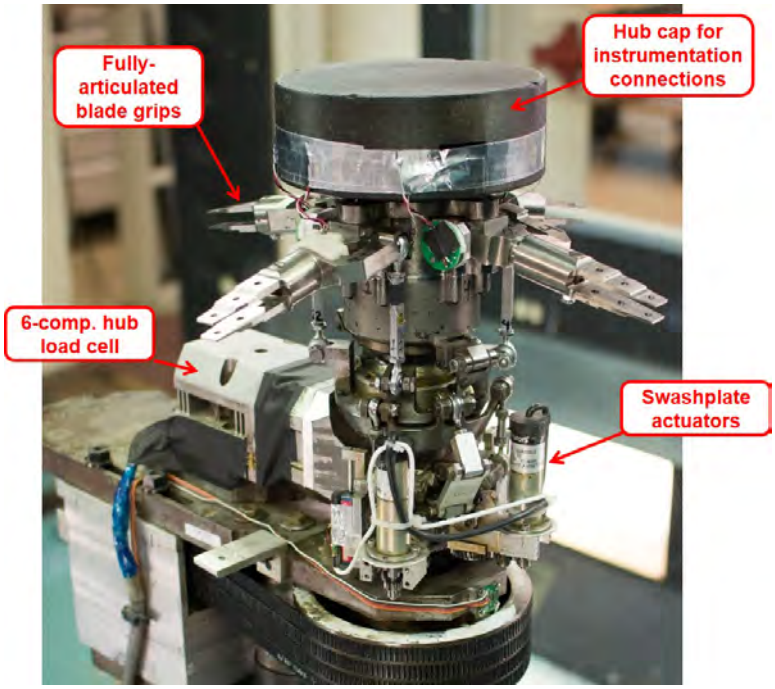

Figure 2.2: Fully-articulated rotor hub with six-axis load cell.

DC motors geared to a lead screw mechanism that prevents back-driving. The linear travel of each actuator is separately measured by linear travel sensors (linear variable differential transformers), which correlate to the collective, longitudinal cyclic, and lateral cyclic settings of the rotor.

A toothed-wheel connected to the rotor drive pulley and an optical sensor provides 60/rev and 1/rev signals for calculating rotor RPM and azimuthal referencing. There is an additional rotary hall-effect sensor that outputs voltage proportional to azimuth position. A three-axis, ±6g accelerometer was mounted on the rotor stand (non-rotating) to monitor stand vibrations during testing and as a check for fixed-frame vibratory load trends.

The rotating sensor signals (shaft torque and the rotor blade instrumentation) were routed from the hub cap down through the hollow rotor shaft and were transferred to the non-rotating frame through two sliprings. The sliprings were mounted below the rotor pulley through flexible couplings. The sliprings were designed and manufactured by Fabricast, and each had 64 rings with 28 gage (AWG) flying lead wires.

2.2 Static Calibration of Rotor Test Stand Hub Balance

A static calibration of the rotor load cell was performed prior to the test. The calibration had to account for interactions between the six axes (i.e. a force in the X axis results in non-zero voltage changes in all other directions). A loading rig was constructed to apply loads in all axes (fig. 2.3). An in-line load cell was used to bypass pulley frictional losses and measure applied force directly. The loading origin was set to be the hub center (where the blade axes intersect with zero flap or lag) as opposed to the balance center. The orientation and offset of the load from the hub center determined the applied forces and moments. Rolling and pitching moments were applied using offset (5.25 inch) vertical loads. Axial and side forces were applied 1.25 inch above the rotor center (A byproduct of the load attachment mount), resulting in applied roll and pitch moments. Rotor load cell strain gage voltages for all six components were recorded for each loading case and for zero load conditions. Yaw moment was not applied but the voltages were recorded to account for any interactions due to other applied forces/moments. Fixed-frame yaw moment in the

Table 2.1: Rotor hub load cell error estimates (lb forces and in-lb moments)

	Axial F_X	Side F_Y	Normal F_Z	Roll M_X	Pitch M_Y	Yaw M_Z
Cal Range	100	100	120	650	650	-
Max Error	0.39	0.41	0.73	4.08	4.16	-
Min Error	-1.89	-0.91	-0.67	-5.84	-11.09	-
95% Confidence	0.47	0.30	0.51	3.04	2.99	-

load cell only captures swashplate bearing friction and was considered negligible. The calibration matrix was calculated using a linear least-squares approach to solve the equation $Rx = F$, where R is the balance voltage response matrix (nx6, for n loading combinations), x is the 6x6 calibration matrix, and F is the balance applied load matrix (nx6). This methodology follows AIAA standards for wind tunnel load cell calibration procedures, with an assumption of linearity within the range calibrated [37]. Table 2.1 summarizes the range of applied loads in the calibration, the results of the calibration, and estimates for the uncertainty in each measurement axis.

2.2.1 Calibration of Shaft Torque Sensor

Static loads were applied to the rotor shaft to calibrate the rotating-frame torque sensor. The drive pulley was clamped to prevent rotation during the calibration. Torque was applied using an offset force using the same loading setup as for the fixed-frame load cell. An uncertainty for the calibration slope was estimated to be 1.5%. Interaction effects with other hub forces and moments were measured and determined to be negligible.

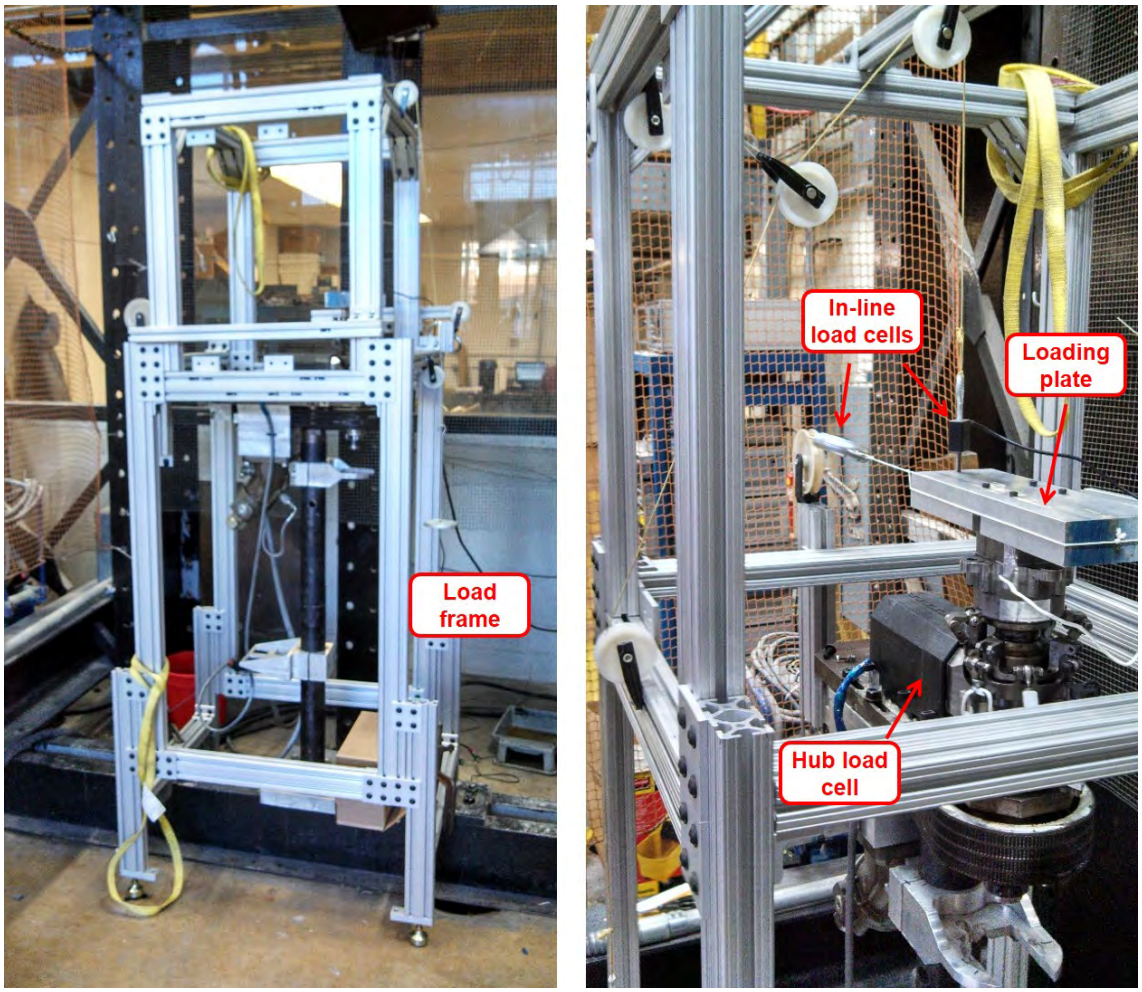

Figure 2.3: Rotor hub load cell static calibration setup. Hub shown with blade grips removed. Simultaneous loading in axial force, normal force, and pitching moment is shown.

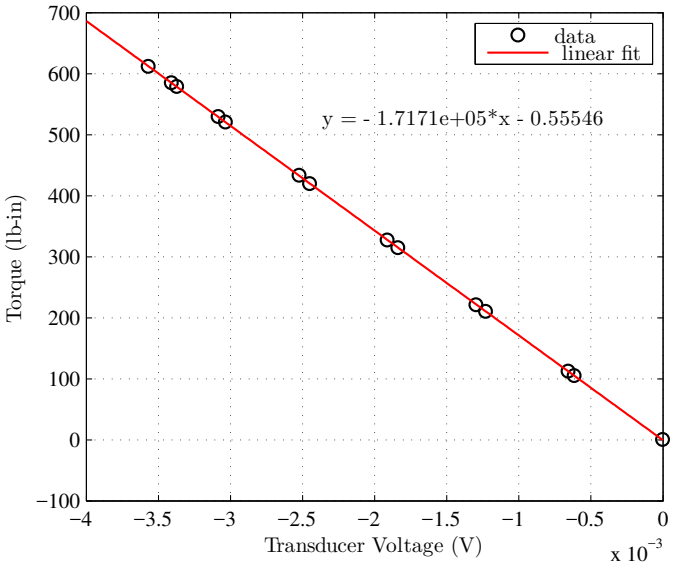

Figure 2.4: Shaft torque sensor calibration.

2.3 Dynamic Calibration of Rotor Test Stand Hub Balance

The time-history of the hub load cell signals was used to measure vibratory hub loads. A dynamic calibration procedure was therefore necessary to remove the effects of the structural responses of the rotor hub and supporting structure. Similar dynamic calibrations for rotor test stands have been reported in the literature [38–41]. The calibration loading procedure was similar to the static calibration, except static loads were replaced with dynamic loads from a shaker. The same rig and load combinations were used as with the static calibration, and the rotor center was again the reference origin (fig. 2.5). A permanent-magnet shaker was used to apply the loads. A tension/compression load cell was mounted in-line with the shaker at the point of load application to measure the applied load.

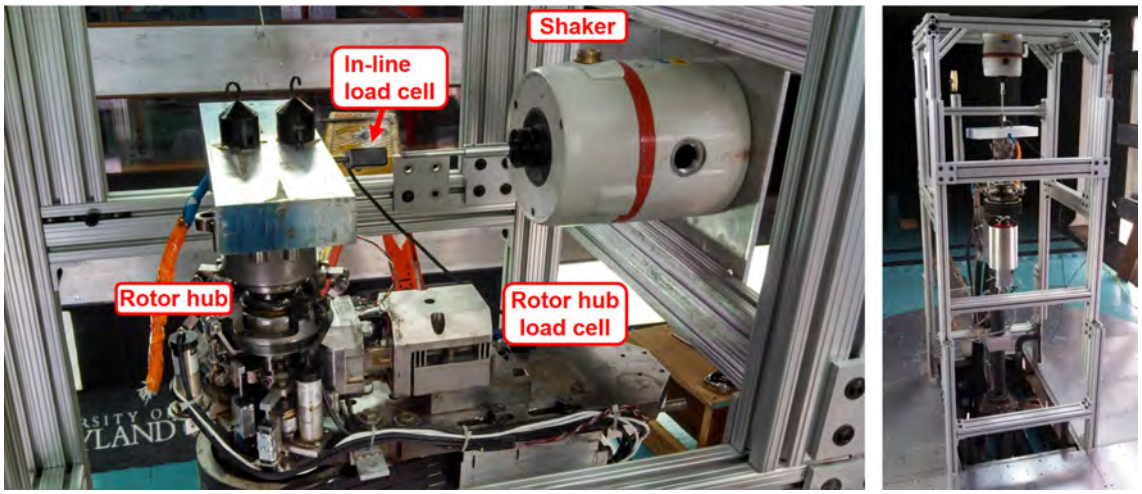

Figure 2.5: Dynamic calibration setup for the rotor hub load cell.

The dynamic calibration was conducted as follows:

1. The load cell and shaker were mounted for a specific load type (e.g. pure F_Z vertical force)

2. A sweeping sine signal was applied to the shaker (e.g. 0–400 Hz over 60 seconds). Data was recorded at a 5 kHz sampling rate. Alternatively, certain discrete frequency points were taken (e.g. sine wave at 46.67 Hz (4/rev at 700 RPM) for 5 seconds).

3. The hub balance voltages were processed at each sample with the hub static calibration matrix and converted into engineering units (lbs and in-lbs). The shaker load cell signal was also converted to applied hub forces and moments in engineering units.

4. Discrete Fourier transforms were performed on both the input (applied loads)

and output (hub balance response) signals. The result was an array of complex numbers that give the magnitude and phase of the signals for each discrete frequency. Transmissibility plots (output/input) for the frequency response of the magnitude and phase were inspected as a check on the process.

5. The complex number (magnitude and phase) at the DFT bin associated with the frequency of interest (e.g. 4/rev at 700 RPM, or 46.67 Hz) was extracted for each signal and stored.

6. Process was repeated for all loading combinations.

The complex numbers for all loading combinations were stored in a matrix of applied loads and response loads. These matrices were processed in the same way as for the static calibration, using a linear least-squares approach to arrive at the 5x5 interactive calibration matrix.

2.3.1 Select Results of the Dynamic Calibration

The transfer function for hub F_Z output given a pure vertical F_Z applied load is shown in fig. 2.7 as an example. The thickness of the band indicates the extent of noise from the input load cell, with magnitude and phase spikes at integer multiples of the 60 Hz building line frequency. The primary frequency of interest for this test was the 4p frequency at 30% RPM, which is 46.67 Hz. Pure vertical force sweeps were repeated with different input amplitudes and had excellent agreement with each other. The red line shows the response of F_Z when subjected to applied F_Z at a longitudinal offset, which also applies a pitching moment M_Y (fig. 2.6).

It is clear that there can be significant interaction affects when other vibratory forces/moments are present. Likewise, there was a strong interaction on F_X from F_Z (not shown). This motivated the interactive calibration approach described in the previous section.

2.3.2 Applying the Dynamic Calibration

For each test case, the hub balance voltage time histories were processed into forces and moments at each sample using the static calibration matrix. For each of the five components (yaw was omitted), an FFT was conducted and the complex number was extracted at the bin of the target frequency (4/rev). The vector of five complex numbers was multiplied by the 5x5 dynamic calibration matrix to give the corrected hub loads. Magnitude and phase data was then extracted from the complex numbers.

Figure 2.8 shows the effect of the dynamic calibration corrections on the 4/rev hub load magnitudes for all cases. The values shown are means of the load magnitudes for all cases, which gives an overall metric of the effect. Vertical force magnitudes (F_Z) were largely unaffected at this frequency (about 5%). F_X, M_X, and M_Y showed large percentage reductions in magnitudes (over 50%), while F_Y had significant percentage increases. It should be noted that F_Y and M_X had relatively small original dimensional magnitudes, so the percentage changes for these are more extreme. Overall, at this particular operating frequency (30% RPM), the results prove the necessity of the dynamic calibration for accurate hub loads, espe-

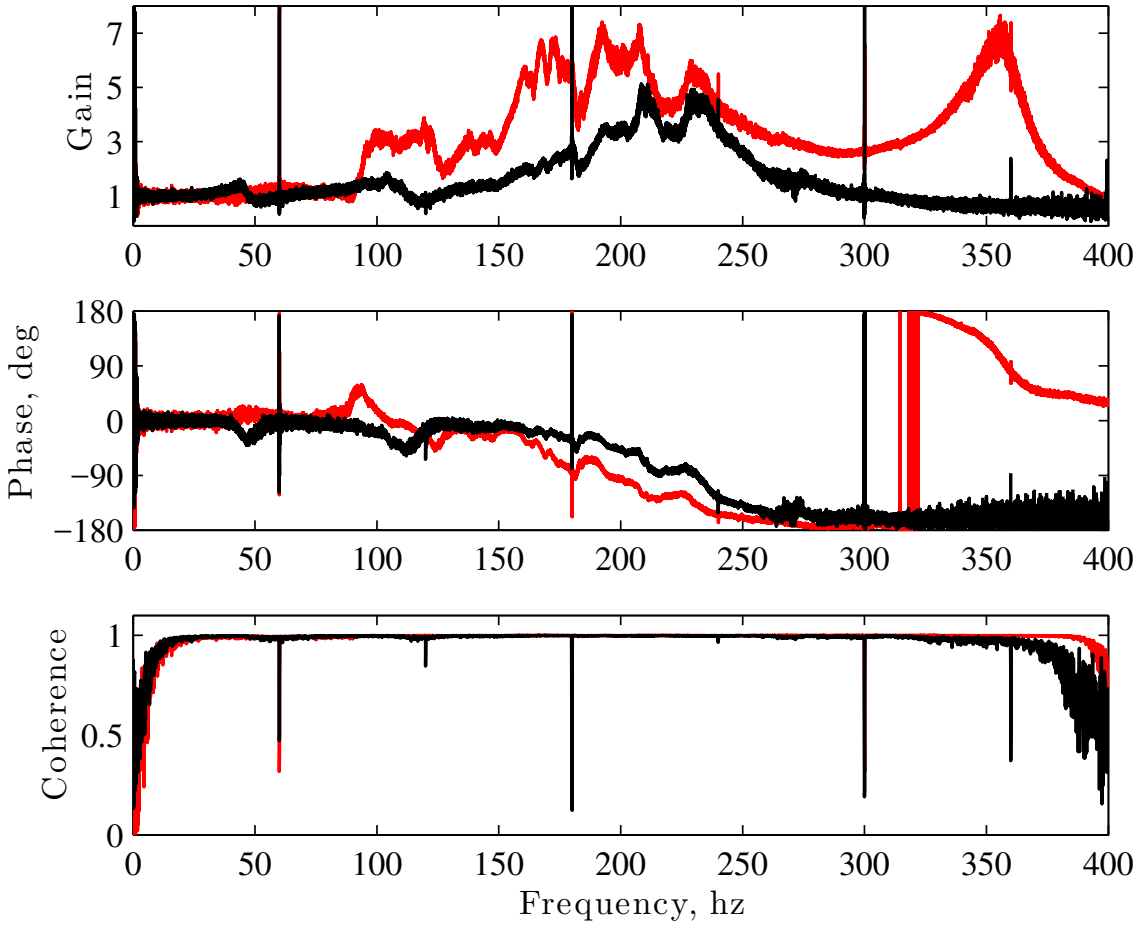

Figure 2.6: Frequency response, gain (upper) and phase (lower), of transfer function of hub F_Z (vertical force) output response to an applied pure F_Z input (black) and to an applied combination F_Z and M_Y (vertical and pitching moment) input (red).

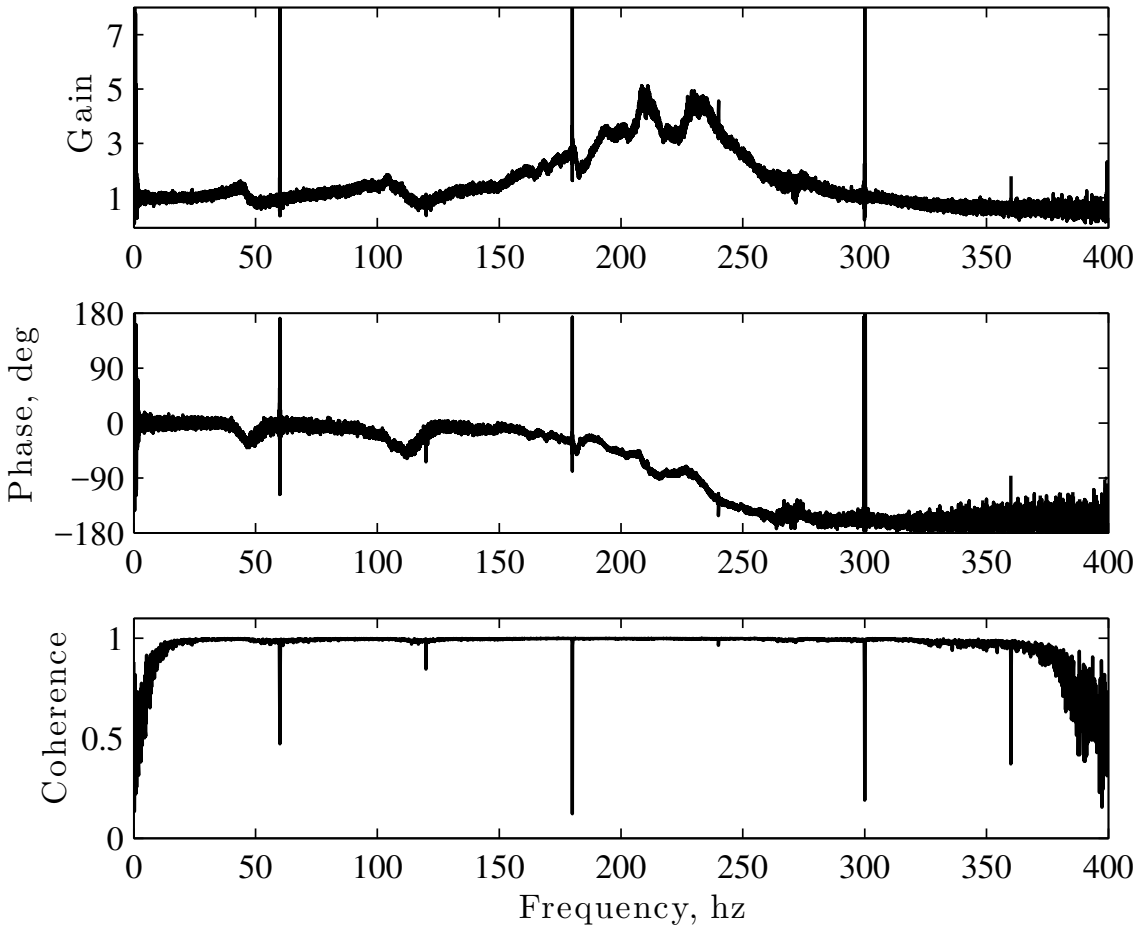

Figure 2.7: Load cell normal force response to normal force input: transmissibility (gain), phase, and coherence.

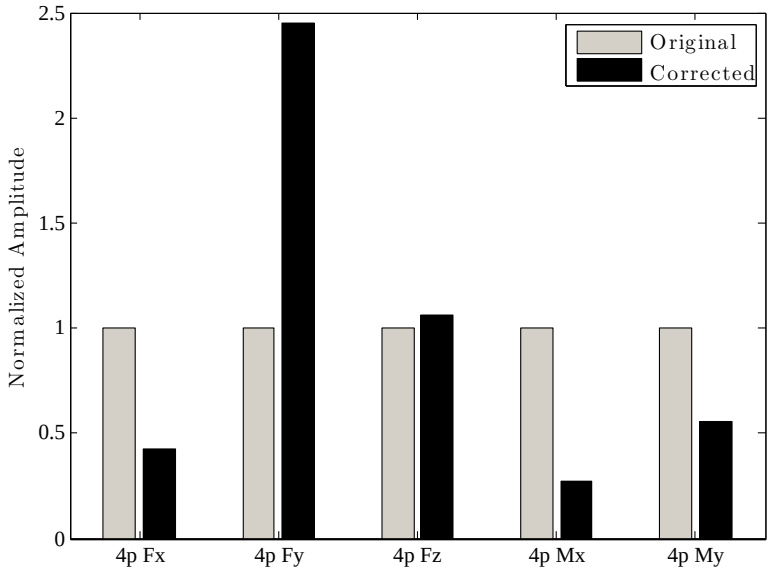

Figure 2.8: Effect of dynamic calibration corrections on 4p hub loads. Results are the mean of 4p magnitudes for all cases, normalized by the uncorrected (original) mean magnitudes.

cially for in-plane loads where the natural frequencies of the support structure were much lower.

2.4 Pressure Sensors

Blade surface pressure measurements are used to elucidate the aerodynamic pressure forces on the blade (airloads). Due to the unsteady nature of rotor aerodynamics in forward flight, the pressure transducers must be capable of sufficient frequency response. Tubing running from the blade surface pressure port to a remotely-located pressure transducer would create untenable phase lag and magnitude response, as demonstrated in controlled experiments performed in the literature [41]. Therefore, the pressure transducers must be mounted as close to the

surface as possible, and there must be a separate transducer for each measurement. The present experiment uses sub-scale rotor blades, with maximum thicknesses of only about 0.25 inch, which drives the requirement for unsteady pressure transducers in a miniature form factor. The following sections detail the two main transducers that were selected and used in testing for this work.

2.4.1 Expected Pressure Range

The range of expected pressure levels on the blade surface can be bounded assuming typical pressure distributions over an airfoil and given the wind tunnel test envelope. The high-advance ratio environment may present unusual pressure distributions, specifically in reverse flow, but, given the sharp trailing edge, the negative pressure is not likely to exceed that experienced on the suction side near the rounded leading edge.

The minimum pressure coefficient a NACA 0012 airfoil will realistically achieve in this test is roughly -6.0 (non-dimensional) due to the onset local supersonic flow (critical pressure coefficient). This would only be possible near the leading edge suction peak, but it is a useful number to provide bounds on the range for all the sensor chordwise locations. The maximum positive pressure coefficient would be 1.0, which is the stagnation or total pressure.

These pressure coefficients can be converted into absolute pressures using the expected local freestream conditions of the blade section. The result was a required absolute pressure range of 8 psia to 16 psia. Only certain sensor ranges are com-

mercially available (without long lead-time customization), and typically the lower limit of commercially-available absolute pressure transducers is 0 psia (vacuum). The available max ratings at the time of sourcing were 10, 15, or 25 psia (and higher). The 10 psia rated transducers remain linear up to 15 psia (150%), and so are acceptable at locations away from potential stagnation points. Likewise, the 15 psia rated transducers have linear ranges that extend beyond the expected maximum pressure for the wind tunnel test, and so are acceptable for use anywhere on the airfoil. 25 psia rated gages and higher were not desired due to lower sensitivity (from the increased range), but were used when availability of the 10 or 15 psia transducers was limited. The Endevco sensors used primarily on the final 2014 test were all 0-15 psia rated.

2.4.2 Kulite Pressure Transducers

Kulite Semiconductor Products manufactures piezoresistive silicon pressure transducers. These transducers have a silicon diaphragm that deflects under application of pressure. This diaphragm has a Wheatstone bridge network of piezoresistive silicon strain gages bonded to it, that creates the bridge output (fig. 2.9). These sensors were chosen for the 2013 wind tunnel test through a survey of commercially available pressure sensors, as well as a literature survey of prior pressure-instrumented rotor tests [42–45]. The Kulite LE-062 model sensor was the smallest form factor for a commercially available packaged sensor (fig. 2.10). Model LL-072 and LE-080 sensors were also used, as there was limited stock of the LE-062 at the

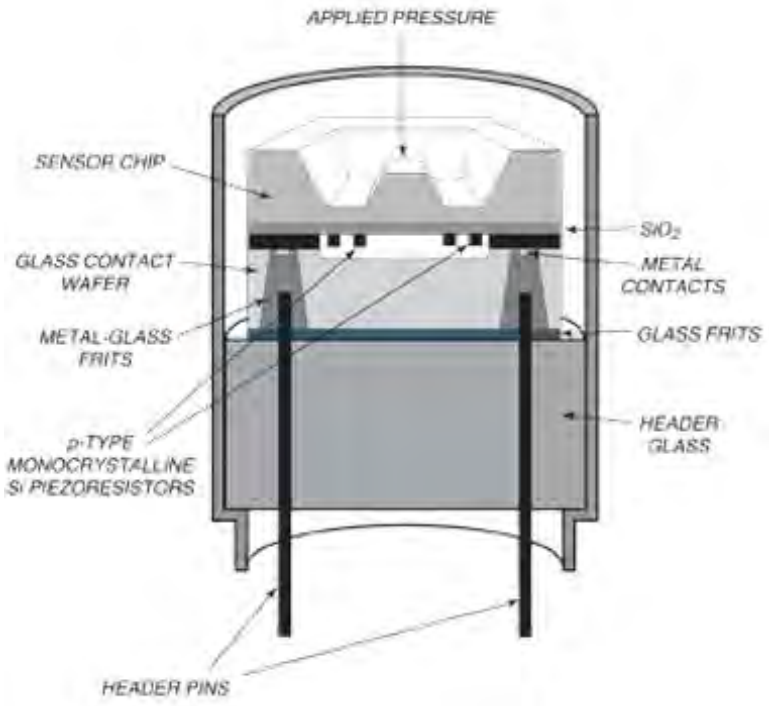

Figure 2.9: Cross-section schematic of a notional Kulite pressure transducer. [46]

time. The three models had the same sensitivity and dynamic range specifications, but differed in form factor.

2.4.3 Endevco Pressure Transducers

For the 2014 tests, an alternative sensor was explored due to long quote lead-times for new Kulite sensors. The pressure transducers were model 40931 silicon piezoresistive sensors from Meggitt Sensing Systems Endevco product line. The functionality is similar to the Kulite sensors described in the previous section. The sensor was supplied in die form (no packaging) with surface-mounting pads. Due to the micro-miniature size of the sensor (1.65 x 1.2 x 0.4 mm), a custom printed

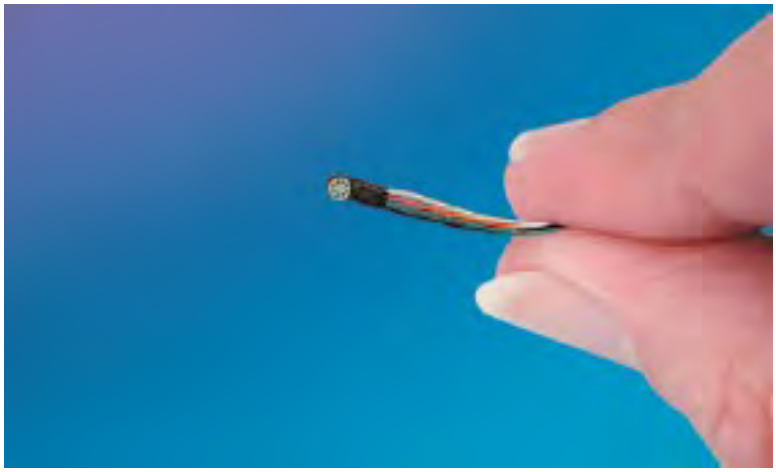

Figure 2.10: Kulite model LE-062. [47]

circuit board was designed to serve as a breakout board for attachment of lead wiring (fig. 2.11). The overall envelope of the resulting PCB with sensor was 19 x 3 x 1.2 mm. The board was manufactured by Electrotek (Oak Ridge, WI) and was a rigid, two-layer, 0.031 inch (0.79 mm) thick board. Due to the miniature nature, the sensor was professionally mounted to the board using conductive epoxy by Zentech Manufacturing in Baltimore. The total cost was around 1/6 that of packaged sensors (either by Kulite or other Endevco models).

2.4.4 Pressure Sensor Verification and Calibration

Common issues with using pressure transducers on rotor blades include influences from acceleration, temperature, and dynamic response issues from sensor topology and/or pneumatic tubing length.

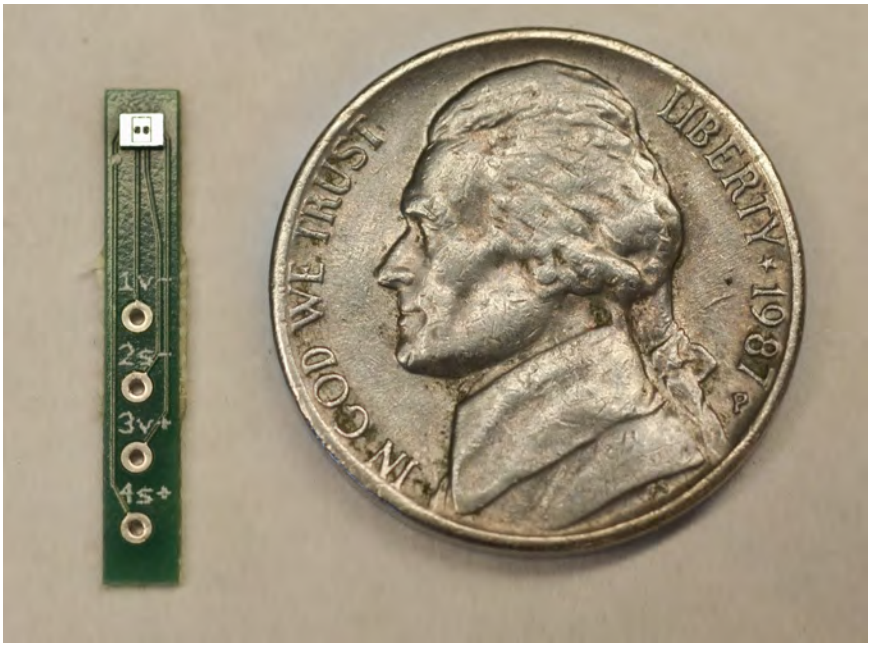

Figure 2.11: Meggitt/Endevco 40931 pressure transducer die mounted on a custom printed circuit board.

2.4.4.1 Temperature Sensitivity

The ambient temperature during wind tunnel testing varies at maximum about 10° F during a run, due to heat from the motor that drives the tunnel propeller. The full Wheatstone bridge circuit in the pressure transducer helps to passively filter out spurious readings due to temperature changes. Any voltage shift due to self-heating of the sensors from the bridge resistance is effectively tared at the beginning of each run, and was accounted for in the static calibration. Additionally, the Kulite sensors have a built-in temperature compensation in the form of a series resistor that is tuned to each specific transducer to minimize overall temperature sensitivity over a given temperature range [48]. The Endevco sensors used in the raw die form did not include a compensation resistor in the circuit.

The Kulite sensors were tested to verify their temperature sensitivity. A heat lamp was used to vary the sensor temperature and observe the variation in pressure reading (fig. 2.12). The sensitivities were within the ranges specified by the manufacturer.

2.4.4.2 Acceleration Sensitivity

For the model-scale rotor used in this research, the acceleration due to rotation experienced on the blade can be up to 5400 g at a full-scale equivalent tip Mach number of 0.65. The pressure sensors in this work were installed at the 0.3R radial location, and were mainly tested in slowed-rotor conditions, but nonetheless the impact of acceleration needed to be accounted for.

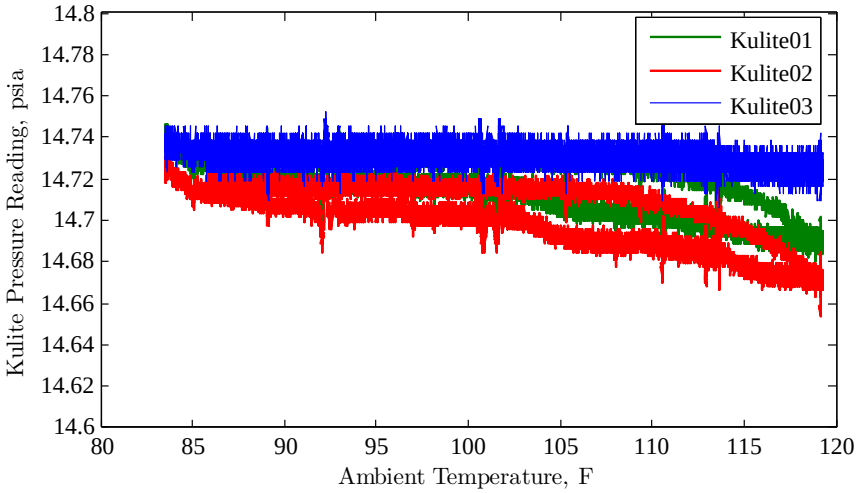

Figure 2.12: Measured Kulite pressure variation due to temperature changes. Wind tunnel temperature range is 70° to 100°F.

Selected Kulite sensors were rotated in a large vacuum chamber to simulate the centripetal acceleration range experienced on the rotor. The pressure in the chamber was reduced to near vacuum to eliminate aerodynamic effects. The voltage change on the sensor was measured with variation in centripetal acceleration (fig. 2.13). The sensitivity of 0.0000103 psi/g was within the range specified by the manufacturer.

The Endevco model pressure transducers (used in the 2014 tests) were tested for acceleration sensitivity in the wind tunnel. The pressure port holes on the blade were sealed to air-flow using tape. A sweep of rotor speed was conducted to vary the centripetal acceleration, and the pressure sensor voltages were recorded (fig. 2.14).

The maximum transverse acceleration sensitivity for the installed Endevco transducers was measured as 0.000206 psi/g (3.00E-05 kPa/g), which was equal to the specification from the manufacturer. The pressure due to steady acceleration

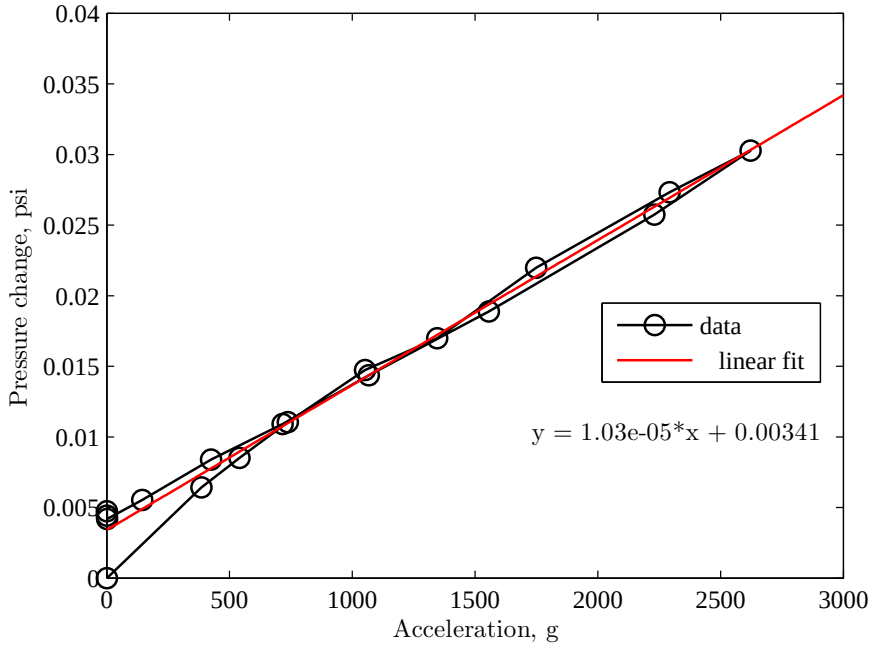

Figure 2.13: Measured transverse acceleration sensitivity of a Kulite LL-072.

from rotor blade rotation was subtracted from that of each sensor according to the individual measured sensitivity constants. Note the Endevco has a higher sensitivity to acceleration than the Kulite, but the difference was not significant for this work.

2.4.4.3 Dynamic Response

The dynamic response of the Endevco and Kulite sensors were compared relative to each other in a controlled experiment (fig. 2.15). The purpose was to compare the Endevco sensor to the more trusted Kulite transducer, of which similar models have been used extensively in the literature. Thus the Kulite was used as a reference.

The two sensors gave identical amplitude and phase up to the maximum frequency of interest for this experiment, 200 Hz, which is >12/rev (fig. 2.16). Higher

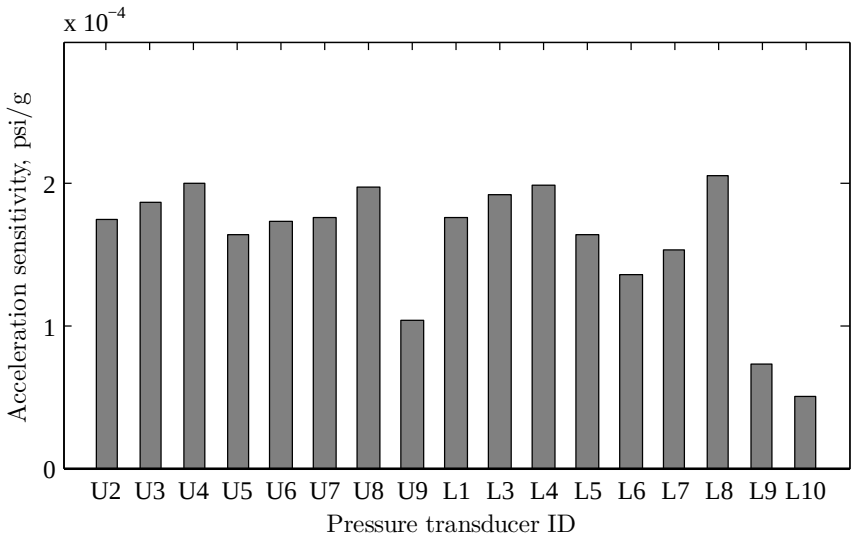

Figure 2.14: Measured Endevco transverse acceleration sensitivity from spin test with port holes sealed.

frequencies were not verified due to testing limitations. The increased noise at higher frequencies is a result of the reduced displacement of the shaker at higher frequencies, thus imparting a smaller pressure amplitude as frequency is increased. An improved setup to measure absolute dynamic response (instead of relative) might consist of a fixed-displacement piston that gives a known reduction in chamber volume.

The results may not be surprising, given the specified resonant frequency of the Kulite and Endevco sensors was greater than 175 kHz, two orders of magnitude above the frequencies of interest for the rotor blade pressure variation and the cut-off frequency of the anti-aliasing filters used in the tests. Thus, the dynamic response of the Endevco sensor was judged as acceptable for this research.

The frequency response affects due to pneumatic tubing length were considered negligible by placing the sensors at the point of measurement just below the surface

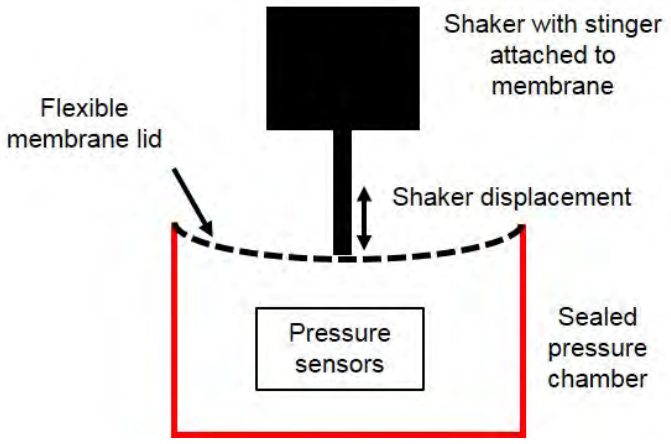

Figure 2.15: Schematic of relative dynamic response testing chamber.

of the blade. Nonetheless, a calculation of organ pipe, cavity (Helmholtz), and tube and cavity resonance was conducted to verify the port hole diameter and internal chamber volume was not such that it degraded the dynamic response (fig. 2.17). The tube and cavity resonance calculation gave the lowest natural frequency, which at 11 kHz (11 times the cut-off frequency of the low-pass hardware filters used) was not a concern. As can be seen in fig. 2.17, increased tube length, increased cavity volume, and decreased port hole (or tube) diameter contribute to reduced natural frequencies. For the geometry used in this research, a tube length of approx 3 inches is the maximum possible before organ pipe resonance reaches 1 kHz.

2.4.4.4 Static Calibration

During the wind tunnel tests, the pressure transducer calibrations were checked *in situ*. Vacuum-bagging was sealed around the location of the pressure ports on the instrumented rotor blade (fig. 2.18). A 3D-printed sleeve was placed between

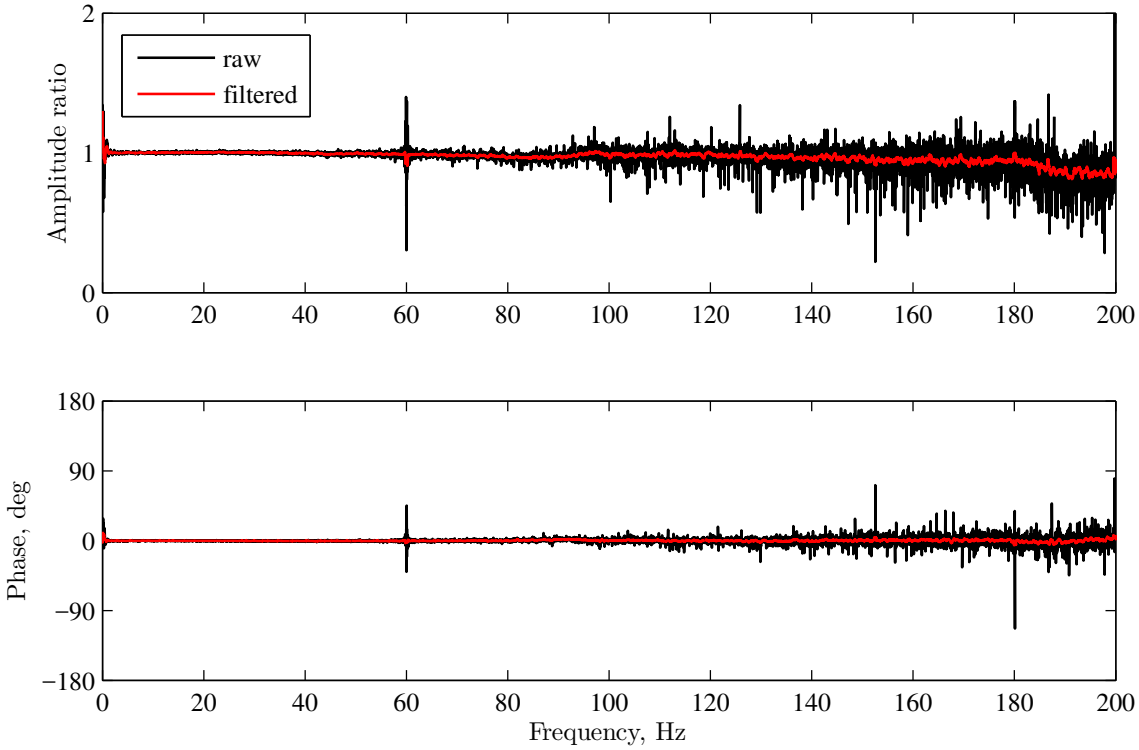

Figure 2.16: Frequency response comparison between Endevco and Kulite sensors. Amplitude ratio given as Endevco/Kulite.

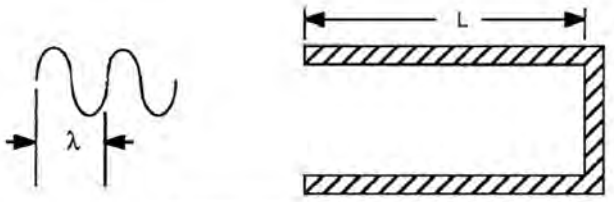

Figure 5-3: Organ Pipe Resonance

$$f_n = \frac{c}{4L}, \frac{3c}{4L}, \frac{5c}{4L}$$

f = frequency
c = speed of sound in the fluid
L = length of pipe

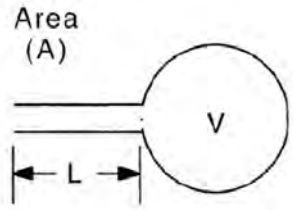

Figure 5-4: Cavity (Helmholtz) Resonances

$$f_n = \frac{c}{2\pi}\sqrt{\frac{A}{LV}}$$

where: c = speed of sound in the fluid

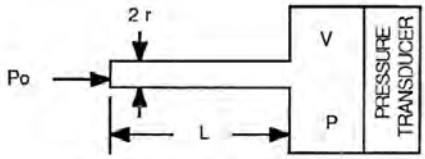

Figure 1.13, Tube and Cavity
Figure 5-5: Tube and Cavity

The natural frequency of the tube and cavity system is:-

$$f_n = \frac{1}{2\pi}\sqrt{\frac{3\pi r^2 c^2}{4LV}}$$

Figure 2.17: Various formulations to estimate the effect of pressure port ducting/tubing on the resonance frequency of the air column system. [49]

the bag and the rotor blade to prevent damage to the sensors, and ensure uniform pressure distribution to all sensors. Two port holes in the sleeve provided access for a NIST-calibrated reference pressure transducer from Mensor (CPT 6100), and the vacuum pump hose. The vacuum pump was manually metered to slowly lower the pressure within the bag while continuously recording measurements from the blade sensors and the reference transducer (fig. 2.19). A slow variation of pressure was necessary to maintain a nearly steady condition in the bag. The Mensor reference sensor is not a dynamic sensor, and the length of tubing from the bag to the sensor would result in poor dynamic response. A linear regression fit of the sensor voltages against the reference pressure reading resulted in the psi/V sensitivity constants (fig. 2.20). This calibration was conducted six separate times over the course of multiple days, and the average sensitivity constants for each sensor were used in the data processing. Standard deviation of the multiple calibrations was on average, 2.5%, with the maximum being 4.0%.

2.5 Blade and Pitch Link Strain Gages

The rotor blade loads were measured using metal foil strain gages bonded to the rotor blade skin. The methods of bonding are covered in the next chapter. Each measurement utilized four strain gages in a Wheatstone bridge configuration (fig. 2.21). The full-bridge arrangement maximizes sensitivity while minimizing temperature effects and eliminating influence from undesired strain directions. The bending full-bridge utilized eliminates axial strain (from blade centrifugal force) and

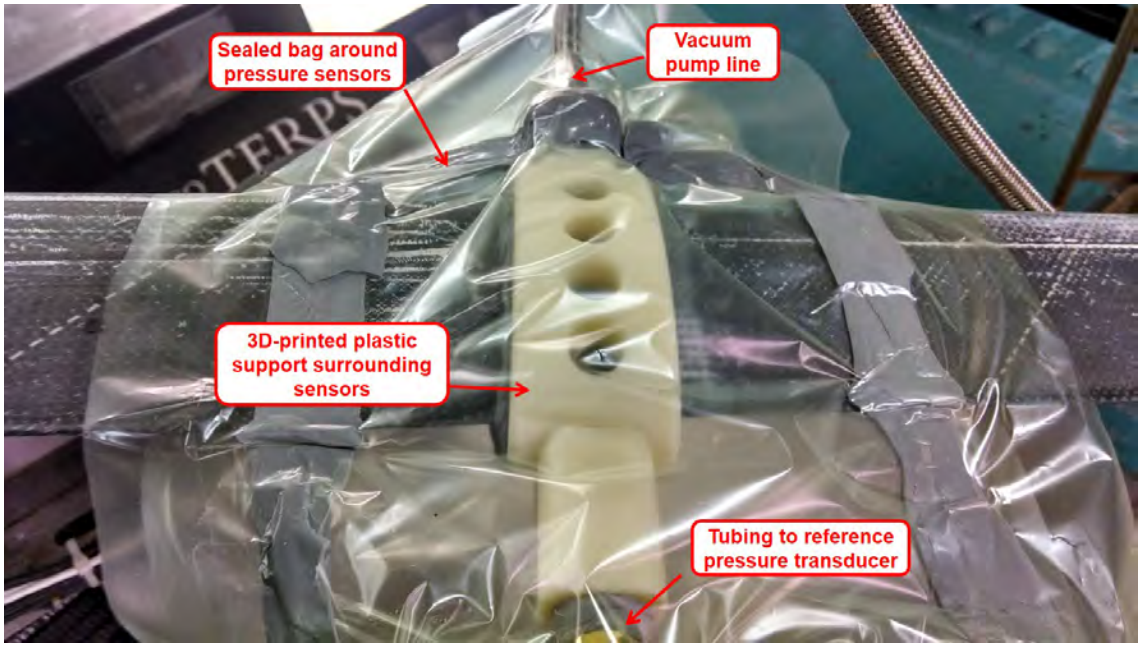

Figure 2.18: In-situ static calibration setup for blade pressure sensors: Vacuum bag sealed around pressure sensor port holes.

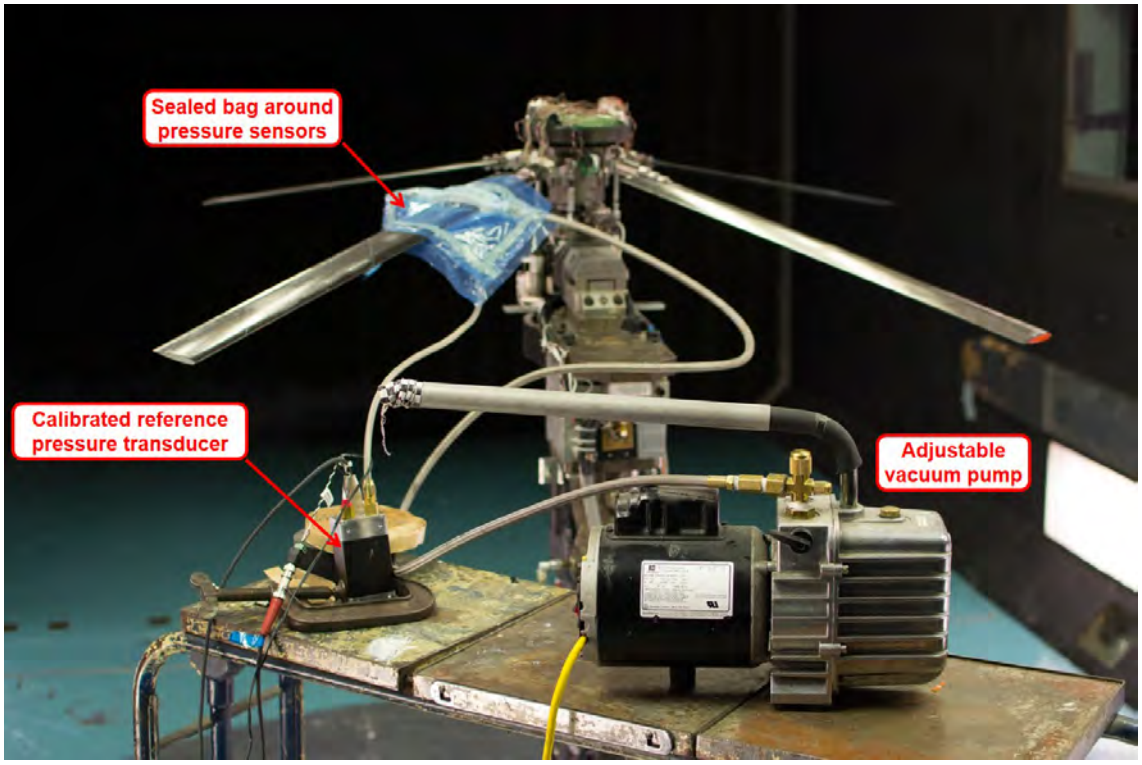

Figure 2.19: In-situ static calibration setup for blade pressure sensors: Vacuum pump and reference pressure transducer.

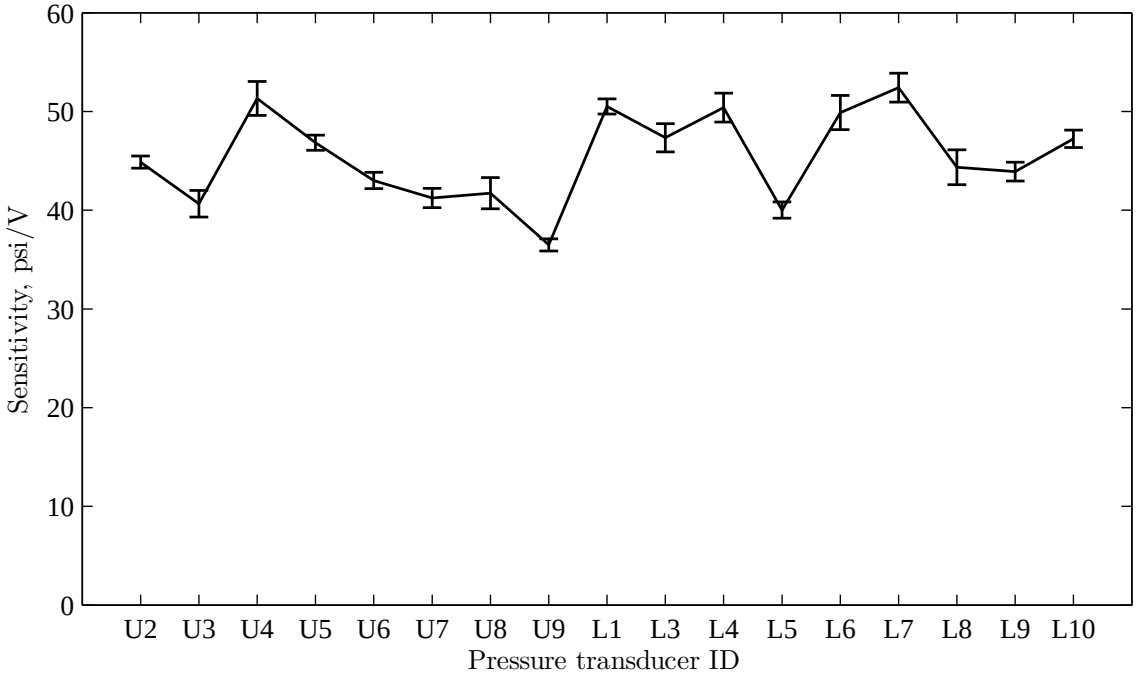

Figure 2.20: Calibration results for pressure transducers over 6 calibrations over multiple days. Error bars denote one standard deviation. Mean standard deviation is 2.5%.

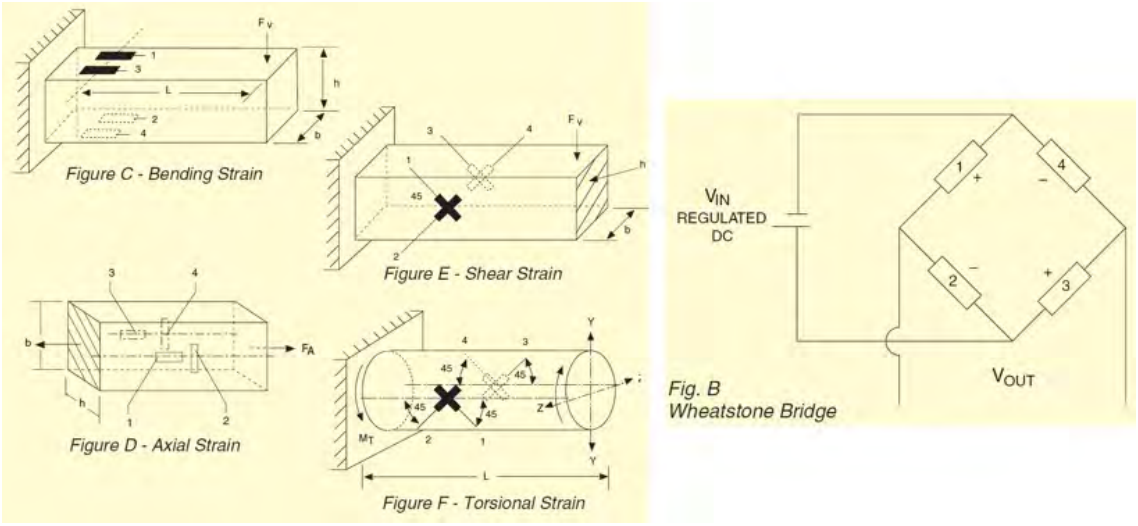

Figure 2.21: Positioning of strain gages for various load types, and the associated Wheatstone bridge circuit. [50]

shear strain from torsion. The torsion full-bridge eliminates axial strain and bending strain.

Blade No. 3 was instrumented with 12 full-bridge strain gages to measure blade loads. Flap-wise bending moment and torsion moment bridges (fig. 2.22) were placed at 30, 40, 50, 60, 70, and 90% radial locations (fig. 2.23). A combination of bending and torsion loadings were applied and a linear regression was performed that accounted for any residual cross-coupling interactions between the two (fig. 2.24). The gages at 0.9R exhibited unacceptable non-linear behavior during the calibration phase, and were therefore not used.

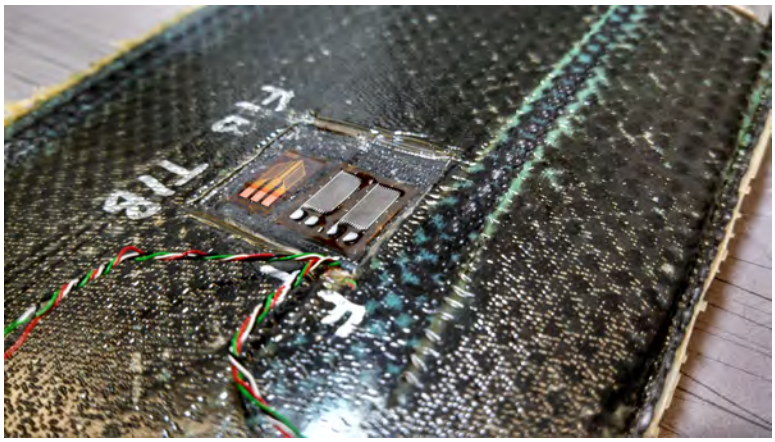

Figure 2.22: Torsion (left) and bending (right) strain gages applied to the surface of a rotor blade.

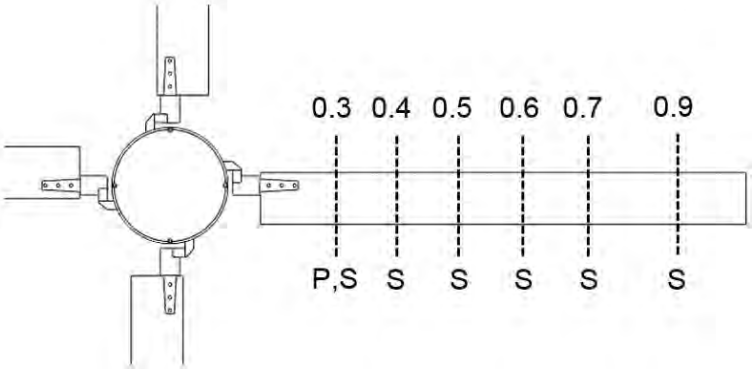

Figure 2.23: Location of pressure transducers (P) and strain gages (S). Location given in fraction of radius.

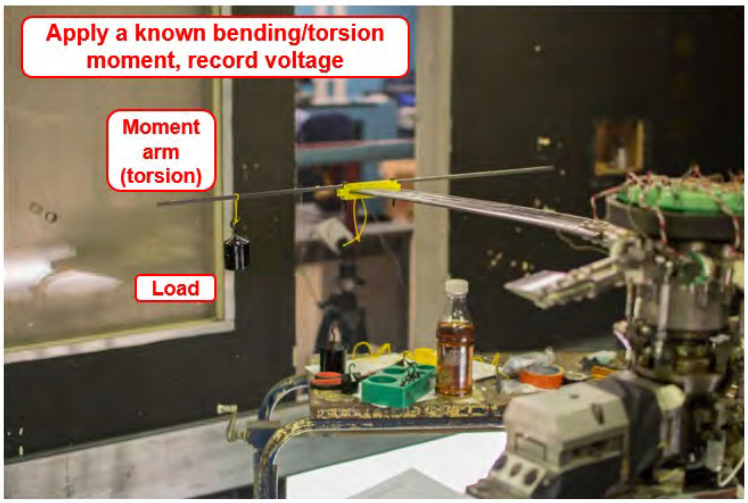

Figure 2.24: Static calibration of blade bending and torsion strain gages in the wind tunnel.

2.6 Data Acquisition Hardware and Software

All signals were recorded at a 5 kHz sampling rate using a National Instruments 16-bit ADC (model USB-6255). Each flight condition was recorded for 10 seconds. Strain gage and pressure sensor signals were processed through SCXI-1520 modules using a 1 kHz low-pass filter (3rd order Butterworth). High-level voltage signals (flap hinges, shaft encoder, accelerometer, swashplate orientation) were processed through SCXI-1102C modules (fig. 2.25). A LabVIEW virtual instrument panel was programmed for monitoring select signals for rotor operation/trimming, safety of flight, and for data file recording (fig. 2.26).

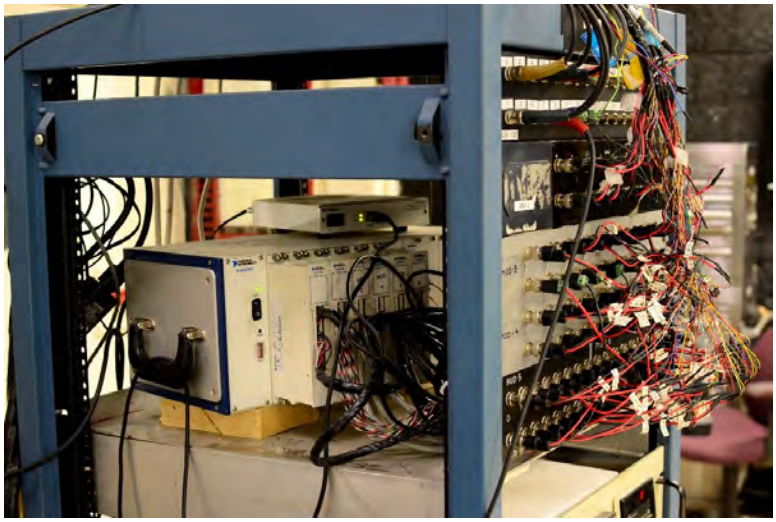

Figure 2.25: Data acquisition equipment with breakout BNC connectors.

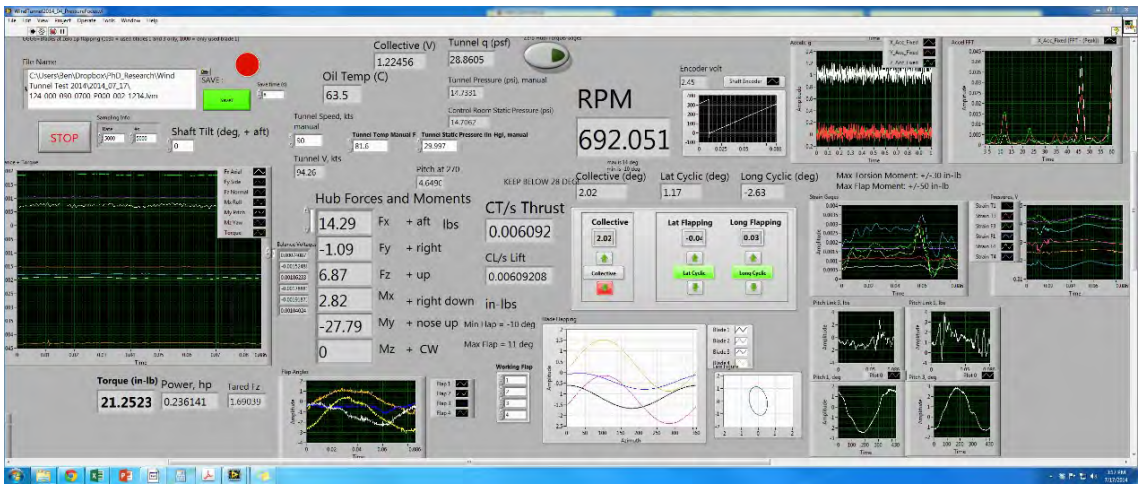

Figure 2.26: Labview virtual instrument (VI) panel.

Chapter 3: Fabrication of Instrumented Composite Rotor Blades

3.1 Construction of Composite Rotor Blades

3.1.1 Blade Design Overview

The rotor blades used in this research were a legacy design that had been used in prior research projects at the University of Maryland. The rotor blade was a rectangular, untwisted design, with a symmetric airfoil, the NACA 0012. The structure consisted of a load-carrying rectangular spar, a foam core, and an outer composite fabric skin (fig. 3.1). The blades were molded in an aluminum two-part female cavity mold. The rotor blades were constructed in-house from a Rohacell 31-IG foam core, an IM8/Patz Resin unidirectional carbon spar, and Hexcel IM7 6K-194-PW/8552 plain weave ±45 degree single layer skin. There was a final outer layer consisting of a single ply of 2-mil fiberglass (E-glass) prepreg (8552 resin) to improve the surface finish. Tungsten-carbide rods (typically 0.125 inch diameter, 3 inch length) were embedded as leading-edge weights for chordwise CG balance. Film adhesive (Cytec FM 300) was used to improve the carbon-to-foam and tungsten-to-foam bond adhesion.

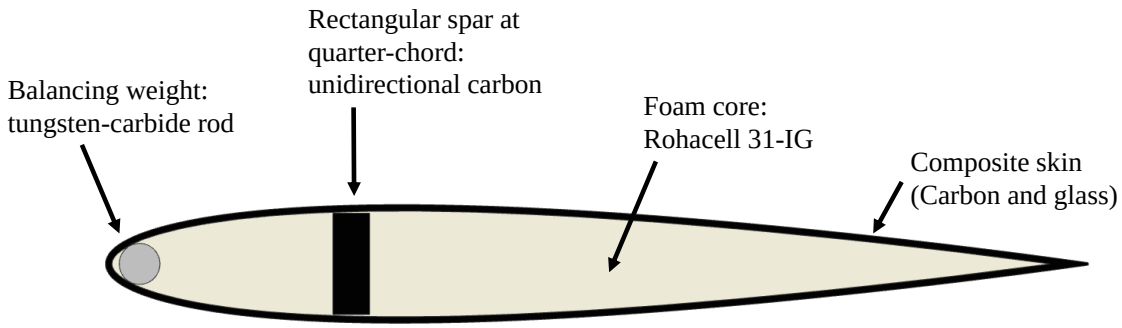

Figure 3.1: Blade cross-section showing structural elements.

3.1.2 Spar Construction

The blade spar was a rectangular design, with a captured aluminum insert at the root, which provided the bolted connection (fig. 3.2). The tear-drop shaped aluminum insert was first machined on a CNC mill, with precision bolt holes being drilled in the same operation. Strips of unidirectional carbon fiber were cut to approximately twice the final spar length. Each carbon pre-preg strip was wrapped around the aluminum root insert, capturing the carbon spar to the root insert. The spar was oven-cured in a clamped aluminum mold according to the material recommendations (typically 1 hour at 350 F). A radial reinforcement wrap of prepreg carbon was then placed at the inflection point of the spar, to prevent debonding and delamination due to tension-induced straightening in that region. A second oven-cure cycle was used to cure this reinforcement.

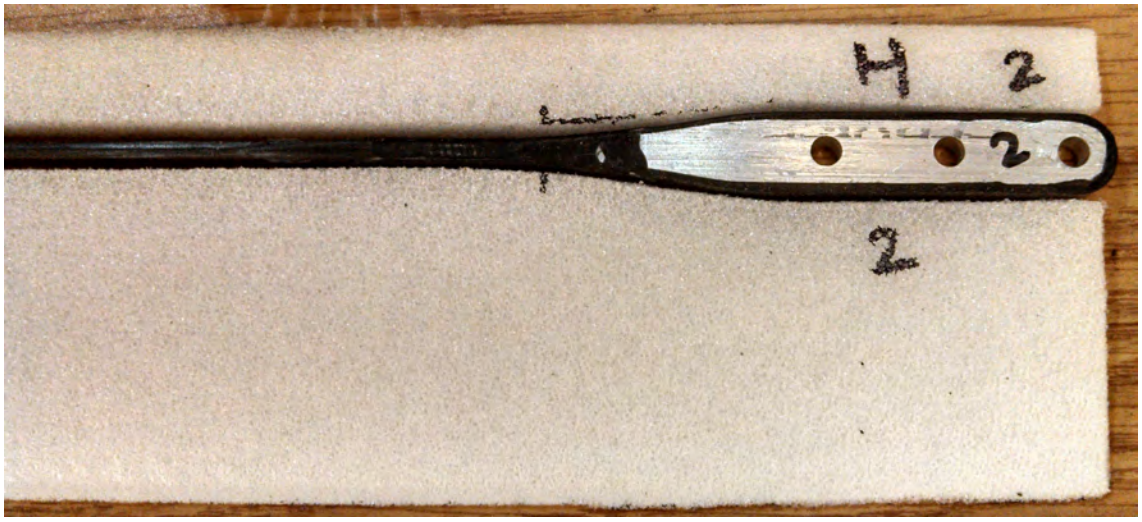

Figure 3.2: Foam core fit to spar root aluminum insert.

3.1.3 Method 1: Co-bonded Skin

The legacy process for rotor blade construction/assembly was to co-bond the uncured outer skin to the foam core and pre-cured spar. This was the typical and preferred process for rotor blades that did not contain embedded instrumentation (pressure sensors, strain gages, etc), and was developed by preceding graduate students in the Rotorcraft Center. The second method, detailed in the next section, is curing the outer skin separate from the core of the blade. Many steps of construction are shared between the two methods. The process for the co-bonded construction is as follows:

1. A rectangular block of Rohacell 31-IG foam, sized slightly larger than the blade mold cavity, was partially compressed into the blade clamshell mold. The mold and foam were heated in the oven to 190 F, and then the mold was

closed completely and let to cool to room temperature. This process essentially thermoformed the foam into the shape of the blade.

2. The foam core was split and trimmed along the quarter-chord, to make room for the spar. The leading edge portion of the foam was milled with a ball end mill to create slots for the leading-edge masses (tungsten-carbide rods).

3. The tungsten rods were wrapped in film adhesive, and set into the foam core leading edge slots. Then the leading edge foam core, trailing edge foam core, and spar were wrapped in film adhesive (fig. 3.3).

4. The core and spar were fit together, and then the carbon fiber pre-preg fabric (cut at ±45 degrees) was wrapped around the entire blade. The fabric skin overlapped itself at the trailing edge, to close out the structure. In some variants, an outer skin layer of a thin fiberglass pre-preg was also used to provide a smoother surface.

5. The blade was then placed back into the mold, which was closed and then placed into the oven for the final cure cycle.

3.1.4 Method 2: Secondarily Bonded Skin

The second method was utilized mainly to ease the process of embedding sensors into the blades. The process for Method 1 was largely followed, with the exception of the final skin layer. In this process, the skin layer in the co-bonding cycle was only the single layer of fiberglass. This produced a cured, complete blade

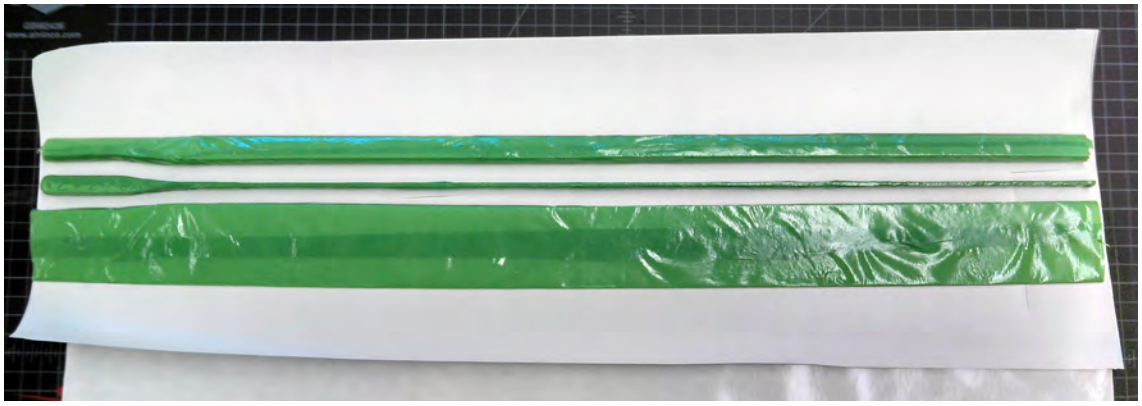

Figure 3.3: Foam core sections (top and bottom) and pre-cured blade spar (middle) wrapped in film adhesive in preparation for oven-cure assembly.

with a single ply of fiberglass holding it together. At this point in the process, cut-outs in the skin/core could be made for the pressure transducers to be embedded, as well as paths for the wiring cables.

A separate outer skin was pre-cured separately out of IM7/8552 (Hexcel) plain weave prepreg with ±45 degree orientation. Once the sensors were embedded and the wires routed, the outer skin was bonded to the blade core using room-temperature epoxy and using the blade mold to provide clamping pressure and maintain the final shape. The following sections on sensor embedment will detail the specific steps taken for these assembly methods.

3.2 Strain Gage Application Techniques

During this work, several methods of applying blade strain gages were explored. The first method was simply bonding the gages to the outside of the blade

skin. The second method was bonding to the outer skin, but first making depressions in the skin to maintain the outer blade shape. The third method was to bond the gages to the inside surface of the blade skin, before the skin was bonded to the blade core.

3.2.1 Method 1: Bonding on Outer Skin

Bonding the gages to the outside skin of the blade has the strong advantages of being simple to apply, not altering the blade structure, and being amenable to rework/inspection. The disadvantage is, of course, that the aerodynamic properties of the blade will be interfered with, which could raise questions when correlating to analysis.

This method was used in initial testing (fig. 3.4), and the effect on hovering performance was quantified and found to be about a 5% penalty in required torque for a given thrust (fig. 3.5). The effect seemed to be confined to profile losses, with minimal effect on induced power in the range tested.

During testing, there were also several failures of the wiring on the blade. Due to the aerodynamic concerns, very thin magnet wire (38 AWG) was used on the blade. Repeatedly in the wind tunnel these wires would break, presumably from fatigue. The easy access made repairs possible, but with a loss of valuable testing time.

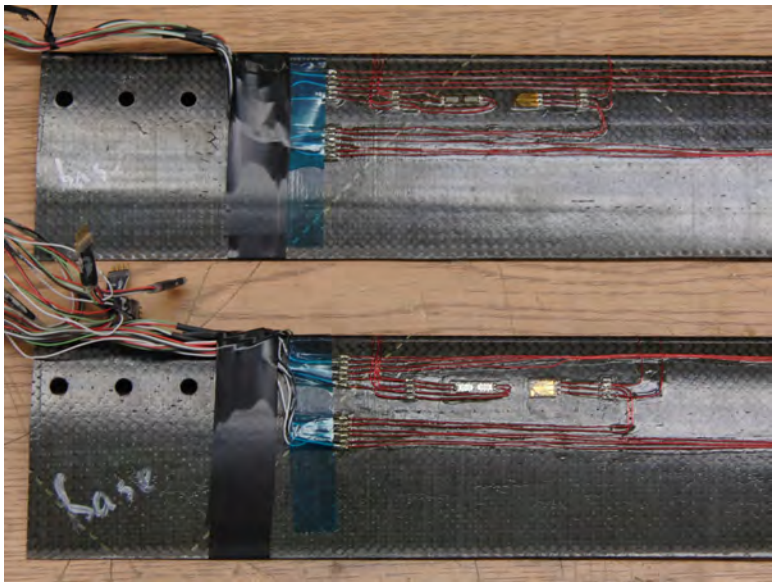

Figure 3.4: Example of external bonding and wiring of strain gages.

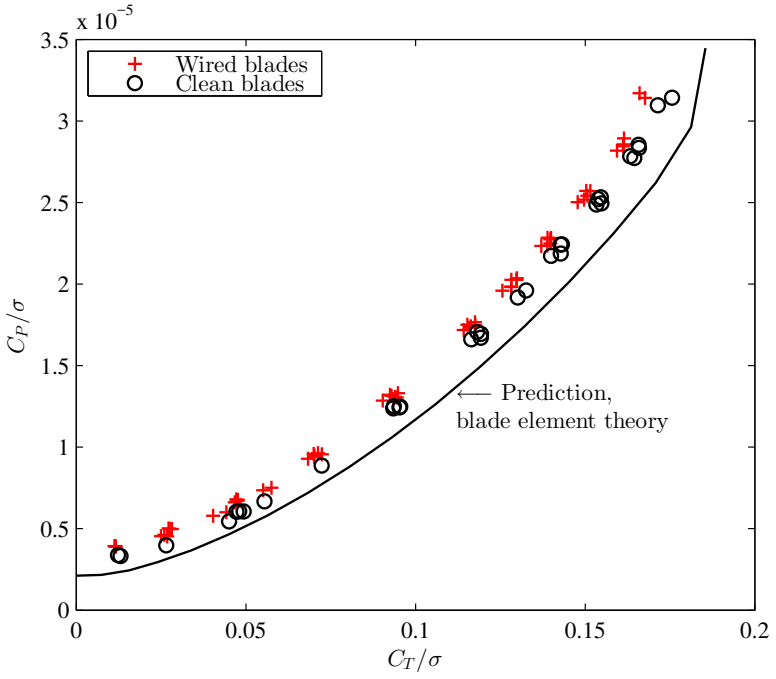

Figure 3.5: Effect of external wiring on hover performance of model rotor blades.

3.2.2 Method 2: Molded Pocket in Skin

Despite the relatively small effect of the external wiring, it is preferable to maintain a clean blade profile, especially when the intent of test data is to compare with predictions that will inherently not include such wiring. To remove the aerodynamic interference of the wiring and gages, a method of embedding these items below the surface of the blade was attempted that kept a similar overall blade assembly process (co-bonding).

The wires were changed from magnet wire to insulated wire for improved resistance to fatigue failures and ease of routing. The wire used was Teflon-insulated, 4-conductor (twisted pair) stranded copper wire, Vishay #436-FTT. The wire was rated to 500° F temperatures, which meant it could survive the composite cure cycles.

During the co-bonding process of blade construction, the wires were laid beneath the carbon skin from the root to the gage location (fig. 3.6(a)). A small pin hole allowed the wires to exit to the outer surface of the blade. At these locations, a metal shim -covered in Teflon release tape—was placed to compress the foam core and push in the carbon skin where the gages were to be placed (fig. 3.6(b)). Excess wire was looped and placed under the shim during the curing process to be available for soldering to the gages after cure.

Post-curing, the shims were removed and the strain gages applied to the depressed area (fig. 3.7). After trimming and soldering the connections, the cavity was filled and faired with epoxy to maintain the intended blade surface profile.

The following difficulties with this approach were encountered:

1. Filling and fairing the cavities back to the curved surface of the blade was difficult. A clamping female mold was used, but significant sanding work was required, which, by nature, introduces deviations from the intended profile.

2. Where the embedded wires emerged from under the skin was typically very close to the final surface. As such, some wires were severed by the sanding operation, which rendered the gages useless in that location.

3. Once there was a lost signal or broken wire, there was nothing to be done to diagnose or repair it, unlike the surface-mount approach.

4. The cavities in the skin have some effect on torsional stiffness and strength, though the effect was not quantified and was thought to be negligible.

3.2.3 Method 3: Bonded To Inner Surface of Skin

To address some of the issues with the previous methods, it was attempted to bond the strain gages directly to the inner surface of the carbon skin before blade assembly. This method requires separate curing of the blade core (with an added thin fiberglass skin to maintain integrity) and carbon blade skin. The fiberglass skin on the core is removed (using a hand-held router) in the locations of the strain gages as well as the wire path (fig. 3.8). This is done to prevent damage to the gages upon final bonding/compression.

The strain gages are bonded onto the inside of the cured carbon blade skin

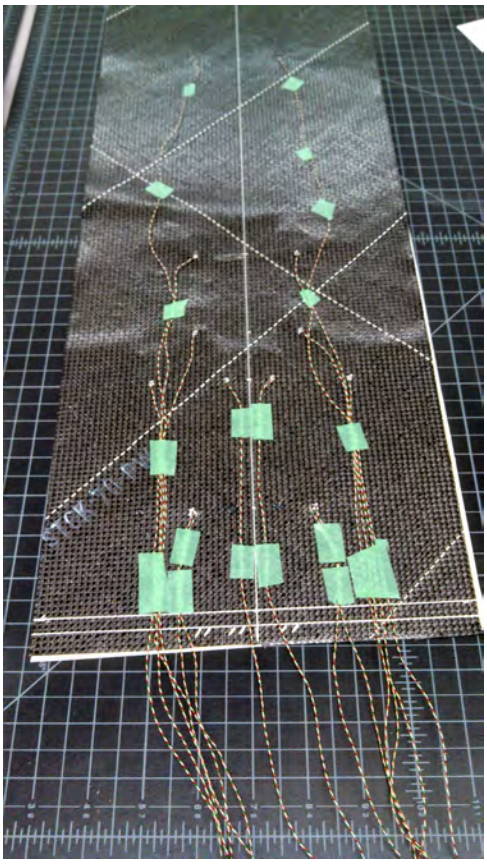

(a) Instrumentation wires routed along the inside of the prepreg skin to emerge at the location of the strain gage.

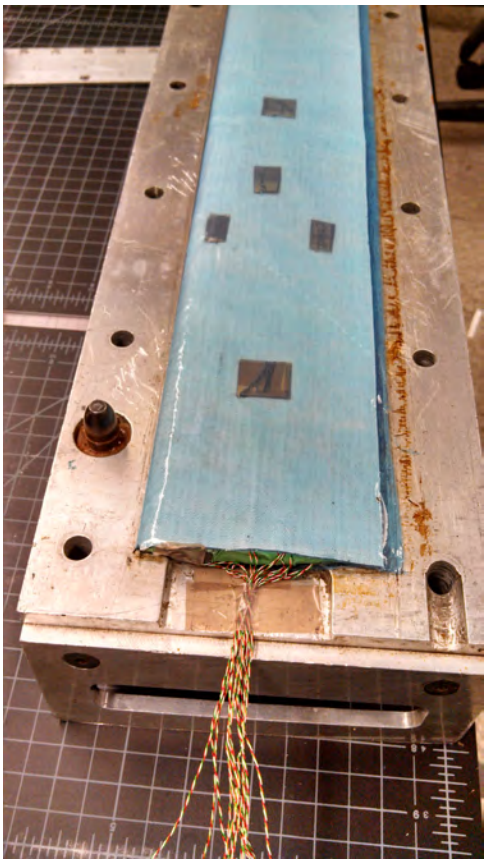

(b) Teflon-covered brass shims were used at the locations of the strain gages to create depressions in the surface during the molding process.

Figure 3.6: Steps to create recessed pockets for strain gage application.

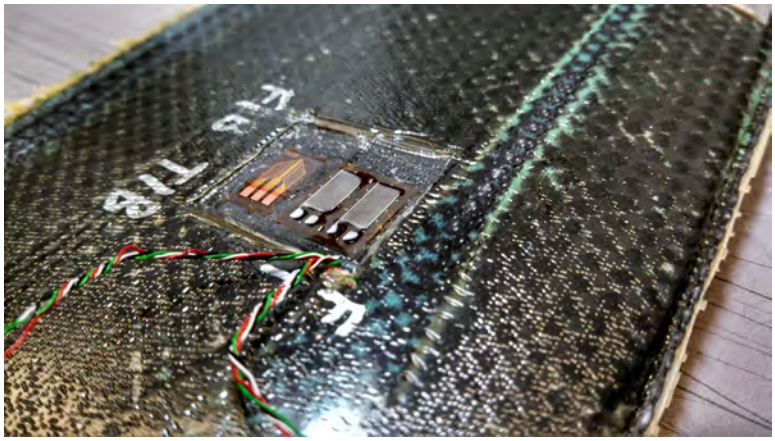

Figure 3.7: After curing, the shims were removed, and strain gages applied in the depression surface. The wires can then be soldered to the strain gages and the depression covered in epoxy resin.

and all wiring connections made. The skin is then bonded to the core using room-temperature two-part epoxy resin. During cure, the blade assembly is compressed using the aluminum two-part blade mold to ensure the final shape is accurate.

This method of assembly provides the best aerodynamic surface with no post-cure sanding needed. However, it has the disadvantage of requiring increased time and skill to accurately place and solder strain gages to the inner surface of skin. An alternative approach would be to have separate top and bottom pre-cured skins, which would make the sensor attachment easier, but may result in a worse leading-edge profile.

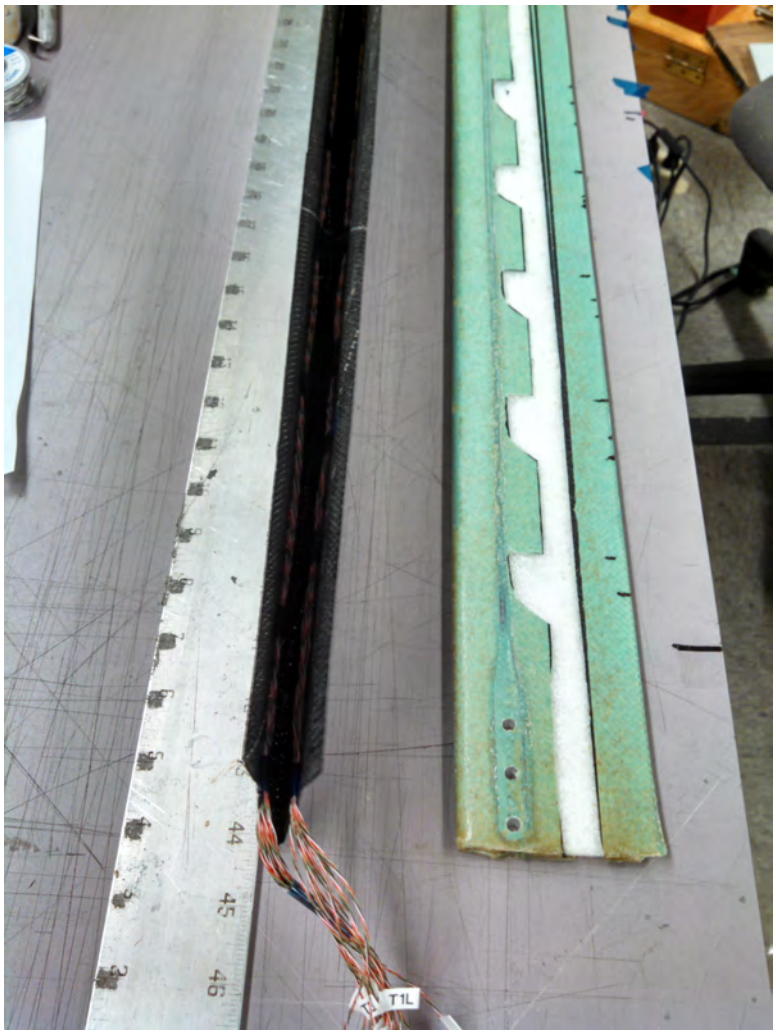

Figure 3.8: Cured carbon skin with strain gages bonded to the inner surface of the skin and wired (left), and blade core with channels removed for wiring and the strain gages (right).

3.3 Pressure Sensor Application Techniques

Embedding pressure sensors into a relatively small and thin rotor blade was a manufacturing and assembly challenge. Even the smallest commercially-available pressure sensors still take up a large percent of the available thickness, especially near the leading and trailing edges. Several methods were attempted over the course of this work, with varying pros and cons. The methods are described in the following sections.

3.3.1 Method 1: 3D Printed Plastic Housing

The leading edge of the rotor blade airfoil cross-section presented a dilemma. This region has the largest surface pressure gradients, while having a very low thickness and volume in which to embed pressure sensors near the surface. A solution to this design challenge was a drop-in replacement of the leading edge nose section, which contained compartments for the pressure sensors (fig. 3.9). The use of additive manufacturing techniques meant that both the slots for the sensors and the pressure port holes could be designed and built-in.

A high-resolution process was required to achieve the small dimensional features on the nose piece. A PolyJet (photopolymer jetting) process was used on an Objet Eden350 printer, using VeroGray RGD850 material. This method has a layer resolution of approximately 16 micron (0.0006), and minimum wall thickness of 0.1–0.3 mm.

The nose piece was designed to bond to the rectangular spar using room tem-

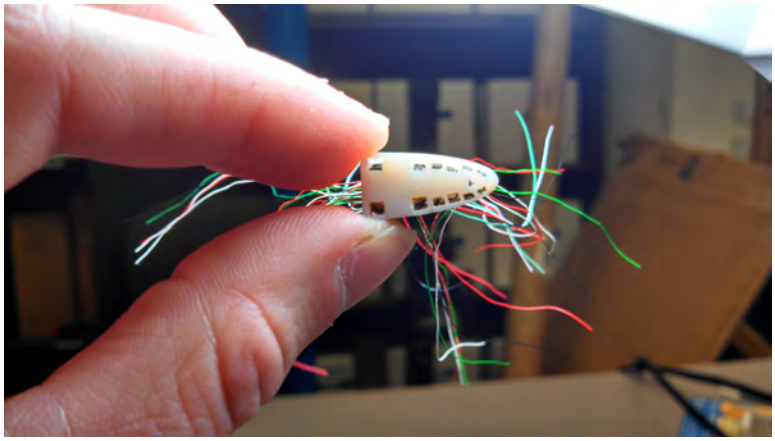

Figure 3.9: Leading edge printed plastic nose piece with built-in compartments for pressure transducers.

perature cure epoxy. The ability of this bond to resist the shear and peeling forces from the rotor blade operation (mainly centrifugal forcing) were verified in representative coupon tests.

3.3.2 Method 2: Molded Pockets in Skin

In areas of low curvature on the rotor blade, away from the leading edge, it was possible to pursue a simpler method of embedding pressure transducers compared with the 3D printed plastic insert. Replacing both the leading and trailing edge of the blade with plastic would have also reduced the strength and stiffness of the blade. In this area, the slots for the pressure transducers could be molded during manufacture, in a similar manner as was done for the strain gage application. A plate of aluminum slightly thicker than the pressure sensors was milled into the shape of the pockets. This plate was covered with release tape and placed in the

mold during the curing cycle and compressed the foam core into the desired shape (fig. 3.10). The end result was not smooth, however, due to the large area that was being molded. The composite fabric deformed and had many wrinkles. Ideally the fabric might be darted appropriately to prevent such wrinkling. In this case, the cured blade was put on a mill so that the pockets could be finalized to the desired shape.

The major difficulty to this method is how to re-create the blade shape once the sensors are placed in the pockets. It was attempted to fill the space to the surface with silicone, but it became difficult to ensure full coverage without damaging or covering the sensing element. It was also a challenge to ensure that the sensing element was flush with the original blade surface (fig. 3.12). The method is feasible, but not recommended compared with the next method discussed.

3.3.3 Method 3: Milled Core with Pre-Cured Skin

The final and recommended method for embedding the pressure sensors was to secondarily bond cured blade skin onto a milled blade core. The drawback of this method is that the density of sensors around the leading edge will be much less than is possible with the 3D printed leading edge concept. However, this method is much easier and cleaner to manufacture, while leaving the skin and outer surface shape intact.

Firstly, the blade core is manufactured as described in the secondarily bonded skin section of this work. That means the blade is first cured with only a thin

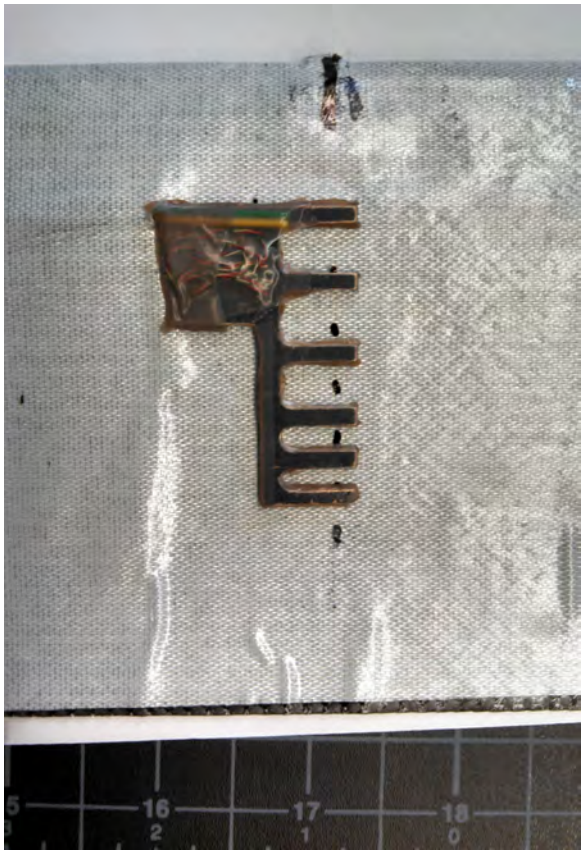

Figure 3.10: Milled aluminum plate on blade ready to be clamped in the mold for baking to create pockets for the pressure sensors.

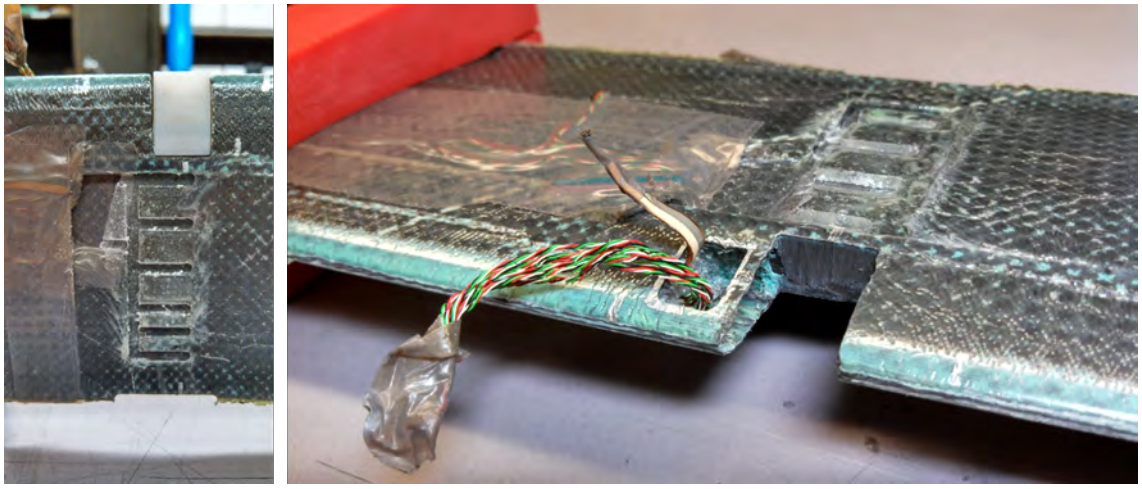

Figure 3.11: Molded and milled compartments in the trailing edge for pressure transducers and the 3D-printed nose piece.

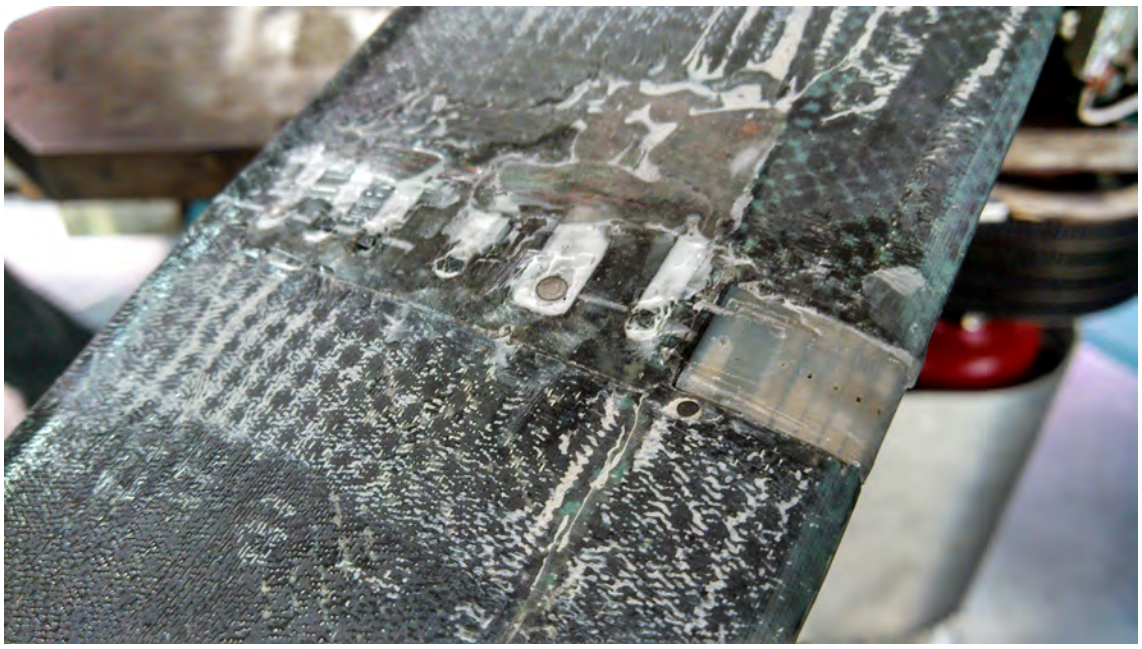

Figure 3.12: The end result of this method showing the difficulty and resulting lack of quality in re-creating the original blade surface.

layer of fiber-glass fabric covering it, to keep everything together. The blade is then covered in release film, and wrapped in the carbon fiber fabric skin, and cured again. This way, the skin is cured separately but still conforms exactly to the blade core. Once removed from the mold, a 3D-printed template is attached to the blade which is used as a drill guide for the pressure sensor port holes. After the pressure ports are drilled, the skin is removed from the blade core.

The slots for the pressure sensors are milled directly into the blade at the appropriate locations, using the drilled holes as guides. For the leading edge sensors, the blade was tilted at the appropriate angle via angle blocks to keep the end mill as close to normal to the local blade surface as possible. The sensors are then placed into the pockets with silicone to secure the sensors in place and isolate them from blade strains. Silicone is also placed around the sensors to create a seal to keep out epoxy during the final bonding operation, and to also seal them so they read pressures without influence from adjacent cells. The carbon skin is then secondarily bonded to the core with room temperature epoxy, and using the mold to provide clamping pressure and ensure the final accurate surface geometry.

3.4 Blade Structural Property Measurements

The rotor blade structural properties are important to quantify to allow accurate dynamic simulation and prediction of vibration.

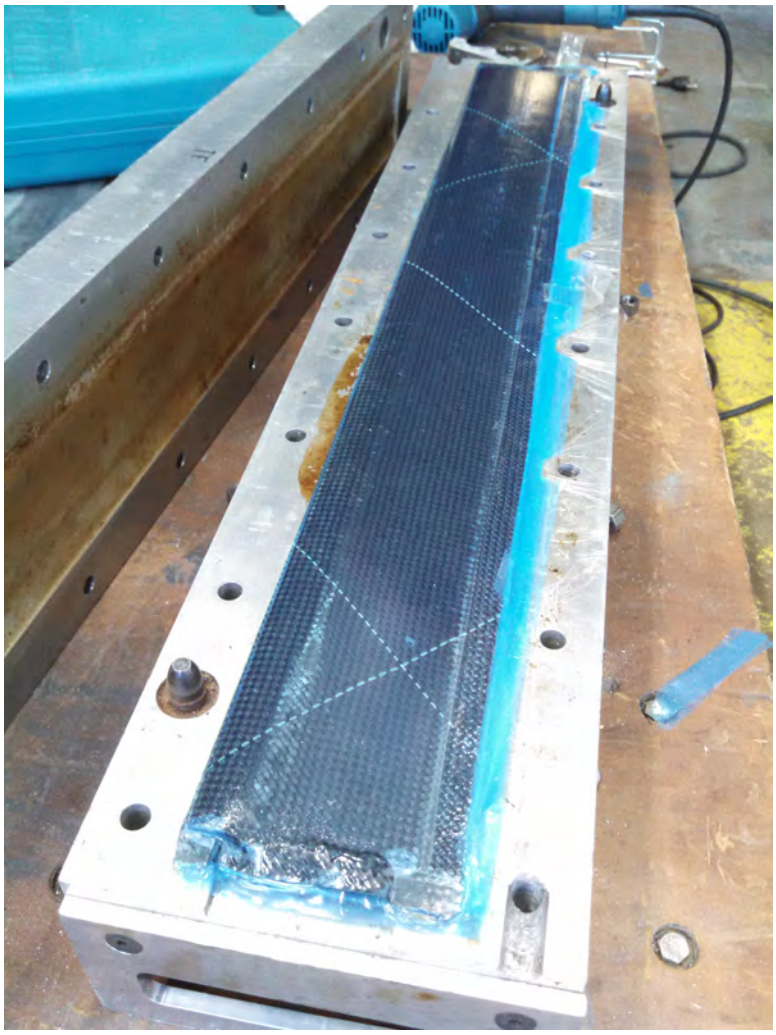

Figure 3.13: Blade coming out of the mold after cure. The carbon skin in this case had a release film layer between it and the core.

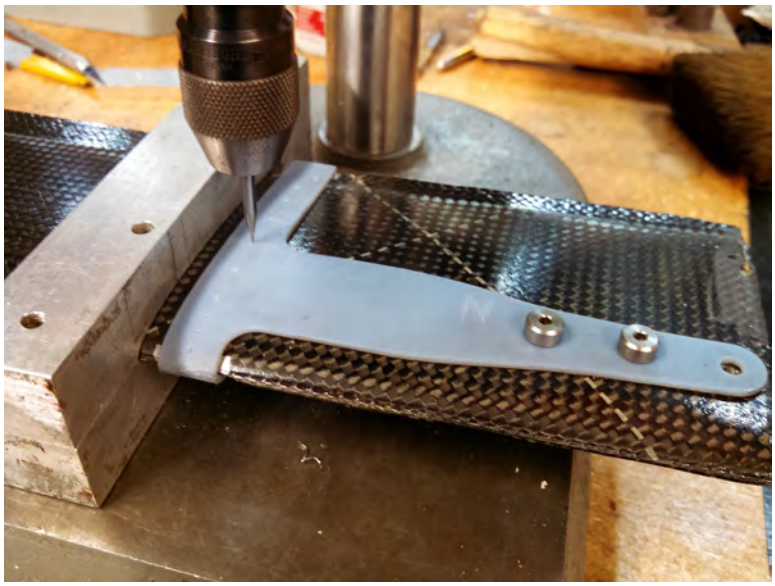

Figure 3.14: Before removing the skin, a 3D printer template for the pressure port hole locations is placed on the blade, and the port holes are drilled through the skin and partially into the core.

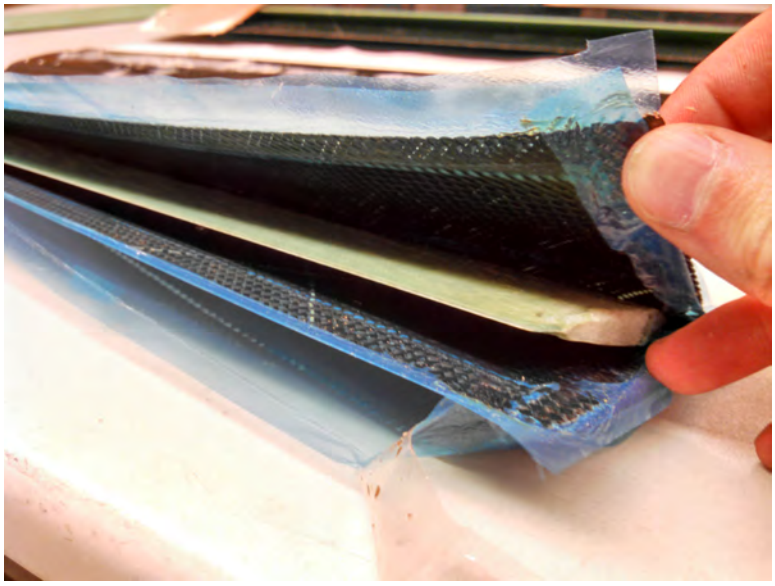

Figure 3.15: The carbon skin had a release layer between it and the core during cure, so the skin is now removed to be bonded to the core at a later stage.

Figure 3.16: After the carbon skin is removed, the pockets are milled into the cured fiberglass skin and foam core, with the drilled holes used as guides.

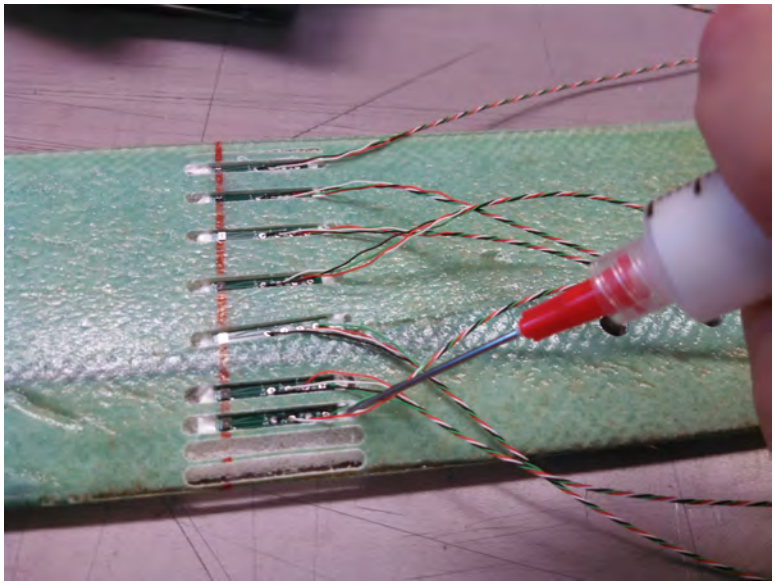

Figure 3.17: Initial placement of the pressure sensors in the milled pockets, with a syringe used to apply silicone adhesive and sealant to secure the sensors.

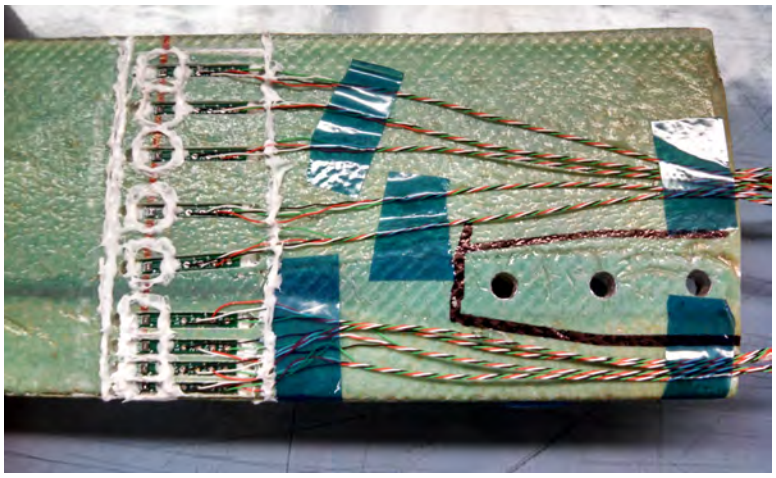

Figure 3.18: Blade core with pressure sensors mounted in the milled pockets. Silicone sealant surrounds the sensors to seal them , and to protect them from the epoxy bonding operation.

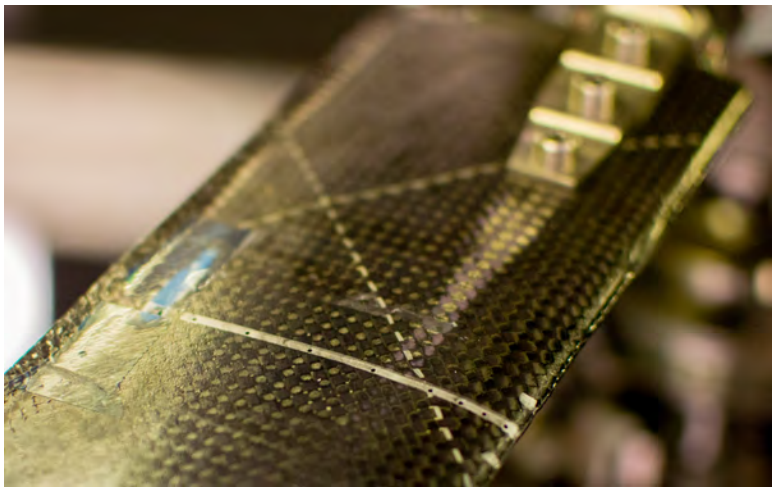

Figure 3.19: Finished blade with pre-cured skin bonded back to the core. The pressure port holes are visible along the silver line.

3.4.1 Blade Flap and Lag Inertia Measurement

To measure the inertia of each blade about the flap and lag hinge point, a pendulum setup was used (fig. 3.20). The blade lag hinge was placed in bearing blocks with a Hall-effect sensor to record angular position (fig. 3.21). The blade was hung vertically and was allowed to swing freely in the lead-lag direction. This was chosen over the flap direction to minimize aerodynamic damping. Since the lag and flap hinges are coincident, the inertia about each axis should be approximately equal. A LabVIEW program was written to calculate the period of the pendulum motions of the blade as it swung (fig. 3.22). To measure the center of mass location, each end of the blade was supported by a digital scale, and static relations used to locate the center of mass. Using the pendulum period, total mass, and the center of mass location, the inertia could be calculated using equation 3.1.

$$I = mgl_{cg}\left(\frac{T}{2\pi}\right)^2 \tag{3.1}$$

3.4.2 Blade Balancing

Rotor blades are typically mass balanced, aero balanced, or both. Aero balancing in the context of this research is the same as rotor blade tracking, which will be covered in the next chapter on wind tunnel test procedures. This section will cover mass balancing. Imbalance in the mass center of the rotor (meaning all rotating components) will cause an oscillating hub side-force in the stationary frame with a frequency of 1/rev for a constant rotor speed. The amplitude of this forcing

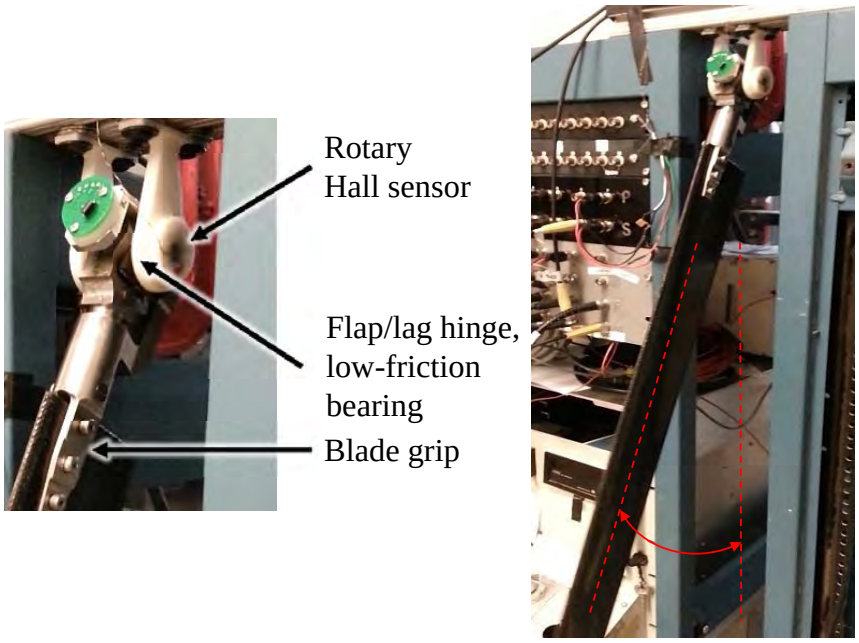

Figure 3.20: Blade flap/lag inertia measurement pendulum setup.

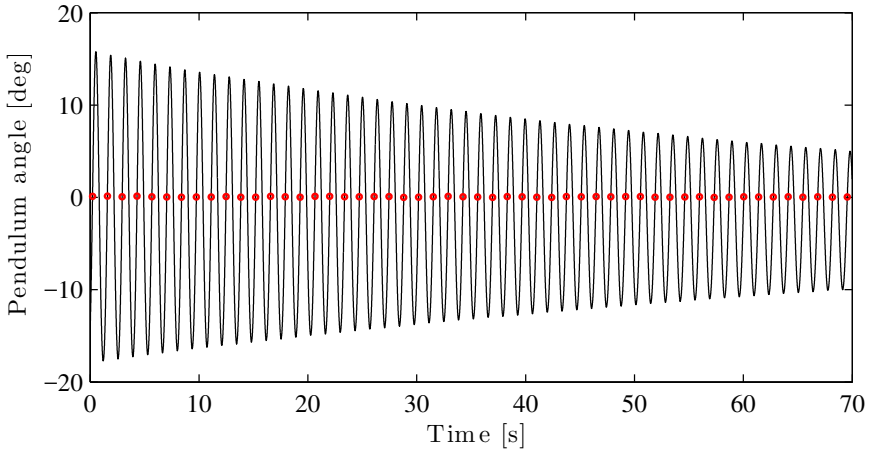

Figure 3.21: Example pendulum angle time history for a rotor blade, with rising zero crossings highlighted.

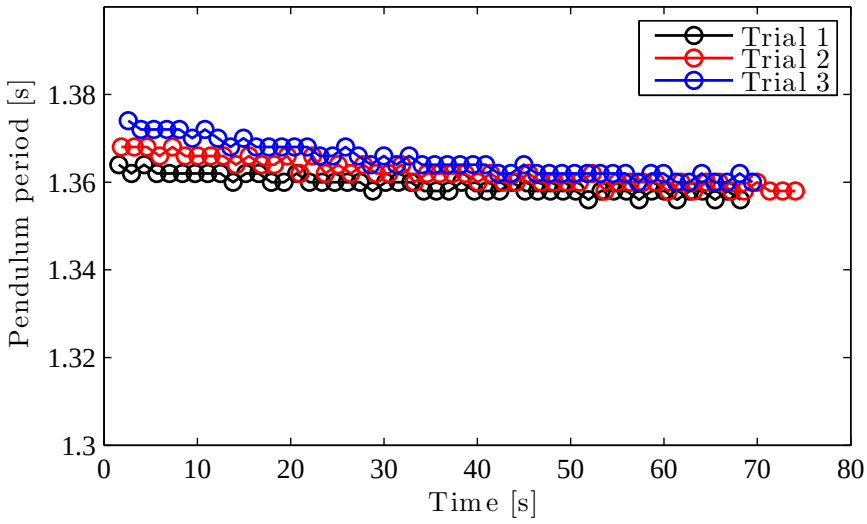

Figure 3.22: Spread of pendulum period results for an example blade, derived from the time histories of three separate trials.

function will be proportional to the square of the rotor angular rate, the radial offset of the center of mass, r_{cg}, and the total mass, since it is a centrifugal force. Adding or subtracting mass to move the center of mass to the rotor center will eliminate this vibration at all rotor speeds. Therefore, opposing blades need to be moment-balanced, meaning the product of total mass and spanwise c.g. location should be equal (first moment of mass). This is equivalent to a teetering or see-saw balancing of the blades, which is the method used in this research.

Opposing blades were mounted in opposition on a balanced aluminum plate, which rested on a central knife-edge pivot (fig. 3.23). Temporary mass (pieces of tape, washers, etc.) were added to the tip of the lighter rotor blade, until balance was achieved. The temporary mass was measured, and then added permanently to the blade tip by pouring an equivalent mass of epoxy resin into a carved out area of

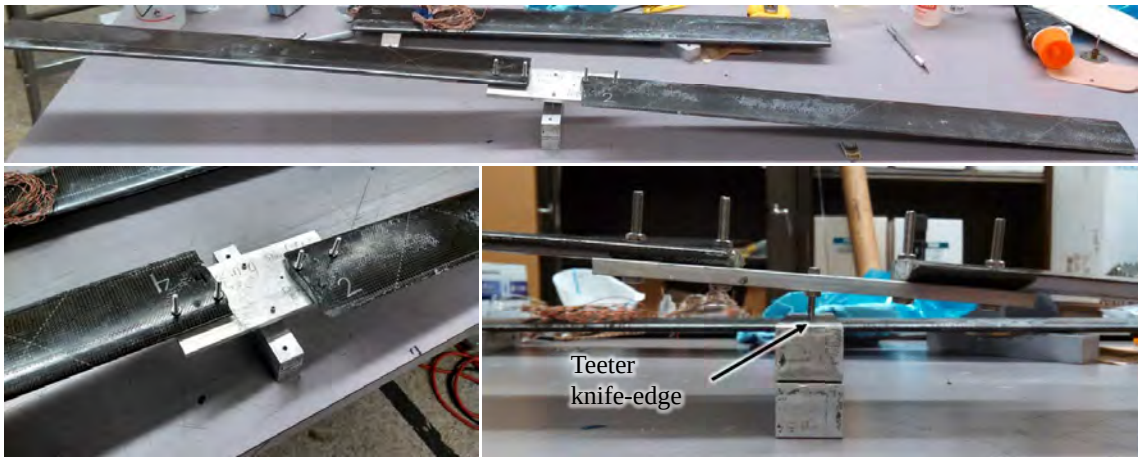

Figure 3.23: Blade mass-moment balancing setup

foam at the tip. If resin was not sufficient to accomplish the balance in a reasonable volume, a steel nut could also be added into the cavity, with the resin forming the structural connection with the composite rotor spar. For small dissimilarities, extra washers could be used on the blade root attachment to achieve balance without tip injection.

Another mass-related dissimilarity between blades would be the flap-wise inertia of each blade about the flapping hinge (second moment of mass). This value is found in the Lock number of the rotor, and has an impact on the flapping response of each blade in flight. Ideally, the blades would be balanced for both first and second moments of mass simultaneously, although in practice this is not easily achieved. It is possible but would typically require adding distributed point masses (2 or more) to each blade to be able to independently vary first and second moment of mass. For this research, the first moment of mass (teetering) was balanced and

no attempt was made to balance the flapping inertias after blade cure.

3.4.3 Blade Stiffness Measurements

The blade sectional stiffness values are required inputs for elastic blade modeling as a 1-D beam in modern comprehensive rotor analysis programs. Typically the flap and torsion stiffnesses are of higher importance than the lag (or chordwise) bending stiffness, due to higher flexibility and therefore lower frequencies.

The rotor blades were cantilevered from a stiff mounting structure using clamp blocks shaped as negatives of the blade root (fig. 3.24). A loading bar was affixed to the blade tip to allow chordwise variation of load application, to allow independent torsion and bending moments. A constant load magnitude was applied to several chordwise positions to extract the location of the shear center (where vertical shear does not induce twist). Varying load magnitudes were then applied to the shear center and deflections measured using a height gage. The blades were assumed to be uniform in structure, so uniform beam bending equations based on Euler-Bernoulli were used to determine the bending stiffness, EI, from the measurements. In a similar manner, varying torsion moments were applied using the loading bar, with the angle of twist deduced from height measurements of each end of the loading bar. These loading cases had applied bending and torsion moments simultaneously, but they were found to be linearly independent (no bending-torsion coupling), so mixed loading could be applied with negligible error. Measured blade properties are given in table 3.1.

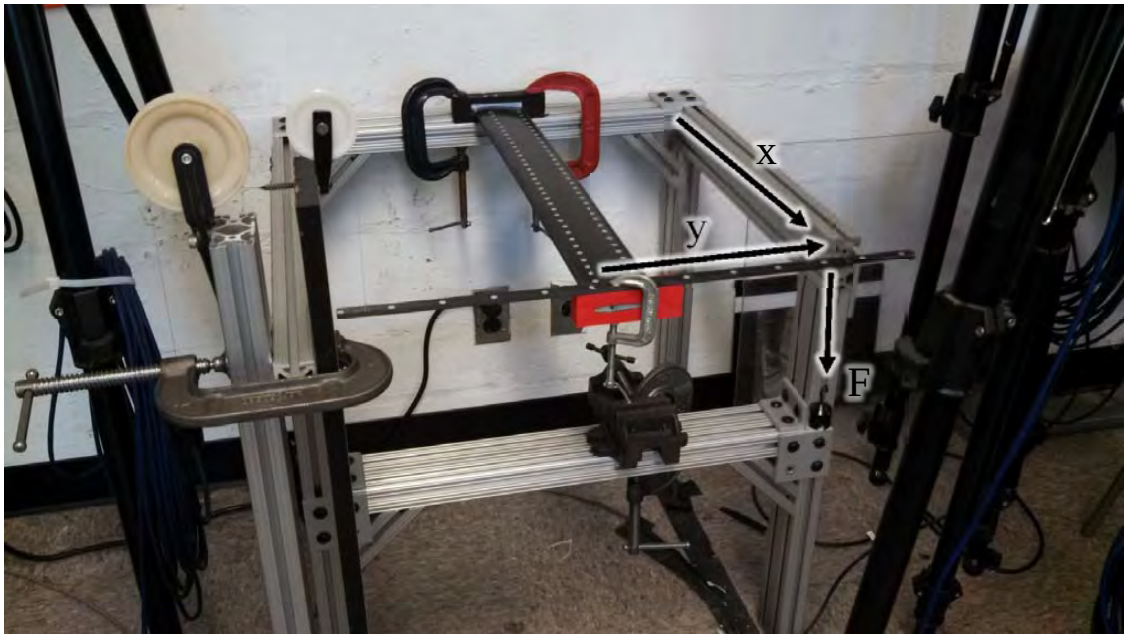

Figure 3.24: Test setup for measuring blade beam stiffnesses.

Table 3.1: Blade inertial and stiffness properties.

	Blade mass, kg	Mass with blade grip, kg	I_y (flap), I_z (lag), kgm^2	Lock Number	EI_y, Nm^2	GJ Nm^2
Blade 1	0.254	0.710	0.0567	5.15	22.3	25.9
Blade 2	0.242	0.699	0.0589	4.95	28.2	28.6
Blade 3	0.253	0.709	0.0581	5.02	30.6	37.7
Blade 4	0.242	0.698	0.0593	4.92	30.1	38.8
Average	0.248	0.704	0.0583	5.01	27.8	32.7

Chapter 4: Wind Tunnel Test Procedures

4.1 Wind Tunnel Description

Testing was performed in the Glenn L. Martin Wind Tunnel (GLMWT), located at the University of Maryland campus. The GLMWT is a closed-return tunnel, with test section dimensions of 7.75 ft high and 11.04 ft wide (2.36 x 3.36 m) (fig. 4.1). The tunnel has a maximum speed of 230 mph/200 kts/103 m/s, or approximately Mach 0.3. Freestream turbulence intensity was reported as 0.21% [51].

4.2 Rotor Blade Tracking

Rotor blade tracking is a procedure to align the rotor blade tips into the same tip-path plane during operation. In edgewise forward flight, the flapping response, and hence tip path plane, of an articulated rotor blade depends on the balance of hinge moments from aerodynamic forces, inertial forces, and centrifugal forces. Assuming the blades are previously mass-balanced and inertially-matched, then tip-tracking is a form of balancing the aerodynamics of the rotor blades. In this research, the aerodynamic-balancing was accomplished by making changes to the root pitch of individual blades via the pitch link rods. In this manner, differences in rotor blade

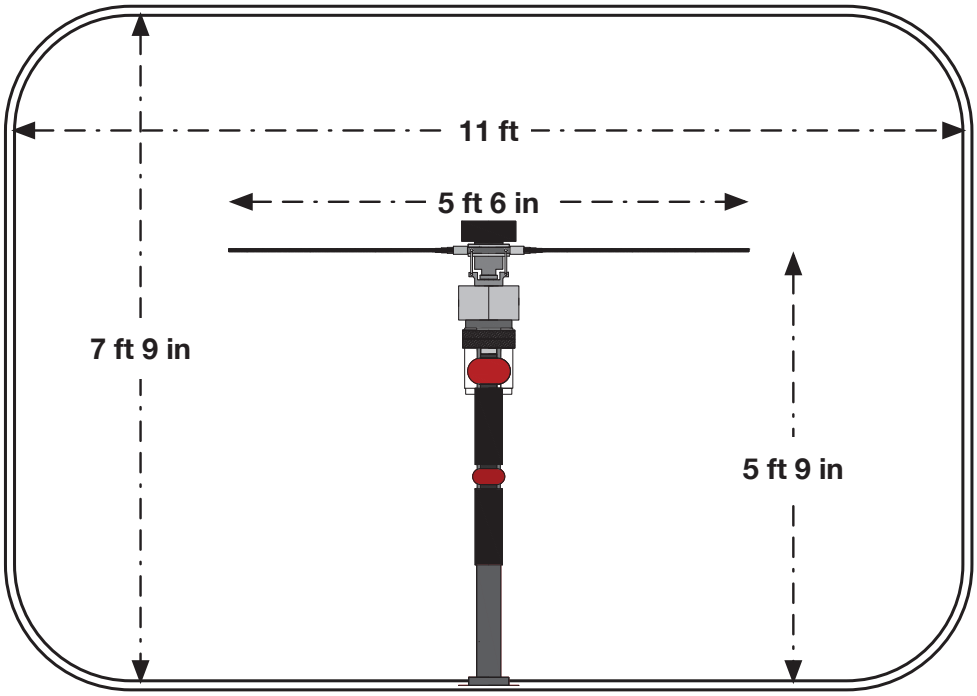

Figure 4.1: Test section dimensions of the GLMWT wind tunnel. [52]

aerodynamics could be balanced out by altering the overall pitch of each blade.

For the purpose of tracking, each blade tip was identified with a uniquely-colored reflective adhesive-backed tape. The tape was retro-reflective, meaning it reflects light in the direction of the light source. When the rotor was at the desired operating condition for tracking, a strobe light was fired towards the edge of the rotor disk at the blade passage frequency (4/rev in this case), in order to freeze the motion of all four blades at the same azimuthal position. The observer could then look in-line with the direction of the strobe light to clearly see the relative differences of each rotor blade (fig. 4.2). When the blades are not in a tracked condition, the observer will see distinct vertical (flap-wise) separations between one or more blade tips. The position of each blade tip relative to a reference blade is noted, and then

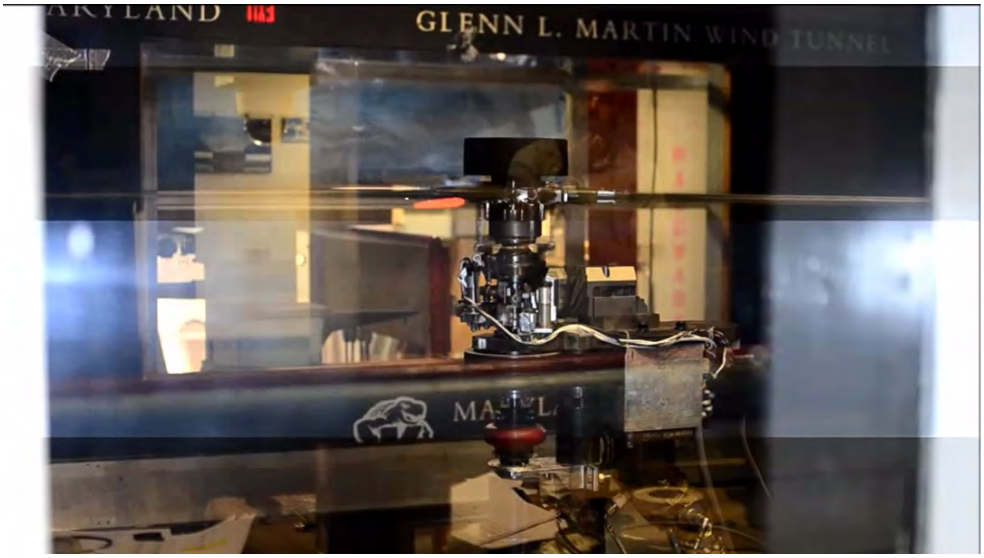

Figure 4.2: Retro-reflective colored tape on each blade tip shows relative blade positions and tracking differences when strobed at the blade passage frequency.

the pitch links are adjusted between runs (fig. 4.3). Tracking is achieved when the blade tips are vertically aligned within about 1/2 blade thickness.

Depending on the azimuth chosen to observe blade tracking, the differences between blades varied substantially. Due to visual restrictions in the wind tunnel, observations were easiest to make at two azimuth angles: 225 and 315 degrees. It was noted that satisfactory blade tracking was easy to achieve at 315 degrees, while the tracking would remain poor when observed at 225 degrees. Since a hinged rotor will have maximum flapping response approximately 90 degrees after the maximum forcing location, and the maximum dynamic pressure is experienced between 45–135 degrees, maximum flapping angles due to aerodynamic differences will be greatest between approximately 135 and 225 degrees azimuth. Therefore, for best tracking results, observations of tip path plane tracking should be made at the azimuth of

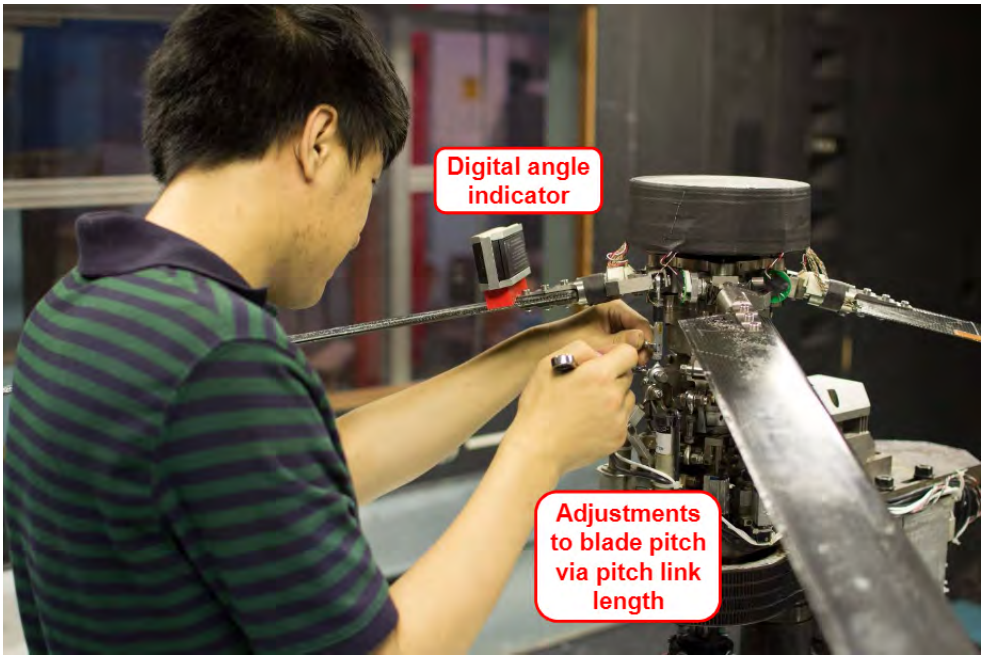

Figure 4.3: The blades can be brought into track by making fine adjustments to the pitch setting of each blade through the pitch link length.

expected maximum flapping, or in this case, 225 degrees.

As the advance ratio was increased during testing, either by reducing rotor speed or increasing wind speed, the rotor blade differences would become more pronounced (fig. 4.4). In this situation, aerodynamic forces dominate the centrifugal forces, and flapping magnitudes increase, all else being equal. Therefore, for high advance ratio studies, rotor blade tracking should be completed at high advance ratio conditions for best results. This was found to be a sensitive and time-consuming process, but necessary for advance ratios above 0.7 (fig. 4.5).

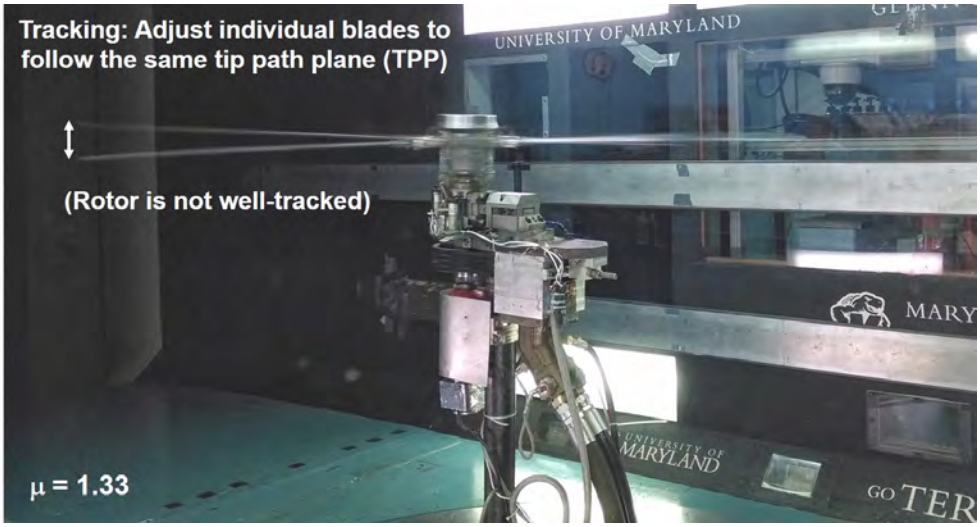

Figure 4.4: Example of rotor blades being out of track at high advance ratio, despite being well-tracked at lower advance ratio.

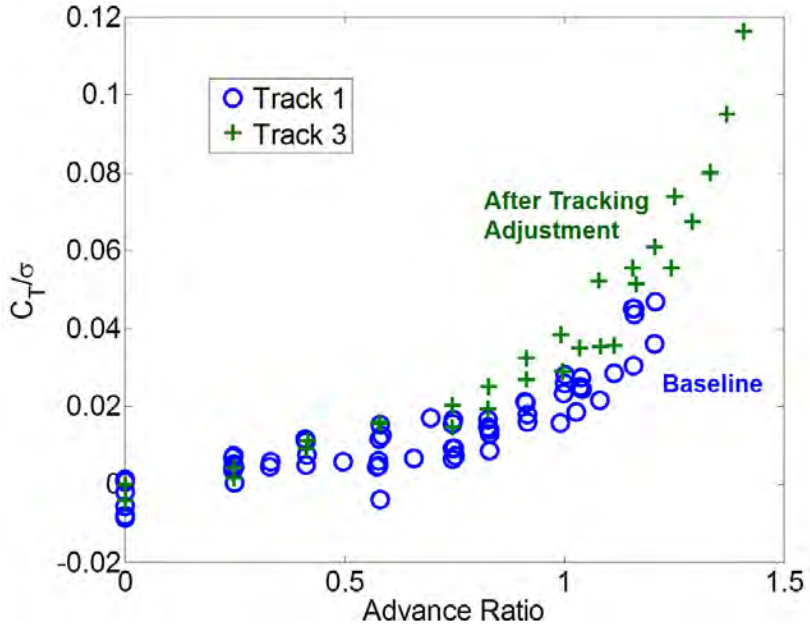

Figure 4.5: Example showing the increased sensitivity of thrust measurements to tracking adjustments as advance ratio increases beyond about 0.7.

4.3 Rotor Trimming Procedure

The trim target for the rotor was zero flapping, which is known as *wind tunnel trim*. More precisely, the rotor was trimmed so that the amplitude of the first-harmonic (one-per-rev, or 1P) of the blade flapping angle was zero. This trim target essentially brings the rotor tip-path plane normal to the shaft. The rotor blades will still have a steady flapping angle (coning) and higher harmonics (2/rev, 3/rev, etc.) that cannot be trimmed out using a traditional swashplate (which can only provide 1/rev inputs).

An alternative trim approach could be to trim to zero hub moments (roll and pitch). A potential difficulty with this approach is the need for accurate real-time hub loads, which need to account for any tare effects from undesired components in the airflow that are measured by the load cell.

The rotor was manually trimmed to zero 1P flapping for each test point. The test operator was aided by a computer readout of the 1P flapping magnitude of the rotor. This was provided by live measurements from four rotary encoders, one mounted to each blade flap hinge. The time history of each hinge angle was converted to azimuthal time by being synchronized with the main rotor shaft encoder. The first harmonic of each blade could then be extracted using harmonic analysis in the Labview software output. Due to blade differences and tracking imperfections, the four rotor blades did not always have the same 1P flapping amplitudes, especially at the highest advance ratios (fig. 4.6). Therefore, to maintain overall trim, the amplitudes of all 4 blades were averaged, and this amplitude was used to meet the

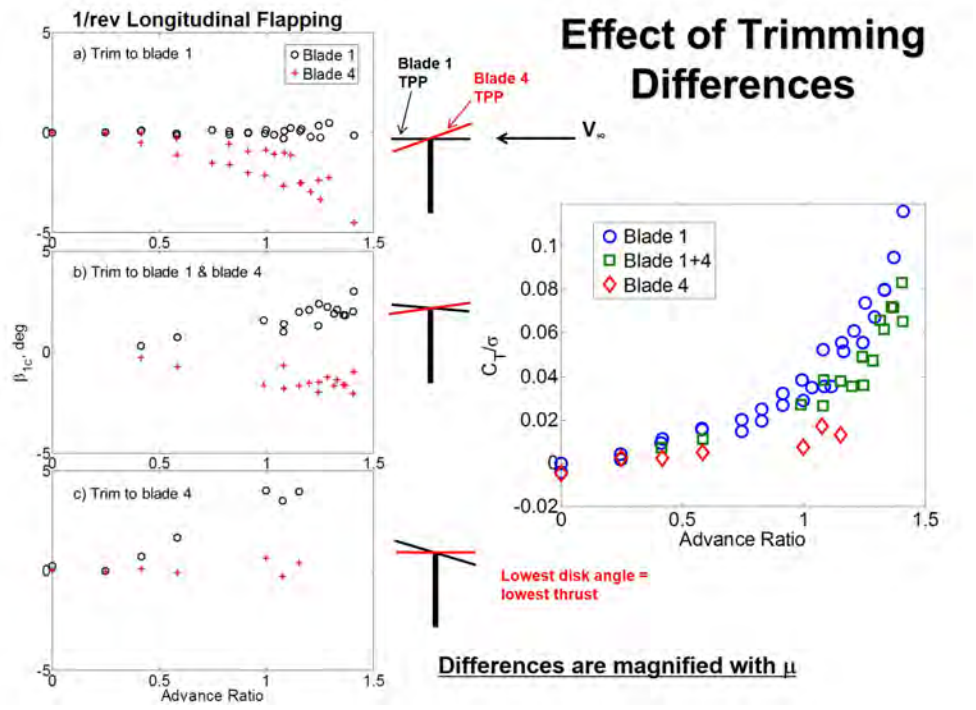

Figure 4.6: Effects of blade choice as trim target on longitudinal blade flapping (disk pitch) and thrust measurements.

trim target.

4.4 Test Plan

The purpose of the wind tunnel tests were to explore rotor behavior at high advance ratios, up to 1.0 and above. Advance ratio being the ratio between tip speed and wind speed, this ratio can be altered by variation of either or both. There are many possibilities, but here are the three that were used by this author:

1. Fixed advancing tip Mach number: One of the strong motivations of a slowed-rotor aircraft is to keep the advancing tip below drag divergence. Therefore, one strategy to replicate this in the wind tunnel would be to set the rotor to a

typical hover tip Mach number (e.g. 0.6), and then increase tunnel speed until the advancing tip reaches the limit previously agreed upon (e.g. $M_{90,1} = 0.8$). From there on, as tunnel speed is increased, the rotor angular speed would be decreased accordingly to maintain this advancing tip Mach number limit. At the maximum tunnel speed (in this case 200 kts or Mach 0.3), the rotor could then be slowed further to explore even higher advance ratio behavior.

2. Fixed wind speed, variable rotor speed: This situation can be seen as similar to the above approach once maximum tunnel speed is reached. A fixed wind speed would be set, and the rotor speed would start high for conventional advance ratio operation, and be successively lowered to increase advance ratio. The benefit of this approach is again more closely replicating the operation of an aircraft employing a slowed-rotor, which would start at conventional rotor speeds and then reduce them at a high wind speed. The high wind and rotor speeds involved also help with signal-to-noise ratios on all the sensors (load cells, strain gages, and pressure sensors).

3. Fixed rotor speed, variable wind speed: In this case, a fixed rotor speed is chosen, based on the maximum advance ratio desired and the tunnel speed limits. The rotor is fixed at this speed, and the wind speed is started low and successively increased to sweep advance ratio. There are two main benefits to this approach from an experimental standpoint. Firstly, the fixed rotor speed means that dynamic loads on the rotor load cell in the stationary-frame will be at fixed frequencies (1/rev, 4/rev, 8/rev, etc.) for all advance ratios. Since

the dynamic response has a complex variation depending on the forcing frequency (see dynamic hub calibration in section 2.3), restricting these to fixed frequencies increases confidence in the overall trends, and simplifies the dynamic calibrations needed. Secondly, the chosen rotor speed will be relatively low in order to reach high advance ratio within the tunnel speed limits. The lower rotor speed and thus centrifugal forces help increase survival rates of embedded blade sensors.

The primary set of data in this work was conducted with a fixed rotor speed and variable tunnel speed. Previous data sets will be covered that conducted sweeps with fixed wind speed and variable rotor speed. No matter what the approach to vary advance ratio, once an advance ratio was set, sweeps were conducted by varying the collective pitch setting and trimming the rotor.

The primary test matrix in terms of advance ratio, collective, and thrust is shown in figs. 4.7 and 4.8.

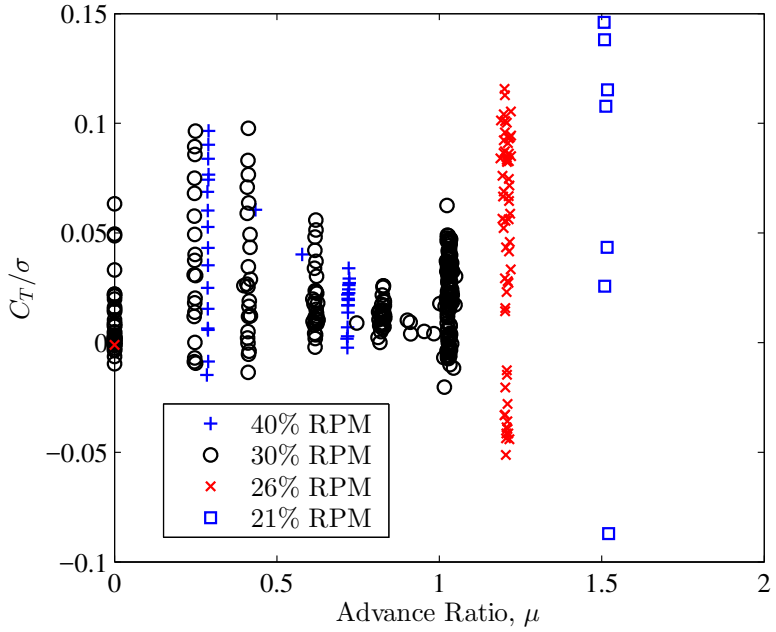

Figure 4.7: 2014 test envelope for thrust and advance ratio, $\alpha_s = 0°$.

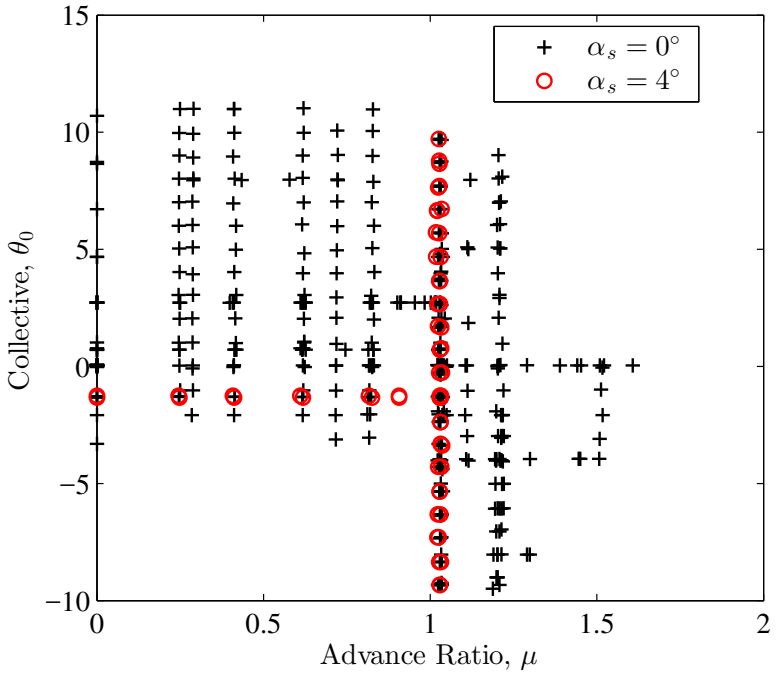

Figure 4.8: 2014 test envelope for collective and advance ratio, all rotor speeds and shaft tilts.

Chapter 5: Data Processing

5.1 Filtering and De-Filtering

The analog tachometer signal was not filtered since the nature of the signal is a spike and the rotor speed and azimuthal position of the rotor are derived from peak counting. The low-pass filtering on the bridge-based sensors will therefore cause a phase lag with respect to the azimuthal position sensor. To correct this phase lag, a de-filtering process was applied to the sensor data. A de-filtering algorithm was written to do the following:

1. Transform time-domain sensor data to the frequency domain via an FFT algorithm.

2. Determine the filter transfer function (poles, zeros, gain), in this case a 3rd order Butterworth filter (fig. 5.1).

3. Using this transfer function, determine the gain and phase at each FFT frequency bin.

4. Apply the inverse of the filter gain and subtract the filter phase from each FFT bin, according to the associated frequency.

5. Set all amplitudes above the cut-off frequency to zero (optional) to avoid applying large amplification factors to signals and noise that have already been highly attenuated.

6. Convert back to the time domain via an inverse FFT.

The impact of this particular filter is quite small in terms of magnitude and phase at frequencies of interest. The phase lag in terms of azimuthal time for the 4/rev frequency is on the order of 1.3 degrees azimuth for the primary rotor speed used in these tests (700 RPM). An example of the de-filtering process results for a time-domain surface pressure sensor signal is shown in fig. 5.2. The high frequency portion of the signal is enlarged to better show the removal of the delay caused by the anti-aliasing filter.

5.2 Ensemble/Phase Averaging

Once the time domain data have been corrected for the effects of the low-pass filter, the periodic signals are ensemble averaged, which is also referred to as cyclic- or phase-averaging. This process converts the time-domain data to azimuthal time (angular position of each sample in the rotor rotation). At this point, statistics can be extracted from the approximately 100 revolutions taken at each test condition (10 seconds per point, main rotor speed was 11.67 Hz). The main statistics used in this work are the average and the standard deviation. The distribution of variance between each revolution is assumed to be normal/Gaussian, and twice the standard deviation (2σ) is taken as a 95% confidence interval above and below the average,

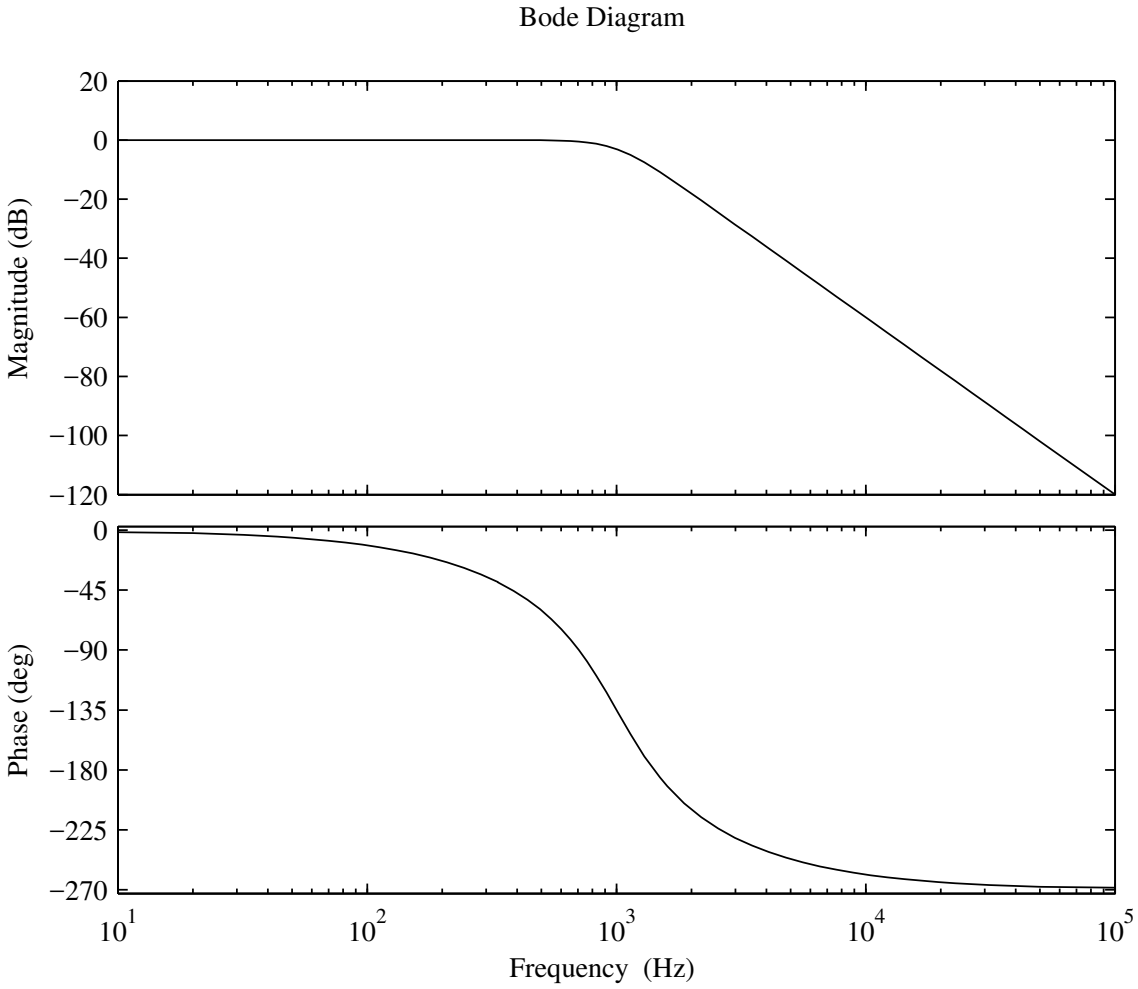

Figure 5.1: 3rd order Butterworth low-pass filter used in testing.

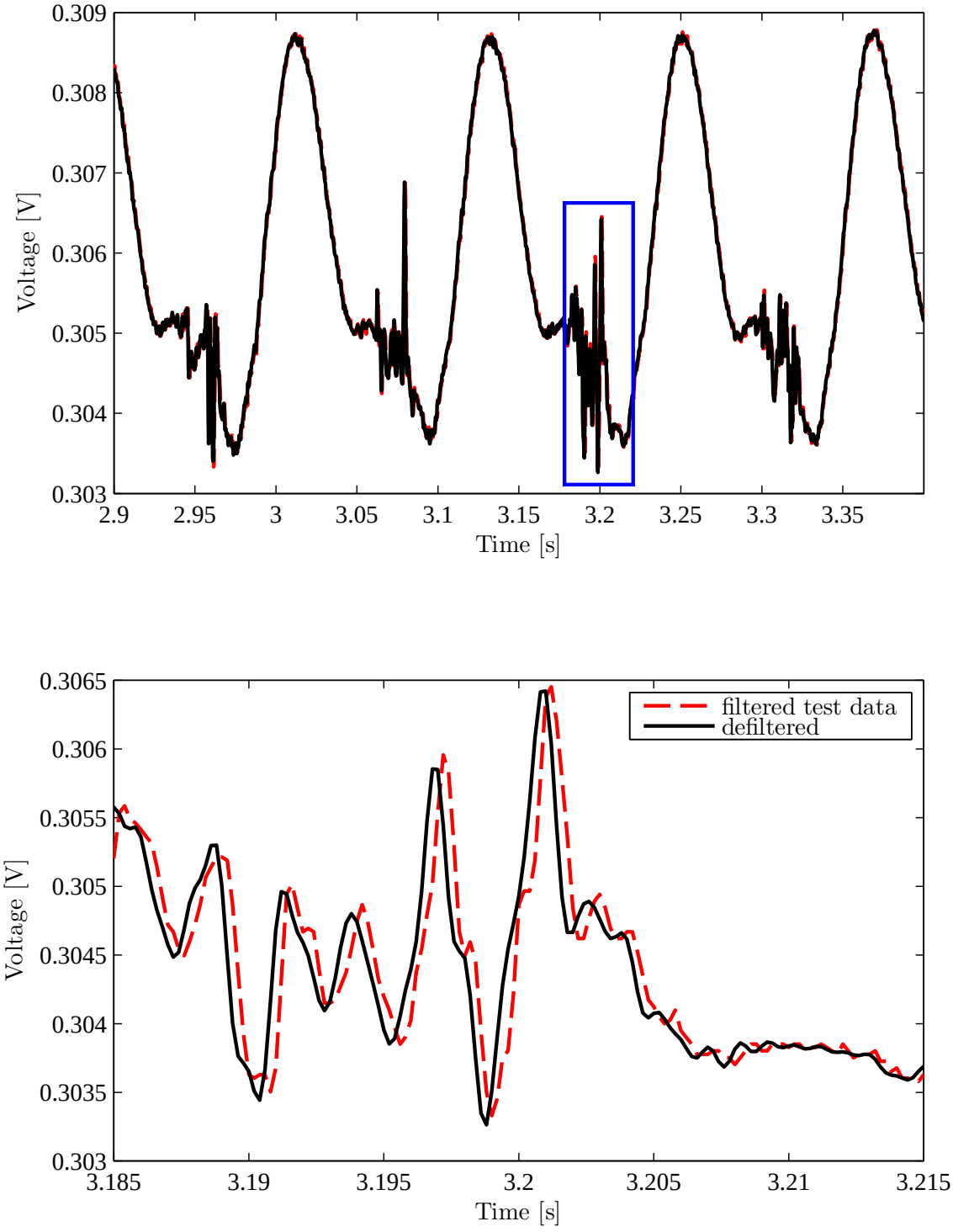

Figure 5.2: Example effect of the defiltering algorithm on a blade surface pressure sensor time history. The impact is more prominent in the higher frequency signals highlighted.

indicating the range of statistical insignificance. Standard error of the mean is taken as twice the standard deviation divided by the square root of the number of samples. For most phase-averaged runs, this would be 0.1 of the 2σ range (100 cycles being averaged).

An example test case and sensor signal demonstrates the ensemble averaging approach used on all sensors. The flap-wise blade bending moment at the 30% radial station for Case 543 is shown as an example. The time history of the calibrated data is shown in fig. 5.3 for the first five rotor revolutions (out of 100). For each azimuth, the samples for every revolution are averaged, and the standard deviation is calculated. Fig 5.4 shows the point cloud of all revolutions, along with the mean and the $\pm 2\sigma$ variation bands.

5.3 Pressure Coefficient Calculation

The blade surface static pressure was measured using pressure transducers mounted flush or just under the blade skin. The sensors output an analog voltage signal, and then converted into engineering units (ψ) using pre-determined calibration factors (after removing known tares/offsets). The dimensional pressures can then be non-dimensionalized into the pressure coefficient. The pressure coefficient, C_p, is defined as follows:

$$C_p = \frac{p_s - p_\infty}{\frac{1}{2}\rho V^2} \tag{5.1}$$

Typically for wings or 2d section testing, the freestream velocity is used in the

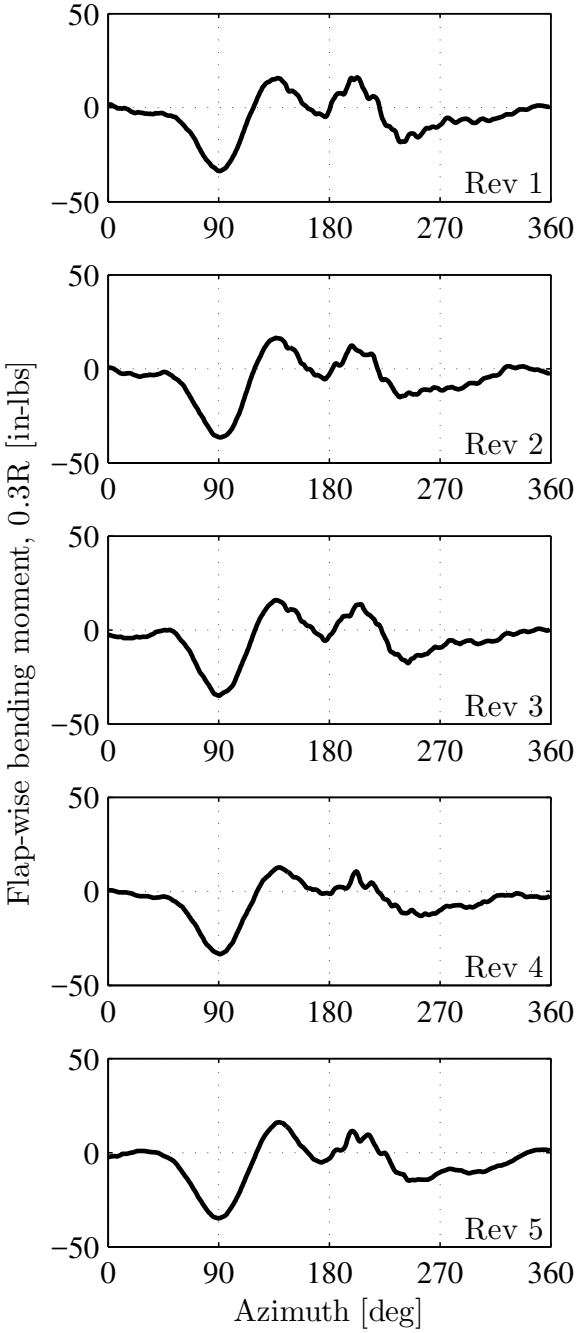

Figure 5.3: The first five individual revolutions (out of 100) for blade flapwise bending moment at the 0.3R spanwise location. Case 543: μ=1.21, θ_0 = -6 deg.

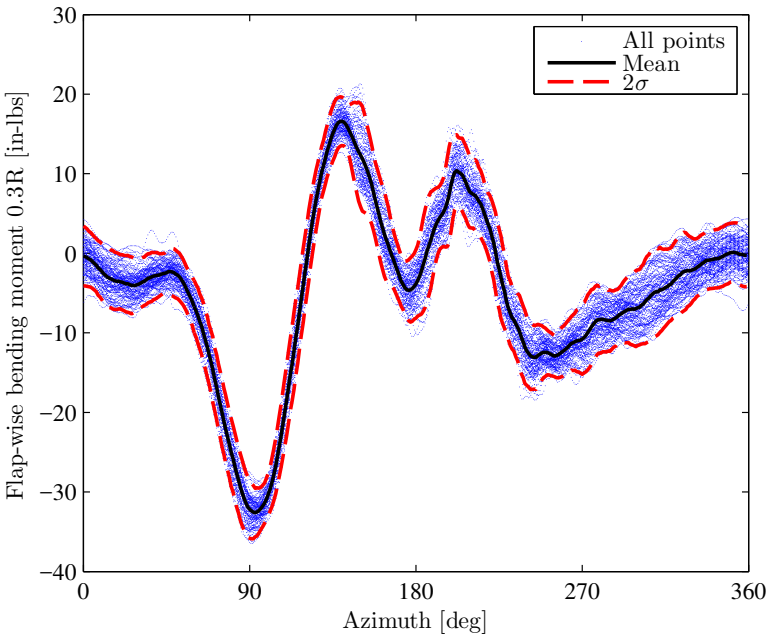

Figure 5.4: Point cloud of calibrated data points for 100 revolutions, phase-average mean, and $\pm 2\sigma$ bands for an example case showing blade bending moment at 0.3R. Case 543: μ=1.21, θ_0 = -6 deg.

denominator. For a rotor blade section, the local freestream velocity is not well-defined or easily measured in an experiment. The tangential velocity components from the rotation (Ωr) and the freestream ($U_\infty * sin(\psi)$) are well-defined, as is the radial velocity component from the freestream, $u_r = V_\infty * cos(\psi)$. However, for a rotor there are additional velocity components from the induced velocity as well as blade flapping and lagging motions. In this work, when C_p is shown, it will be using the defined tangential and radial velocity components, resulting in equation 5.2.

Another convention for communicating pressure coefficient is to use the speed of sound as the velocity in equation 5.3. The resulting pressure coefficient is essentially M^2C_p, where C_p is the traditional definition using the exact local relative velocity (which is unknown, but cancels out when multiplying by the square of the local Mach number). This allows the velocity term to be well-defined for any condition. Another benefit of using this definition for high-advance ratio rotor tests is it avoids asymptotes where the local section velocity goes to zero as the blade transitions from forward to reverse flow, and vice-versa. Integrated force and moment coefficients will be presented as M^2c_l, M^2c_d, M^2c_n, M^2c_a, and M^2c_m for the same reasons, and is additional useful to provide a global representation of blade loads [53]. In certain cases, it is of use to examine the normal force coefficients using as close to true local velocity as possible to determine proximity to stall. In these situation, c_n will be normalized similarly to C_p as shown in 5.2, using the well-defined velocity components tangent and radial to the blade section (see red

dash line in fig. 5.10).

$$C_p = \frac{p_s - p_\infty}{\frac{1}{2}\rho[(\Omega r + V_\infty sin(\psi))^2 + (V_\infty cos(\psi))^2]} \tag{5.2}$$

$$M^2 C_p = M^2 \frac{p_s - p_\infty}{\frac{1}{2}\rho V^2} = \left(\frac{V^2}{a^2}\right) \frac{p_s - p_\infty}{\frac{1}{2}\rho V^2} = \frac{p_s - p_\infty}{\frac{1}{2}\rho a^2} \tag{5.3}$$

5.4 Pressure Sensor Integration

The surface pressure measurements around a blade section were integrated to obtain estimates of the normal force coefficient, c_n, and moment coefficient, c_m, of the section. In this experiment, the geometric constraints of the rotor blade limited the achievable resolution in pressure sensor placement. With this in mind, the accuracy of the integrated coefficients is reduced, but the trends can still inform regarding the overall behavior. Simulated surface pressure distributions were used to estimate the error from integration. CFD simulations by Potsdam, Datta and Jayaraman of a full-scale UH-60A rotor at high advance ratio were used as representative of the flow environment that would be encountered in the present work [31]. The results from Case 9175 in [31] were used, which was measured at the following conditions: Advance ratio = 1.0, tip Mach number = 0.26, shaft angle = 0°, radial station = 0.225R. The simulations from [31] provided continuous chordwise pressure distributions at a similar radial station and advance ratio, allowing testing of discrete sensor integration in both forward and reverse flow. Distributions in forward flow over the advancing blade ($\psi = 90°$) are shown in figure 5.5, with the intended

pressure sensor placement and as-tested pressure sensor placement. Two sensors, one at the lower trailing edge, and one at the upper leading edge, failed during blade assembly and were not functional. Fig 5.6 shows the retreating blade ($\psi = 270$ deg) for the intended and as-tested pressure sensor placement. In all cases, the axial force coefficient has significant error due to the absence of coverage at the leading edge. Pitching moment and normal force coefficient have approximately 10% error for the forward flow case with all sensors functional (fig. 5.5). When the non-functional sensors are removed, the normal force error doubles to 22%, and the pitching moment error increases to 91%. The errors in reverse flow (fig. 5.6) are even greater for normal force coefficient, due to poor sensor coverage at the geometric trailing edge.

To mitigate the errors caused by the lack of coverage at the geometric trailing edge (and the leading edge), a few extrapolation processes were studied. The first was to assume the leading and trailing edge points ($x/c = 0.0, 1.0$) were equal to the freestream pressure ($C_p = 0$). The second method was to linearly extrapolate the existing measurements. The results of all three integration methods (including no extrapolation) are shown in figs. 5.7 and 5.8.

The chord/axial force is now over-predicting, because the leading edge is carrying a large pressure (magnitude) due to the extrapolation technique. Some refinement of the extrapolation technique could probably be done, but is not attempted here and the chord force integration is not used for correlations or interpretation of phenomena.

From these checks, it is clear that the integrated coefficients from this study may not be useful for direct quantitative correlation with predicted sectional co-

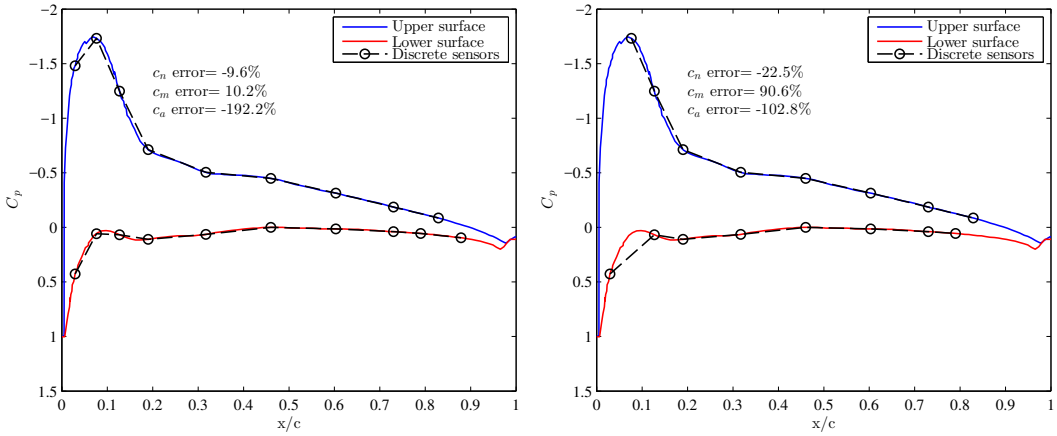

(a) Intended sensor layout

(b) As-tested

Figure 5.5: Intended pressure sensor layout and as-tested (after failures), advancing blade ($\psi = 90^o$). Data from Case 9175 of [31].

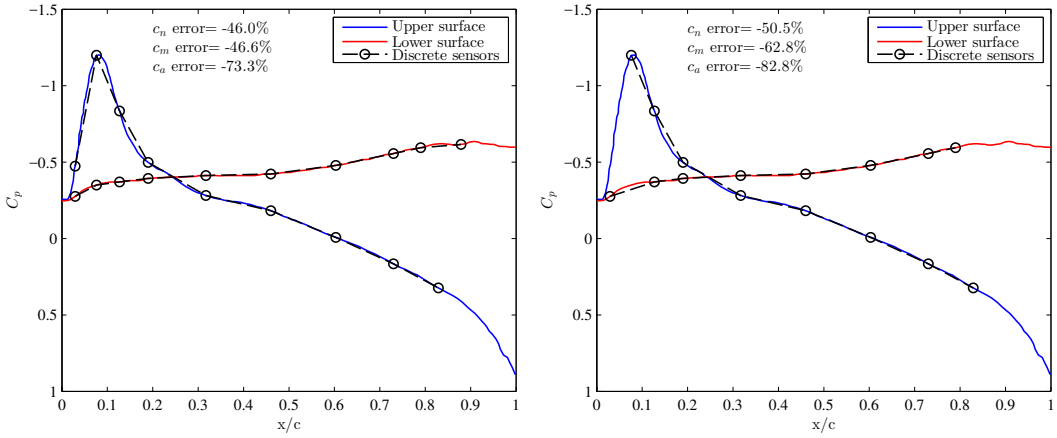

(a) Intended sensor layout

(b) As-tested

Figure 5.6: Intended pressure sensor layout and as-tested (after failures), retreating blade ($\psi = 270^o$). Data from Case 9175 of [31].

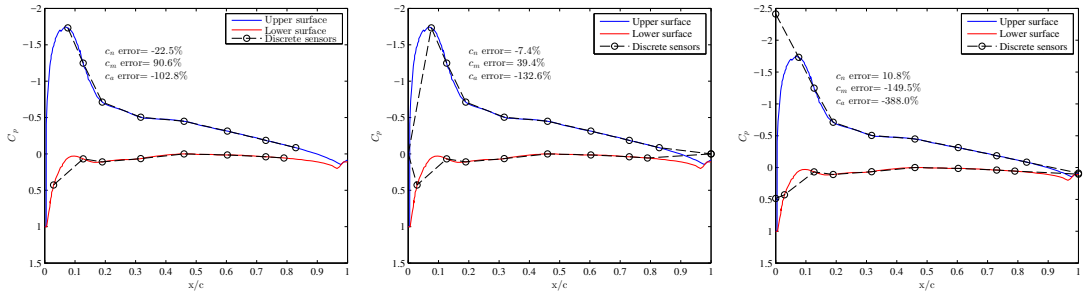

(a) No extrapolation (b) Set LE, TE = 0 (c) LE, TE linearly extrapolated

Figure 5.7: Advancing blade ($\psi = 90^o$) chordwise pressure distribution, with three extrapolation methods. Data from Case 9175 of [31].

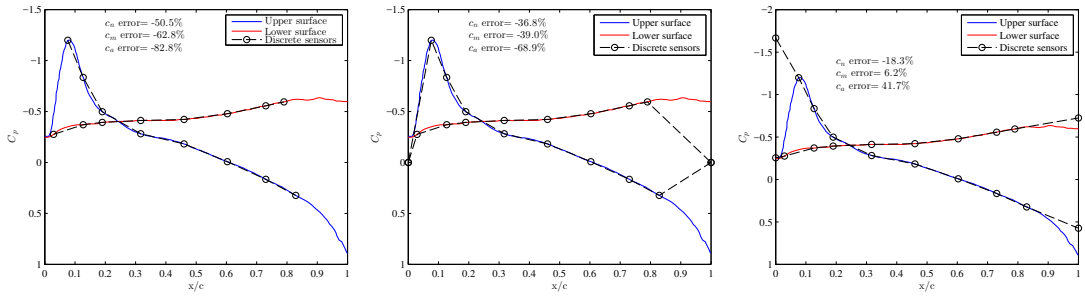

(a) No extrapolation (b) Set LE, TE = 0 (c) LE, TE linearly extrapolated

Figure 5.8: Retreating blade ($\psi = 270^o$) chordwise pressure distribution, with three extrapolation methods. Data from Case 9175 of [31].

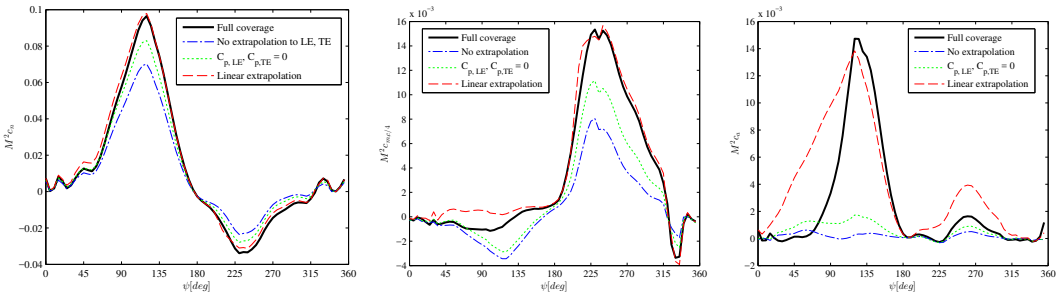

(a) Normal force (b) Pitching moment (c) Chord force

Figure 5.9: Effect of pressure extrapolation methods on integrated force and moment coefficients. Data from Case 9175 of [31].

efficients from rotorcraft comprehensive analysis or CFD. However, the qualitative trends through a full revolution are well-captured for normal force and pitching moment coefficients, as shown in fig. 5.9. The chord force coefficient is not reliably captured, even in trend, and will not be used for qualitative analysis in this study. Fig 5.10 re-plots fig. 5.9(a), but also includes c_n notation normalized by two choices for local section velocity, as discussed in section 5.3. When using only the blade section tangential velocity, u_t, asymptotic behavior which passes through two zero velocity points in the rotation at high advance ratio results. Adding (vector sum) u_r to the section velocity normalization eliminates the asymptotes, and reduces the coefficient magnitudes compared with using u_t alone. The M^2c_n coefficients will mostly be used in this work (for a well-defined normalization that is invariant of radius or azimuth), but occasionally when studying stall characteristics, c_n using u_t and u_r will be used to better compare with expected maximum force coefficients from the airfoil lookup tables.

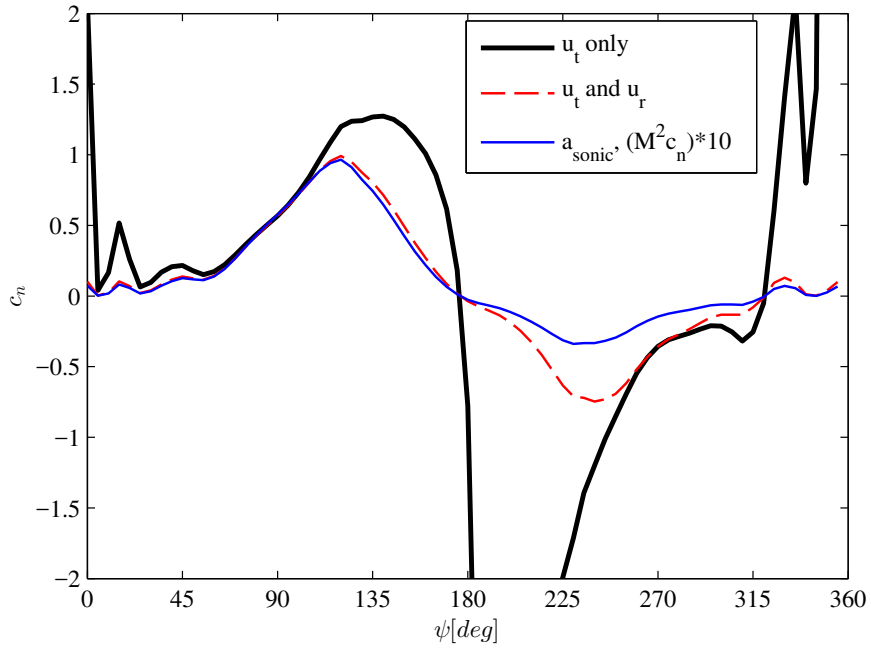

Figure 5.10: Normal force coefficient integrated from the chord-wise calculated pressure distribution, normalized by three different velocities. Data from Case 9175 of [31].

5.5 Vibratory Load Harmonics Calculation

A rotor in forward flight experiences periodic forcing on each blade due to the variation of local velocity on each blade, the sinusoidal variation of blade pitch through cyclic input, and the blade flapping motion. The combined periodic forcing occurs at frequencies equal to integer multiples of the rotation frequency of the rotor (i.e., 1/rev, 2/rev, 3/rev, etc.). These blade loads are in a rotating coordinate system that is attached to each blade. The hub loads are taken to be the loads at a point at the rotation center (shaft axis) of the rotor, and are in the non-rotating frame. In these experiments, these fixed-frame hub loads are measured by the hub load cell. The hub loads are a summation of the blade loads from all blades. Assuming the blades are perfectly balanced and tracked, this summation process results in a cancellation, or filtering, of all harmonics except the integer multiples of the blade passage frequency (N_b/rev, $2N_b$/rev, $3N_b$/rev, etc.). Therefore, for a 4-bladed rotor, the vibratory hub loads will be primarily be at 4/rev, 8/rev, 12/rev, etc.

To extract the vibratory load amplitudes at each frequency, a harmonic decomposition based on the Fourier sine and cosine transform was performed on the time history data. Discrete Fourier transform (DFT) using the built-in FFT function in MATLAB was also used to visualize the frequency content of sensor data. See [54, 55] for further background on vibratory loads.

Chapter 6: Collective-Thrust Control Reversal

6.1 Description

At high advance ratio, μ, an edgewise rotor will exhibit a *collective-thrust control reversal*. The reversal manifests as a decrease in rotor thrust for an increase in collective pitch, the opposite of normal. This is only true for a trimmed rotor, either trimmed to zero flapping (as in this research for a wind tunnel model) or trimmed for zero hub moments. The reversal is not sudden, but gradually occurs as advance ratio increases, and has been shown to occur about an advance ratio of 0.8 to 1.0. Several authors have observed and given explanations for this phenomenon [13, 16, 18, 21, 28, 56].

In the present study, the trend of rotor thrust with collective pitch angle is shown in fig. 6.1. The dashed lines are a linear fit of the data at low collective angles, so that deviations due to stall do not affect the slope. The trend of the thrust sensitivity derivative with collective is shown in fig. 6.2 for several rotor tests, with the reversal occurring at the crossing of zero sensitivity. For the rotor tested in this work, the reversal occurred around $\mu = 0.9$.

The underlying cause of this phenomenon is the growing reverse flow region on the retreating side of the rotor disk. In reverse flow an increase in geometric pitch

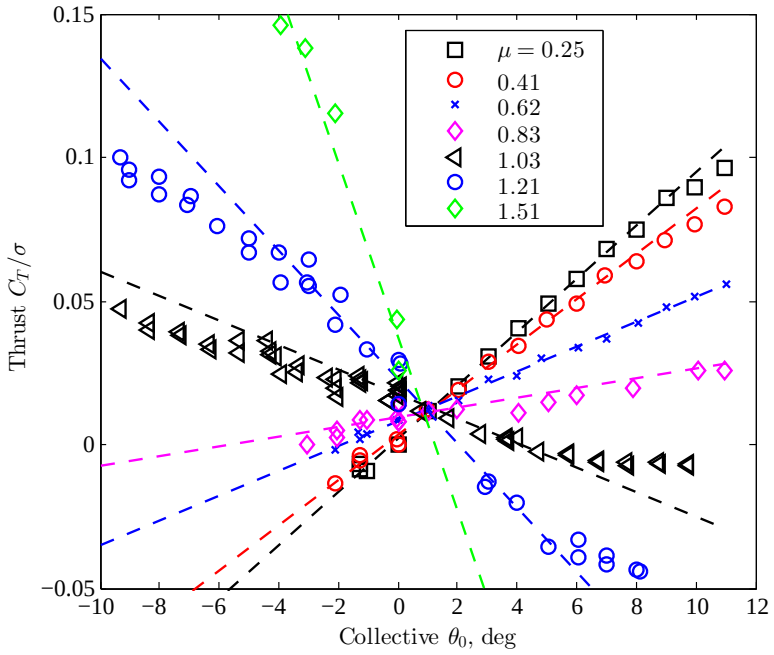

Figure 6.1: Thrust vs. collective data for varying advance ratio at α_s = 0°, trimmed to zero flapping. Linear fit for low angles shown dashed.

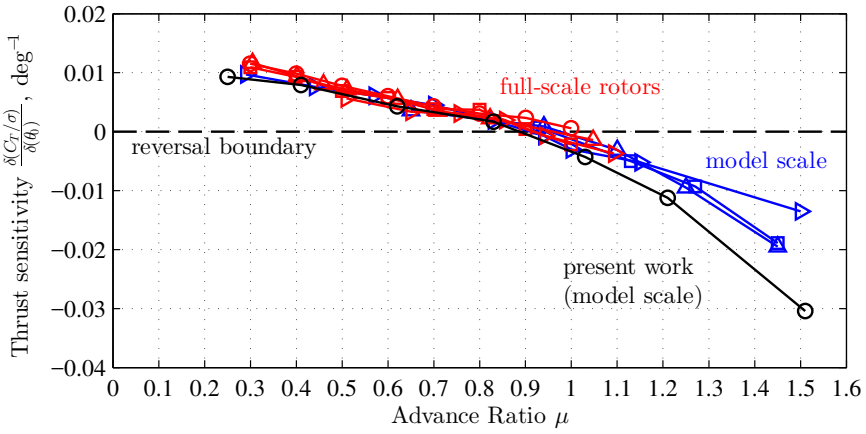

Figure 6.2: Thrust sensitivity to collective for trimmed rotors vs. advance ratio from the present work and from published data. Full-scale rotors: ○ □ UH-60A (two α_s) [18], ▷ UH-1 [15, 21], and △ H-34 [14, 21]. Model-scale rotors: □ △ Jenkins (two α_s) [13] and ▷ Ewans and Krauss [16].

angle results in a decrease in reverse pitch angle. As advance ratio increases, the proportion of the retreating blade that experience reverse flow becomes larger. The definition of the tangential velocity of a blade section is given in eq. 6.1 and non-dimensionalized by tip-speed in eq. 6.2. The boundaries of the reverse flow region will occur when U_t switches from positive to negative. Setting $u_T = 0$ and solving for r gives the radial location of the reverse-flow boundaries at a given azimuth angle eq. 6.3.

$$u_T = V \sin\psi \cos\alpha_s + \Omega y \tag{6.1}$$

$$\frac{u_T}{\Omega R} = \frac{V}{\Omega R} \sin\psi \cos\alpha_s + \frac{\Omega y}{\Omega R} = \mu \sin\psi + r \tag{6.2}$$

$$r = -\mu \sin\psi \tag{6.3}$$

From this result the reverse-flow region as a fraction of the retreating blade span is proportional to the advance ratio. Therefore, at an advance ratio of 0.5, the retreating blade sections inboard of 50% radius experience reverse flow. At an advance ratio of 1.0, the entire retreating blade is in reverse flow. More generally, the reverse flow region is a circle of diameter μ, centered on the retreating blade ($\psi = 270°$) at radial location $\mu/2$. It is also apparent that for a constant dimensional velocity, V, increasing the shaft or disk tilt away from zero degrees (either positive or negative) will decrease the advance ratio, μ, and therefore also decrease the size of the reverse flow region. For a constant advance ratio, disk tilt does not affect the

size of the reverse flow region.

For a rotor blade airfoil section in reverse flow, the geometric trailing edge now becomes the aerodynamic leading edge. For a typical airfoil, such as the NACA 0012 used in this study, this means the airfoil now has a sharp aerodynamic leading edge and a blunt aerodynamic trailing edge. Several authors have experimentally measured the quasi-steady properties of the NACA 0012 airfoil in both forward and reverse flow [57–62].

An airfoil operating in reverse flow will still generate lift proportional to angle of attack, albeit at higher drag levels due to the blunt trailing edge [60]. The lift behavior in reverse flow for the NACA 0012 is similar to that of a flat plate airfoil (fig. 6.3), as discussed by Lind [60, 63]. Notice the NACA 0012 in reverse flow maintains a similar lift-curve slope as compared to forward flow. The reverse flow stall is gentle and the lift coefficient remains relatively flat post-stall compared to forward flow. The low forward flow $c_{l,max}$ is a consequence of the Reynolds number, and Lind found that forward flow $c_{l,max}$ increased with Reynolds number, while reverse flow $c_{l,max}$ was largely unchanged [63].

Returning to the explanation of the collective-thrust control reversal, consider the rotor used in this research: constant chord, no twist, NACA 0012 airfoil section. To physically understand the why increased collective could result in decreased thrust, it is useful to step through the process of trimming, while comparing the relative lift and moment on the advancing and retreating sides of the rotor disk. Consider the aforementioned rotor geometry at zero collective pitch, zero cyclic pitch, and zero shaft tilt relative to oncoming wind.

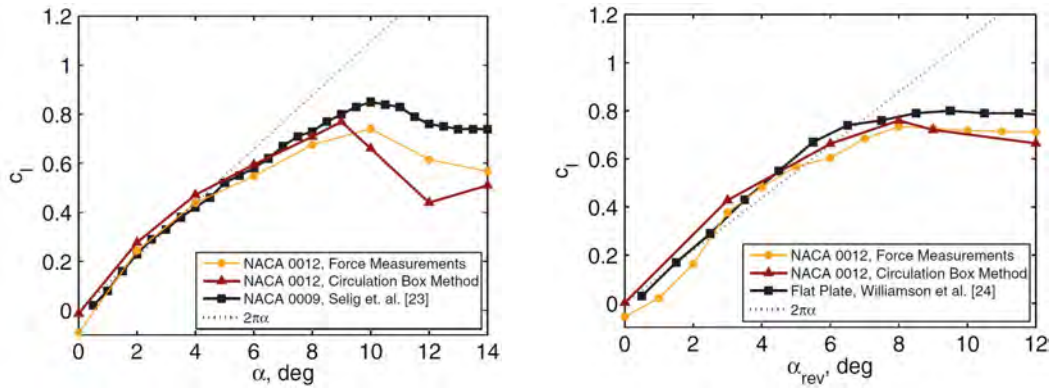

(a) Forward flow [60, 64]

(b) Reverse flow [60, 65]

Figure 6.3: NACA 0012 section lift coefficient measurements in forward and reverse flow, Re=1.1e5. Figures from Lind, et. al. [60].

For a low advance ratio condition (μ=0.15), the reverse flow region is small and mostly encompasses the hub and root cutout. For a unit increase in collective pitch, the advancing blade will increase in lift, and the retreating blade will increase in lift, but less than the advancing blade due to lower dynamic pressure. The asymmetry in lift and root moment is due to the asymmetry of resultant tangential velocities due to the wind velocity (eq. 6.1). To satisfy the trim condition and equalize the root moments, longitudinal cyclic pitch (θ_{1s}) has to be introduced in such a way to decrease the pitch on the advancing (high-velocity) blade while increasing the pitch on the retreating (low-velocity) blade. This is a negative increment in longitudinal cyclic pitch. The increment needed in cyclic for trim is less than the increase in collective pitch, otherwise the advancing blade would be back at zero lift (or negative) while the retreating blade would still have positive lift. Therefore, the final effect of the collective pitch increase, after trimming cyclics are applied,

is a net positive rotor lift. We have ignored the fore and aft portions of the rotor disk since forward flight does not create as severe an asymmetry (especially when ignoring coning) as it does with the port and starboard portions of the disk.

For a high advance ratio condition (μ=1.0), the reverse flow region now encompasses the entirety of the retreating blade. For a unit increase in collective, the advancing blade will increase in lift, as before. On the retreating blade, the reverse flow condition means a geometric increase in pitch angle will result in an aerodynamic decrease in pitch angle and thus a reduction in lift. The asymmetry in lift and moment across the disk laterally is therefore much larger than in the low advance ratio example. To equalize the root moments (trim), negative longitudinal cyclic will again be used. However at this advance ratio, negative longitudinal cyclic decreases the lift on the advancing blade but also *decreases* (further) the lift on the retreating blade. In this situation, trim can only be achieved once the advancing blade pitch is reduced enough to equal the negative lift on the retreating blade. Once the longitudinal cyclic delta is equal to the collective delta, the advancing blade will be back at zero lift, while the retreating blade is still producing negative lift. Some increment further of longitudinal cyclic will reduce the advancing blade lift to equal the retreating blade lift. Thus, the final trimmed lift on both sides of the disk is negative, and the longitudinal cyclic input will need to be greater than the increment of collective. This agrees with the measurements of longitudinal cyclic sensitivity to collective being less than -1 deg/deg near the advance ratio of thrust reversal (fig. 6.4).

In summary, this reversal effect relies on the following conditions:

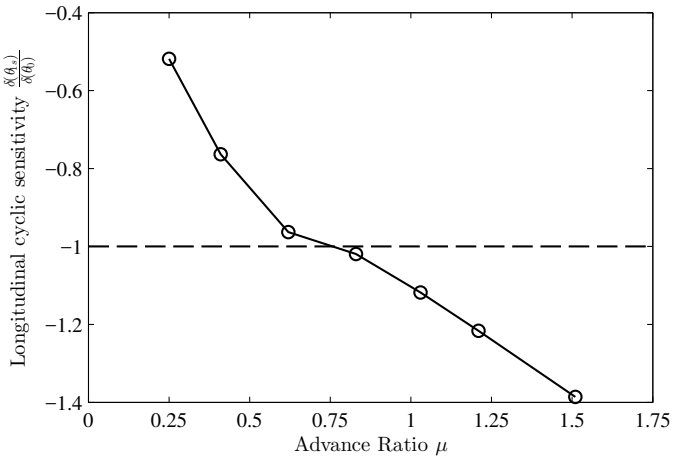

Figure 6.4: Measured longitudinal cyclic pitch sensitivity to collective for trimmed rotor vs. advance ratio.

1. Rotor trimmed such that the advancing and retreating sides are in moment-balance or zero flapping.

2. Reverse flow on the retreating blade such that an increase in geometric pitch reduces lift.

3. Ability of the airfoil to produce lift in reverse flow at a comparable level to forward flow.

Thus the reversal trend can be expected to break down once the retreating blade stalls in reverse flow. This will be explored in the next chapter.

It is of interest to determine the modeling needed to accurately predict this behavior. Given the prior explanation, it would seem clear the method needs to at least minimally capture the presence of the reverse-flow region, correctly account for the airfoil lift behavior in reverse flow, and model the trimmed rotor to zero flapping

(or zero moment).

6.1.1 Thrust Distribution

The spatial thrust distribution across the rotor disk changes as the advance ratio increases. It was shown that collective-thrust reversal occurs due to the size increase of the reverse-flow region. To maintain roll balance with the retreating blade (which experiences much lower net in-plane velocity, u_T), the advancing blade lift must decrease through longitudinal cyclic to account for the asymmetry in velocities. Using a simple numerical blade element theory (BET) program (mentioned in more detail in section 6.3) with uniform inflow, the change in the thrust distribution with advance ratio was explored to verify this hypothesis (fig. 6.5). At $\mu = 0.2$, the thrust is nearly symmetric and weighted towards the blade tips on both sides of the disk. As the advance ratio is increased to $\mu = 0.5$, the reverse-flow region is contributing negatively to the overall thrust, and the tip region of the retreating blade has to compensate with higher lift. The advancing blade is at nearly zero lift to achieve balance. The next point is $\mu = 1.0$, which is already past the collective-thrust reversal. The inboard section of the retreating blade is now the largest contributor, and there is a large negative gradient of lift towards the tip, which is near zero net velocity. The advancing blade balances the moment with a smaller force over a larger moment arm. As the advance ratio increases further, the gradient in u_T along the retreating blade decreases as the freestream component of velocity—which is uniform—dominates the velocity due to rotation, which is linear. If the advance

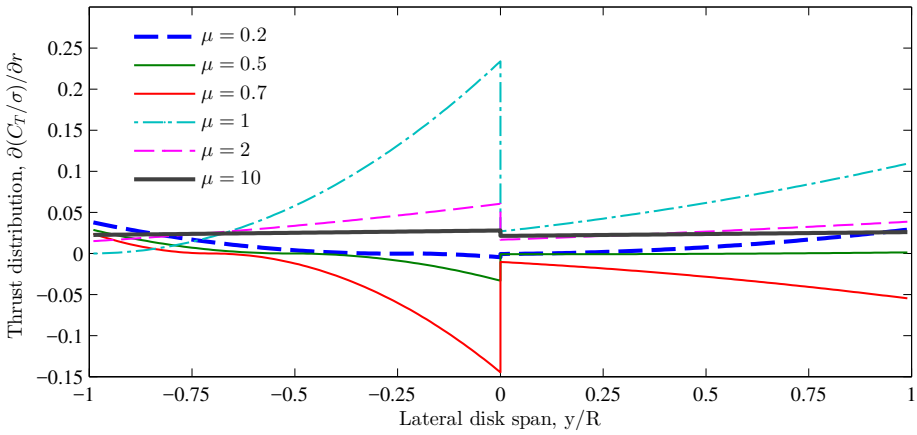

Figure 6.5: Spanwise thrust distribution over advancing (0 to 1) and retreating blade (0 to -1) as advance ratio increases. View is from aft of rotor disk, with y/R = 1 being the advancing blade tip at ψ = 90°. All cases at C_T/σ = 0.05, zero hub moments, and uniform inflow.

ratio goes to infinity (stopped rotor), the blades become fixed-wings with the port blade operating in reverse flow. In this limiting case, the two blades then have a uniform (excluding wake effects) and symmetric lift distribution again.

The conclusion here is that the inboard blade section lift behavior does indeed drive total rotor lift for rotors under collective control at advance ratios between 0.7 and 2.0. At extreme advance ratios approaching that of a stopped rotor (μ = 10 in fig. 6.5), the lift distributions approach that of a fixed-wing and becomes symmetric again and uniform with respect to the blades at ψ = 90° and ψ = 270°, which are now responsible for 100% of the total rotor thrust (lift).

6.2 Analytical Prediction of Reversal Behavior

A minimal prediction approach would be to use blade element theory, which can capture all of these effects analytically or numerically. Wheatley [66] outlined the basic method that can be used for high advance ratios where reverse flow is significant. Johnson [55] and Leishman [6] concisely summarize the method, and Harris [21] used these basics to solve for the reversal-onset advance ratio, as below.

This approach separates the radial and azimuth blade element integral expressions into those of forward and reverse flow regions. The reverse flow region lift expression is modified from the forward flow region as a change in sign of section pitch angle and tangential velocity (and assuming the inflow velocity is still positive down through the disk, same as in forward flow). The result is the same lift expression as for forward flow, but with a sign change in the lift expression. See Leishman or Johnson for more details.

The following assumptions can be made to simplify the expressions to allow for manageable integration and a closed-form result:

1. Constant-chord blade with no twist

2. Zero root cut-out

3. Linear lift curve slope in forward and reverse flow, $a = a_{rev} = 2\pi$

4. Uniform inflow, no tip loss

5. Small angle assumption for inflow angle

6. Rigid rotor, zero flapping, zero coning

7. Zero disk tilt

8. Strictly valid for $\mu \leq 1.0$

The result of the thrust and roll moment coefficients are summarized in eqns. 6.4 and 6.5. The induced velocity, λ, is a function of the thrust coefficient, C_T, for the uniform inflow assumption, but this relationship will be neglected for now. This simplification is justified for determining the critical advance ratio where thrust reversal occurs since at that operating point, thrust and inflow are not a function of collective. The error introduced by this assumption for other advance ratios will be explored later with a numerical solution.

$$\frac{2C_T}{\sigma a} = \theta_0 \left(\frac{1}{3} + \frac{1}{2}\mu^2 - \frac{4}{9\pi}\mu^3 \right) + \theta_{1s} \left(\frac{1}{2}\mu + \frac{1}{8}\mu^3 \right) + \lambda \left(-\frac{1}{2} - \frac{1}{4}\mu^2 \right) \tag{6.4}$$

$$\frac{2C_{M_x}}{\sigma a} = \theta_0 \left(-\frac{1}{3}\mu - \frac{4}{45\pi}\mu^4 \right) + \theta_{1s} \left(-\frac{1}{8} - \frac{3}{16}\mu^2 + \frac{5}{192}\mu^4 \right) + \lambda \left(\frac{1}{4}\mu - \frac{1}{16}\mu^3 \right) \tag{6.5}$$

The sensitivity of thrust, C_T/σ, with respect to collective pitch, θ_0, can be found with a partial derivative of eqn. 6.4, as shown in eqn. 6.6. Again, this neglects the fact that λ is a function of C_T. However, this expression also assumes longitudinal cyclic, θ_{1s}, does not vary with collective, and hence ignores the impact to the trim state of the rotor, particularly the rolling moment.

$$\frac{\partial (C_T/\sigma)}{\partial \theta_0} = \frac{a}{2} \left(\frac{1}{3} + \frac{1}{2}\mu^2 - \frac{4}{9\pi}\mu^3 \right) \tag{6.6}$$

For a trimmed rotor, the rolling moment must be made zero through longitudinal cyclic control. The cyclic to accomplish this trim can be found by setting $C_{M_x} = 0$ in eqn 6.5 and solving for θ_{1s}. This gives the required longitudinal cyclic input to trim to zero rolling moment as a function of collective, inflow, and advance ratio (eqn 6.7). Harris [21] noted that this expression might predict trimming difficulty when the denominator goes to zero at $\mu = 2.8$, however this expression was derived using integration limits that are only strictly valid for $\mu \leq 1.0$, so extrapolation to such an advance ratio should be done with caution. Numerical studies (shown later) showed no such singularity of longitudinal cyclic up to $\mu = 3.0$.

$$\theta_{1s} = \frac{-\theta_0\left(-\frac{1}{3}\mu - \frac{4}{45\pi}\mu^4\right) - \lambda\left(\frac{1}{4}\mu - \frac{1}{16}\mu^3\right)}{\left(-\frac{1}{8} - \frac{3}{16}\mu^2 + \frac{5}{192}\mu^4\right)} \tag{6.7}$$

Eqn 6.7 can then be substituted into eqn 6.4 to give an expression for rotor thrust as a function of advance ratio for zero rolling moment:

$$\begin{aligned}\frac{2C_T}{\sigma a} = {} & \theta_0\left(\frac{1}{3} + \frac{1}{2}\mu^2 - \frac{4}{9\pi}\mu^3\right) \\ & + \left(\frac{-\theta_0\left(-\frac{1}{3}\mu - \frac{4}{45\pi}\mu^4\right) - \lambda\left(\frac{1}{4}\mu - \frac{1}{16}\mu^3\right)}{\left(-\frac{1}{8} - \frac{3}{16}\mu^2 + \frac{5}{192}\mu^4\right)}\right)\left(\frac{1}{2}\mu + \frac{1}{8}\mu^3\right) \\ & + \lambda\left(-\frac{1}{2} - \frac{1}{4}\mu^2\right)\end{aligned} \tag{6.8}$$

Now taking the partial derivative with respect to collective gives the thrust sensitivity to collective for zero rolling moment:

$$\frac{\partial(C_T/\sigma)}{\partial\theta_0} = \frac{a}{2}\left[\left(\frac{1}{3} + \frac{1}{2}\mu^2 - \frac{4}{9\pi}\mu^3\right) - \frac{\left(\frac{1}{3}\mu + \frac{4}{45\pi}\mu^4\right)\left(\frac{1}{2}\mu + \frac{1}{8}\mu^3\right)}{\left(\frac{1}{8} + \frac{3}{16}\mu^2 - \frac{5}{192}\mu^4\right)}\right] \tag{6.9}$$

Setting the partial derivative to zero and solving for μ gives the critical advance ratio where collective-thrust reversal will occur, about $\mu = 0.85$. Therefore a relatively simple blade element analysis with the aforementioned assumptions is able to predict the occurrence of the collective-thrust reversal phenomenon.

The sensitivity was re-derived with various assumptions removed to check the necessity. Fig. 6.6 shows the results of the comparisons. The red lines are modeled without trimming the rotor to zero rolling moment. One is with reverse flow modeled (eqn. 6.6), and one is for neglecting the existence of the reverse flow region (as is sometimes done for traditional helicopter flight regimes of $\mu < 0.35$). The blue dash-dot line is for a trimmed rotor, but without including the reverse flow region in the calculations. The blue line with x-symbols includes the reverse flow region, but assumes the airfoil is non-lifting when operating in reverse flow (lift curve slope = 0). The solid black line is eqn. 6.9, which models reverse flow with a 2π lift curve slope, and is trimmed to zero rolling moment. This is the only set of modeling assumptions that results in the prediction of a reversal. Therefore, it is clear that the collective-thrust reversal does indeed occur due to all three of the following: the existence of a large extent of reverse flow, the ability of the blade airfoil to produce lift in reverse flow, and the rotor being trimmed to zero moments using cyclic pitch.

Additionally, from eqn. 6.9, the lift curve slope value, a, does affect the collective-thrust sensitivity, but not when the sensitivity is zero. When solving for the critical advance ratio, the thrust sensitivity (left-hand side of eqn. 6.9) is set to zero, at which point solution for μ becomes independent of a. This means the specific lift-curve slope of the blade sections will not influence the advance ratio

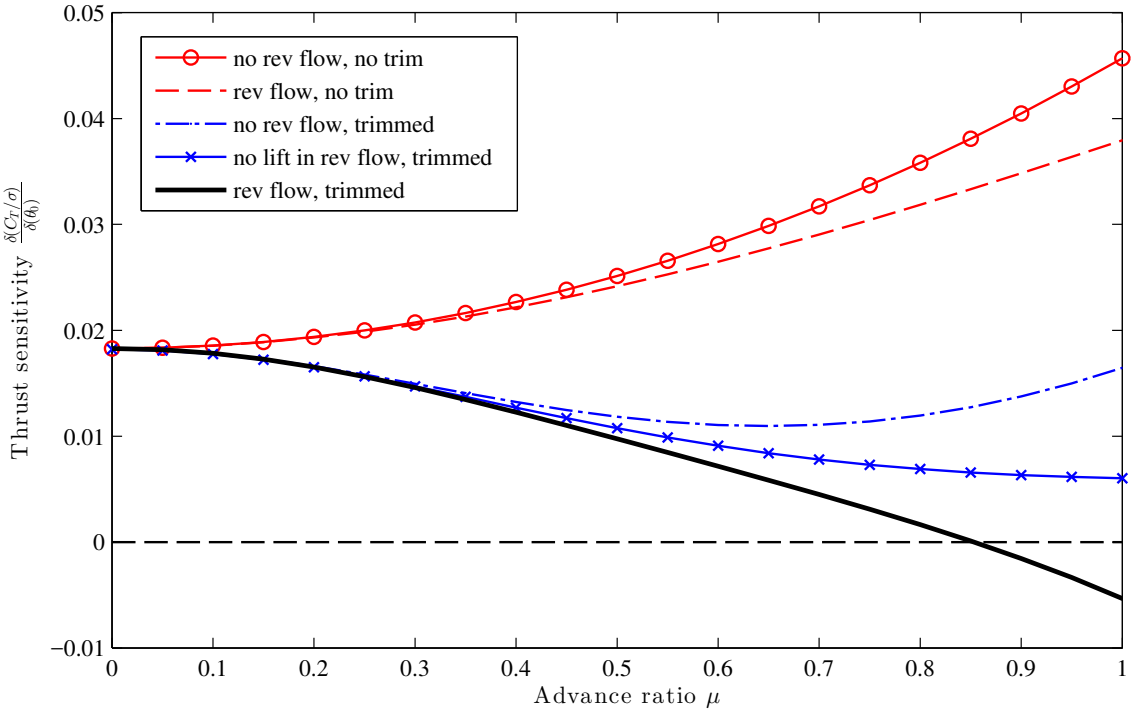

Figure 6.6: Blade element analysis predictions of a simplified rotor for thrust sensitivity to collective pitch for various assumptions. Collective-thrust reversal (thrust sensitivity = 0) is only predicted if the analysis correctly models the reverse flow region lift behavior and trims to zero rolling moment.

of reversal. This conclusion only holds when the sections have identical lift-curve slopes in forward and reverse flow. The impact of a reduced lift-curve slope is shown in fig. 6.7.

6.2.1 Effect of root cutout, blade pre-twist, and disk tilt

The same analytical approach was followed but the assumptions of no root cutout, no blade twist, and no disk/shaft tilt were removed. Numerical solutions are free of all assumptions regarding the rotor geometry, kinematics, elasticity, and

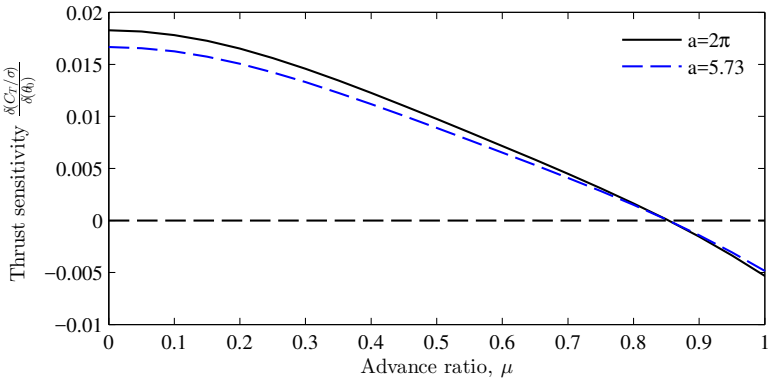

Figure 6.7: Analytical predictions of the effect of blade section lift-curve slope, a, on thrust sensitivity.

inflow modeling, and will be investigated in following sections.

Root cutout is modeled in the equations by simply integrating along the blade span from r_0 to 1 instead of 0 to 1. Blade geometric pre-twist (as opposed to aeroelastic twist) is modeled by including a linear distribution of blade pitch along the span, $\theta(r,\psi) = \theta_0 + \theta_{tw} r + \theta_{1c} cos\psi + \theta_{1s} sin\psi$. Disk tilt angle, α_s, enters as an additional inflow velocity term, $\lambda_{\alpha_s} = -\mu \tan \alpha_s$. Disk angle also affects the advance ratio for a given wind speed, but when solving as a function of edgewise advance ratio, it is lumped inside μ and does not appear.

$$\begin{aligned}\frac{2C_T}{\sigma a} = {} & \theta_0 \left(\frac{1}{3} + \frac{1}{2}\mu^2 - \frac{4}{9\pi}\mu^3 - \frac{2}{\pi} r_0^2 \mu \right) \\ & + \theta_{1s} \left(\frac{1}{2}\mu + \frac{1}{8}\mu^3 - \frac{2}{3\pi} r_0^3 - \frac{4}{3\pi} r_0 \mu^2 \right) \\ & + \theta_{tw} \left(\frac{1}{4} + \frac{1}{4}\mu^2 - \frac{1}{32}\mu^4 + \frac{1}{4} r_0^4 - \frac{4}{3\pi} r_0^3 \mu \right) \\ & + \lambda \left(-\frac{1}{2} - \frac{1}{4}\mu^2 - \frac{1}{2} r_0^2 + \frac{2}{\pi} r_0 \mu \right)\end{aligned} \tag{6.10}$$

$$\begin{aligned}\frac{2C_{M_x}}{\sigma a} &= \theta_0\left(-\frac{1}{3}\mu - \frac{4}{45\pi}\mu^4 + \frac{1}{2\pi}r_0^4 + \frac{2}{3\pi}r_0^2\mu^2\right)\\ &+ \theta_{1s}\left(-\frac{1}{8} - \frac{3}{16}\mu^2 + \frac{5}{192}\mu^4 + \frac{8}{9\pi}r_0^3\mu\right)\\ &+ \theta_{tw}\left(-\frac{1}{4}\mu - \frac{1}{96}\mu^5 + \frac{2}{5\pi}r_0^5 + \frac{4}{9\pi}r_0^3\mu^2\right)\\ &+ \lambda\left(\frac{1}{4}\mu - \frac{1}{16}\mu^3 - \frac{2}{3\pi}r_0^3\right)\end{aligned} \tag{6.11}$$

$$\begin{aligned}\frac{\partial(C_T/\sigma)}{\partial\theta_0} = \frac{a}{2}\Bigg[&\left(\frac{1}{3} + \frac{1}{2}\mu^2 - \frac{4}{9\pi}\mu^3 - \frac{2}{\pi}r_0^2\mu\right)\\ &- \frac{\left(\frac{1}{3}\mu + \frac{4}{45\pi}\mu^4 - \frac{1}{2\pi}r_0^4 - \frac{2}{3\pi}r_0^2\mu^2\right)\left(\frac{1}{2}\mu + \frac{1}{8}\mu^3 - \frac{2}{3\pi}r_0^3 - \frac{4}{3\pi}r_0\mu^2\right)}{\left(\frac{1}{8} + \frac{3}{16}\mu^2 - \frac{5}{192}\mu^4 - \frac{8}{9\pi}r_0^3\mu\right)}\Bigg]\end{aligned} \tag{6.12}$$

As before, the longitudinal cyclic, θ_{1s}, is solved for zero rolling moment, C_{M_x}, in eqn 6.11 and then substituted into the thrust equation (eqn 6.10). Taking the partial derivative of the resulting equation (not shown) results in the sensitivity of thrust with respect to collective (eqn 6.12). It can be seen from eqn 6.12 that the twist rate, θ_{tw}, falls out when taking the partial derivative, implying that the blade pre-twist will not effect the critical advance ratio or thrust sensitivity to collective.

Similarly, the inflow velocity due to disk tilt angle also falls out when the derivative with respect to collective is taken. Therefore, it would be expected that positive or negative disk tilt angles do not influence the collective-thrust sensitivity or reversal advance ratio.

Root cutout, r_0, remains in the partial derivative as a factor for the thrust sensitivity. The effect of increasing root cutout, shown in fig. 6.8, is to delay the collective-thrust reversal to higher advance ratios. The reverse flow lift in the root region of the retreating blade dominates the reversal behavior, so an increasing root

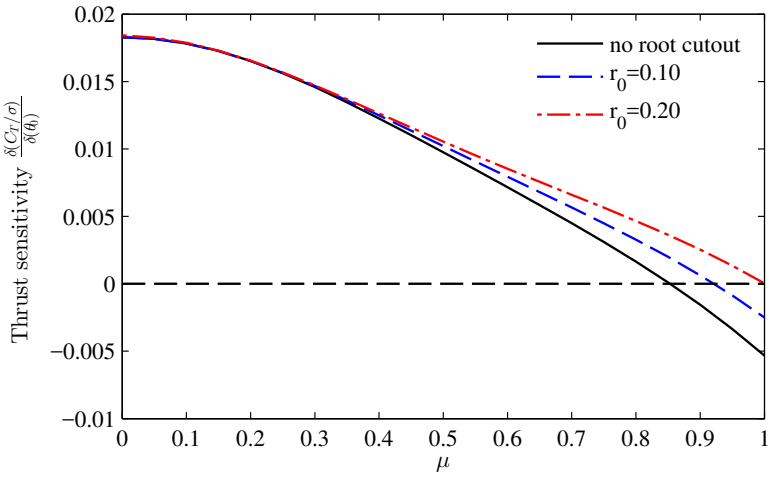

Figure 6.8: Effect of root cutout on the critical advance ratio for collective-thrust reversal. Analytical prediction is from the simplified blade element analysis derivation with inflow neglected.

cutout reduces the effect.

6.3 Simplified BET: Numerical Approach

The analyses so far have been restricted to $\mu \leq 1$, and have neglected the inflow velocity for convenience of the closed-form analytical solutions. A numerical solution to the blade element formulation can more easily model additional rotor geometry complexity, inflow models, and elasticity, as well as model $\mu > 1$ conditions.

The same basic example rotor was considered as in the analytical solution (rigid, no flapping/coning, zero profile drag, zero disk tilt, no root cutout, 2π lift curve slope in forward and reverse flow), but with a uniform induced inflow model applied. The comparison shows that the critical advance ratio, μ_{crit} , where thrust sensitivity changes sign was not affected by the assumption of neglecting inflow in

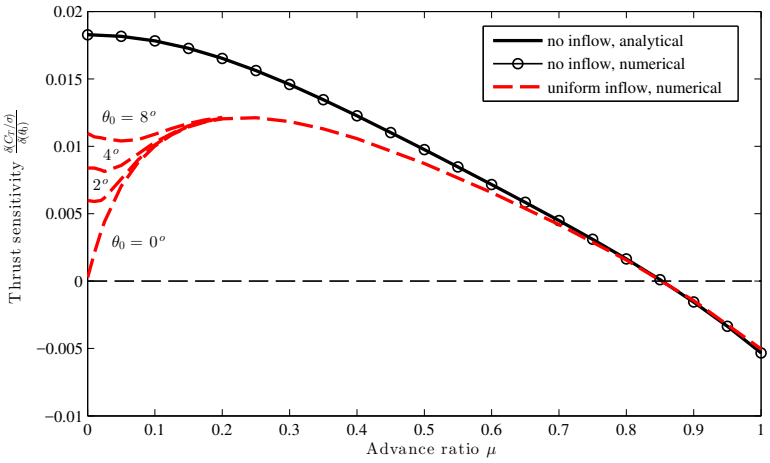

Figure 6.9: The analytical solution for collective-thrust sensitivity with no inflow compared with numerical solutions for no inflow and uniform inflow for zero disk tilt.

the analytical solution (fig. 6.9). There are however, large errors introduced by this assumption at low advance ratio, where the induced velocity is significant. When accounting for the induced inflow velocity, the behavior of the thrust derivative for $\mu < 0.2$ depends on the baseline collective pitch because of the non-linear relationship between pitch and thrust in the low-speed and hover regime. For $\mu > 0.2$, pitch and thrust have a linear relationship, due to the linear relationship of thrust and induced inflow velocity (fig. 6.10).

It is also apparent that for a constant dimensional velocity, V, increasing the shaft or disk tilt away from zero degrees (either positive or negative) will decrease the advance ratio, μ, and therefore also decrease the size of the reverse flow region. For a constant advance ratio, disk tilt does not affect the size of the reverse flow region.

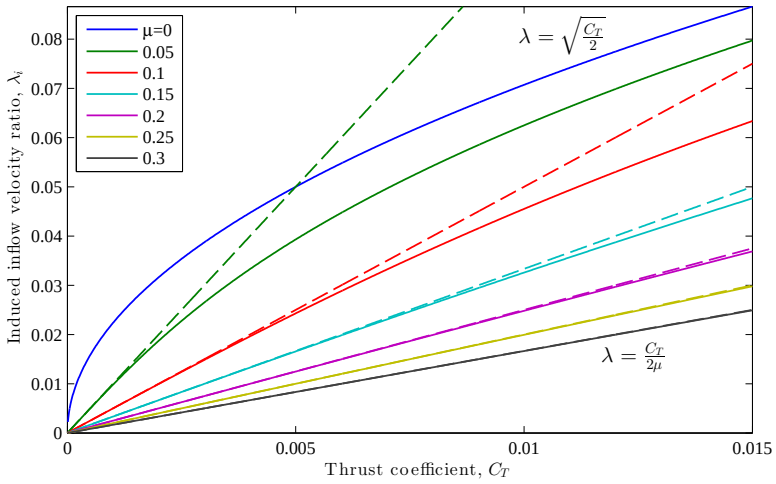

Figure 6.10: Induced inflow velocity is non-linear with rotor thrust at low speeds but becomes linear above $\mu \approx 0.2$. The collective pitch to thrust relation follows similarly (non-linear at low speed, linear at high speed).

Numerical studies confirm that disk tilt does not affect the reversal behavior directly, for a constant advance ratio. For the more-realistic design scenario of a constant target forward speed, disk tilt (in either direction), will reduce the size of the reverse-flow region, and therefore delay the collective-thrust reversal.

6.3.1 Effect of Shaft Tilt

From the earlier description of reverse flow for an edgewise rotor, the reverse-flow region has boundaries given by $r = -\mu \sin\psi$. This means the reverse-flow region is a circle of diameter μ, centered on the retreating blade at a radial location of $\mu/2$. The advance ratio is a measure of the component of the forward velocity that is parallel to the rotor disk, $\mu = V \cos\alpha_s$. Therefore, for a constant advance ratio a variation of the disk tilt, α_s, will not affect the size of the reverse flow region.

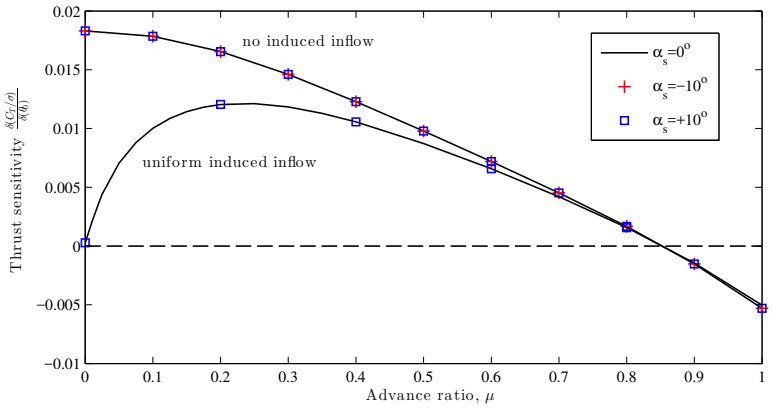

Figure 6.11: Rotor disk angle is predicted to have no effect on thrust sensitivity to collective pitch. Predictions from numerical solution to blade element theory neglecting inflow and with uniform inflow.

The earlier analytical derivations showed that the inflow velocity component due to disk tilt does not affect the collective-thrust sensitivity. Numerical sweeps in the simplified blade element program verify that shaft tilt does not effect the collective-thrust derivative for a given advance ratio (fig. 6.11). However, an aircraft with a given dimensional forward velocity will experience a lower edgewise advance ratio with increasing shaft tilt by the factor $\cos\alpha_s$, with the size of the reverse flow region decreasing accordingly. Therefore the collective-thrust reversal will be delayed to a higher dimensional forward speed by the factor $\frac{1}{\cos\alpha_s}$, which for a 10^o shaft tilt is only about 1.5%.

6.3.2 Effect of Blade Pre-Twist

The analytical derivations of collective-thrust reversal showed that a linear pre-twist of the blade pitch did not influence the sensitivity of thrust to collective

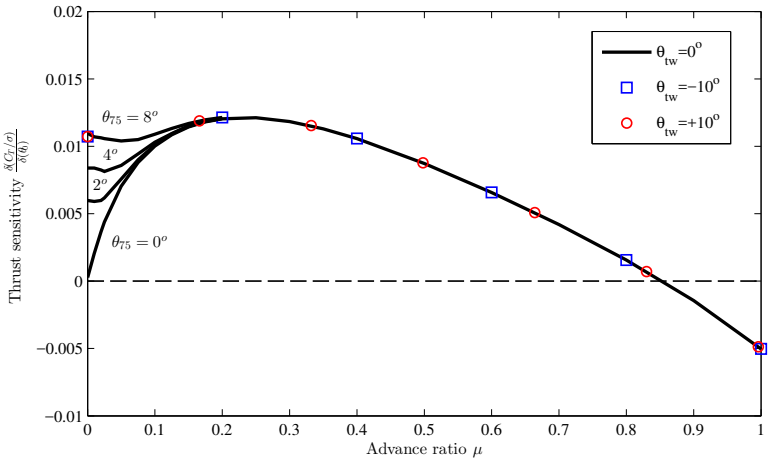

Figure 6.12: Linear blade twist rate is predicted to have no effect on thrust sensitivity to collective pitch. Predictions from numerical solution to blade element theory with uniform inflow.

pitch changes at any advance ratio. This makes intuitive sense when assuming fully attached flow (in both forward and reverse-flow regions) and uniform inflow, where the pre-twist does not change the size of the reverse flow region (as root cutout or shaft tilt at a fixed velocity does), or the lift-curve slope of the blade sections. Numerical sweeps using the simple BET formulation and uniform inflow were conducted, and the lack of influence on thrust sensitivity as predicted by the analytical formulation was verified (fig. 6.12).

6.3.3 Effect of Blade Taper

It has been shown in the root cutout study that the inboard blade section has a large influence on the collective-thrust reversal behavior. Therefore, it would be expected that a blade that has a larger chord near the root would lower the critical

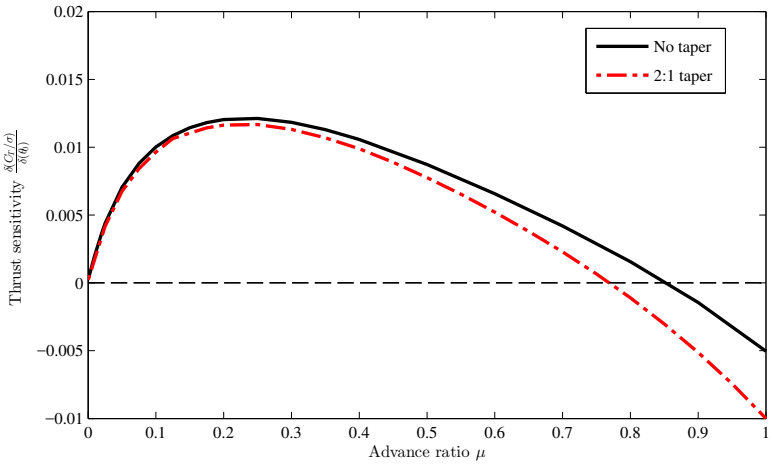

Figure 6.13: Effect of linear chord taper ratio on thrust sensitivity and reversal. Constant thrust-weighted solidity is enforced. Taper ratio defined as ratio of root chord to tip chord.

advance ratio—the opposite effect of a root cutout. The numerical blade element program with uniform inflow was again used on a generic rotor geometry, and the effect of a 2:1 taper (taper defined as the ratio of root chord to tip chord) for a zero root cutout blade—with thrust-weighted solidity held constant—is shown in fig. 6.13. As expected, the critical advance ratio where thrust reversal occurs is moved lower, from about 0.85 to 0.77.

6.4 Comprehensive Analysis Predictions

Comprehensive analysis in the rotorcraft community typically refers to a software package that can analyze all of the aspects of helicopter aeromechanics, including the fuselage, tail rotor, etc. In the context of this work (isolated rotor), the important additions above the simplified BET methods outlined earlier are non-

uniform inflow models (including unsteady aerodynamics), blade motion (flap/lag hinge kinematics), and blade elasticity. The specific program used is UMARC, the University of Maryland Advanced Rotorcraft Code [67].

The input file corresponding to the rotor geometry used in this experiment was provided by Graham Bowen-Davies, who conducted initial correlations with these experiments using UMARC [24]. The blade geometry, beam stiffnesses, and mass distributions were input as measured from the experiments earlier in this work.

The specific focus of this section is the impact of modeling enhancements on the prediction of the thrust-reversal trends. Thrust sensitivity sweeps were conducted with the modeling enhancements added one at a time to gauge the impact (fig. 6.14). Blade elasticity appeared to have very little impact on the thrust sensitivity to collective for low collective pitch perturbations. Under more impulsive conditions such as stall or local shocks, the torsion response may become more significant, but this was not explored. The addition of a non-uniform inflow model had the most significant effect on the trends, with a shift of the thrust sensitivity lower and closer to the measured data. Bowen-Davies [24] showed that modeling the near-wake (so that it deforms with the freestream) in the reverse-flow region works to reduce the angle of attack locally, which would reduce the sensitivity of thrust to pitch changes. There still appears to be an over-prediction at the highest advance ratios (under-prediction of sensitivity magnitude). However, it should be noted that the test data at the highest advance ratios becomes very sensitive to small changes in control angles, and hence the measurement uncertainty increases. This is also demonstrated in the comparison with other high advance rotor tests from the

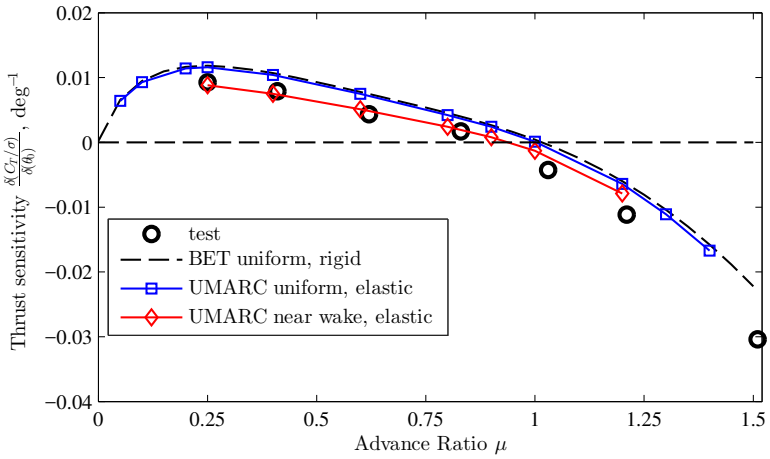

Figure 6.14: Effect of blade elasticity and non-uniform inflow models on the prediction of collective-thrust sensitivity with advance ratio.

literature (fig. 6.2), which showed a diverging of correlation above approximately $\mu = 1$. In general this data set appears at the lower end (higher sensitivity) of the available data sets.

6.5 Chapter Summary

Analytic forms of blade element theory were derived and utilized to predict collective-thrust reversal trends at high advance ratio conditions. The necessary components for this reversal were determined to be the existence of the reverse-flow region on the retreating blade, the ability of the blade section to still produce lift proportional to pitch angle while in reverse flow, and the condition that the rotor be trimmed to zero steady hub moments or zero 1P flapping. If any of these conditions are not met, the collective-thrust reversal may not occur.

The analytic and numerical blade element theory formulations were used to

explore the design features of a rotor that impact the advance ratio at which the collective-thrust reversal occurs. Root cutout has the largest effect, with increasing cutout acting to delay the critical advance ratio to larger values. Blade taper also has a large effect, because it also affects the relative lifting ability of the inboard retreating blade. Increasing the blade taper ratio for constant solidity (larger root chord relative to tip chord) moved the critical advance ratio to lower values, causing thrust reversal earlier. Blade pre-twist, shaft tilt, and section lift-curve slope do not appear to affect the collective-thrust behavior in any fundamental sense.

In terms of modeling approaches, accounting for blade elasticity or blade flapping/lagging kinematics are not essential to predict the critical advance ratio (for a trimmed rotor). The use of a non-uniform induced inflow model, such as a free-vortex wake method, gave the most significant improvement to predicting the thrust sensitivity at all advance ratios, and should be considered essential.

Chapter 7: Reverse Flow Stall Behavior

Because the collective-thrust reversal trend relies on the airfoil producing lift in reverse flow, this reversal can be expected to break down once the retreating blade stalls in reverse flow. This has been shown in previous theoretical studies [24, 28], but has not been observed in experimental measurements. In prior work, most high μ tests were conducted at low collective pitch angles ($< 4°$), with the exception of Jenkins [13] and Ewans [16]. The present work includes a larger range of both positive and negative collective pitch angles at high advance ratio than the prior work. This allows a broader range with which to correlate analysis beyond the expected reverse stall angles.

The thrust behavior of the rotor beyond small blade pitch angles at high advance ratio is now examined. During the present experiments, collective sweeps were performed at a $\mu = 1.03$ and 1.2 at $\alpha_s = 0°$ and $\mu = 1.03$ at $\alpha_s = 4°$ (aft tilt), which give insight into the stall characteristics of the rotor at high advance ratio (fig. 7.1). Predictions are included assuming linear aerodynamics ($a = a_{rev} = 2\pi$, no stall), and with $\pm 180°$ angle of attack tables for the NACA 0012 airfoil. Uniform inflow, rigid blades, and zero flapping were also assumed. The non-zero thrust offset at zero collective and zero shaft angle in the measured data are not well understood, but

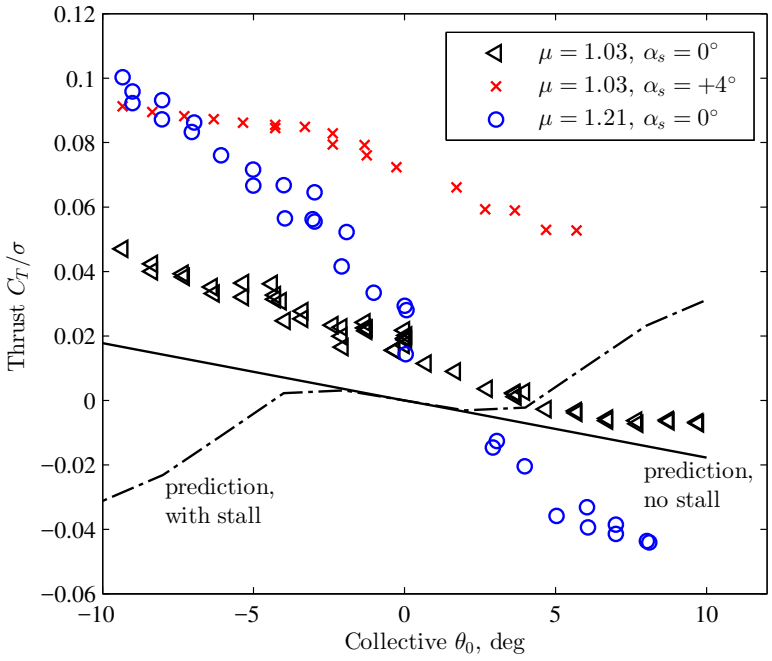

Figure 7.1: High advance ratio ($\mu \geq 1.0$) collective sweeps. Predictions shown with and without airfoil static stall modeled.

could be a consequence of difficulty with blade tracking and stand wake interference (evident in blade pressure measurements).

The measured lift behavior in fig. 7.1 remains close to linear behavior for higher collective angles, and then has a gradual roll-off. By contrast, the predictions using the 2-D lookup tables show a relatively sharp change in sign of the thrust trend corresponding to the stall of the retreating blade in reverse flow. When comparing measured thrust trends to predictions, it is apparent that the blade is not stalling according to the 2-D steady lookup tables for the NACA 0012.

The pressure sensor measurements from the 0.3R radial position also show the integrated normal force coefficient continuing to increase in magnitude at high

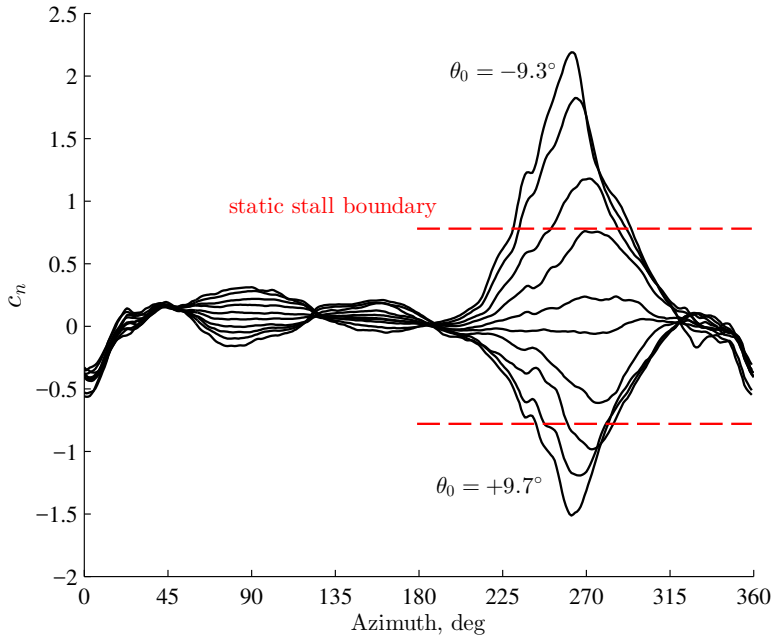

Figure 7.2: Normal force coefficient at 0.3R for a collective sweep: μ = 1.03, $\alpha_s = 0°$, $\theta_0 = -9.3°$ to $+9.7°$. Reverse-flow static stall c_n denoted by the dotted line.

collective angles, well past angles of attack where the airfoil tables predict stall of the section (fig. 7.2). This behavior is likely the result of stall delay of the airfoil section. In particular, at high advance ratio the inboard blade sections of the retreating blade dominate the lifting behavior (fig. 6.5), and as such it is likely a delay in stall in that region that is driving this behavior.

7.1 Stall Delay Mechanisms

There are three main types of stall delay experienced by rotors: Dynamic stall, yawed/radial flow, and rotational (static) stall delay [68].

7.1.1 Dynamic stall

An airfoil undergoing time-varying oscillations in angle of attack can experience a lift overshoot (greater than static max c_l) above the static stall angle [69, 70]. The mechanism of this stall delay has contributions from unsteady pressure gradient reductions, induced camber from pitch rate, and vortex lift [6, 71]. as a vortex shed from the leading edge passes over the suction side of the airfoil surface, enhancing lift. Since this source of enhanced lift is translating across the surface, an increase in negative pitching moment is experienced as the vortex moves farther aft. The airfoil section will experience lift stall after the vortex departs the surface. McAlister et. al. published a suite of dynamic stall tests on a NACA 0012 wing in forward flow along with a discussion of the aforementioned behavior [72].

Lind and Jones [63, 73] conducted experiments on static and oscillating airfoils in reverse flow conditions. They reported the dynamic stall behavior in reverse flow for a sharp-edged airfoil (NACA 0012) was similar in lift morphology to that of forward flow, with the exception of the former exhibiting a secondary shed leading-edge vortex causing additional lift in the second half of the pitching cycle (referred to as the secondary dynamic stall vortex, SDSV). The secondary vortex was only observed for combinations of relative low reduced frequency and high mean and amplitude of the airfoil pitch motion. Lind [62] also concluded that the reverse-flow stall behavior was independent of Reynolds number due to the sharp aerodynamic leading edge acting as the separation point, in contrast to blunt (conventional) leading edge airfoils in which the boundary layer behavior dominates the separation behavior.

Another important conclusion they made was the effect of reduced frequency on the reverse-flow dynamic stall behavior.

The implications for this present study is that if classical dynamic stall was dominating the lift behavior, similar morphology could be expected. Lind also measured strong aperiodicity in phase-averaged measurements during periods of stall, represented as increased magnitude of the standard deviation at a particular point in the cycle.

Bowen-Davies developed a dynamic stall model, modified from a Leishman-Beddoes approach, for use in the reverse-flow region for traditional sharp trailing edge airfoils [74]. Correlations with the high advance ratio UH-60A test data [17, 18] showed good prediction of load impulse locations, but mixed predictions of magnitude.

7.1.2 Yawed/radial flow

Radial flow along the blade spanwise axis has been shown to delay stall when only considering the chordwise velocity components [68]. This delay in stall is attributed to the spanwise flow thinning the boundary layer. The primary source of the radial flow in edgewise rotors is oblique/yawed flow from the freestream velocity field component along the blade span ($V \cos \psi$). This effective blade sweep is maximum at the fore and aft portion of the rotor disk. Hence this correction would not be expected to have a large impact on delaying the reverse-flow stall behavior that is dominating the error between prediction and measurement. Bowen-

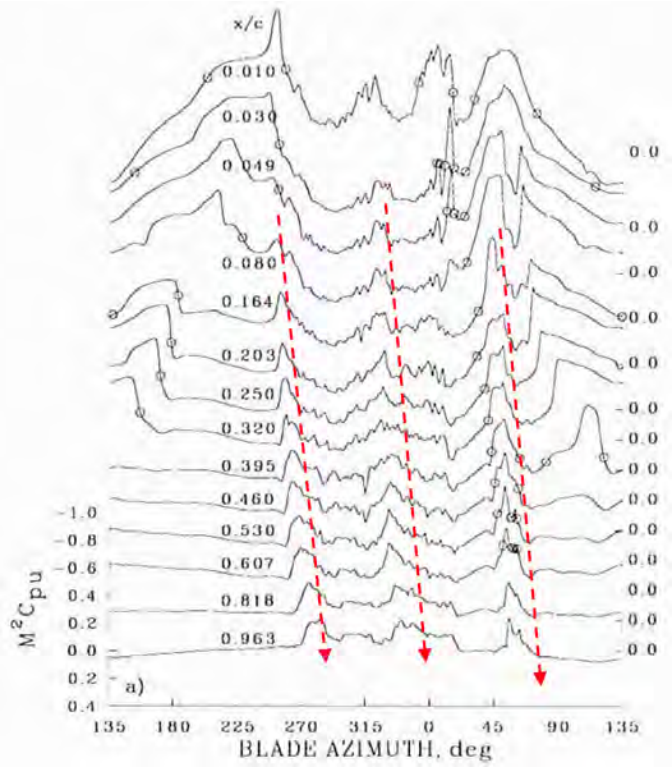

Figure 7.3: Surface pressure offset plot showing dynamic stall in the UH-60A flight test data during the UTTAS pull-up maneuver [53]

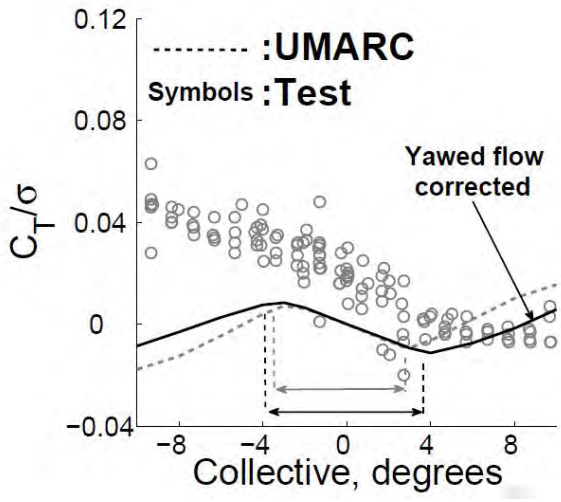

Figure 7.4: Impact of yawed flow correction on the thrust curve at $\mu = 1.03$ [24]

Davies [24] implemented this yawed flow correction in UMARC and found slight improvement in correlation with the high μ test data, but no significant change to the trend (fig. 7.4).

7.1.3 Rotational (static) stall delay

There is a third type of stall delay that occurs on rotating surfaces that does not require unsteady aerodynamics or a spanwise component of freestream velocity. Experiments on pressure-instrumented propellers and horizontal-axis wind turbines have shown that rotation postpones stall of the blade sections relative to static 2-D airfoil tests (fig. 7.5) [75–78]. The effect is attributed to centrifugal acceleration causing outward radial flow in the boundary layer. This radial flow is then subject to Coriolis forces that accelerate the flow towards the trailing edge, reducing the adverse pressure gradient [68, 79–82]. This 3-D stall delay effect is most prominent

closer to the root of the blade, and becomes negligible outboard of roughly 50% span.

The effect has also been noted to occur on tilt-rotors in hover and low-speed forward flight [55]. Generally this type of stall delay is neglected on helicopter rotors due to lower twist rates (relative to tilt-rotors or propellers) and hence less possibility of root stall in normal conditions. Also helicopters can have relatively large root cutouts to accommodate the hub, pitch mechanisms, and hinges, that all act to further mitigate the impact of this effect.

In the case of the high-advance ratio rotor, the root region on the retreating blade has a much larger impact on total thrust (fig. 6.5). Accurate prediction of the stall behavior near the root can thus become quite important for performance and loads predictions. However, it is unclear whether such models are appropriate for high advance ratio edgewise rotors, where the freestream velocity component is large compared to the rotational velocity, especially near the root in the reverse flow region. Typical airfoils will also have a sharp aerodynamic leading edge in reverse flow, which is not in common with experimental observations of the effect.

In the reverse-flow region of a rotor, the Coriolis forces on the boundary layer should still be accelerating the flow towards the geometric trailing edge, which is now the aerodynamic leading edge. In this situation, these effects should increase the adverse pressure gradient, not reduce it as in forward flow.

Du and Selig [80] suggested the outboard portions of a rotating blade experience less rotational stall delay due to larger Reynolds numbers and reduced boundary layer thicknesses. If true, this would mean the inboard section of the re-

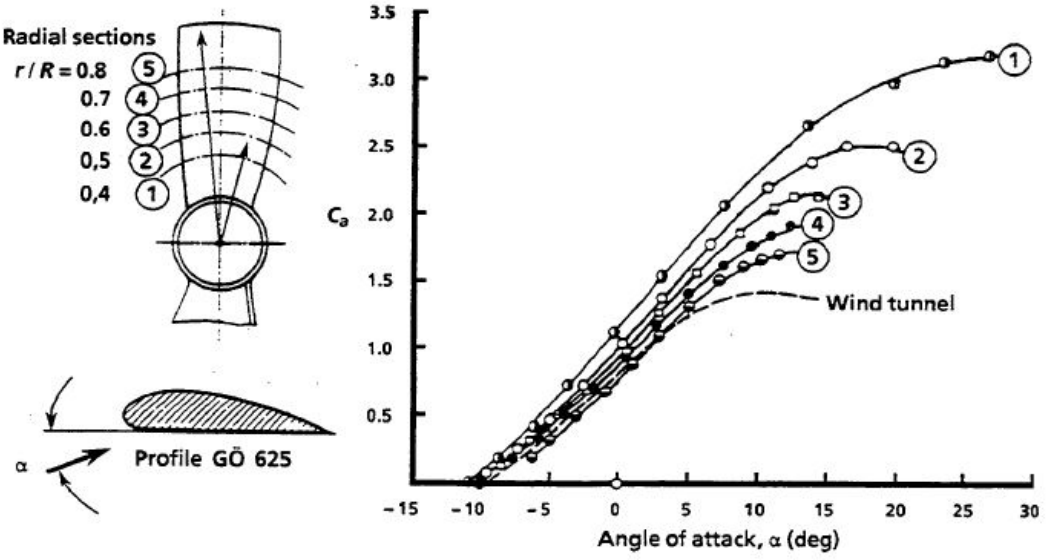

(a) Propeller

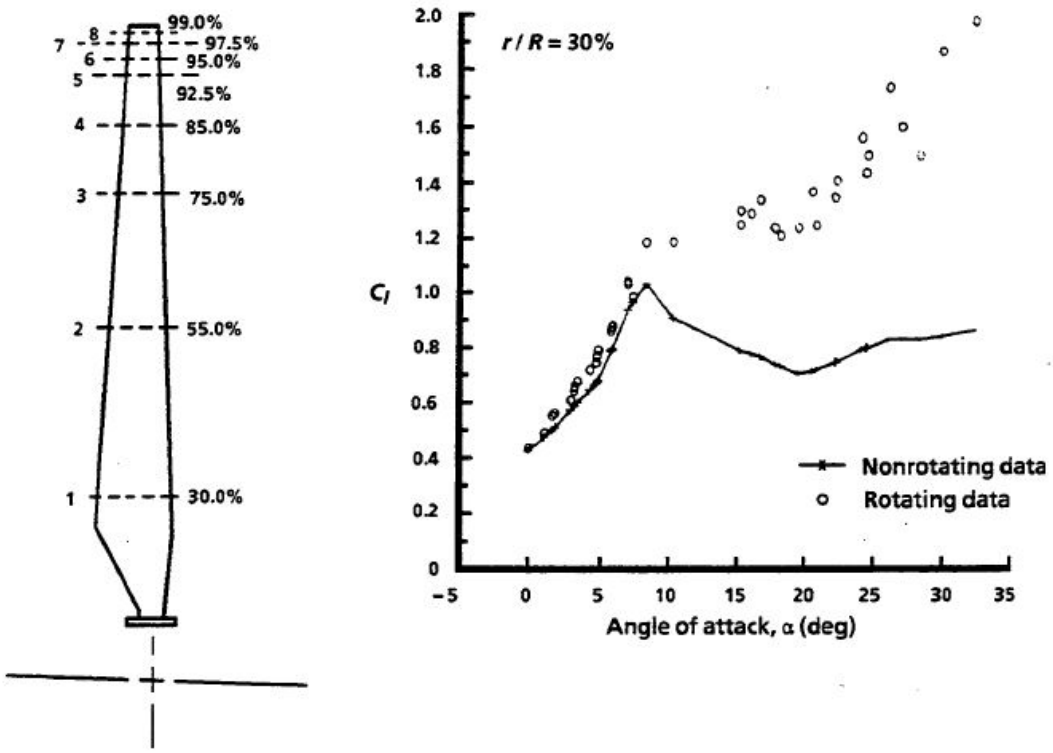

(b) Wind turbine

Figure 7.5: Measurements of rotational stall delay on a propeller and a horizontal axis wind turbine. Figures from Corrigan [77].

treating blade of the high advance ratio rotor may not experience this form of stall delay, due to higher Reynolds numbers than the outboard section of the retreating blade.

The 3-D rotating boundary layer effects of a rotor in reverse flow need further investigation [6, 83], although study would be complicated due to the dynamic environment of a reverse-flow rotor. Spinning a conventional rotor blade set backwards in hover would give insight into the static stall delay characteristics of a sharp leading edge, blunt trailing edge rotor. However, in such a test setup the sign of the shaft angular rate (Ω) would be reversed relative to the direction of the net tangential section velocity (u_T) in a real edgewise rotor's reverse flow region, flipping the effect of boundary-layer Coriolis forces as mentioned above. Clearly the reverse-flow region of a helicopter rotor is a challenging flow environment to reproduce under laboratory conditions.

7.2 Reverse-Flow Dynamic Stall in Test Data

This section explores the observations of stall phenomena from the test measurements. As mentioned in the introduction to this chapter, there were many test cases where the measured normal force coefficient exceeded the expected maximum assuming 2-D steady conditions.

Figure 7.6 is an offset plot, showing the separate time histories of all upper- and lower-surface pressure sensors but with each being offset in the y-axis for ease of visualization. For this high advance ratio case, the upper surface (fig. 7.6(a)) is

the suction side on the retreating blade which is fully in reversed flow. A translating low-pressure region can be observed, which has the signature of a shed dynamic stall vortex convecting from the aerodynamic leading edge to the aerodynamic trailing edge. The lower surface, which is the pressure side of the airfoil, experiences low-pressure peaks near the aerodynamic trailing edge, caused by the curvature of the airfoil shape in that region (geometric leading edge of the NACA 0012), and the influence of the shed upper surface dynamic stall vortex. Potsdam [31] observed the trailing edge vortex influence in CFD studies of the UH-60A rotor at high-advance ratio, as well as Lind [73] through detailed 2-D reverse-flow dynamic stall experiments.

This section will analyze the flow features of reverse-flow dynamic stall using measured test data from the present experiment. The effects of reduced frequency and pitch amplitude on normal force, pitching moment, and vortex kinematics will be explored. Comparisons will be made with 2-D oscillating airfoil experiments to judge whether 3-D effects or varying freestream velocity significantly alter the expected 2-D behavior.

7.2.1 Collective sweep

A collective sweep at this flight condition is shown in fig. 7.7. This time it is an offset plot for varying collective pitch angle, with each plot focusing on the surface pressure at a fixed chordwise station. The solid lines indicate the phase-averaged values (over 100 revolutions), with the blue shaded bands indicating the

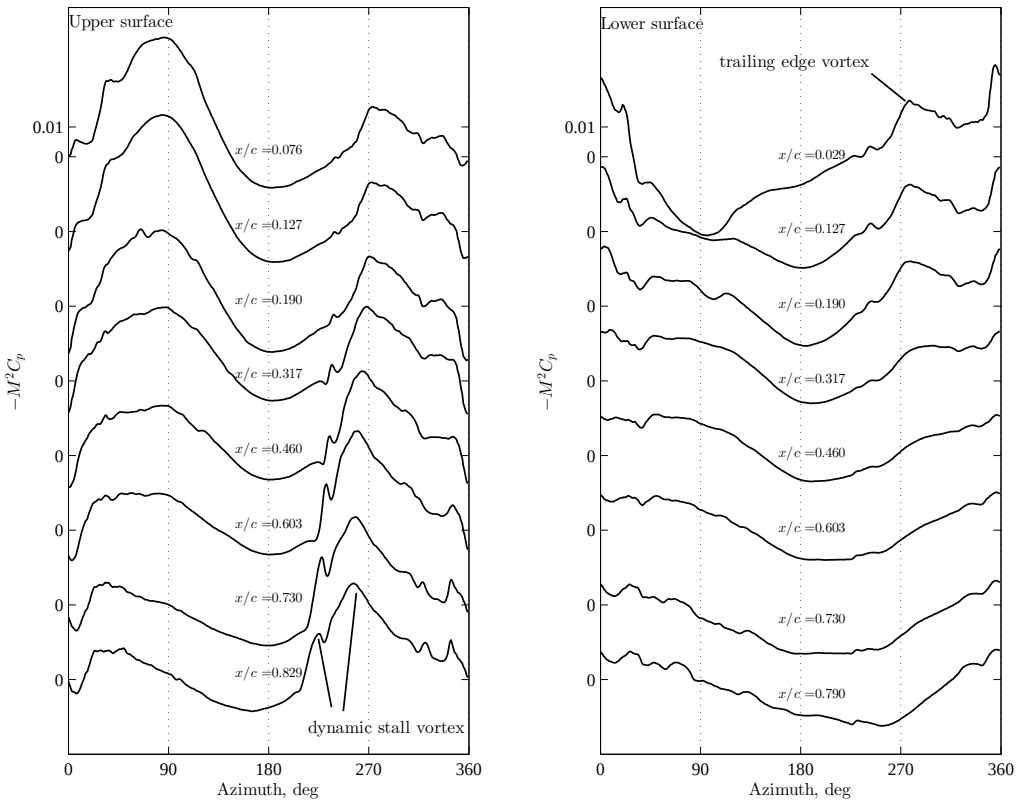

(a) Upper surface

(b) Lower surface

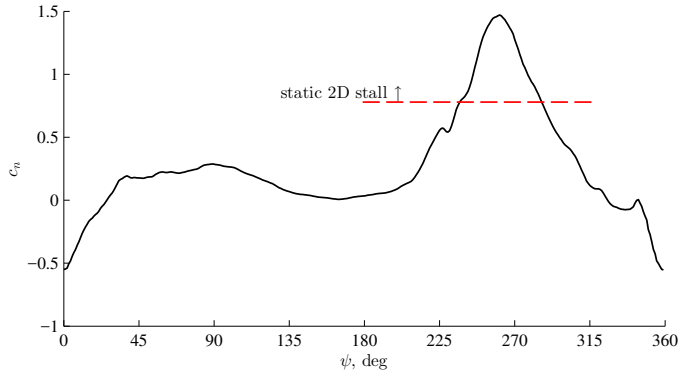

(c) Normal force coefficient

Figure 7.6: Chordwise surface pressure measurements at 0.3R radial station showing signatures of dynamic stall in the reverse flow region. Normal force coefficient vs azimuth showing c_n exceeding the static stall angle for the NACA 0012 in reverse flow. Case 543, μ = 1.21, θ_0 = −6°, α_s = 0°

$\pm 2\sigma(M^2 C_p)$ variation of each azimuth location as a measure of the unsteadiness (twice the standard deviation). High unsteadiness in the pressure measurement indicates turbulence or other flow aperiodicity that typically relates to separated flows or vortices [63].

The sweep in fig. 7.7 is from 0° to −8° collective, which corresponds to positive rotor thrusts at μ = 1.21 due to collective thrust reversal, discussed in Chapter 6. In the reverse flow region of the retreating blade at $0.3R$, the upper surface is the low-pressure side of the airfoil. This plot shows two chordwise pressures sensor locations for the lower surface, and two for the upper surface. Below the offset plots are the normal force and pitching moment coefficients vs. azimuth for the same sweep. These coefficients were integrated from the surface pressure measurements (see section 5.4 for discussion of integration errors), and use both tangential and radial velocities (u_T and u_R) to normalize (to avoid asymptotes). Therefore, the integrated coefficients should be considered approximate, yet are still useful to investigate the stall behavior. The reverse flow region based on u_T is denoted by the vertical dash-dot lines in each plot.

At θ_0 = 0°, all sensors and positions show attached flow, with tight 2σ bands of surface pressure. The steep pressure change and large unsteadiness in the aft portion of the rotor disk (ψ = 330° to 40°) at all angles are thought to be due to the turbulent wake caused by the rotor hub and possible interactions with blade root vortices. The steep pressure change is more pronounced near the leading edge, however increased unsteadiness is apparent at all chordwise locations. Separation at the blunt aerodynamic trailing edge in reverse flow would be expected in the

forward-most pressures sensors, but is not readily apparent from this dataset when examining the $x/c = 0.029$ or $x/c = 0.076$ sensors.

At $\theta_0 = -1°$, the unsteadiness of the upper surface sensor near the aerodynamic leading edge ($x/c = 0.829$) begins to increase at $\psi = 228°$, reaching a maximum 2σ at $\psi = 285°$ where there is also a small negative pressure peak. This unsteadiness is limited in chordwise extent to the $x/c = 0.829$ and $x/c = 0.730$ sensors on the upper surface. The upper surface sensors forward of this position ($x/c = 0.603$ to 0.076) do not exhibit unsteadiness or a low-pressure peak. This is likely a localized separation bubble forming, which has been observed in experiments by Critzos [57] and Lind [62] and numerical simulations by Smith [84]. For small angles, the sharp aerodynamic leading edge causes a large adverse pressure gradient and boundary layer reversal, leading to a separation zone that reattaches downstream as a turbulent boundary layer.

At $\theta_0 = -2°$, the region of unsteady upper-surface pressure spreads to include $0.829 \geq x/c \geq 0.603$. The normal force coefficient plot (fig. 7.7, bottom left) shows that $\theta_0 = -2°$ is very near the static stall c_n of the airfoil in reverse flow (red dotted line).

At $\theta_0 = -3°$, the unsteady region for $x/c = 0.829$ and is larger in unsteadiness and in magnitude of the low-pressure peak. The integrated normal force coefficient near $\psi = 270°$ is now above the expected max c_n based on steady 2-D data. The unsteadiness over the entire upper surface has increased, including near the geometric leading edge ($x/c = 0.190$). A leading edge vortex is shed across the upper surface, but appears to be weak and only influences $1 \geq x/c \geq 0.46$.

At $\theta_0 = -4°$, evidence of a trailing edge vortex (See Lind and Jones for discussion [73]) can be seen at $x/c = 0.029$ on the lower surface, which grows in strength as the collective is increased further. This corresponds with the growing low-pressure region on the upper surface near the aerodynamic trailing edge. The aerodynamic leading edge sensor on the pressure side ($x/c = 0.790$, lower surface) shows no increase in unsteadiness at any collective in the reverse flow region. The translating low-pressure region is evident at $\theta_0 \leq -4°$, and is similar in nature to that shown in fig. 7.6, denoting a strong shed dynamic stall vortex.

As the negative collective increases from $\theta_0 = -4°$ to $\theta_0 = -8°$, there are progressive increases in the magnitude of the pressure peaks, but no fundamental change in shape. At $\theta_0 = -8°$ the suction peak on the lower surface at $x/c = 0.029$ is particularly sharp, and the effect is to reduce the normal force earlier in the cycle compared to lower collectives.

Another observation from the pressures and the integrated coefficients in fig. 7.7, is a trend at higher collectives toward earlier peak values of maximum normal force and maximum pitching moment. The peaks were identified and plotted to show the migration with collective pitch (fig. 7.8). Oscillating airfoil measurements in reverse flow by Lind and Jones [73] showed increasing pitch amplitude correlated with an earlier formation of the dynamic stall vortex, which moves the peak normal force and peak pitching moment earlier in the cycle. This same behavior is observed here, with increasing collective pitch (combined with increased cyclic for rotor trim) resulting in higher blade pitch mean and amplitudes in the reverse flow region.

In conventional dynamic stall, the pitching moment (about $c/4$) reaches a

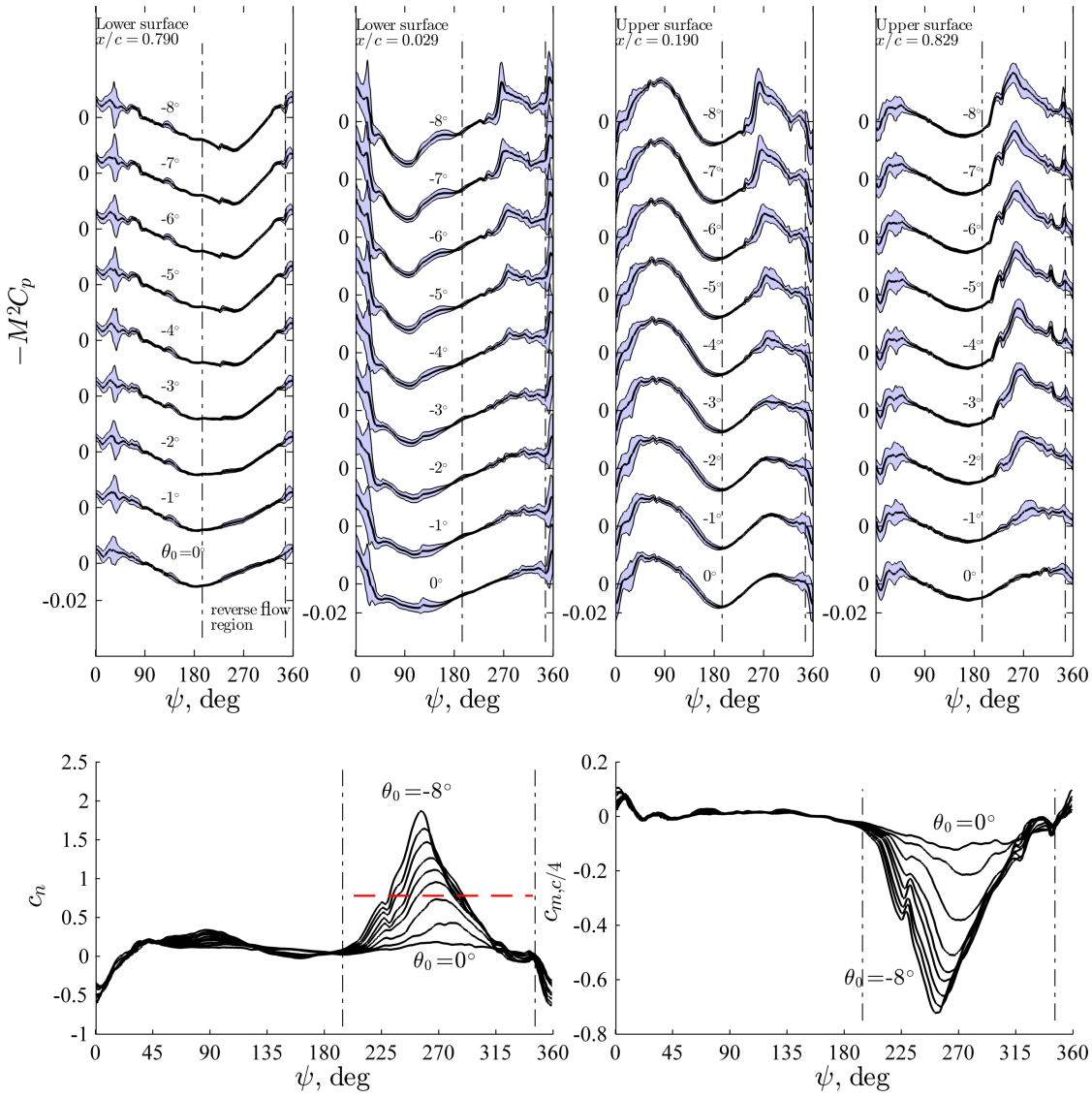

Figure 7.7: Offset plots of a collective sweep showing surface pressures with 2σ bands at fixed chordwise positions (upper surface), and integrated normal force and pitching moment coefficients (bottom). $\mu = 1.21$, $\theta_0 = 0°$ to $-8°$, $\alpha_s = 0°$

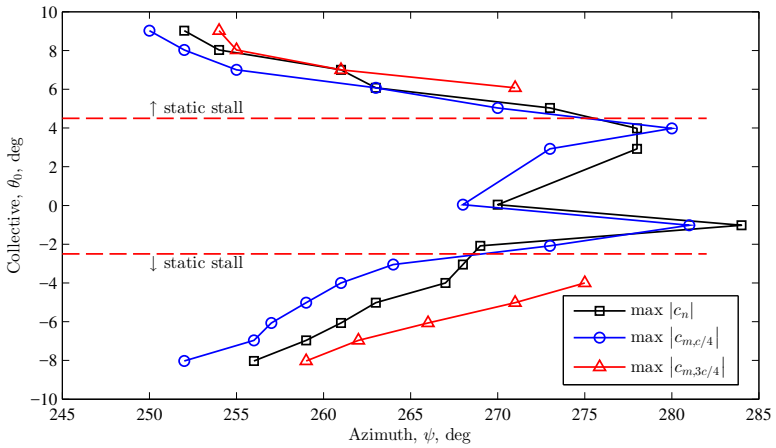

Figure 7.8: Azimuth of peak normal force and pitching moment in the reverse flow region. $\mu = 1.21$, $\theta_0 = -8°$ to $+9°$, $\alpha_s = 0°$

maximum after the normal force or lift coefficient reaches a maximum. This is due to the shed dynamic stall vortex convecting from leading edge to trailing edge, and hence moving the center of pressure aft, further from $c/4$.

In reverse flow dynamic stall, the shed dynamic stall vortex should actually reduce the pitching moment as it progresses across the airfoil surface, moving the center of pressure closer to the geometric quarter-chord. After passing the geometric quarter-chord (aerodynamic $3c/4$), the pitching moment contribution from the low-pressure of the shed vortex should reverse sign. Therefore, it would be expected to see the maximum pitching moment magnitude occurring prior to maximum normal force during reverse flow dynamic stall. For the highest collective pitch shown in fig. 7.7, case 546, the peak negative c_m occurs at $\psi = 255°$ and the peak positive c_n indeed occurs later at $\psi = 264°$. A compilation of the azimuthal time of peak normal force and pitching moment for a collective sweep is shown in fig. 7.8. The peak $c_{m,c/4}$

is shown to precede the peak c_n for cases with dynamic stall. Also included in fig. 7.7 is the pitching moment coefficient about the three-quarter chord, $c_{m,3c/4}$, which is the aerodynamic quarter-chord in the reverse flow region. The peak moment at $0.75c$ is shown to occur later in the cycle compared to c_n, which is comparable to conventional forward-flow dynamic stall studies.

7.2.2 Stall events

Further exploring the timing and behavior of normal force and pitching moment in reverse flow, case 546 is chosen for detailed examination. This case is at $\mu = 1.21$ and $\theta_0 = -8°$, which is a high positive thrust case. The trim cyclic pitch angles were set to $\theta_{1s} = 8.2°$ and $\theta_{1c} = 1.2°$, which means the root pitch at $\psi = 270°$ was $\theta = -16.2°$.

The surface pressures and integrated coefficients are shown in fig. 7.10, with the integrated coefficients separated into upper and lower surface contributions. Pitching moment is given both about $0.25c$ and $0.75c$. Pitching moment about $0.75c$ is taken as the aerodynamic center in reverse flow on the retreating blade, which is useful for comparisons with dynamic stall studies which typically give pitching moment behavior about the aerodynamic $0.25c$. The sign convention for both pitching moments is kept as positive for a pitch up about the geometric leading edge, therefore $c_{m,3c/4}$ is shown negated to represent a reverse-flow perspective.

Focusing on the moment about $0.75c$ (fig. 7.10(e)), there are three main events to discuss. The first is the small pitching moment perturbation with peak magnitude

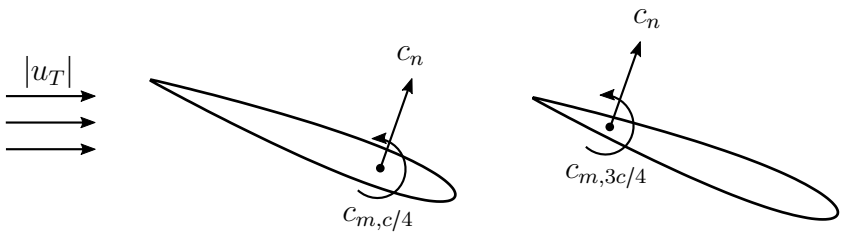

Figure 7.9: Notation and sign convention of force and moment coefficients relevant to the reverse-flow region, with pitch moment shown about both $0.25c$ and $0.75c$.

at ψ = 220°, with a sign of aerodynamic leading edge pitch up (positive in the negated plot). This moment is caused entirely by the upper surface, which is shown separately as the red line of fig. 7.10(e). The root cause can be seen in the upper surface pressures of fig. 7.10(a), where a low-pressure disturbance is seen progressing across most of the airfoil from about ψ = 200° to 239°. Pitch down moment about $3c/4$ would be induced by a center of pressure aft of $0.75c$, and indeed when the pitch down moment is at a maximum, the sensor furthest aft at x/c = 0.829 experiences the peak low-pressure from the disturbance. As the disturbance cascades towards the leading edge, the pitching moment returns to zero, and then begins to increase. This has the signature of a shed vortex from the aerodynamic leading edge, as opposed to a vortex interaction from the wake, since the effect is isolated to the upper surface. The $0.317c$ station upper surface pressure (fig. 7.10(a)) most clearly shows the signature of the first passing vortex. There is a pressure increase (remember the y-axis is inverted, so a pressure increase is down) as the vortex approaches (ψ = 230°), followed by a pressure decrease as the vortex core passes (ψ = 236°).

This vortex does not appear to be the primary dynamic stall vortex, as it occurs fairly early in the pitch cycle. McAlister, et al [72] observed a similar behavior which they called a *pre-stall break* and related it to the transition behavior of the NACA 0012 (in forward flow) as the point where a separation bubble re-attaches. Perhaps then it is a leading edge separation bubble developing and then shedding followed by re-attachment.

Staying with fig. 7.10(e), the next event of interest is moment stall occurring around $\psi = 240°$, which is the beginning of a sharp increase in moment. In conventional dynamic stall, moment stall occurs a short time after the primary dynamic stall vortex has shed from the leading edge, after it passes aft of $0.25c$. This behavior is matched by correlating with the sharp increases in low-pressure on the upper surface (fig. 7.10(a)). Again the moment stall is driven by the upper surface pressures (red line, fig. 7.10(e)). By contrast, it is difficult to discern this moment stall behavior when plotting the reverse-flow pitching moment about the geometric quarter-chord, as in fig. 7.10(d), where continuous decreases in pitching moment are measured beginning at approximately $\psi = 200°$, well before any vortex shedding.

Once the upper surface dynamic stall vortex approaches the aerodynamic trailing edge, two events occur. Firstly, the peak $c_{m,c/4}$ is reached at $\psi = 252°$ as the vortex is in close proximity to $0.25c$ and hence the low-pressure wave loses influence or even induces pitch-up moments. Secondly, the lower surface trailing edge experiences suction induced by the trailing edge vortex and the local surface curvature of the rounded trailing edge. These suction peaks are evident in fig. 7.10(b), starting at $\psi = 252°$ and reaching a peak at $\psi = 266°$. The strong suction on the lower

surface reduces c_n, and the effect is clearly seen in the lower-surface contribution to c_n (fig. 7.10(c), blue line). The departure of the dynamic stall vortex, combined with the lower surface suction results in lift stall at $\psi = 256°$ as c_n descends from peak magnitude of 1.87 (compared to a static $c_{n,max}$ of approximately 1.0).

This sharp decrease in normal force near the geometric leading edge also induces pitch-down moments about $0.75c$, which can be seen in the lower-surface pitching moment integration (fig. 7.10(e), blue line). The upper-surface contribution (red line) is still increasing positively, but soon after the net-moment (black line) reaches a peak at $\psi = 259°$ and begins decreasing. This point is typically taken as when the dynamic stall vortex leaves the aerodynamic trailing edge, although the upper-surface reaches a peak moment shortly thereafter, at $\psi = 262°$, which is likely coinciding with the waning influence of vortex lift.

Plotting the integrated coefficients as a function of the root pitch, rather than azimuth position, may give some insight and comparison with 2-D oscillating airfoil studies.

7.2.3 Effect of blade pitch kinematics

The collective sweeps conducted during the wind tunnel test provide a dataset to explore the effect of pitch angle kinematics on the reverse-flow dynamic stall behavior. The detailed 2-D reverse-flow experiments by Lind and Jones [63, 73] provide guidance on the relevant features and expected sensitivities. In particular, they found the dynamic stall type depending on both reduced frequency and the pitch

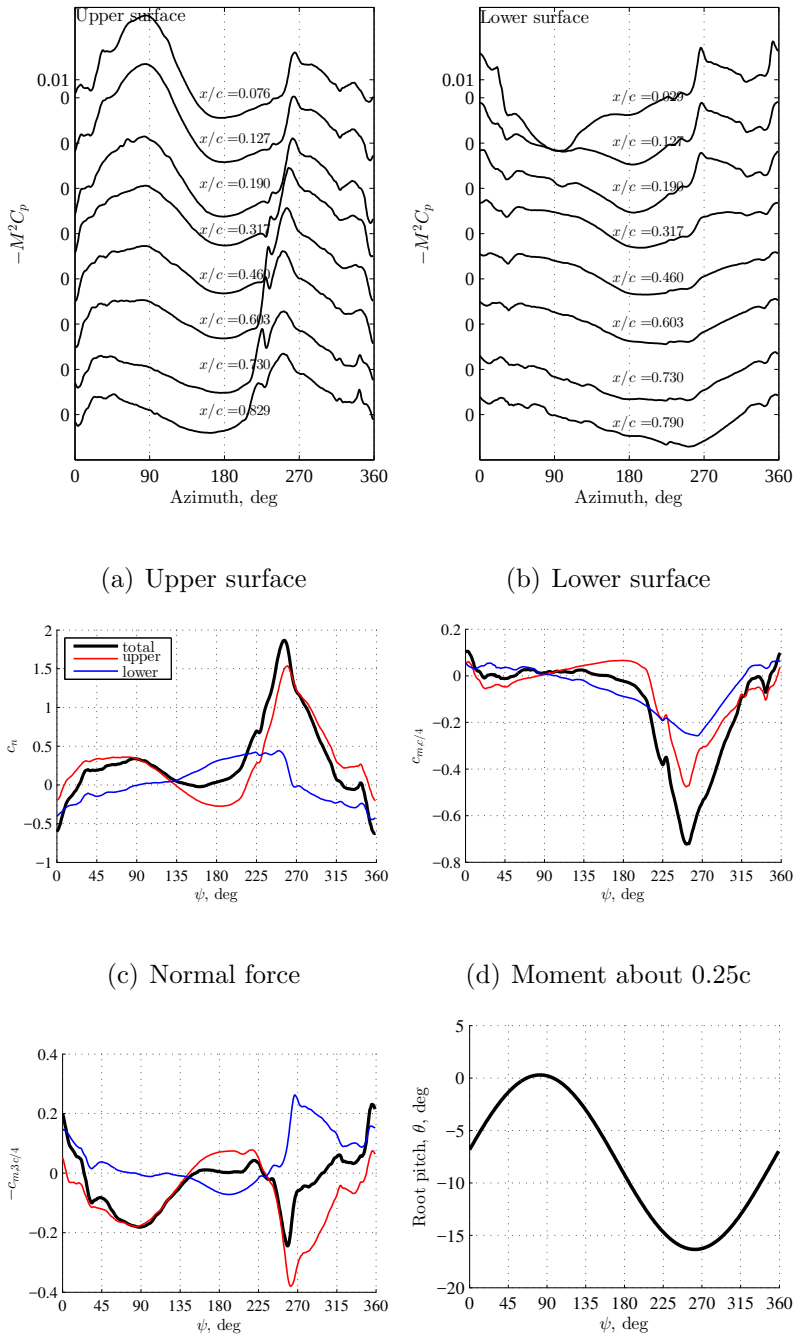

(a) Upper surface

(b) Lower surface

(c) Normal force

(d) Moment about 0.25c

(e) Moment about 0.75c

(f) Swashplate pitch angle

Figure 7.10: Chordwise surface pressures on upper and lower surfaces, with normal force and pitching moment coefficients (about both $0.25c$ and $0.75c$. Integrated values separated by upper and lower surfaces of the airfoil section. Case 546: $\mu = 1.21$, $r/R = 0.3$, $\theta_0 = -8°$, $\alpha_s = 0°$

angle kinematics (mean and amplitude of angle of attack). Reynolds number was not found to significantly influence behavior due to the sharp aerodynamic leading edge fixing the transition/separation point. The dynamic stall type was identified by the number of discrete vortex events within a single pitch cycle. Dynamic stall types of I–IV were identified in their 2-D experiments on the NACA 0012 in reverse-flow.

In the present rotor experiments, the pitch kinematics were set by the swashplate angles needed to trim the rotor to minimize blade flapping. The swashplate settings give the 1/rev variation of pitch, however the region of interest is the reverse-flow portion of the disk, which only experiences a subset of this pitch cycle. Within the reverse-flow region, there is also time-varying velocity from the freestream, induced inflow, and higher harmonic blade flapping components (>1/rev). All of these factors make the definition of the reduced frequency and angle of attack variation difficult to define. However, comparisons can still be made to verify if the 3-D environment at the blade sections in reverse-flow dynamic stall exhibit the same nominal behavioral trends as the 2-D experiments by Lind and Jones.

To simplify the comparison with 2-D oscillating airfoil experiments, the reverse-flow region was isolated and the azimuth location was normalized in time to be one cycle of pitch (Eq. 7.1). Figure 7.11 shows the effect of increasing maximum pitch on the dynamic stall characteristics. The advance ratio is constant so the reduced frequency is also constant. The highlighted cases are for a shaft tilt of $\alpha_s = 4^\circ$ (pitch up/back), which increases the maximum reverse-flow pitch angle relative to the freestream by acting as additional effective longitudinal cyclic. The total effective pitch angle is shown in fig. 7.11(d) for each case. It should be noted that the pitch

kinematics are periodic with each rotor rotation but do not contain a full cosine period within the reverse flow region itself. This notable difference with oscillating airfoil studies does not appear to significantly alter the dynamic stall behavior, as will be shown later.

$$t/T = \frac{\psi - \psi_{rev,start}}{\psi_{rev,end} - \psi_{rev,start}} = \frac{\psi - \left(\pi + \sin^{-1}(r/\mu)\right)}{\pi - 2\sin^{-1}(r/\mu)} \tag{7.1}$$

The normal force (fig. 7.11(a)) and pitching moment (fig. 7.11(b)) coefficients are shown for increasing maximum pitch angle (fig. 7.11(d)). Case 314 ($\theta_0 = -2.4°$) shows mild pitching moment variations and a wide maximum normal force, indicative of a weak dynamic stall vortex that remains strongest near the aerodynamic leading edge and loses strength near the trailing edge. Case 316 ($\theta_0 = -4.3°$) develops a sharper peak normal force at a higher maximum value for both normal force and pitching moment. The chordwise pressure time histories (not shown) indicate a mild trailing edge vortex forming. Case 318 ($\theta_0 = -6.3°$) again has increased normal force and pitching moment, with evidence of a stronger trailing edge vortex and the beginnings of a secondary dynamic stall vortex near $t/T = 0.6$. Case 320 ($\theta_0 = -8.4°$) now shows the signature of primary, trailing edge, and secondary vortices. The trailing edge vortex effect is seen in the steep drop in normal force and pitching moment just after $t/T = 0.4$. The secondary dynamic stall vortex influence is evident around $t/T = 0.6$ as an increase in normal force and pitching moment as the vortex traverses across the chord.

Late in the cycle ($t/T > 0.8$, there is a trend of lower normal force with increas-

ing pitch amplitude. Examining the individual surface pressures revealed differing behavior only at the location closest to the aerodynamic leading edge on the suction side (upper surface), shown in fig. 7.11(c). A second suction peak is strongest for the lowest pitch (Case 314), and is not present at the highest pitch (Case 320). This is the only chordwise location where this was measured (the other locations had similar pressure values for all cases), so this does not appear to be caused by a shed vortex or blade-vortex interaction from another blade. The higher pitch cases may be more deeply stalled/separated after the secondary vortex departs the surface leading to higher hysteresis. The lower pitch cases may also be the only ones to reach a low enough pitch angle for the leading edge suction surface to fully re-attach.

The normal force trends compare well qualitatively with the 2-D trends reported by Lind fig. 7.12. The dip in normal force late in the cycle for higher pitch amplitudes is also present in Lind's data, indicating the root cause is not a 3-D or rotation effect. The salient features of reverse-flow normal force behavior are present in both datasets.

1. Increasing $c_{n,max}$ with pitch amplitude initially
2. Saturation/plateau of $c_{n,max}$ at some critical c_n
3. Increasing of dynamic stall type (number of discrete vortex events) with maximum pitch angle
4. Increasing amplitude of the secondary dynamic stall vortex (SDSV) with pitch, even after the primary vortex c_n plateaus.
5. Movement of peak c_n earlier in the cycle with increasing pitch

A comparison of the max c_n and min c_m (maximum negative magnitude) is given in fig. 7.13 and compared with reverse flow data from Lind [63] and forward

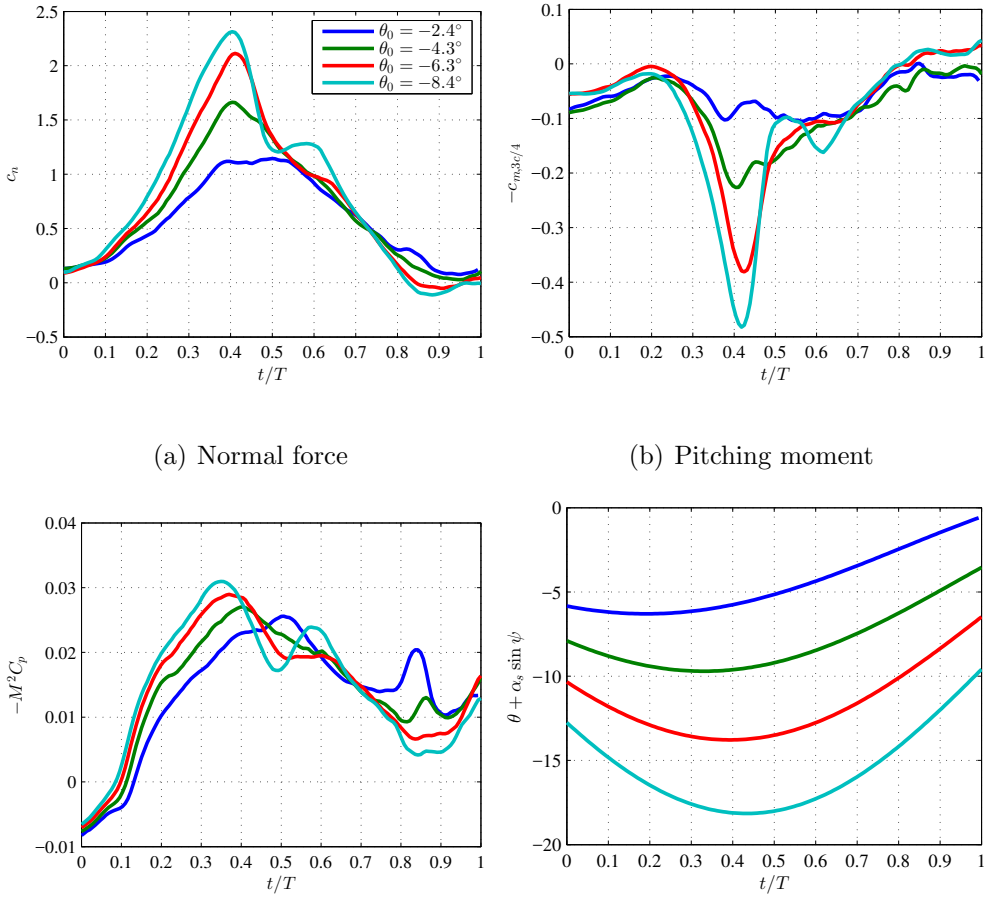

(a) Normal force

(b) Pitching moment

(c) Surface pressure, $x/c_{upp} = 0.829$

(d) Pitch angle

Figure 7.11: Effect of increasing maximum pitch angle on reverse-flow dynamic stall. Cases 314, 316, 318, and 320, $\mu = 1.03$, $r/R = 0.3$, $\alpha_s = 4°$, $k_{rev} = 0.159$, $k_\Omega = 0.064$

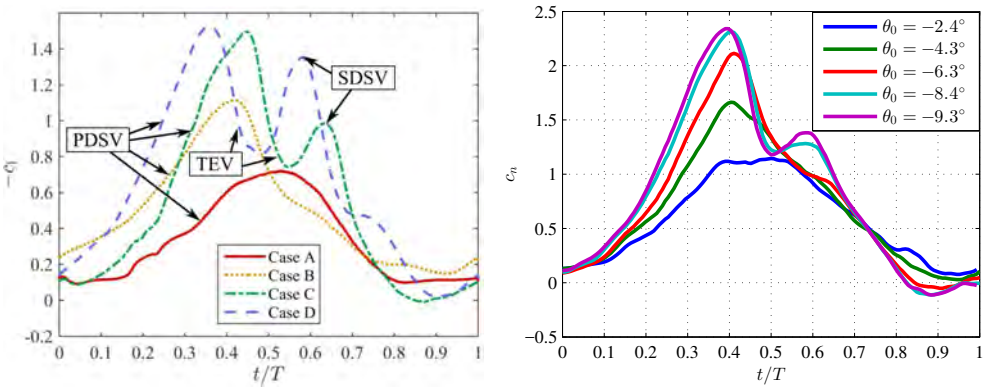

(a) Oscillating airfoil

(b) Section of rotor blade

Figure 7.12: Comparison of (a) an oscillating NACA 0012 in reverse flow from Lind and Jones [73], k = 0.160, $\alpha_{rev,max}$=(A: 9.0°, B: 14.0°, C: 18.8°, D: 24.1°) to (b) the reverse-flow region measurements of a rotor blade section at r = 0.3, μ = 1.03, k_{rev} = 0.159, k_Ω = 0.064

.

flow data aggregated fit from Bousman [85], both for the NACA 0012. The measured data from the present work show good agreement with both data sets, despite the possibility of potential errors with surface pressure integration. Most interesting is the good agreement with Bousman's forward-flow dynamic stall data fit, despite the nearly 40% reduction in steady $c_{l,max}$ between a NACA 0012 in forward flow (at Re = 4e6) and in reverse flow. This indicates the dynamic stall vortex may be dominating the maximum dynamic lift capability. Previous research by Ham and Garelick concluded that the maximum lift in dynamic stall primarily depends on the angle-of-attack rate [55, 86]. McCroskey [87], through compilation of 2-D dynamic stall test data from several airfoils, also concluded that the unsteady motion appeared to have more impact on the dynamic-stall airloads than the airfoil shape.

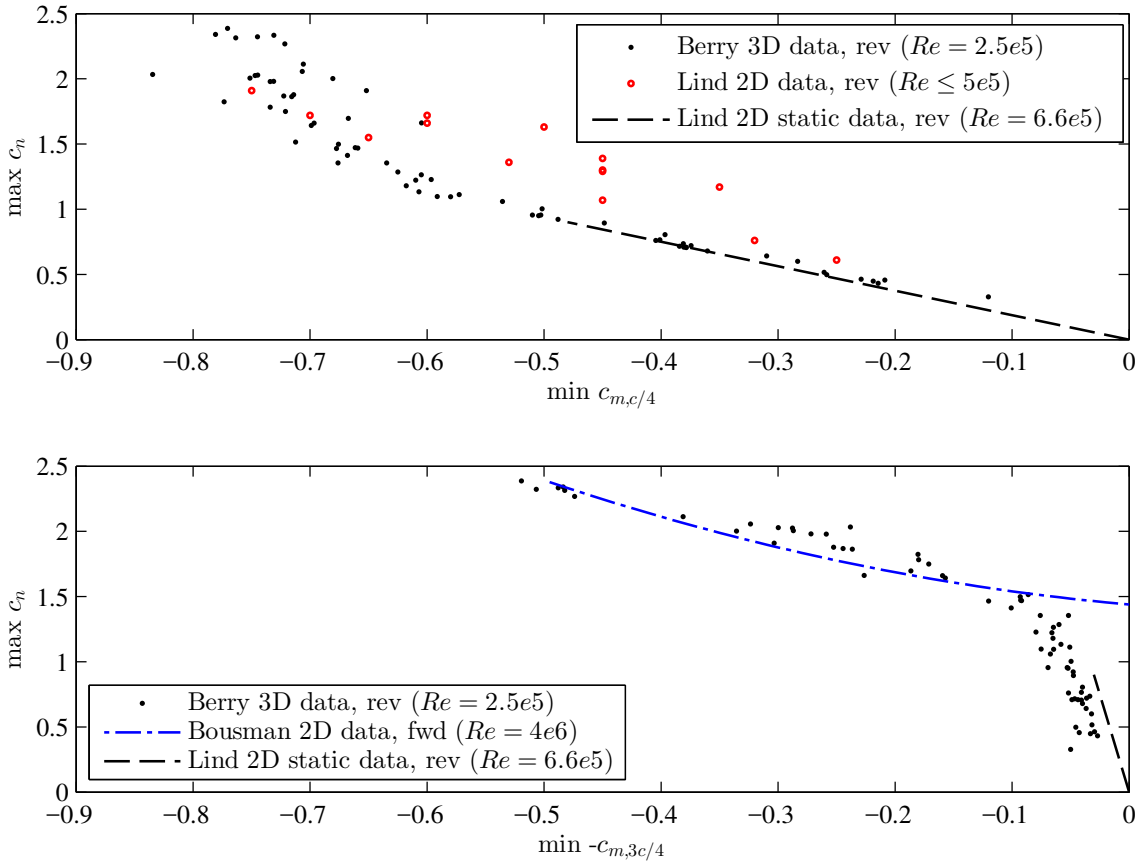

Figure 7.13: Maximum normal force and minimum pitching moment for the reverse flow region for μ = 1.03 (α_s = 0°,4°) and μ = 1.21 (α_s = 0°). Compared with 2D reverse and forward flow data (oscillating and steady) from Lind [63] and forward flow oscillating 2D data (curve fit) from Bousman [85], both for the NACA 0012 airfoil.

The effect of reduced frequency sweep with constant pitch amplitude was investigated through an advance ratio sweep (fig. 7.14). Increasing advance ratio decreases the reduced frequency, through an increase in velocity (denominator) and an increase in the period of the reverse-flow region (decrease in dimensional frequency). The latter effect is not present if using rotor Ω as the dimensional frequency. To isolate the effect of reduced frequency, the cases were chosen to have similar maximum pitch angle in reverse flow, although there were some unavoidable phase differences due to the introduction of increasing lateral cyclic to trim with higher advance ratios.

Examining fig. 7.14, the peak magnitudes of normal force and pitching moment are similar for all cases. There is a trend of increasing peak normal force (fig. 7.14(a)) with reduced-frequency (decreasing advance ratio), along with a slight phase delay. The phase delay may be simply due to the pitching kinematic phase differences (fig. 7.14(d)). However, it is noteworthy that the peak normal force increases slightly with reduced frequency, despite lower peak pitch angle (angle of attack not known). Lind and Jones [73] demonstrated that increasing reduced-frequency during reverse-flow dynamic stall delays the phase at which the stall vortex first forms and keeps the vortex closer to the blade surface for a longer portion of the cycle. These effects can partially be seen in these data, although the reduced-frequency range tested here is much lower than in Lind's tests.

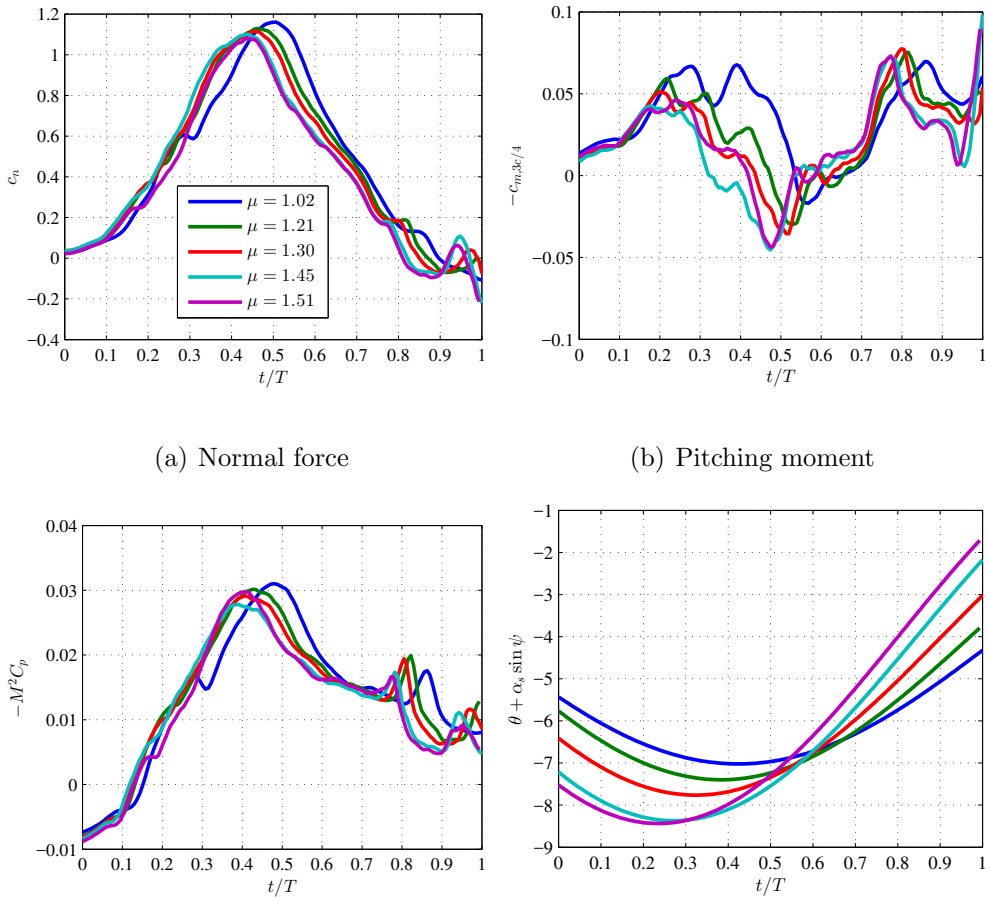

(a) Normal force

(b) Pitching moment

(c) Surface pressure, $x/c_{upp} = 0.829$

(d) Pitch angle

Figure 7.14: Effect of reduced frequency (increasing advance ratio) on reverse-flow dynamic stall. Case 475 (μ = 1.03,k_{rev} = 0.159), Case 476 (μ = 1.21,k_{rev} = 0.123), Case 477(μ = 1.30,k_{rev} = 0.111), Case 479(μ = 1.45,k_{rev} = 0.095), and Case 480(μ = 1.51,k_{rev} = 0.078). All cases: θ_0 = −4°, $r/R = 0.3$, $\alpha_s = 0°$

7.2.4 Vortex kinematics

To further explore the shed vortex kinematics, the vortex convection speed was extracted from the surface pressure measurements. A typical technique is to track the chordwise position and time of the minimum pressure [71, 88]. The convection speed of a conventional dynamic stall vortex has been measured as being one third to one half of the freestream velocity [6].

The convection speed of the shed vortices in this dataset were calculated. The method consisted of identifying global or local minimum surface pressures in the reverse flow region at each chordwise station on the suction surface (fig. 7.15(a)). The azimuthal timestamp of the minimum pressures were then plotted against the chordwise locations. A linear fit determined the velocity (fig. 7.15(b)). This was then compared to the local freestream value (tangential only) at the local azimuth location. This process was automated and repeated for all test cases at high μ, with the linear fit restricted to fit quality of $R^2 \geq 0.95$ (fig. 7.16). Measurements from this dataset suggest the convection speed in reverse flow dynamic stall is between $0.2u_T$ to $0.4u_T$, which is in line with the oscillating reverse-airfoil studies by Lind and Jones [73].

7.3 Chapter Summary

Surface pressure measurements (and integrated force and moment coefficients) at the $0.3R$ blade station were analyzed to investigate the stall behavior in the reverse-flow region at high advance ratios.

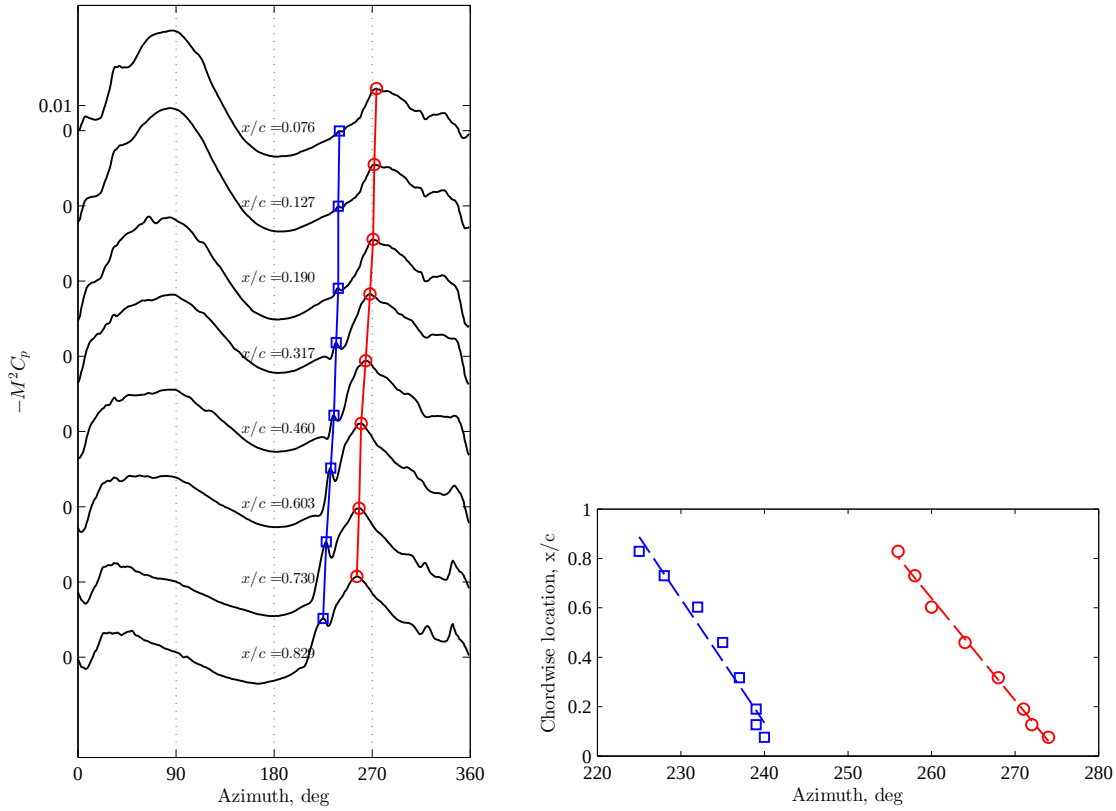

(a) Surface pressures, upper surface

(b) Vortex position with linear fit

Figure 7.15: Tracking the convection velocity of two shed vortices during dynamic stall events. Case 543, $\mu = 1.21$, $\theta_0 = -6°$, $\alpha_s = 0°$

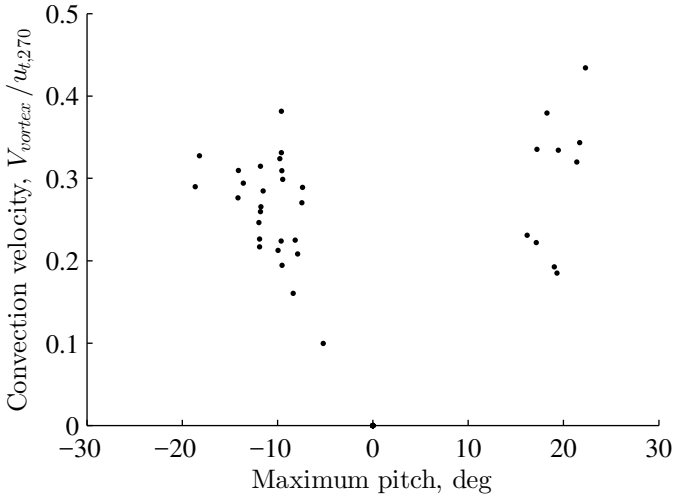

Figure 7.16: Dynamic stall primary vortex convection speed for all cases at $\mu \geq 1.0$.

The post-stall behavior appears to be dominated by unsteady aerodynamic effects, rather than static rotational stall delay. Evidence of shed vorticity from the aerodynamic leading edge convecting across the section chord indicate dynamic stall. The qualitative morphology of the integrated normal force and pitching moment coefficients agreed well with 2-D reverse-flow dynamic stall experiments from Lind and Jones [63, 73]. The quantitative trends of peak normal force and peak pitching moment matched well with 2-D forward-flow dynamic stall data presented by Bousman [85] as well as the reverse-flow data from Lind. These two findings indicate that dynamic stall behavior of a rotating blade in reverse-flow is largely dominated by 2-D effects, as is classical forward-flow dynamic stall. This indicates similar modeling approaches may be successful.

The agreement with forward-flow data for peak force and moment indicate

the peak loads are driven by shed vorticity and the airfoil shape (sharp vs. blunt leading edge) may be less influential on those values.

Chapter 8: Performance and Trim

8.1 Control Angles

The wind tunnel test was conducted with parameter sweeps of collective, advance ratio (rotor RPM and tunnel speed), and shaft tilt. At each condition, the rotor was trimmed to a target of zero 1P blade flapping amplitude using longitudinal and lateral cyclic pitch inputs. The trends of required cyclic for collective sweeps at each advance ratio are shown in fig. 8.1, along with the associated thrust for that collective. The linear fit slopes (for low collective angles) is then given in fig. 8.2.

Longitudinal cyclic, θ_{1s}, requirements show a linear trend with collective at all advance ratios (fig. 8.1(b)). The increasingly negative slope with increasing advance ratio is due to the increasing lift asymmetry across the lateral portion of the rotor disk (advancing vs. retreating blades). The cyclic requirement remains linear with collective even for cases where portions of the disk are experiencing stall and the thrust-to-collective trend becomes non-linear.

Lateral cyclic, θ_{1c}, has a non-linear trend with collective at lower advance ratios, and also at higher advance ratios when there is reverse-flow stall occurring (fig. 8.1(c)). Lateral cyclic requirements are typically most influenced by the rotor coning angle and the non-uniform induced inflow distribution, more-so than longi-

tudinal cyclic [55].

Bowen-Davies was able to satisfactorily predict both cyclic trends at all advance ratios using UMARC with a non-uniform inflow model (free-wake) [24]. The longitudinal cyclic trends with advance ratio also seem to be well-predicted with the uniform inflow model presented in section 6.3, as well as the analytical model that neglects induced inflow (fig. 8.3). This indicates that the longitudinal cyclic requirement to trim is influenced more from the in-plane velocity components determined by the advance ratio as opposed to the induced velocity distribution.

The analytical formulation is repeated here as the longitudinal cyclic sensitivity to collective pitch for zero rolling moment trim (eq. 8.1). The cyclic sensitivity rapidly approaches a ratio of -1 deg/deg, which means that for a given collective pitch increase, the longitudinal cyclic is applied equally such that the advancing blade ends up with zero net change. This would be needed where the retreating blade has a net zero sensitivity to pitch changes, due to a mix of forward and reverse-flow regions, both of which are at low dynamic pressures and are roughly equal in effect. At higher advance ratios, the retreating blade is either mostly or fully in reverse flow, but the dynamic pressure is now increasing due to the freestream component. Since the retreating blade can now support net lift, the longitudinal cyclic per collective for trim moves away from -1 deg/deg to more negative values.

$$\frac{\partial \theta_{1s}}{\partial \theta_0} = \frac{\left(\frac{1}{3}\mu + \frac{4}{45\pi}\mu^4\right)}{\left(-\frac{1}{8} - \frac{3}{16}\mu^2 + \frac{5}{192}\mu^4\right)} \tag{8.1}$$

Lateral cyclic is typically required in forward flight due to non-uniform inflow

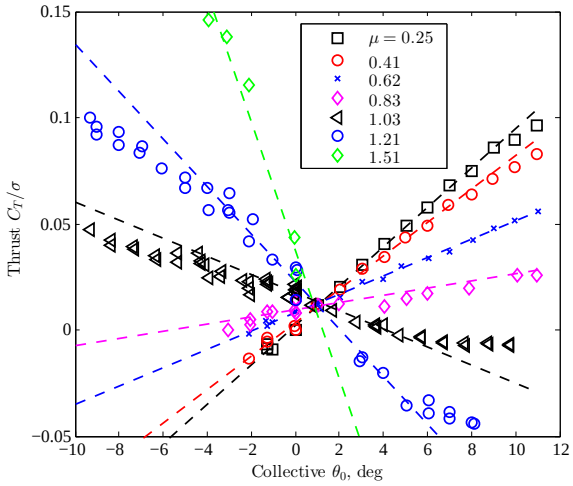

(a) Thrust (trimmed)

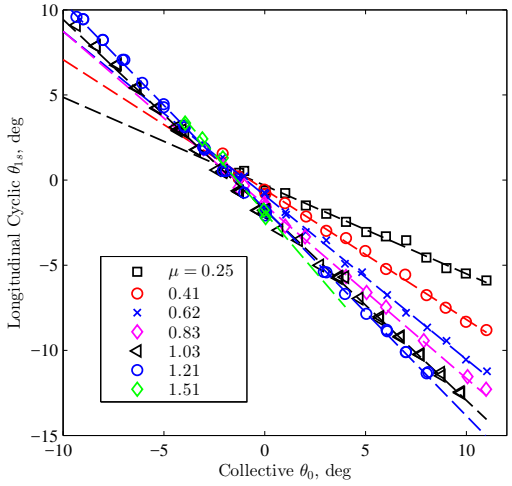

(b) Longitudinal cyclic

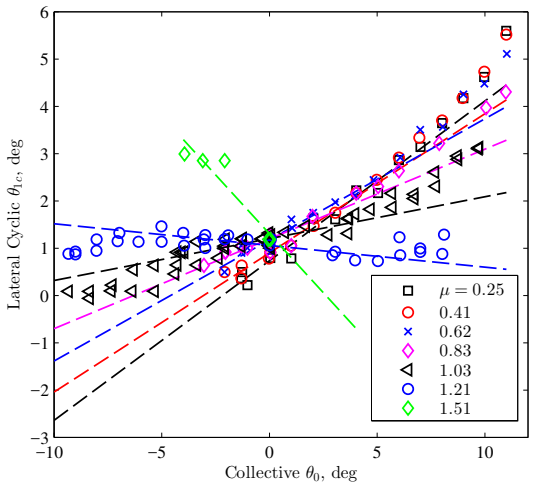

(c) Lateral cyclic

Figure 8.1: Cyclic swashplate control angles required to trim rotor at a given collective pitch angle with linear fit lines.

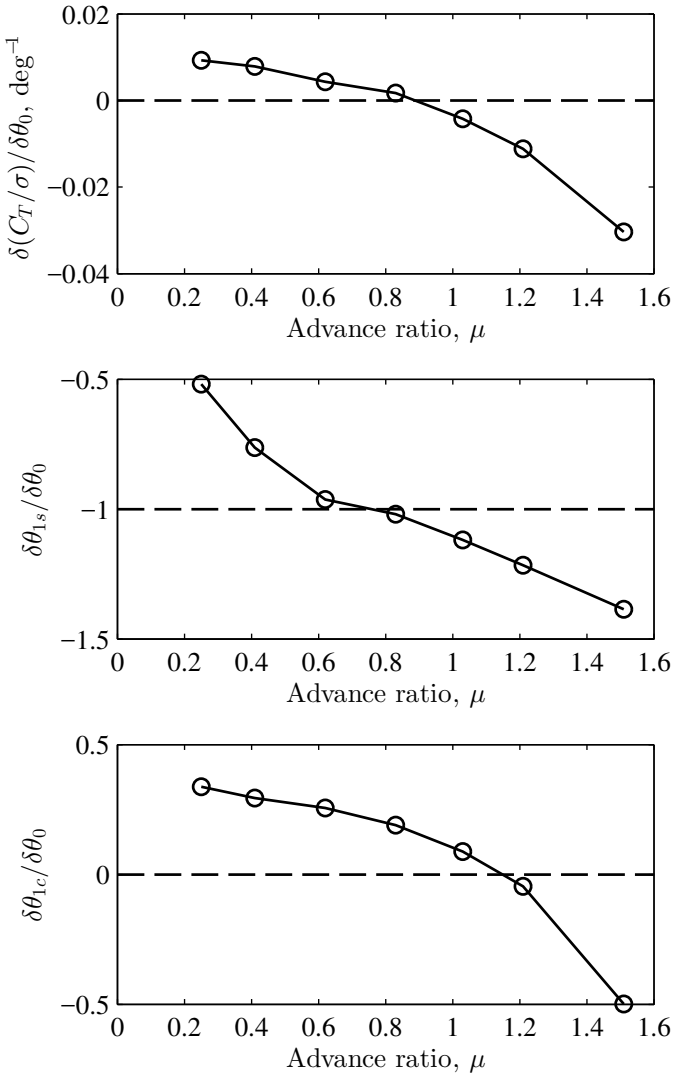

Figure 8.2: Sensitivities of thrust, longitudinal cylic, and lateral cyclic to collective pitch changes, as advance ratio increases.

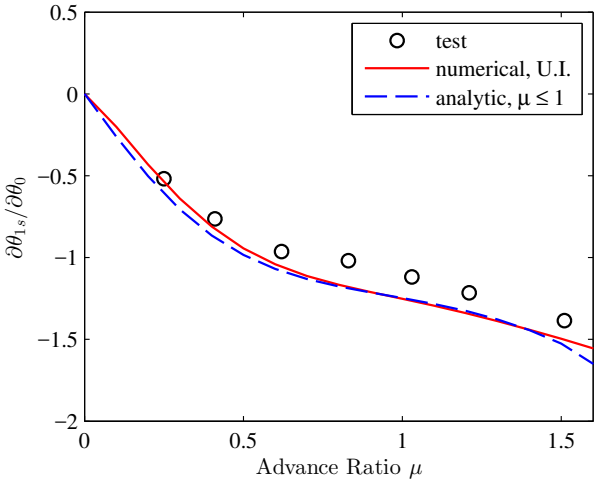

(a) Longitudinal cyclic per collective

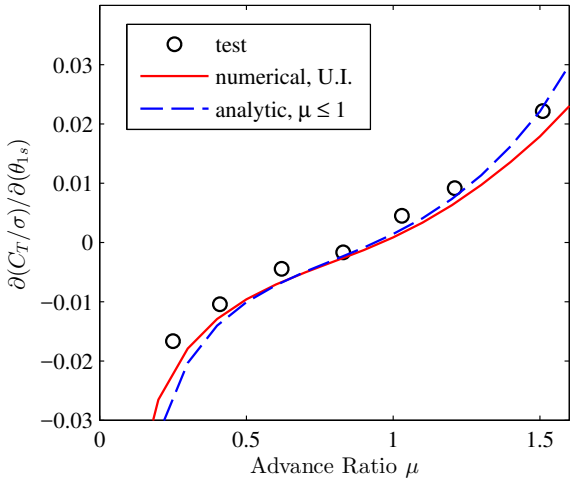

(b) Thrust per longitudinal cyclic

Figure 8.3: Trimmed longitudinal cyclic sensitivities to collective and thrust with correlations to simple numerical and analytical rotor models.

velocity distributions and other wake interactions as well as blade coning. The analytical formulation ignores these effects, so lateral cyclic is not included at all. From inspection of the trends in figs. 8.1(c) and 8.2, positive lateral cyclic is needed to trim out collective increases up until near μ = 1.15. This positive θ_{1c} cyclic indicates the front of the disk was carrying more thrust than the rear. The sign change coincides roughly with the collective-thrust reversal (albeit at the higher μ of 1.15), as thrust affects both coning/flapping angles and induced inflow velocities.

8.2 Blade Flapping

Flapping angle time histories were recorded using hall-effect sensors on the flapping hinge for all four blades. The time histories were converted to the frequency domain, and the 1P component of cyclic flapping was analyzed to determine whether the trim target was met within tolerance. Blade-to-blade differences in inertia, shape, and root pitch can lead to dissimilar flapping angles. Tracking of the rotor (see section 4.2) was conducted to minimize these differences through root pitch adjustments. At increasing advance ratio, the differences in 1P flapping between the four blades increased. An example of the increase in the out-of-track condition as advance ratio increases is shown in fig. 8.4(a). The rotor was trimmed to zero flapping by using the flap angle signal for blade 1 (black circles). The effect of this is that the rotor can have several trim states, determined by which blade's flapping response is used to target zero β_{1c} and β_{1s}. The trim target was set to Blade 1 when pressure measurements were of interest (since Blade 1 contained the surface

pressure sensors), and the trim target was set to an average of all four blades when performance metrics were of interest.

The traditional swashplate on the test stand is only capable of steady and 1P inputs, therefore the rotor could still have non-zero flapping amplitude due to higher harmonic content (2P and higher). As the advance ratio increases, it was observed that the 2/rev flapping amplitude increases (fig. 8.4(b)). Plotting the harmonic spectrum for a limited selection of advance ratios shows that for the trimmed rotor the 2P dominates, but 3P and 4P are present as well (fig. 8.4(c)). Higher harmonic flapping (2P and above) has origins in the increasingly non-uniform inflow velocity distribution [55].

8.3 Rotor Lift

Measured rotor lift for collective sweeps at each advance ratio is shown in fig. 8.5. All cases are shown that meet a specified trim target threshold of minimum 1P flapping angle. The threshold was generally relaxed with increasing advance ratio as the rotor tracking and flapping sensitivity increased.

The collective-thrust reversal trend is evident and was discussed in the chapter dedicated to that topic (chapter 6). The decrease in collective-lift slope with advance ratio is evident. The aft shaft tilt case (fig. 8.5(i)) shows increased lift over the same advance ratio with no shaft tilt (fig. 8.5(f)). Recall that rotor lift is defined as $L = T\cos\alpha_s - H\sin\alpha_s$, which reduces to $L = T$ for the zero shaft tilt case.

The trends of collective pitch required for a given rotor lift coefficient are given

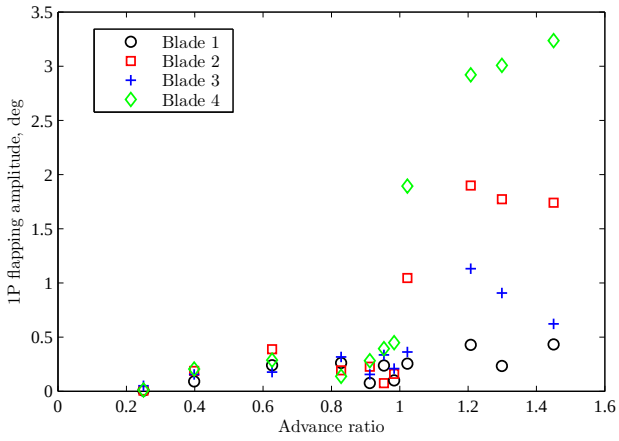

(a) 1P Flapping, Trimmed to Blade 1

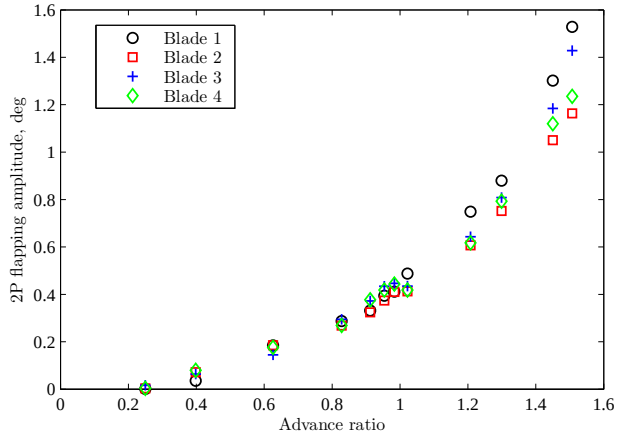

(b) 2P Flapping

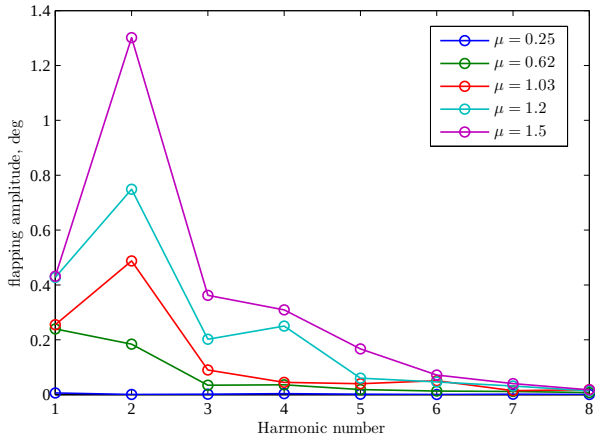

(c) 1P–8P Flapping, Blade 1

Figure 8.4: Blade flapping harmonic amplitudes for varying advance ratio.

in fig. 8.6, along with predictions from the blade element analysis discussed in section 6.3, assuming uniform inflow. Starting from hover ($\mu = 0$), collective pitch initially decreases as the increased mass flow in forward flight reduces the induced inflow velocity. The pitch then begins to increase as the reverse-flow region grows and the collective-lift sensitivity reduces. There is a singularity at the critical advance ratio, μ_{crit}, where rotor lift cannot be controlled with collective (when trimmed to zero flapping or moment). This is the point of the collective-lift reversal where the slope changes sign.

After the singularity at the critical advance ratio, the trim collective pitch angle switches sign, and then reduces in magnitude as the advance ratio increases further. At higher advance ratios, the rotor is capable of high lift coefficients at low collective pitch angles. Collective control of lift is therefore only ineffective within a band of advance ratios of around 0.7 to 1.2, depending on the rotor-specific critical advance ratio. This result is in agreement with analysis predictions made by Ormiston [26–28].

It is noteworthy that for several advance ratio sweeps, the zero lift point does not correspond to zero collective pitch. This does not match the expectation, or analysis (see Bowen-Davies and Chopra [24]), for a rotor disk with no angle of attack. Possible causes are error in the control angle calibration, a systematic tare error, or aerodynamic interaction from the test stand.

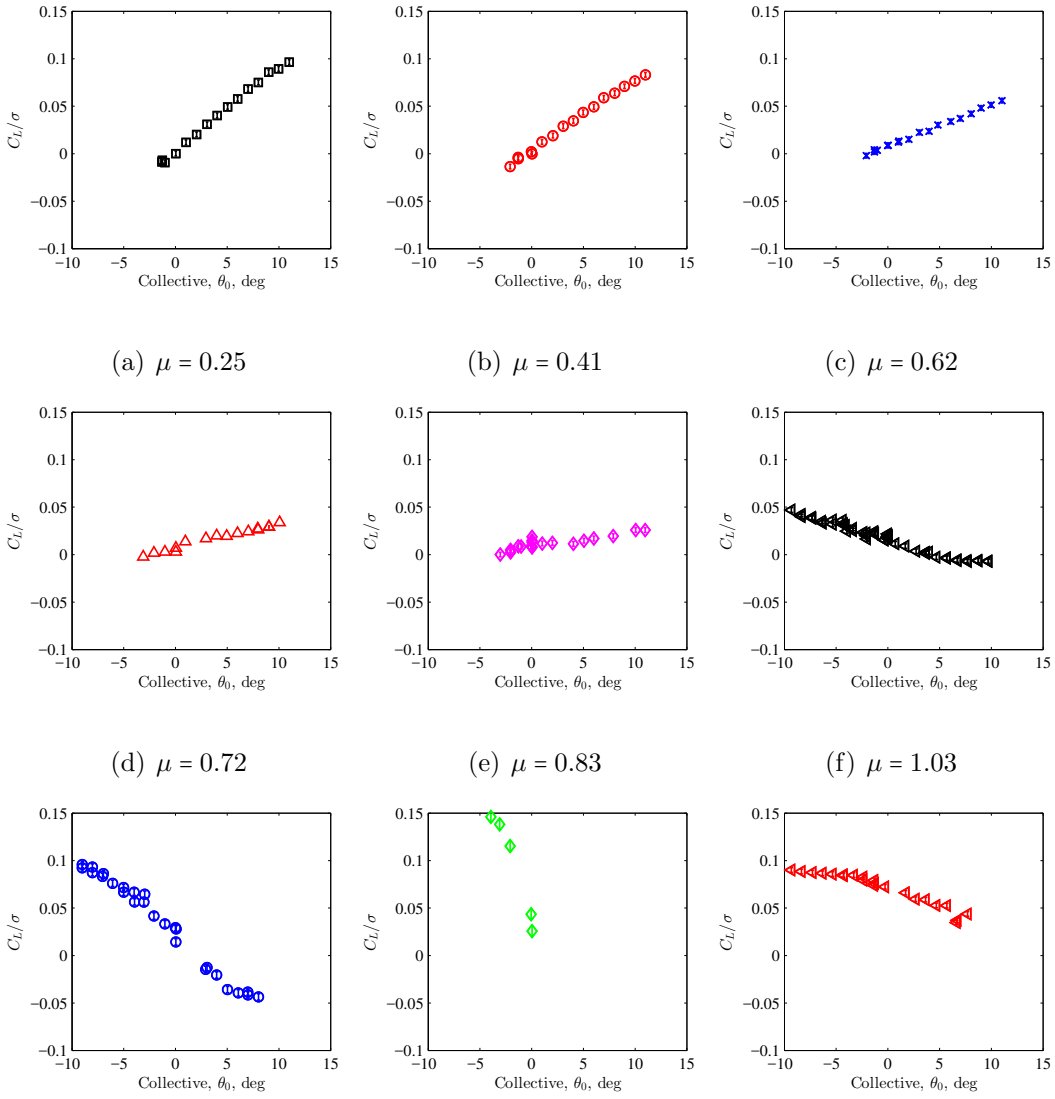

(a) $\mu = 0.25$ (b) $\mu = 0.41$ (c) $\mu = 0.62$

(d) $\mu = 0.72$ (e) $\mu = 0.83$ (f) $\mu = 1.03$

(g) $\mu = 1.21$ (h) $\mu = 1.51$ (i) $\mu = 1.03$, $\alpha_s = 4°$

Figure 8.5: Rotor lift coefficient for collective sweeps at each advance ratio. Shaft tilt $\alpha_s = 0°$ except where noted. Error bars denote 2σ uncertainty estimate based on hub load cell calibration.

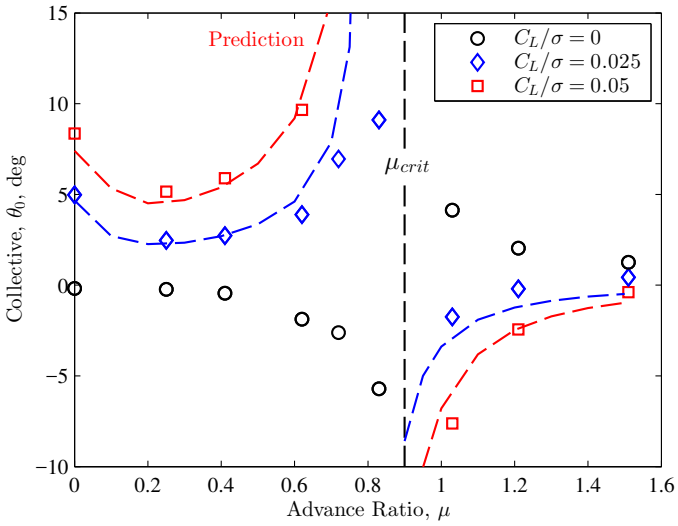

Figure 8.6: Collective pitch angle versus advance ratio for constant rotor lift coefficient. Shaft tilt $\alpha_s = 0°$. Prediction shown with dotted lines.

8.4 Rotor Drag

Rotor drag force is the wind-axis longitudinal force, defined as $D = T \sin \alpha_s + H \cos \alpha_s$, which reduces to $D = H$ for zero shaft tilt. Measured rotor drag for collective sweeps at each advance ratio are shown in fig. 8.7. The drag force measurements have more scatter compared to the rotor lift measurements. The uncertainty bars on the drag coefficients are much larger as well, indicative of the low dimensional drag forces on the blades after subtracting the hub tare. The rotor is operating at reduced RPM, and hence the in-plane forces are quite low. The exception is the sweep at $\mu = 0.72$ (fig. 8.7(d)), which shows tighter trends and a smaller error bar. This condition was met at a higher RPM (1000 versus 700 or less) than the other runs, increasing the dimensional rotor drag.

Rotor drag plotted with rotor lift is shown in fig. 8.8. In some cases, particularly $\mu = 1.21$, the scatter is reduced compared to the drag-collective plots. This may indicate some hysteresis in the control angle measurements, although other sweeps are not significantly improved.

The drag levels are lower than expected, particularly at low collective or low rotor lift. In certain cases the measured drag is negative. This is possible for a lifting rotor, due to an increase in induced drag on the retreating blade relative to the advancing blade, resulting in a net forward in-plane force [26]. However, the results here are still generally lower than analysis predicts [89], with the caveat of the large error bands understood.

In general, rotor drag for a given lift sharply increase above $\mu = 0.62$, but then reduces at $\mu = 1.21$ and higher. This is consistent with the lift behavior observed in the previous section.

8.5 Rotor Power

Rotor power as measured by shaft torque and rotor speed is given in figs. 8.9 and 8.10 as a function of collective pitch and rotor lift coefficient, respectively. The tight bands with collective and low uncertainty bands indicate a precise measurement.

Noteworthy trends with advance ratio are best analyzed at a constant rotor lift, given in fig. 8.11. These data points were interpolated from polynomial fits of the data in fig. 8.10. At $C_L/\sigma = 0$, the power is relatively flat with advance ratio,

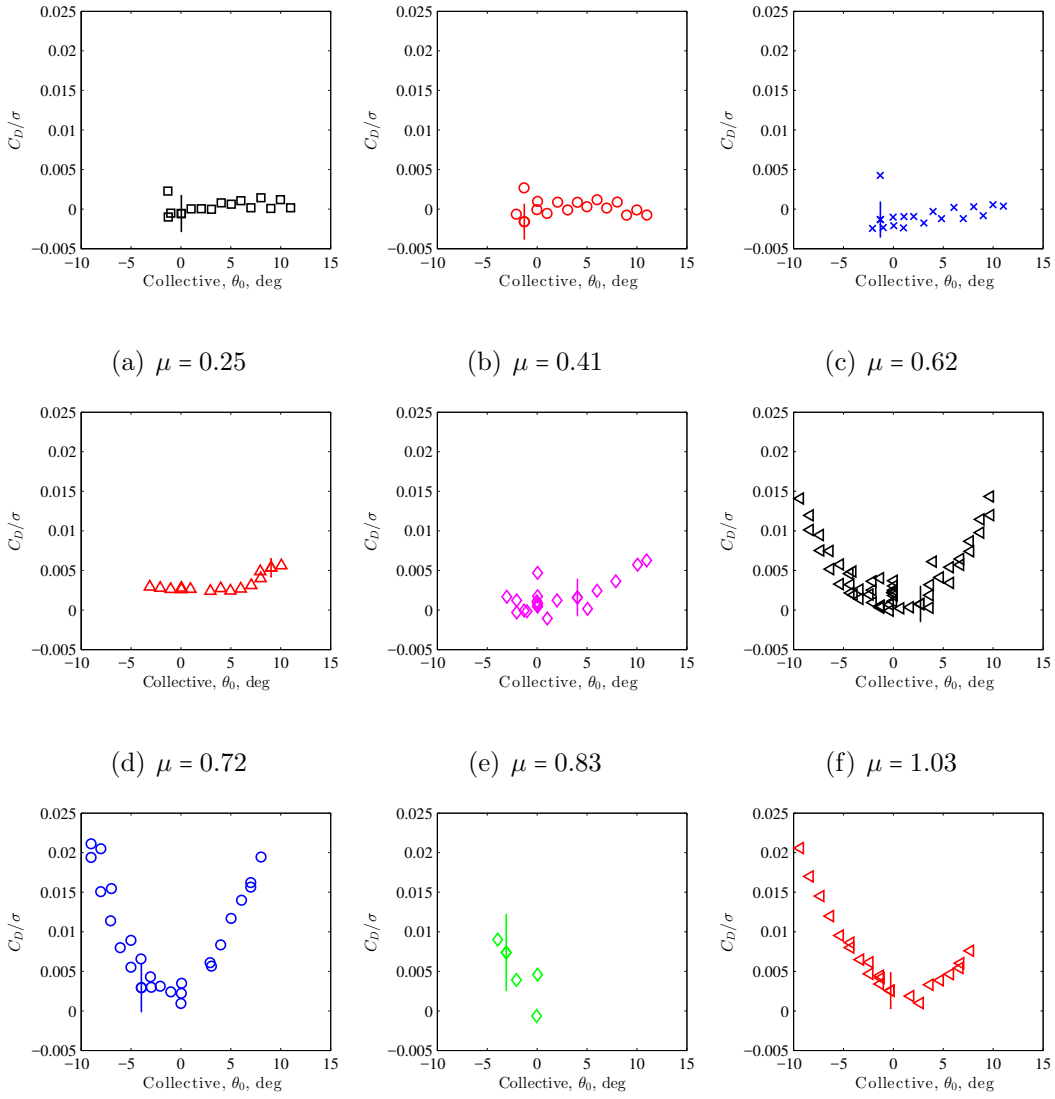

(a) $\mu = 0.25$ (b) $\mu = 0.41$ (c) $\mu = 0.62$

(d) $\mu = 0.72$ (e) $\mu = 0.83$ (f) $\mu = 1.03$

(g) $\mu = 1.21$ (h) $\mu = 1.51$ (i) $\mu = 1.03$, $\alpha_s = 4°$

Figure 8.7: Rotor drag coefficient for collective sweeps at each advance ratio. Shaft tilt $\alpha_s = 0°$ except where noted. Error bars denote 2σ uncertainty estimate based on hub load cell calibration.

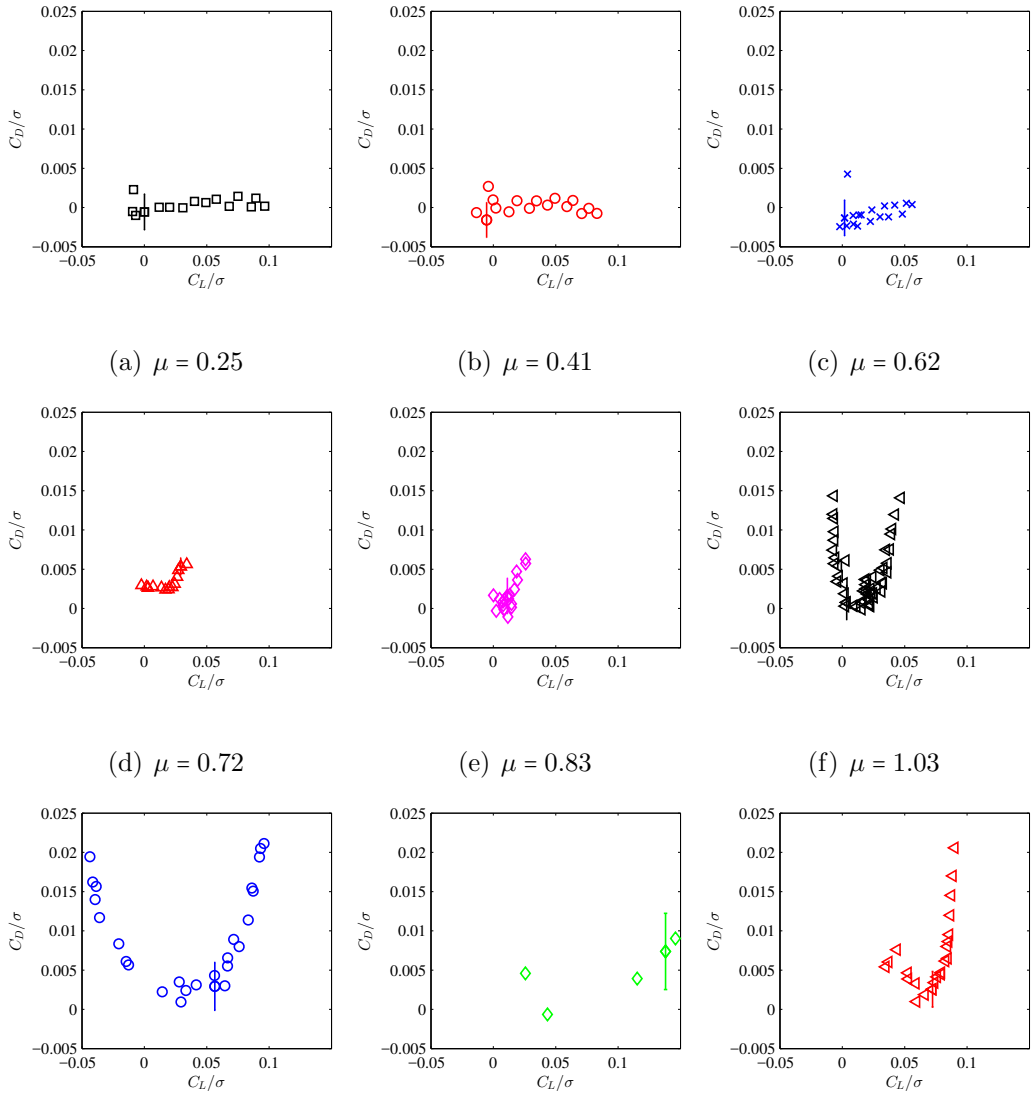

(a) $\mu = 0.25$ (b) $\mu = 0.41$ (c) $\mu = 0.62$

(d) $\mu = 0.72$ (e) $\mu = 0.83$ (f) $\mu = 1.03$

(g) $\mu = 1.21$ (h) $\mu = 1.51$ (i) $\mu = 1.03$, $\alpha_s = 4°$

Figure 8.8: Rotor drag coefficient versus rotor lift coefficient at each advance ratio. Shaft tilt $\alpha_s = 0°$ except where noted. Error bars denote 2σ uncertainty estimate based on hub load cell calibration.

and is a measure of the rotational profile power, $C_{Q,0}$ (the μC_H term). For the higher advance ratio cases, figs. 8.10(f) and 8.10(g), the "minimum" power trough is not at zero lift, although it does appear to be minimum at zero collective pitch. Correlation of comprehensive analysis with this data set by Bowen-Davies [24, 89] showed minimum power and zero lift occurring at zero collective (with zero shaft tilt) at all advance ratios.

For positive rotor lift coefficients, C_L/σ = 0.025 and C_L/σ = 0.05, the rotor power decreases initially with advance ratio, signaling the expected reduction in induced power that accompanies a rotor in forward flight. As the advance ratio increases further, the rotor power increases sharply, reaching a singularity again around the critical advance ratio, μ_{crit} = 0.9. The rotor, when trimmed, is not capable of non-zero lift at μ_{crit} when using collective for control. With an aft shaft tilt, as in fig. 8.10(i), the rotor does not encounter the same singularity, and is capable of positive lift at μ_{crit}. Ormiston [27, 28] has described these differences in collective mode versus angle of attack mode at high advance ratio through numerical studies.

After the critical advance ratio, the lifting rotor has negative shaft power, indicating the relative wind is driving the rotation of the rotor blades. This is evident in the C_L/σ = 0.05 data especially, but negative shaft power also occurs at both positive and negative rotor lifts at high advance ratio figs. 8.10(f) and 8.10(g).

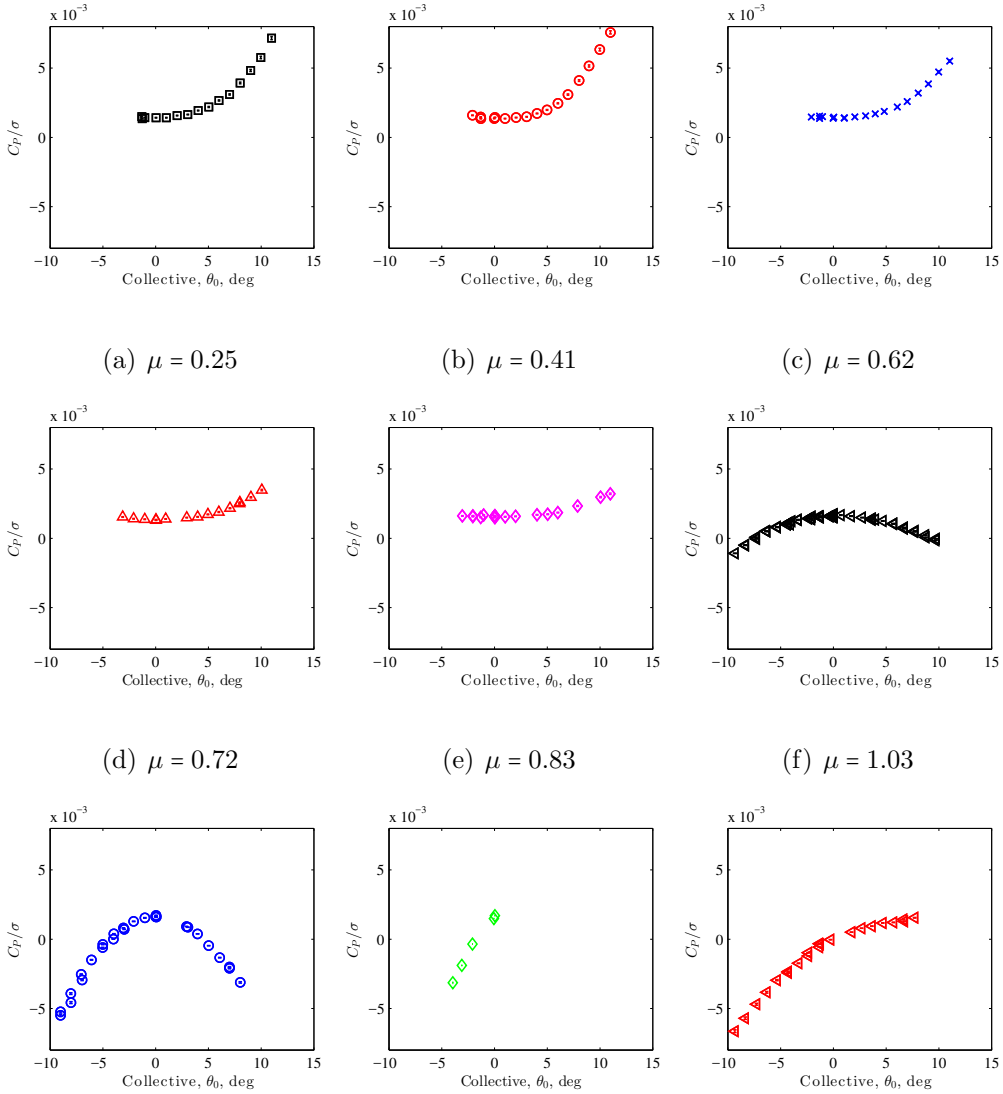

(a) $\mu = 0.25$ (b) $\mu = 0.41$ (c) $\mu = 0.62$

(d) $\mu = 0.72$ (e) $\mu = 0.83$ (f) $\mu = 1.03$

(g) $\mu = 1.21$ (h) $\mu = 1.51$ (i) $\mu = 1.03$, $\alpha_s = 4°$

Figure 8.9: Rotor shaft power coefficient for collective sweeps at each advance ratio. Shaft tilt $\alpha_s = 0°$ except where noted.

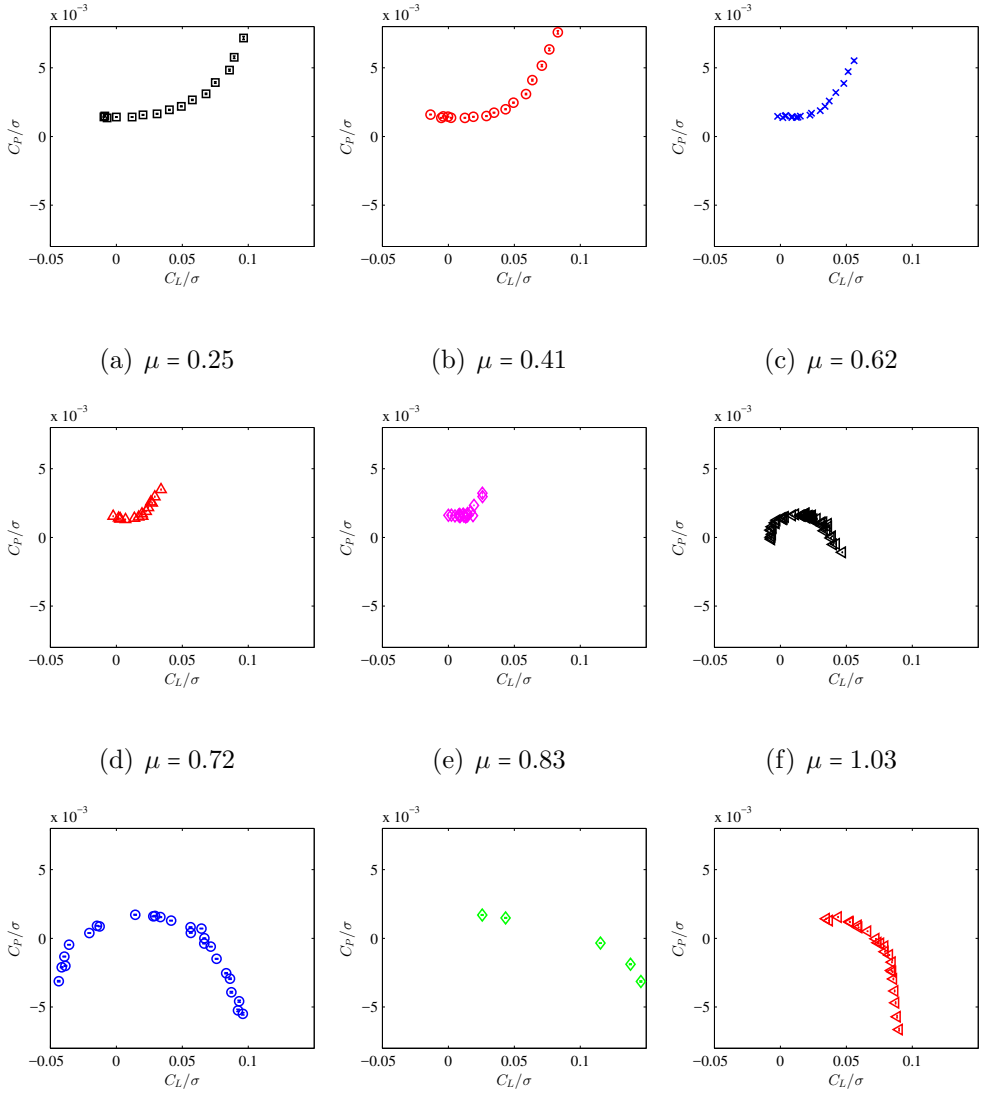

(a) $\mu = 0.25$ (b) $\mu = 0.41$ (c) $\mu = 0.62$

(d) $\mu = 0.72$ (e) $\mu = 0.83$ (f) $\mu = 1.03$

(g) $\mu = 1.21$ (h) $\mu = 1.51$ (i) $\mu = 1.03$, $\alpha_s = 4°$

Figure 8.10: Rotor shaft power coefficient versus rotor lift coefficient at each advance ratio. Shaft tilt $\alpha_s = 0°$ except where noted.

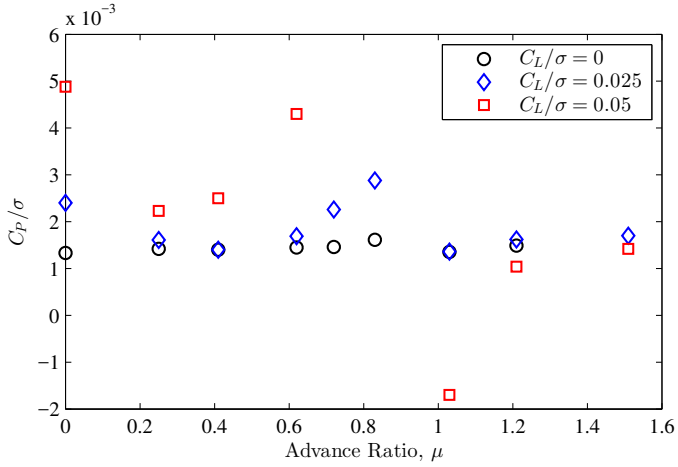

Figure 8.11: Rotor shaft power coefficient versus advance ratio for constant rotor lift coefficient. Shaft tilt $\alpha_s = 0°$ for all cases.

8.6 Lift-to-Drag Ratio

The shaft power and wind-axis drag of a rotor in forward flight can be combined into an equivalent drag metric (eq. 8.2 and 8.3) [55]. The rotor lift-to-drag ratio from the wind tunnel measurements can then be calculated using eq. 8.4. Here the rotor drag D is equal in magnitude and sign to the wind-axis force, X.

The equivalent drag versus lift (fig. 8.12) shows similar trends to power at low advance ratio, and drag at high advance ratio, depending which dominates. The uncertainty is high and is driven by the drag estimate. This uncertainty carries over into the lift-to-drag ratio (figs. 8.13 and 8.14), where especially at low equivalent drag conditions, there is high uncertainty. The points where uncertainty is larger than ±2 in L/D_E have been grayed out. The uncertainty and scatter makes it difficult to clearly plot trends in L/D_E with advance ratio from this data set. The

exception is again $\mu = 0.72$ (fig. 8.14(d)), which had reduced uncertainty due to the higher operating RPM and higher dimensional drag.

Despite the error bands, it can be concluded that at a high advance ratio, for example $\mu = 1.21$, fig. 8.14(g), the rotor is capable of efficient lift. The lift-to-drag ratios are on par with the lower advance ratios and better than the advance ratios in the critical range. As shown earlier, near the critical advance ratio, the edgewise rotor loses the ability to carry a net thrust when trimmed using collective and cyclic. This is similar to the trends shown in prior analysis by Ormiston [26].

$$D_e = \frac{P}{V} + D \tag{8.2}$$

$$C_{D_e} = \frac{C_P}{\mu} + C_D \tag{8.3}$$

$$\frac{L}{D_E} = \frac{L}{P/V + D} = \frac{C_L}{C_P/\mu + C_D} \tag{8.4}$$

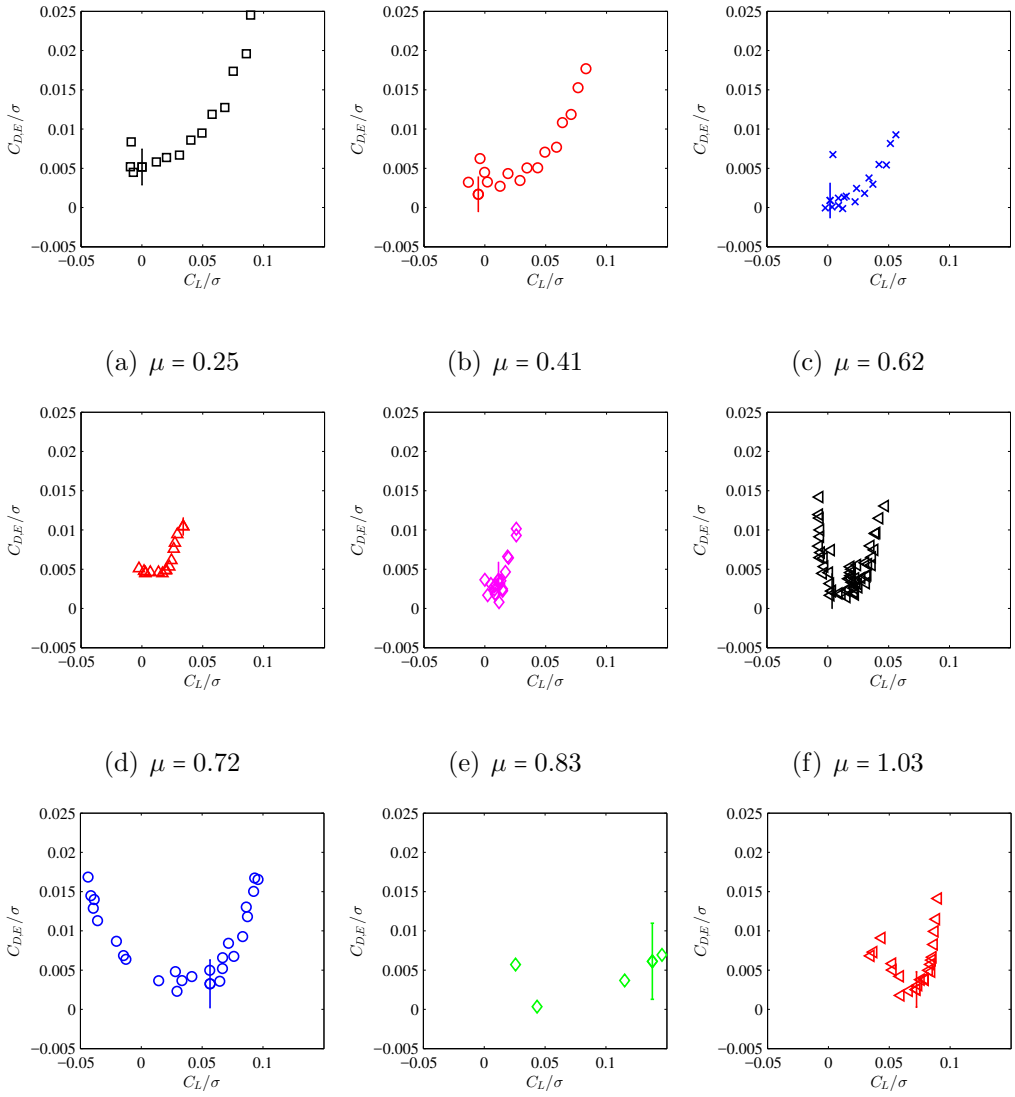

(a) $\mu = 0.25$ (b) $\mu = 0.41$ (c) $\mu = 0.62$

(d) $\mu = 0.72$ (e) $\mu = 0.83$ (f) $\mu = 1.03$

(g) $\mu = 1.21$ (h) $\mu = 1.51$ (i) $\mu = 1.03$, $\alpha_s = 4°$

Figure 8.12: Rotor effective drag coefficient versus rotor lift coefficient at each advance ratio. Shaft tilt $\alpha_s = 0°$ except where noted. Error bars denote 2σ uncertainty estimate based on hub load cell calibration.

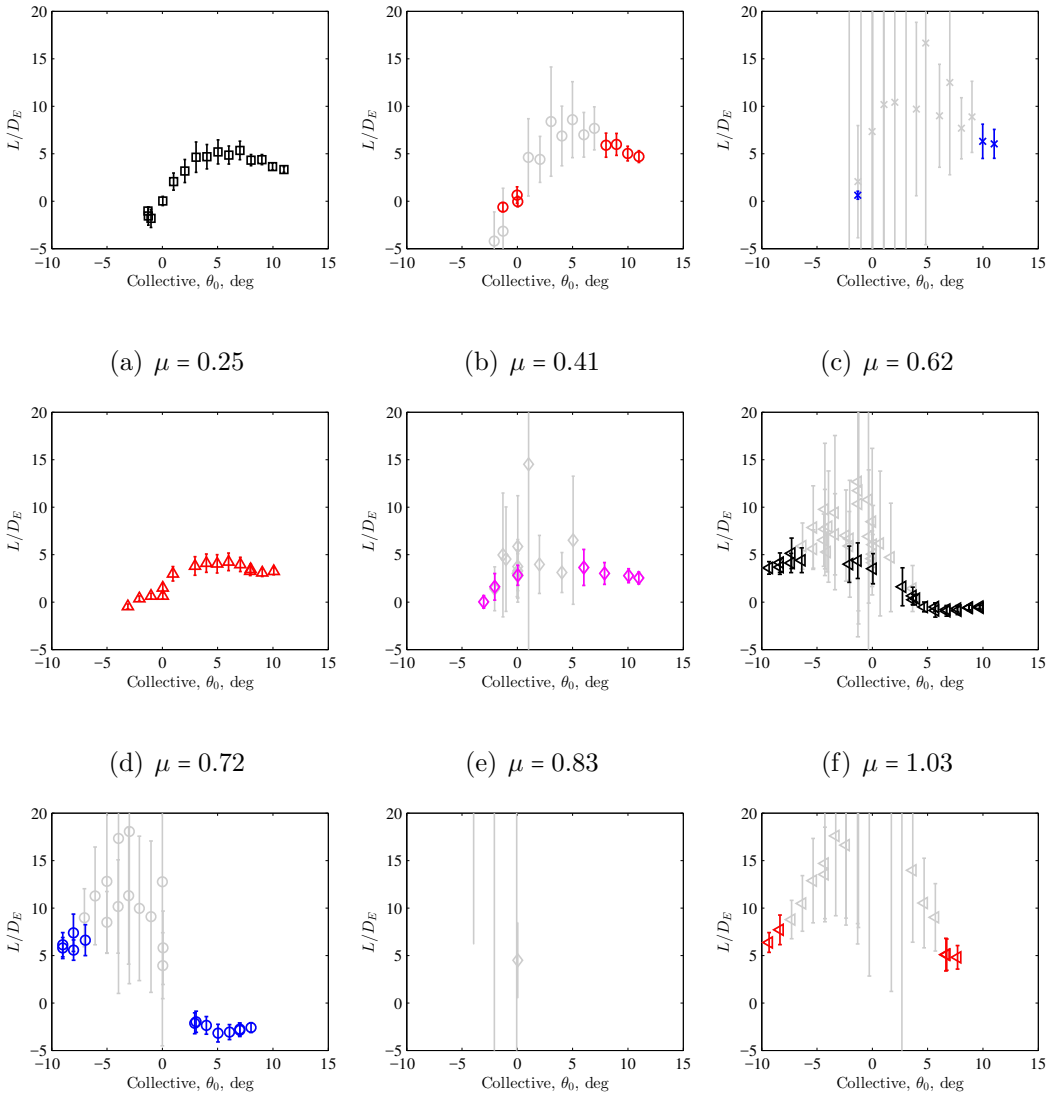

(a) $\mu = 0.25$ (b) $\mu = 0.41$ (c) $\mu = 0.62$

(d) $\mu = 0.72$ (e) $\mu = 0.83$ (f) $\mu = 1.03$

(g) $\mu = 1.21$ (h) $\mu = 1.51$ (i) $\mu = 1.03$, $\alpha_s = 4°$

Figure 8.13: Rotor lift-to-effective drag ratio for collective sweeps at each advance ratio. Shaft tilt $\alpha_s = 0°$ except where noted. Grayed out data indicates uncertainty in L/D_E ratio higher than ±2.

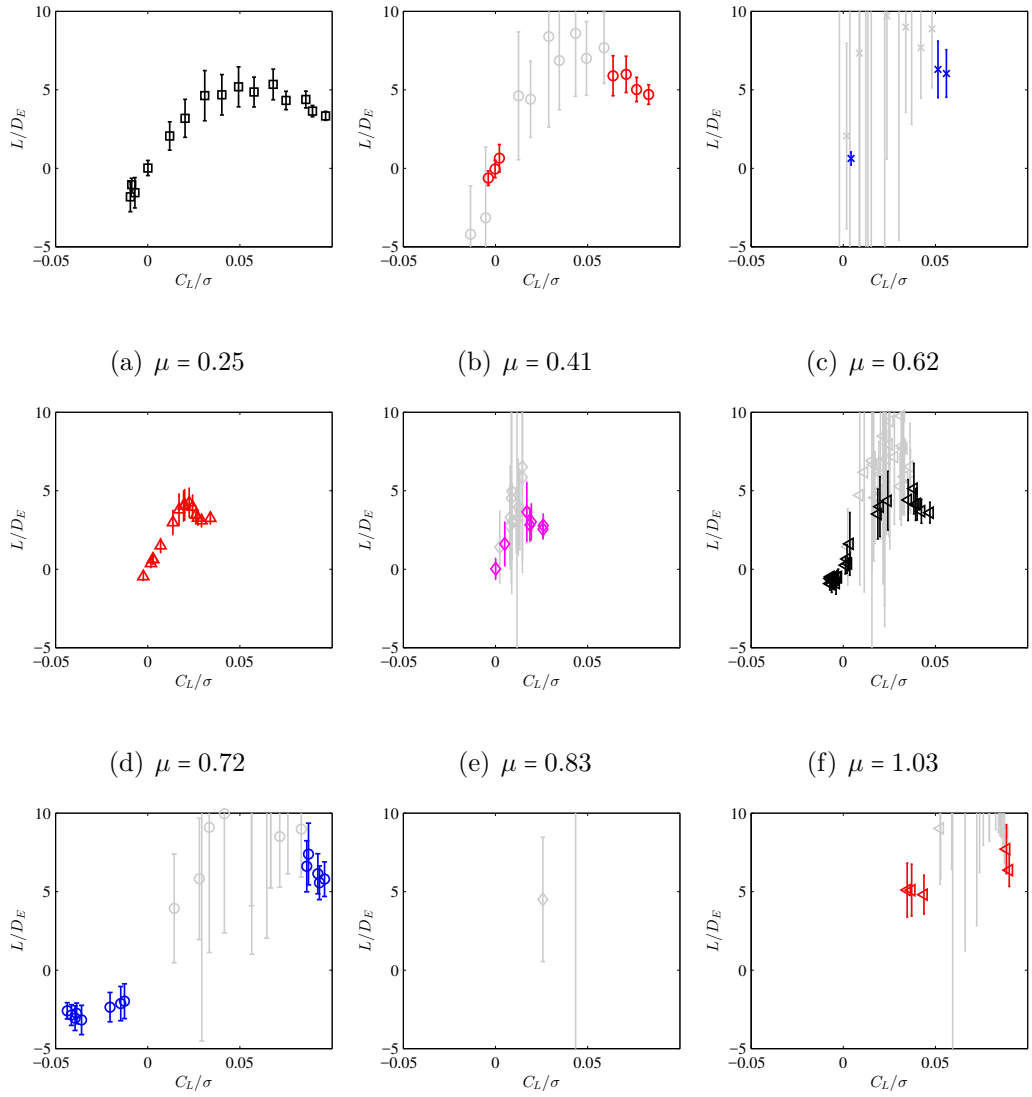

(a) $\mu = 0.25$ (b) $\mu = 0.41$ (c) $\mu = 0.62$

(d) $\mu = 0.72$ (e) $\mu = 0.83$ (f) $\mu = 1.03$

(g) $\mu = 1.21$ (h) $\mu = 1.51$ (i) $\mu = 1.03$, $\alpha_s = 4°$

Figure 8.14: Rotor lift-to-drag ratio versus rotor lift coefficient at each advance ratio. Shaft tilt $\alpha_s = 0°$ except where noted. Grayed out data indicates uncertainty in L/D_E ratio higher than ±2.

Chapter 9: Vibratory Loads

Vibrations in the non-rotating frame (e.g., the fuselage in a helicopter) are expected to be dominated by the harmonics which are integer multiples of the blade passage frequency, or pN_b/rev harmonics, where p is an integer. The loads that contribute to these vibrations are called *vibratory loads*, while the other harmonics are referred to as *oscillatory loads* [54]. For a 4-bladed rotor, the vibratory loads occur at 3/rev and higher, while the oscillatory loads are 1/rev and higher. Measurements of the vibratory loads of the hub and the oscillatory loads of the pitch link and blade structure at high advance ratio will be reported in this chapter.

9.1 Hub Loads

The experimental hub loads data confirms the expected trend across all advance ratios, with the 4/rev harmonic dominating, followed by the 8/rev (fig. 9.1). There is a moderate 1/rev component for some of the higher advance ratios, which can be typically attributed to an imbalance. The in-plane shear does not show a similar 1/rev component, which means the source is likely an aerodynamic imbalance rather than a mass imbalance.

The 4/rev (4P) harmonic amplitudes of hub vertical shear and H-force will be

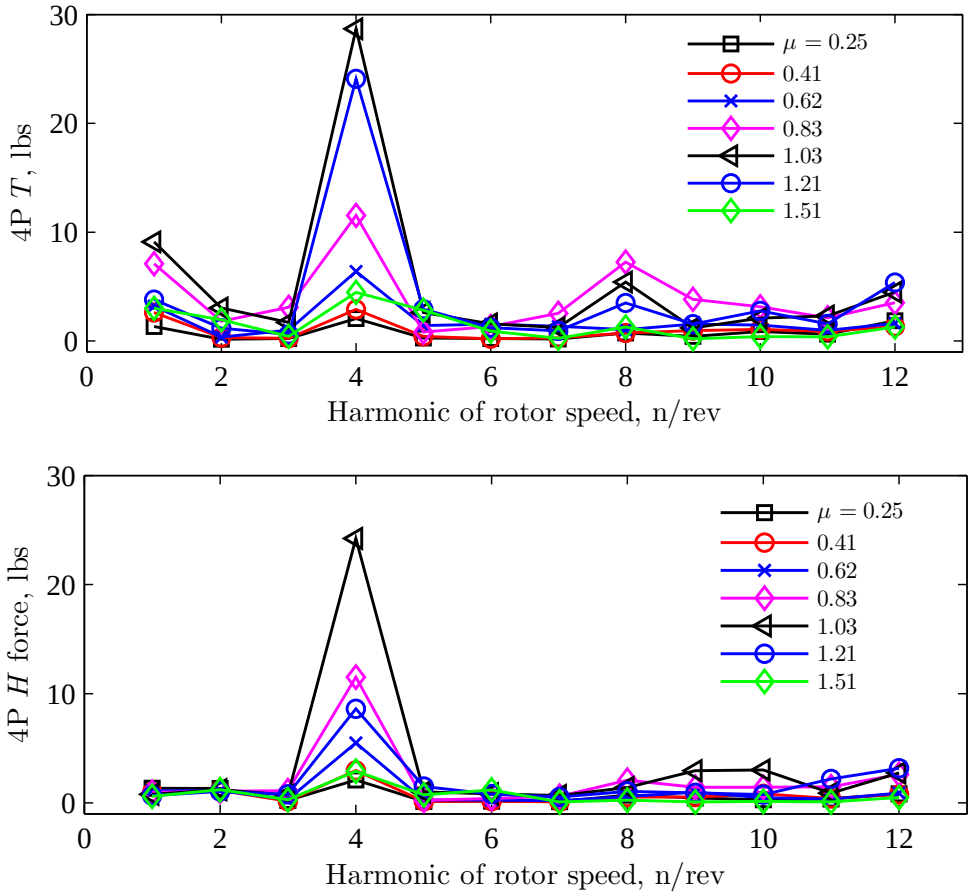

Figure 9.1: Oscillatory hub load harmonic amplitude for vertical out-of-plane shear ($T = F_z$) and longitudinal in-plane shear ($H = F_x$). The envelope of maximum harmonic amplitude among all test cases is shown for each advance ratio. Amplitudes here are without dynamic calibration correction.

discussed since they were the dominant shear directions measured. Side force, roll moment, and pitch moment vibrations were minimal in comparison (see Appendix B for the full set of 4/rev hub load results).

Vertical shear and in-plane shear amplitude have clear correlation with the trim collective pitch (figs. 9.2 and 9.3). The correlation with mean rotor lift coefficient is less clear, and likely influenced indirectly through the relationship between collective and lift. The amplitude of the 4/rev forces are similar at low collective pitch for all advance ratios. As collective increases, the amplitude increases rapidly for the high advance ratio cases, similarly to the pitch link loads. When plotting against rotor lift (fig. 9.2, right), it is clear that the 1.21 advance ratio case shows a decrease in amplitude for similar thrust levels compared to the 1.03 advance ratio cases. This reflects the improved thrust generation capability of the retreating blade at lower pitch angles (due to increased mean retreating blade dynamic pressure).

The measurements are arranged as sweeps of advance ratio for fixed collective and fixed rotor lift coefficient (figs. 9.4 and 9.5). The amplitudes rise sharply starting around $\mu = 0.6$. The vibratory loads peak around $\mu = 1$, and in several cases begin to decrease at higher advance ratios. More data would be needed at higher advance ratios to validate this trend.

The trends at fixed rotor lift show more mixed results at each rotor lift, but the overall envelope trend shows a similar peak at $\mu = 1$ and decrease thereafter. The stronger connection to collective pitch is likely driven by the retreating blade reverse-flow stall loads, which can still generate high unsteady loading even if the mean rotor lift is low. It should be noted that the 4P vertical force peak measurement at

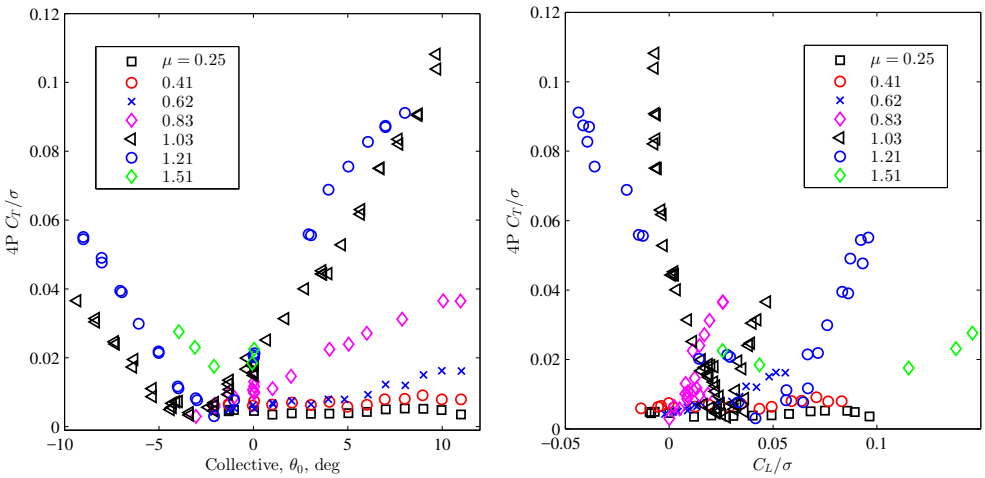

Figure 9.2: 4/rev hub vertical force coefficient amplitude for all advance ratio collective sweeps. Plotted versus collective and lift coefficient. Shaft tilt $\alpha_s = 0°$.

$\mu = 1.2$ for the $\theta_0 = 8°$ sweep (fig. 9.2(a)) is a lower dimensional vertical force than at $\mu = 1.0$. The coefficient form ends up larger due to the decreasing RPM for points at $\mu > 1.03$. The trend of decreasing vibration in the test stand accelerometer readings (see section 9.2) seems to agree well with the conclusion that peak vibrations occur around $\mu = 1$.

Also of note is that the minimum vibratory loads occur at a negative collective pitch of about $-2°$ to $-3°$, and not at $0°$ or at zero rotor lift. Bowen-Davies [24, 89] performed correlation studies on this data set using UMARC, which predicted both zero mean lift and minimum vibratory loads at zero collective pitch. He attributed this offset to a possible hub-wake interaction in the experiment. This was not investigated further but is noted as a curiosity to explore in future testing.

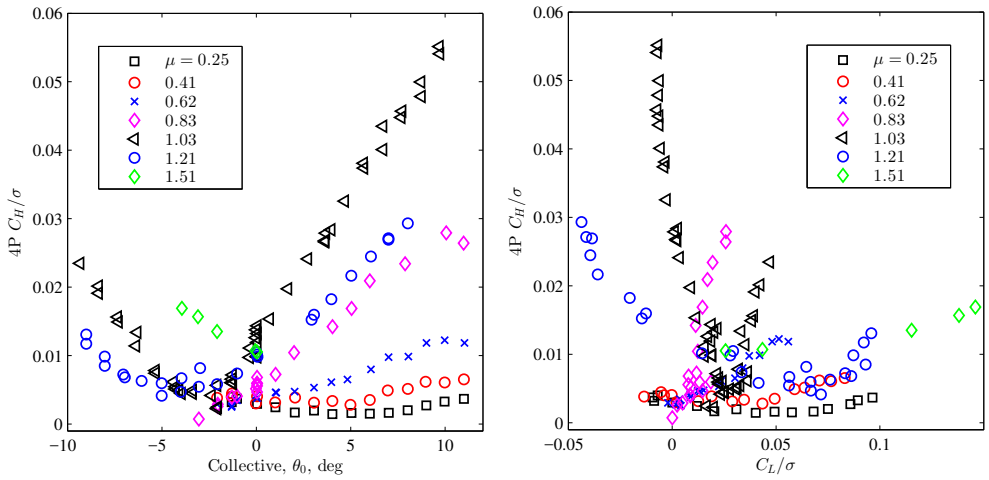

Figure 9.3: 4/rev hub H-force coefficient amplitude for all advance ratio collective sweeps. Plotted versus collective and lift coefficient. Shaft tilt $\alpha_s = 0°$.

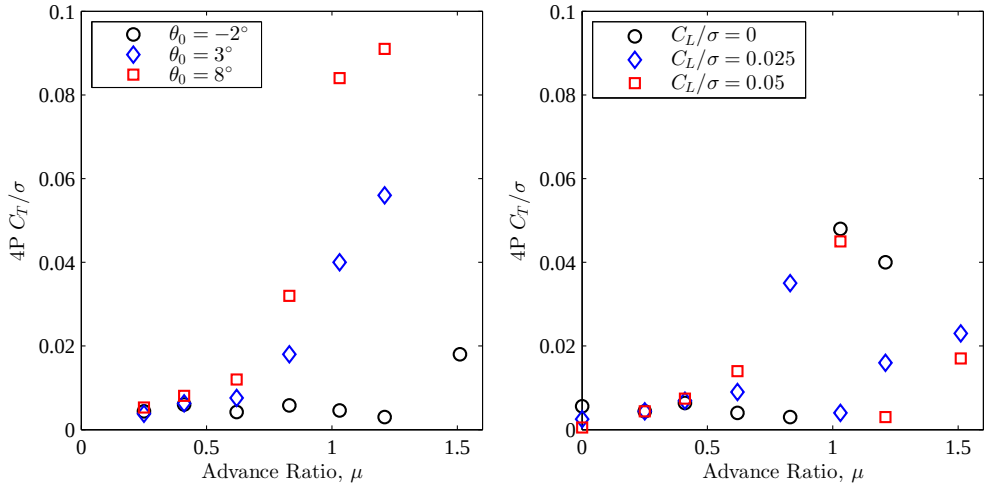

(a) Fixed collective

(b) Fixed lift

Figure 9.4: 4/rev hub vertical force amplitude versus advance ratio for fixed collective and fixed rotor lift coefficient. Shaft tilt $\alpha_s = 0°$.

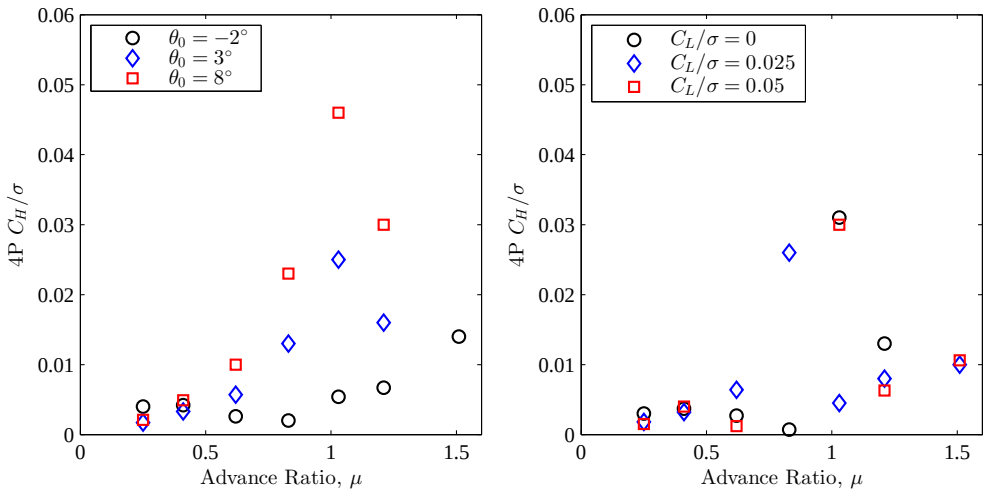

(a) Fixed collective

(b) Fixed lift

Figure 9.5: 4/rev hub H-force amplitude versus advance ratio for fixed collective and fixed rotor lift coefficient. Shaft tilt $\alpha_s = 0°$.

9.2 Test Stand Vibrations

As a check on the hub load 4P amplitude measurements (and the associated dynamic calibration procedure), accelerometer measurements measuring 3-axis accelerations of the test stand were also analyzed. The maximum amplitudes recorded for each harmonic of rotor speed were again plotted to verify that the 4/rev was dominant (fig. 9.6). The vertical acceleration is larger than the in-plane accelerations, as with the hub loads. There is higher harmonic content for the in-plane accelerations for non nN_b/rev harmonics, but the magnitude is small. It is apparent from this plot that the $\mu = 1$ condition experienced the largest accelerations.

The vertical (fig. 9.7) and in-plane (fig. 9.8) vibrations follow similar trends

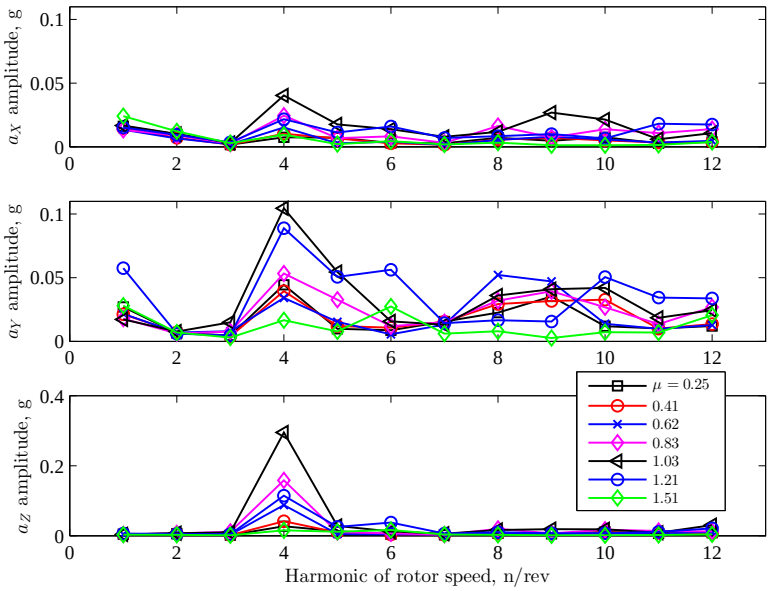

Figure 9.6: Envelope of maximum test stand accelerations in each axis among all test cases for each advance ratio. X is longitudinal/rearward, Y is lateral/side, Z is vertical.

with collective and lift coefficient as with the hub loads. As stated, the main difference is the trend at higher advance ratio. The acceleration measurements show a marked decrease in vibration at advance ratios above 1.0 for both vertical and in-plane directions.

9.3 Blade and Pitch Link Loads

The rotating vacuum mode frequencies of the rotor blade were calculated using UMARC by Bowen-Davies [89], and are presented as a fanplot in fig. 9.9. He also calculated frequency bands assuming a ±10% variation in the blade section stiffnesses from table 3.1. The second flap bending mode is near 4/rev for the main operating

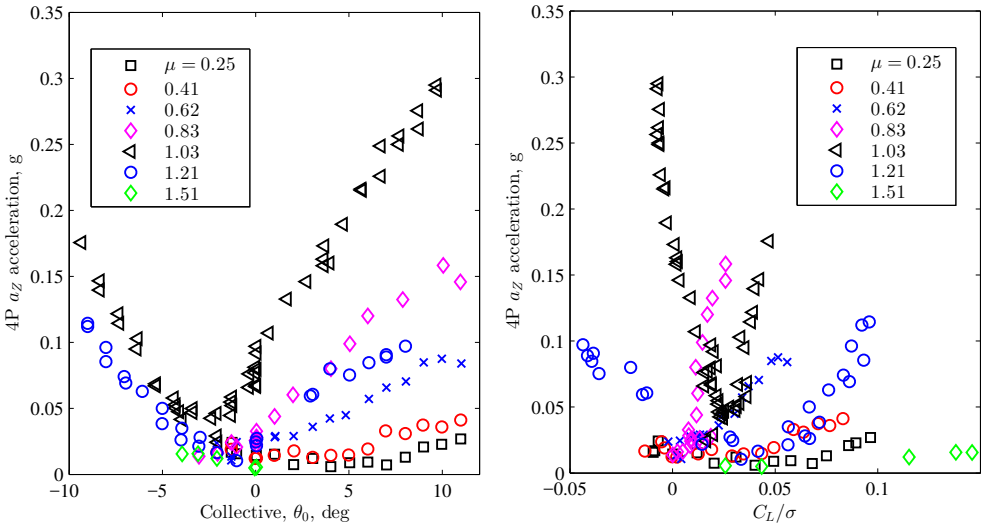

Figure 9.7: Test stand 4/rev vertical acceleration amplitude for all advance ratio collective sweeps. Plotted versus collective and lift coefficient. Shaft tilt $\alpha_s = 0°$.

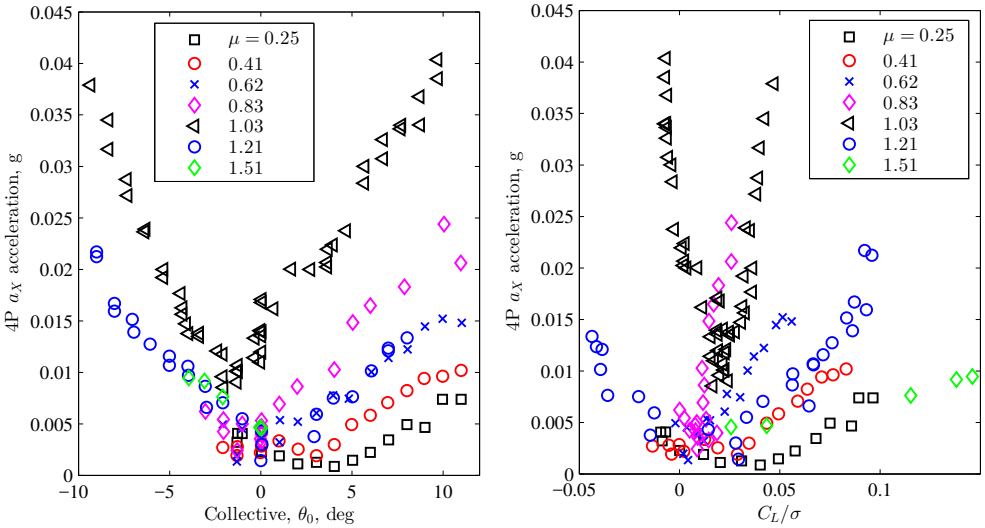

Figure 9.8: Test stand 4/rev rearward in-plane X acceleration amplitude for all advance ratio collective sweeps. Plotted versus collective and lift coefficient. Shaft tilt $\alpha_s = 0°$.

rotor speeds of 700 RPM (μ = 0.25–1.03) and 600 RPM (μ = 1.21). For μ = 1.51, the rotor speed is 480 RPM, or 21% of nominal, which puts the second flap mode closer to 5/rev.

Oscillatory blade loads were extracted from the time-history of the strain gauge data, and converted to frequency domain harmonics. An overview of maximum envelope of the 1–12/rev harmonics of rotor blade flap bending moment and torsion moment at each advance ratio is shown in fig. 9.10. The 4/rev is the dominant harmonic for flap bending moment, due to proximity to the blade second flap bending mode resonance. For the μ = 1.51 condition, the flap bending moment 4/rev is significantly reduced, and the 5/rev is now the largest vibratory load harmonic. This is due to the lower RPM and shift of the second flap bending mode from 4/rev to 5/rev. Due to the changing of advance ratio as well as resonant frequency when going from μ = 1.03 to μ = 1.51, it is difficult to determine the root cause of the reduction in blade (and hub) 4/rev loads.

The blade torsion moments are dominated by the 1/rev harmonic, but the 2/rev and 3/rev is also significant. The first torsion mode is predicted to be above 12/rev in the slowed-rotor configuration, and is not obviously present in this view of the data.

The azimuthal time history of a high advance ratio case for relevant torsion loads is given in fig. 9.11. There is clear agreement between the section aerodynamic pitching moment, blade root torsion moment, and pitch link load. The pitch link loads for Blade 1 and Blade 3 also agree well. The strong nose-down pitching moment is due to reverse-flow and reverse-flow stall as discussed in chapter 7. After

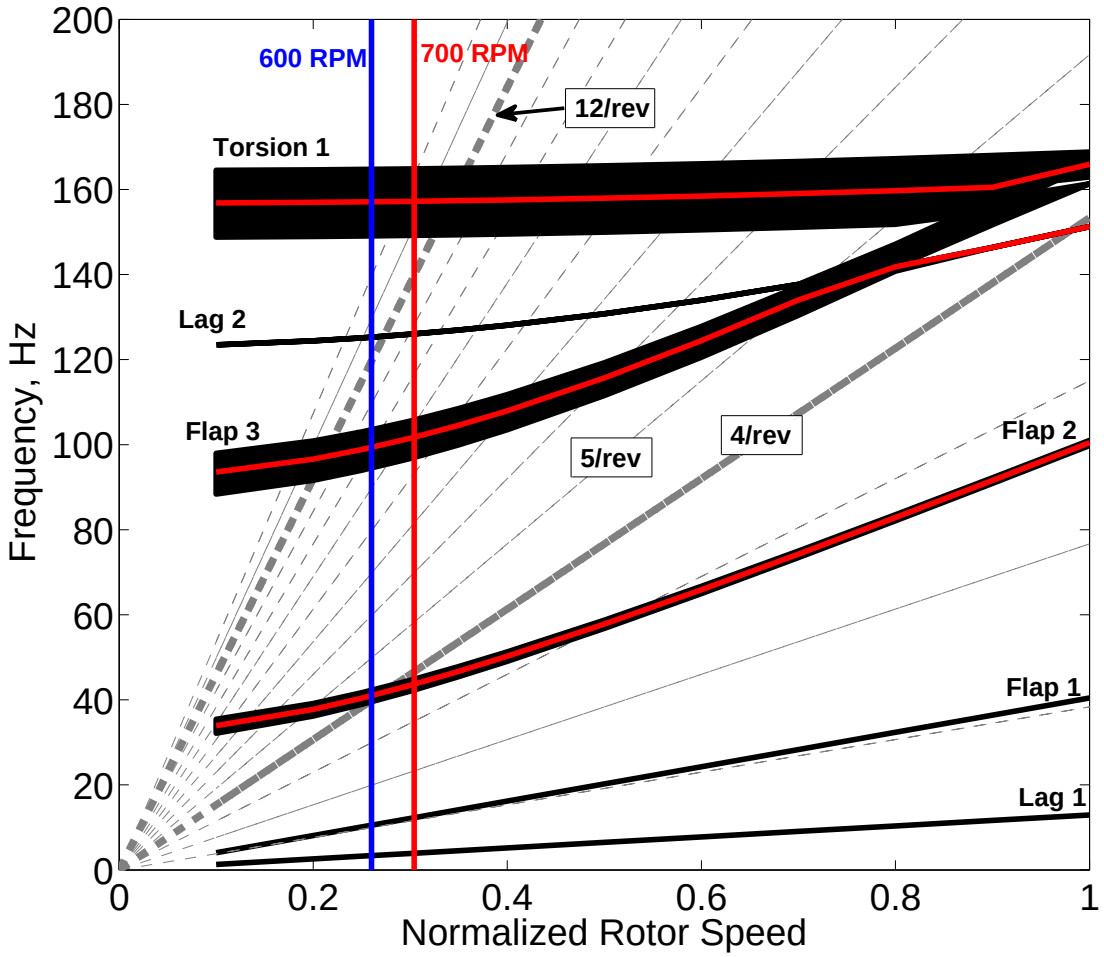

Figure 9.9: Calculated fanplot of the rotor blade, with the relevant test operating RPM values highlighted. Lines thickened to demonstrate the impact of a ±10% uncertainty in section stiffnesses [89].

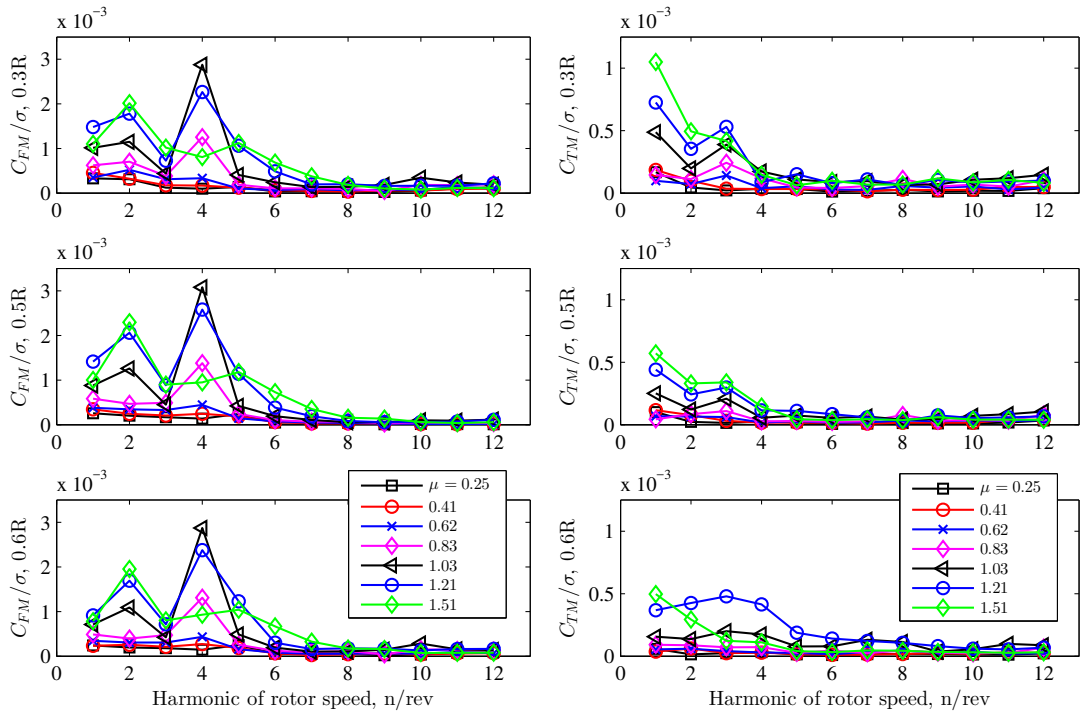

(a) Flapwise bending coefficient

(b) Torsion coefficient

Figure 9.10: Envelope of maximum blade flap bending moment and torsion moment amplitudes for three spanwise locations (0.3R, 0.5R, and 0.6R).

this impulse, the blade has an elastic response in torsion that persists from about 330° to 116° azimuth. The response is at approximately 15/rev, which for this rotor speed of 600 RPM, is near the first torsion mode natural frequency of about 150–160 Hz. The torsion response appears to be lightly damped.

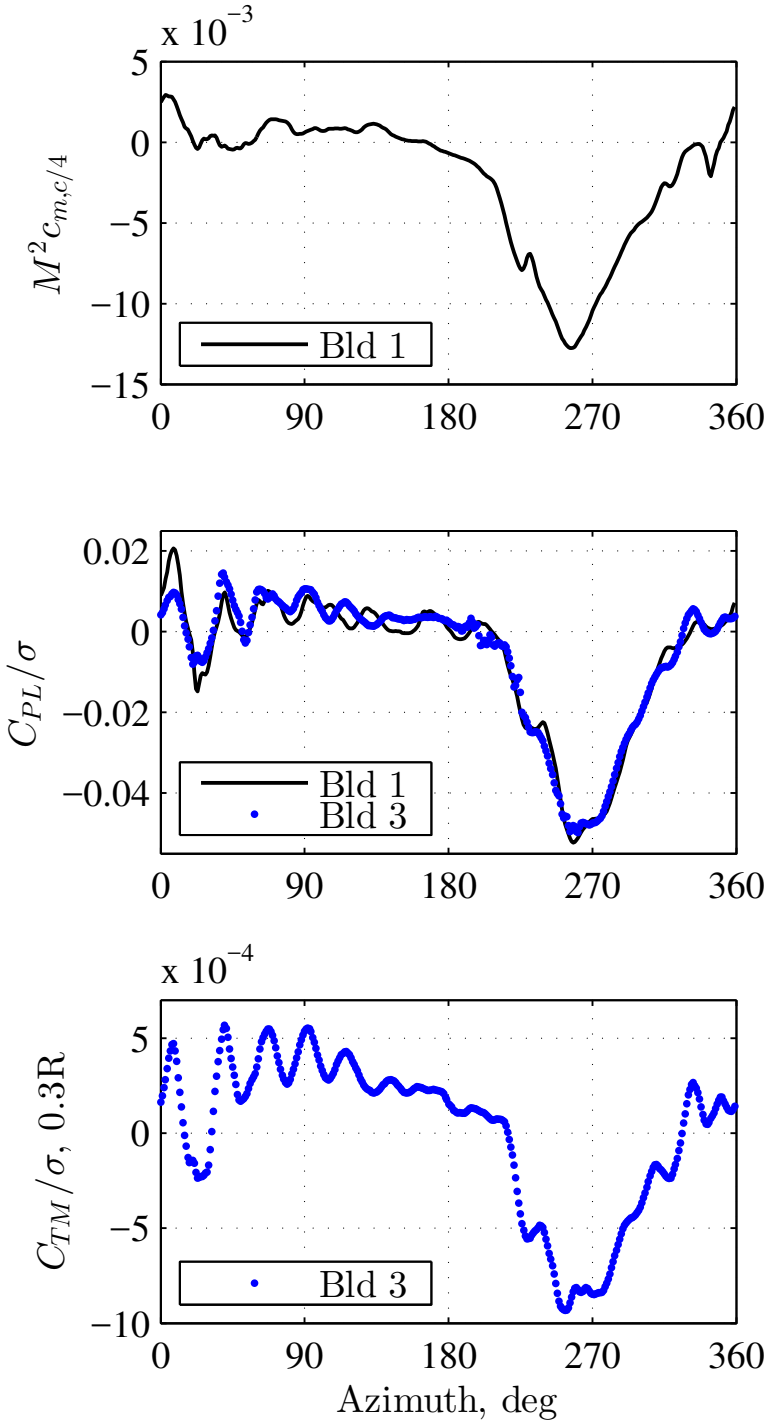

Figure 9.11: Section aerodynamic pitching moment at 0.3R (top), pitch link tension (middle), and blade oscillatory root torsion moment (bottom), for Case 543: μ = 1.21, θ_0 = −6°, C_L/σ = 0.082, Ω = 26% = 600 RPM.

Chapter 10: Conclusion

10.1 Summary of Research

The aeromechanics of edgewise rotors at high advance ratio was researched through wind tunnel testing of a model rotor, and analysis of the resulting data set. High advance ratio rotors have application with high-speed helicopters, particularly compound helicopters. In this research, an instrumented model rotor was constructed and tested up to a maximum advance ratio of μ = 1.6 in the Glenn L. Martin Wind Tunnel at the University of Maryland. The goal was to explore phenomena unique to the high advance ratio flight regime, and create a data set to benchmark analysis and predictive methods.

The model rotor blades utilized a geometry with no taper, no twist, and a well-understood symmetric airfoil, the NACA0012. The test matrix included collective pitch sweeps at a wide range of advance ratios, and limited sweeps with the rotor set to positive shaft tilt angles (tilt back). The data set includes steady and unsteady rotor hub forces and moments (performance and vibratory loads), blade structural loads (bending and torsion moments), blade flapping angles, swashplate control angles, and unsteady blade airloads (surface pressure transducers). Several interesting phenomena were observed, and summarized below.

10.2 Key Conclusions

1. Edgewise rotors trimmed to zero flapping (or zero hub moment) experience a reduction in thrust sensitivity to collective inputs as advance ratio increases. As the reverse flow region grows, the retreating blade loses dynamic pressure, and so the advancing blade must also reduce lift (through cyclic) to trim. At a *critical advance ratio* (μ_{crit}), the sensitivity of thrust with collective becomes zero, and the rotor thrust cannot be controlled by collective pitch. At advance ratios beyond μ_{crit}, the collective-thrust sensitivity changes sign, such that positive collective pitch changes result in a lower thrust after trim. This typically occurs at μ_{crit} = 0.85–1, and is caused by the retreating blade operating in reverse flow, and generate lift opposite of the intended control pitch input.

2. The collective-thrust reversal occurs at high advance ratio due to the reverse flow region, the ability of the rotor blade airfoil to produce lift in reverse flow, and the requirement of roll or flapping trim. If any of these three conditions are not present, the reversal of sensitivity may not occur. Examples could be if the blade section were to stall in reverse flow, or if the rotor need not be in trim equilibrium, such as with high-speed coaxial helicopters.

3. The critical advance ratio for collective-thrust reversal can be determined analytically for simple rotor geometry and induced inflow assumptions, using existing blade element formulations with modifications for the reverse-flow

region.

4. The critical advance ratio is influenced by root cutout and blade taper ratio. Increasing root cutout delays the critical advance ratio to higher μ, by removing blade area from the root which has the highest reverse flow dynamic pressure. Similarly, a blade with a taper ratio such that the root chord is larger than the tip will experience a lower μ_{crit}.

5. The critical advance ratio is not influenced by linear blade twist, shaft/disk tilt, or airfoil section lift-curve slope. A twisted blade may encounter root stall at lower collectives, but the twist does not effect the sensitivity of thrust to collective inputs. The lift-curve slope of the airfoil effects the collective-thrust sensitivity, but not the critical advance ratio. Longitudinal disk or shaft tilt does not effect the critical advance ratio, when defining advance ratio as parallel to the disk.

6. The collective-thrust sensitivity of the test was predicted in trend by the simple analytical and numerical blade element theory (BET) using uniform inflow. Modeling the elasticity or flapping behavior of the blade in a comprehensive analysis, such as UMARC, had no significant change to the prediction from the simplified formulation. Adding in a non-uniform wake model had the largest improvement to test correlation for collective-thrust sensitivity.

7. At high advance ratios and moderate collective pitch settings, the retreating blade experiences stall in the reverse flow region. The post-stall behavior in-

dicates sustained section lift well beyond static stall expectations, and is dominated by unsteady aerodynamics. Reverse flow dynamic stall is evidenced by the signatures of shed vorticity convecting across the chord from the geometric trailing edge to leading edge.

8. The reverse flow dynamic stall behavior at $0.3R$ span qualitatively and quantitatively agrees with published 2-dimensional airfoil reverse-flow dynamic stall studies for the same airfoil. The correlation indicates that 3-D reverse-flow dynamic stall can likely be predicted using models developed from 2-D data, as with forward flow conventional dynamic stall.

9. For a fixed target lift coefficient, a trimmed rotor approaching the critical advance ratio experiences (in analysis) a singularity in required collective and required rotor power. This is due to the net lifting ability of an edgewise rotor ($\alpha_s = 0°$) vanishing at μ_{crit}.

10. As advance ratio increases beyond μ_{crit}, the rotor is again able to reach high lift coefficients. The sensitivity of thrust to collective increases (negatively), such that high blade-loading coefficients can be reached with very low collective input.

11. The rotor experiences increased vibratory loads as advance ratio is increased, with a peak observed at $\mu = 1$. The loads generally decreased beyond this point.

12. Blade flap bending moment experienced dominant 4/rev amplitudes due to

proximity of the second flap bending mode natural frequency to 4/rev. For the advance ratio where the rotor RPM was reduced further, the 4/rev was replaced by a 5/rev component dominating.

13. At high advance ratio, the reverse-flow imparts a pitching moment impulse to the retreating blade. This causes high pitch link loads, and blade torsion. The blade also elastically responds by oscillating at the first torsion mode, which in this case was approximately 15/rev. The mode is lightly damped and persists for over a quarter of a revolution.

10.3 Recommendations for Future Work

There are several aspects of high advance ratio rotor aeromechanics that could be explored as follow-on to this work.

1. **Performance-focused tests:** One major lesson-learned through the testing program was that embedded blade sensors, especially pressure sensors, increase the difficulty of a wind tunnel test significantly. There is much to learn about the performance and vibratory hub loads of rotors at high advance ratio, and such a test does not require any rotating-frame measurements beyond flapping angles for trim. Testing non-instrumented blades to higher advance ratio at higher RPM should increase the dimensional forces such that the uncertainty decreases to acceptable levels. For this test, an RPM of at least 1000 was found to improve the results considerably.

2. **Angle of attack mode:** As part of the performance-focused tests, the shaft

tilt control mode should be investigated. Published analysis and limited test data has shown a high-advance ratio rotor can control lift much more efficiently near the critical advance ratio by using aft shaft tilt instead of collective. This also avoids the reversal phenomenon discussed in this dissertation. The published analyses by Ormiston (fig. 1.36) should be validated through testing.

3. **Stability:** The stability boundaries for articulated rotors at high advance ratio should be explored. First analytically, and then verified in the wind tunnel. A method for introducing perturbations would need to be devised, with the response measured by flap and lag sensors. Any stability issues for hingeless rotors should also be explored, as these are typically the rotor types used for high advance ratio compound rotorcraft concepts.

4. **Aerodynamics:** The aerodynamics of the reverse-flow region are of interest for high advance ratio rotors. Performance and loads when attached flow exists seem to be well-predicted by modern analysis, but not once reverse-flow stall occurs. Testing with a more rigid rotor (not articulated) may help focus solely on the aerodynamic measurements. In such a setup, embedded pressure sensors can be used, as well as optical methods such as PIV, to interrogate the flow field. Any measurements of the induced velocity distribution above $\mu > 0.8$ would be valuable for analysis correlation. The effect of fuselage upwash, or rotor stand aerodynamic interference, should also be investigated. And finally, an instrumented fixed-wing could be added to the test setup, to represent a compound helicopter. The mutual interference would be measured

via independent load cells and surface pressure sensors.

Appendix A: Steady Forces and Moments

This appendix contains the rest of the steady forces and moments that were not discussed in the main body of the dissertation: side force, rolling moment, and pitching moment. Side force is positive starboard, rolling moment is positive port blade down, pitching moment is positive nose up. They are presented here without discussion.

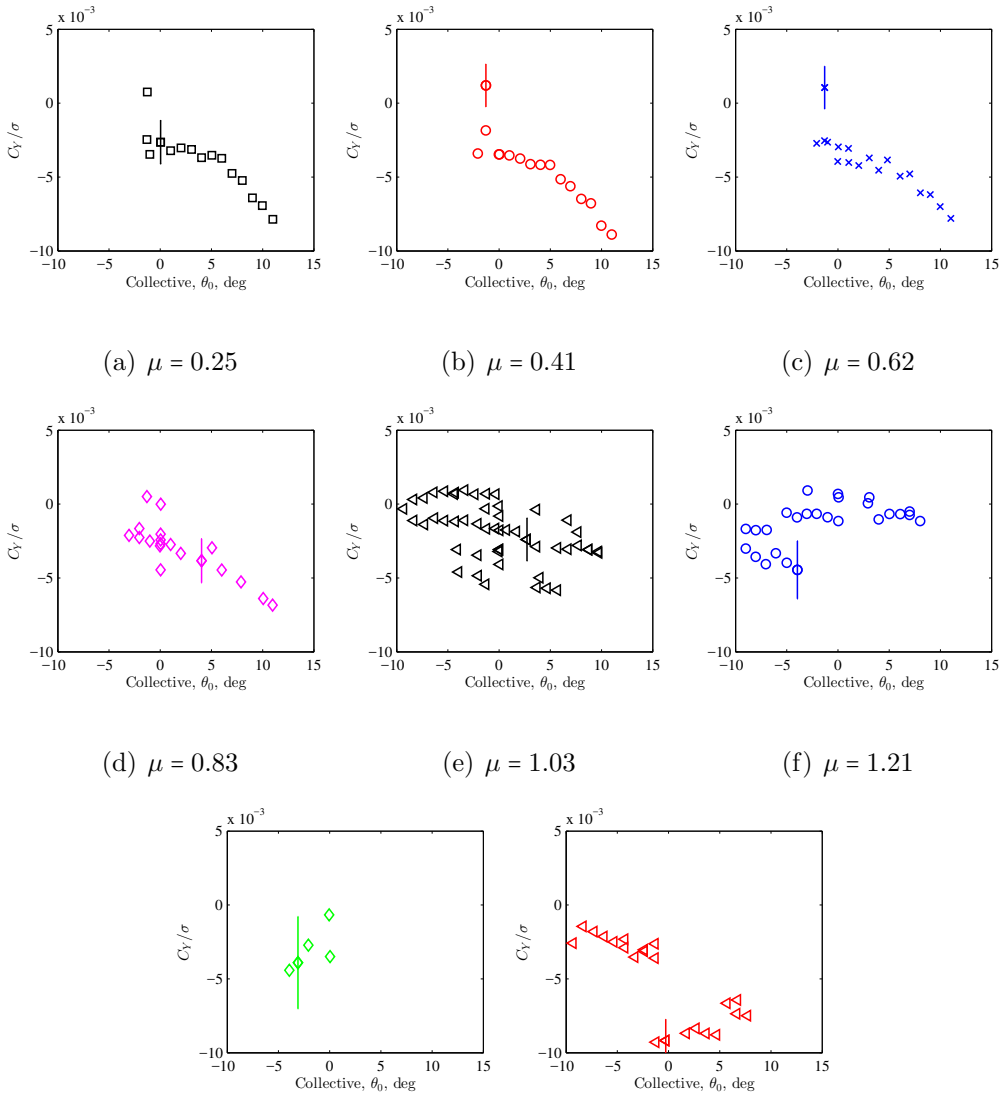

(a) $\mu = 0.25$ (b) $\mu = 0.41$ (c) $\mu = 0.62$

(d) $\mu = 0.83$ (e) $\mu = 1.03$ (f) $\mu = 1.21$

(g) $\mu = 1.51$ (h) $\mu = 1.03$, $\alpha_s = 4°$

Figure A.1: Rotor side force coefficient for collective sweeps at each advance ratio. Shaft tilt $\alpha_s = 0°$ except where noted. Error bars denote 2σ uncertainty estimate based on hub load cell calibration.

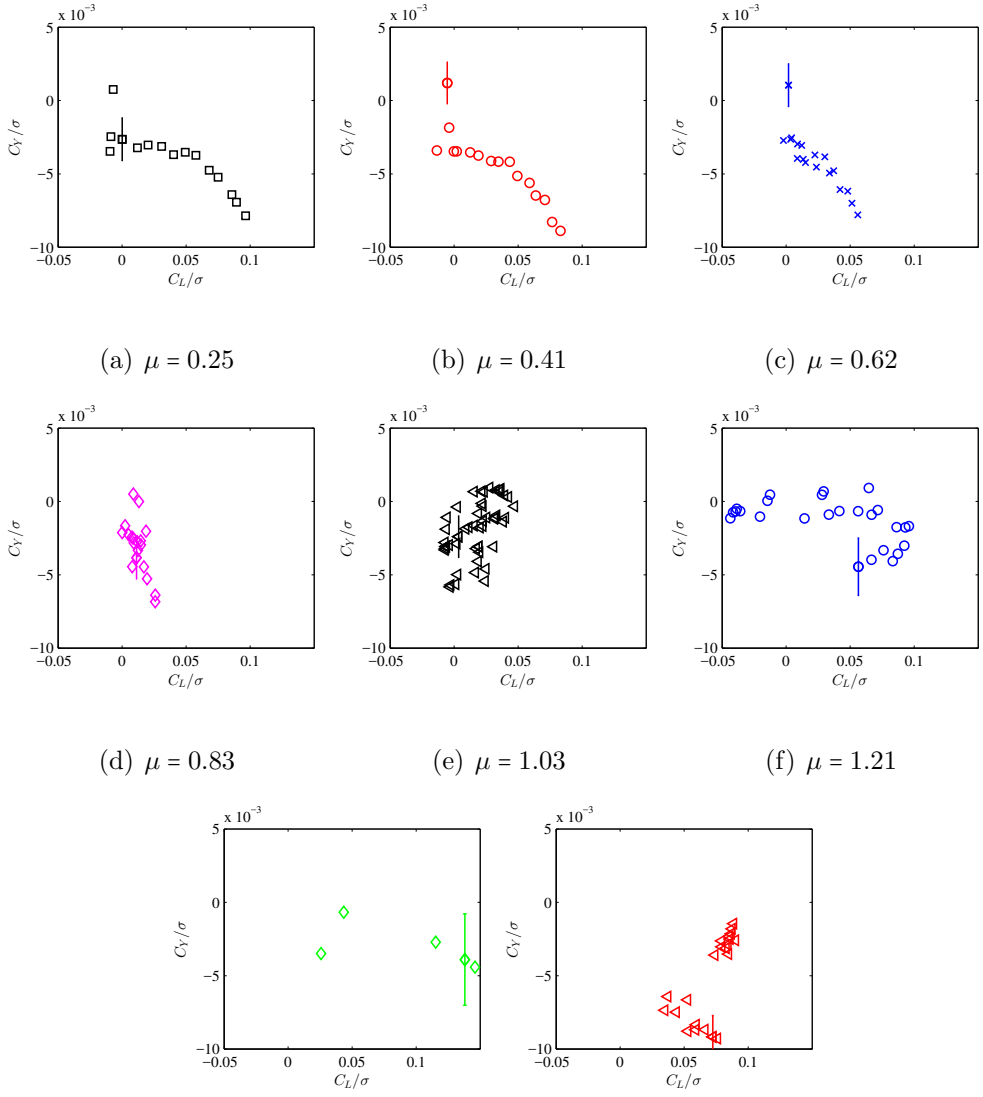

(a) $\mu = 0.25$ (b) $\mu = 0.41$ (c) $\mu = 0.62$

(d) $\mu = 0.83$ (e) $\mu = 1.03$ (f) $\mu = 1.21$

(g) $\mu = 1.51$ (h) $\mu = 1.03$, $\alpha_s = 4°$

Figure A.2: Rotor side force coefficient versus rotor lift coefficient at each advance ratio. Shaft tilt $\alpha_s = 0°$ except where noted. Error bars denote 2σ uncertainty estimate based on hub load cell calibration.

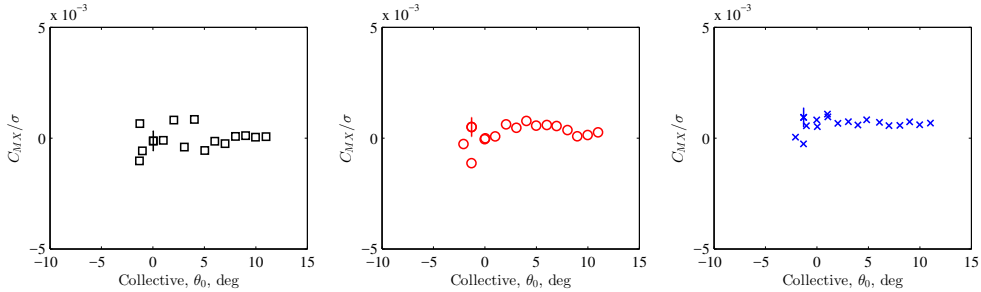

(a) $\mu = 0.25$ (b) $\mu = 0.41$ (c) $\mu = 0.62$

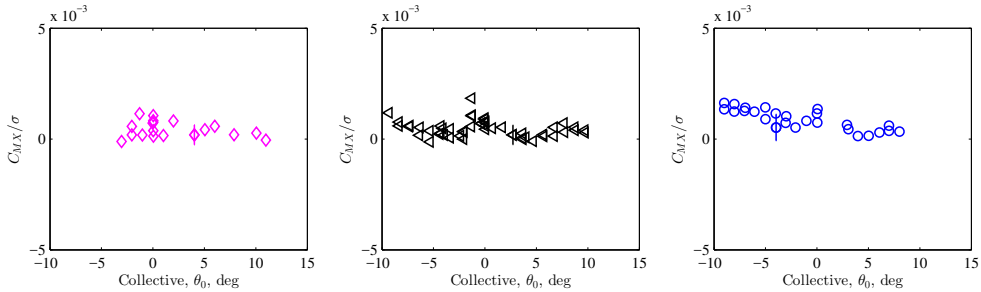

(d) $\mu = 0.83$ (e) $\mu = 1.03$ (f) $\mu = 1.21$

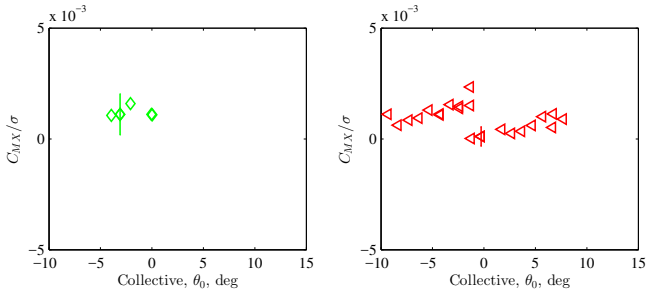

(g) $\mu = 1.51$ (h) $\mu = 1.03$, $\alpha_s = 4°$

Figure A.3: Rotor rolling moment coefficient for collective sweeps at each advance ratio. Shaft tilt $\alpha_s = 0°$ except where noted. Error bars denote 2σ uncertainty estimate based on hub load cell calibration.

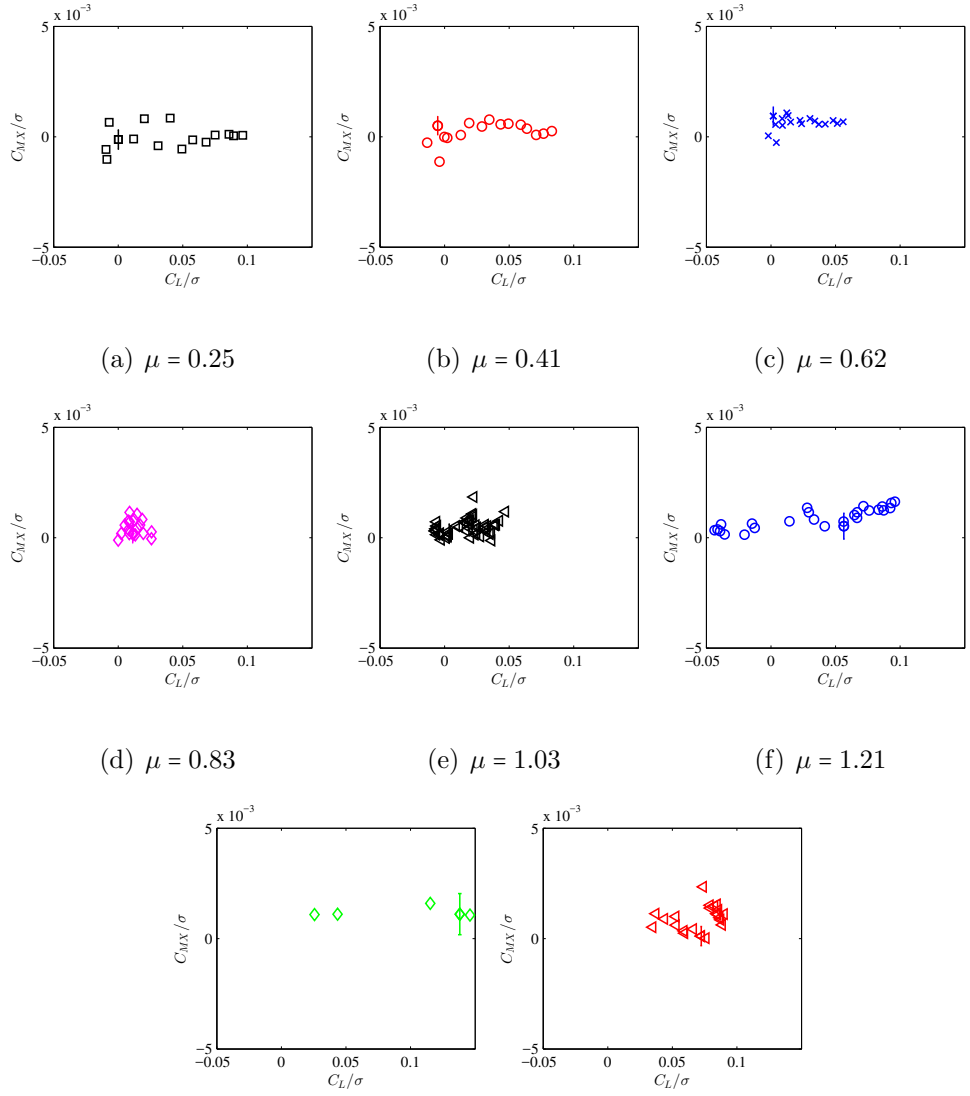

(a) $\mu = 0.25$ (b) $\mu = 0.41$ (c) $\mu = 0.62$

(d) $\mu = 0.83$ (e) $\mu = 1.03$ (f) $\mu = 1.21$

(g) $\mu = 1.51$ (h) $\mu = 1.03$, $\alpha_s = 4°$

Figure A.4: Rotor rolling moment coefficient versus rotor lift coefficient at each advance ratio. Shaft tilt $\alpha_s = 0°$ except where noted. Error bars denote 2σ uncertainty estimate based on hub load cell calibration.

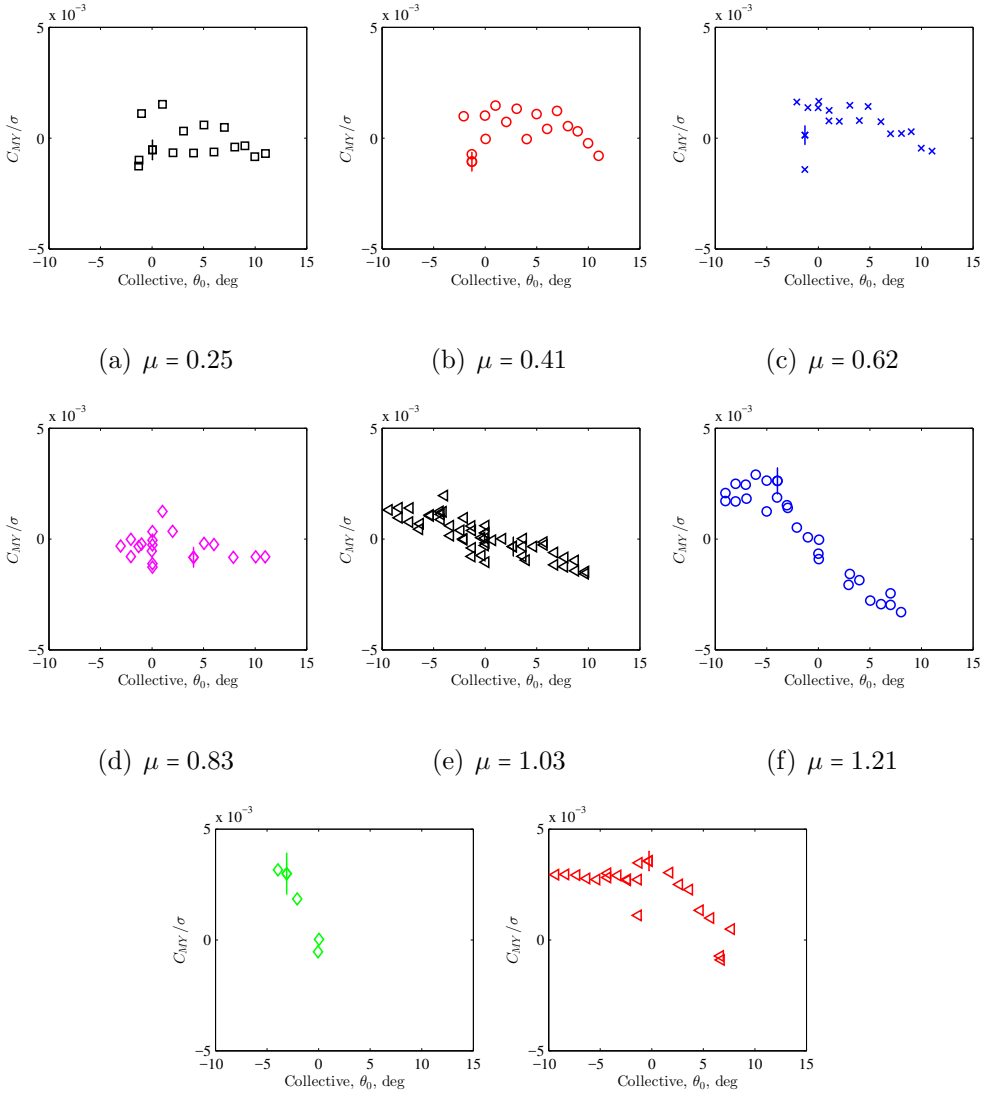

(a) $\mu = 0.25$ (b) $\mu = 0.41$ (c) $\mu = 0.62$

(d) $\mu = 0.83$ (e) $\mu = 1.03$ (f) $\mu = 1.21$

(g) $\mu = 1.51$ (h) $\mu = 1.03$, $\alpha_s = 4°$

Figure A.5: Rotor pitching moment coefficient for collective sweeps at each advance ratio. Shaft tilt $\alpha_s = 0°$ except where noted. Error bars denote 2σ uncertainty estimate based on hub load cell calibration.

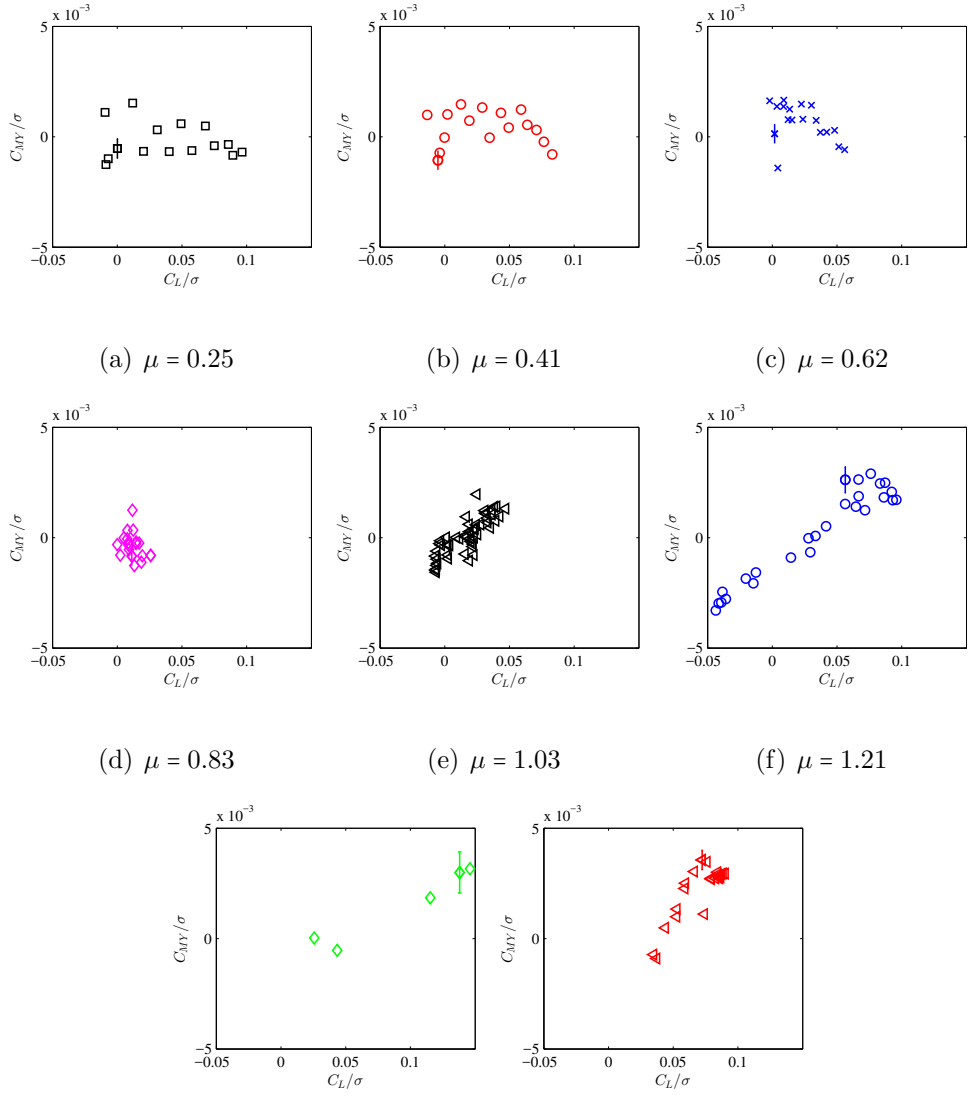

(a) $\mu = 0.25$ (b) $\mu = 0.41$ (c) $\mu = 0.62$

(d) $\mu = 0.83$ (e) $\mu = 1.03$ (f) $\mu = 1.21$

(g) $\mu = 1.51$ (h) $\mu = 1.03$, $\alpha_s = 4°$

Figure A.6: Rotor pitching moment coefficient versus rotor lift coefficient at each advance ratio. Shaft tilt $\alpha_s = 0°$ except where noted. Error bars denote 2σ uncertainty estimate based on hub load cell calibration.

Appendix B: Vibratory Hub Loads

This appendix contains the vibratory 4/rev hub load amplitudes (forces and moments), plotted against collective and rotor lift coefficient. All cases were set to the given collective pitch and then trimmed to minimize first harmonic root blade flapping angle using lateral and longitudinal cyclic. The results are presented here without further discussion.

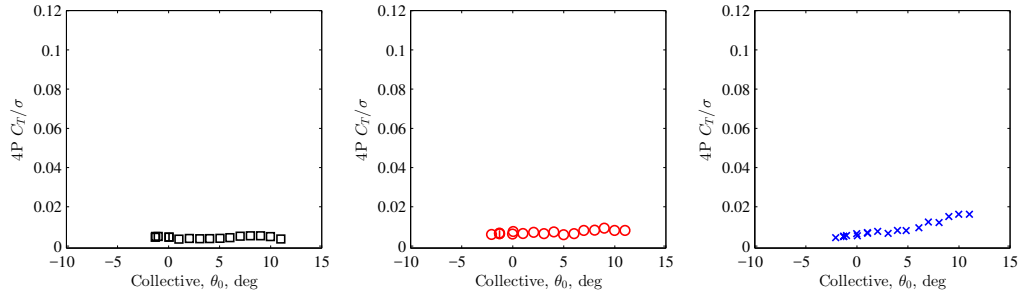

(a) $\mu = 0.25$ (b) $\mu = 0.41$ (c) $\mu = 0.62$

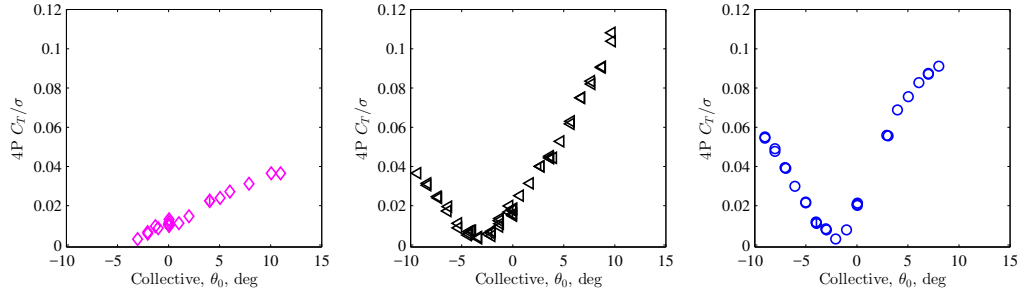

(d) $\mu = 0.83$ (e) $\mu = 1.03$ (f) $\mu = 1.21$

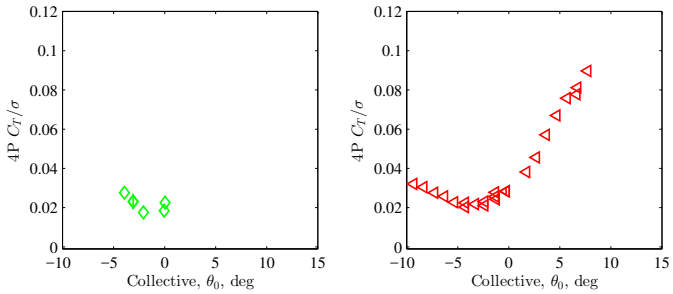

(g) $\mu = 1.51$ (h) $\mu = 1.03$, $\alpha_s = 4°$

Figure B.1: 4/rev hub vertical force amplitude for collective sweeps at each advance ratio. Shaft tilt $\alpha_s = 0°$ except where noted.

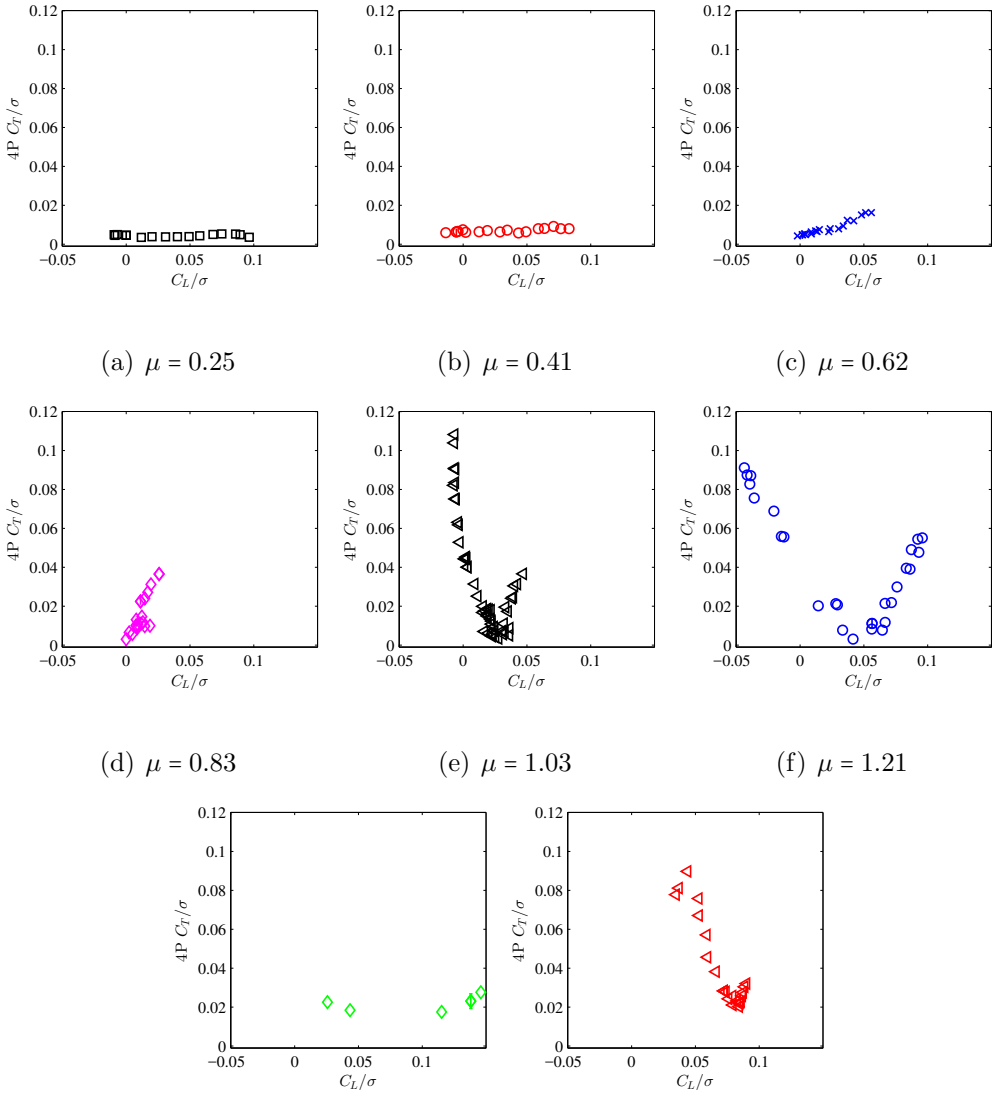

(a) $\mu = 0.25$ (b) $\mu = 0.41$ (c) $\mu = 0.62$

(d) $\mu = 0.83$ (e) $\mu = 1.03$ (f) $\mu = 1.21$

(g) $\mu = 1.51$ (h) $\mu = 1.03$, $\alpha_s = 4°$

Figure B.2: 4/rev hub vertical force amplitude versus rotor lift coefficient at each advance ratio. Shaft tilt $\alpha_s = 0°$ except where noted.

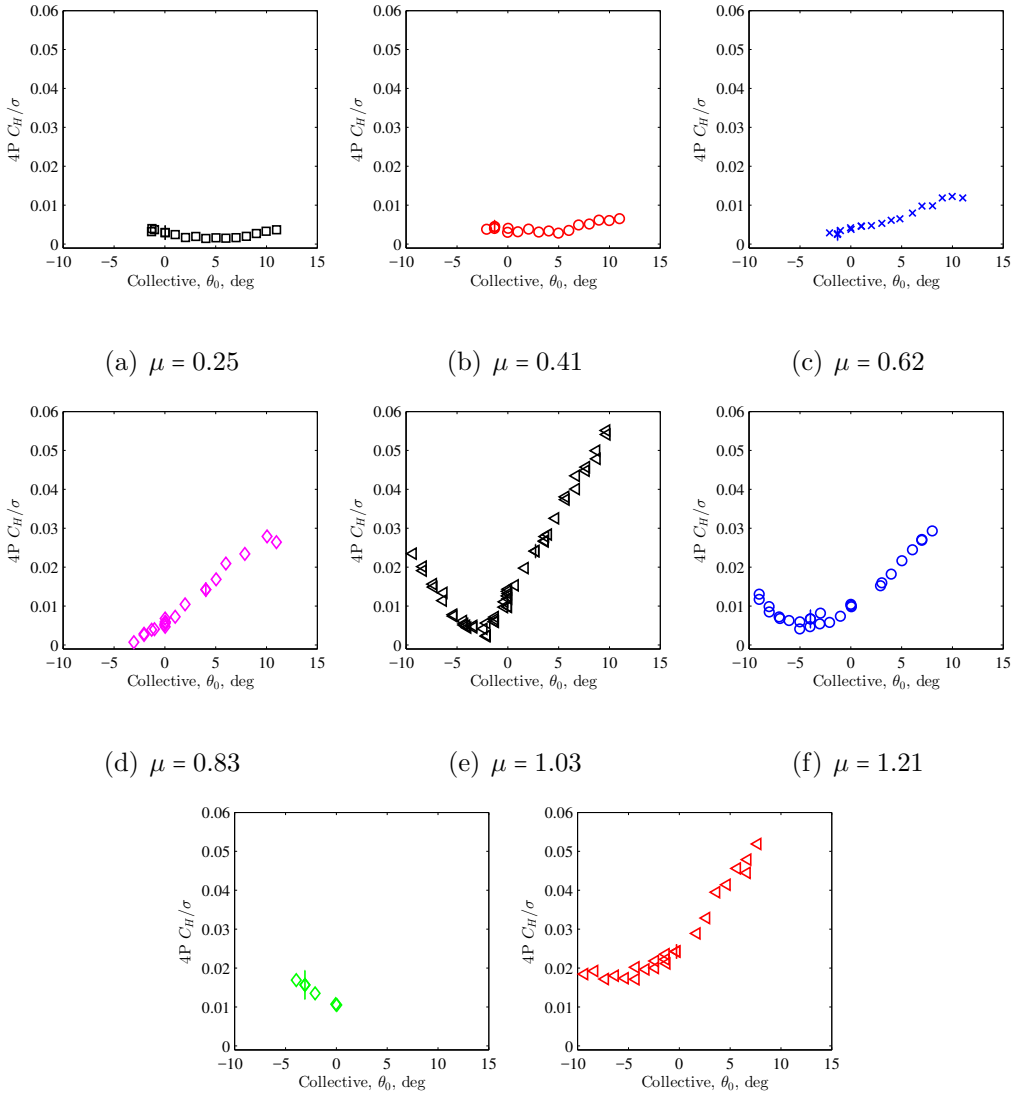

(a) $\mu = 0.25$ (b) $\mu = 0.41$ (c) $\mu = 0.62$

(d) $\mu = 0.83$ (e) $\mu = 1.03$ (f) $\mu = 1.21$

(g) $\mu = 1.51$ (h) $\mu = 1.03$, $\alpha_s = 4°$

Figure B.3: 4/rev hub H-force amplitude for collective sweeps at each advance ratio. Shaft tilt $\alpha_s = 0°$ except where noted.

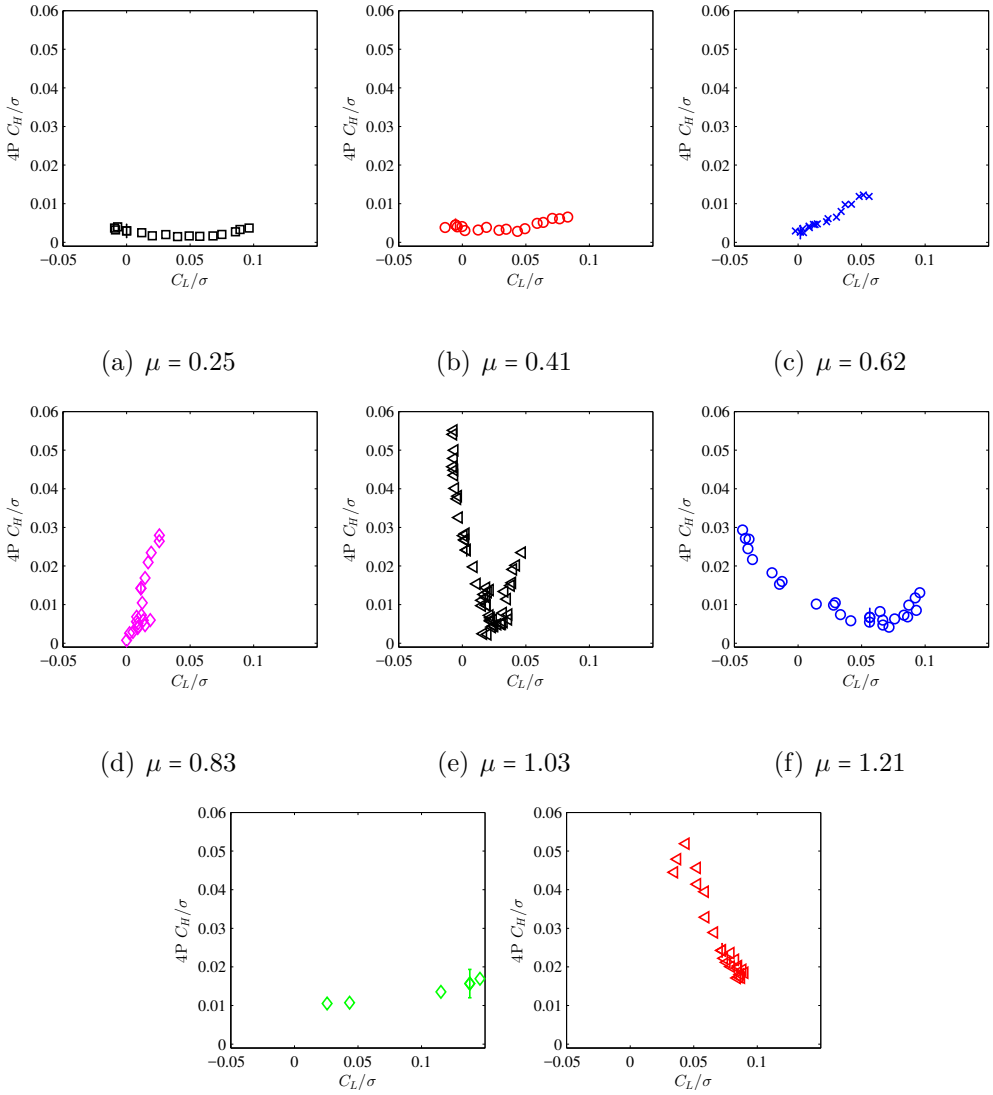

(a) $\mu = 0.25$ (b) $\mu = 0.41$ (c) $\mu = 0.62$

(d) $\mu = 0.83$ (e) $\mu = 1.03$ (f) $\mu = 1.21$

(g) $\mu = 1.51$ (h) $\mu = 1.03$, $\alpha_s = 4°$

Figure B.4: 4/rev hub H-force amplitude versus rotor lift coefficient at each advance ratio. Shaft tilt $\alpha_s = 0°$ except where noted.

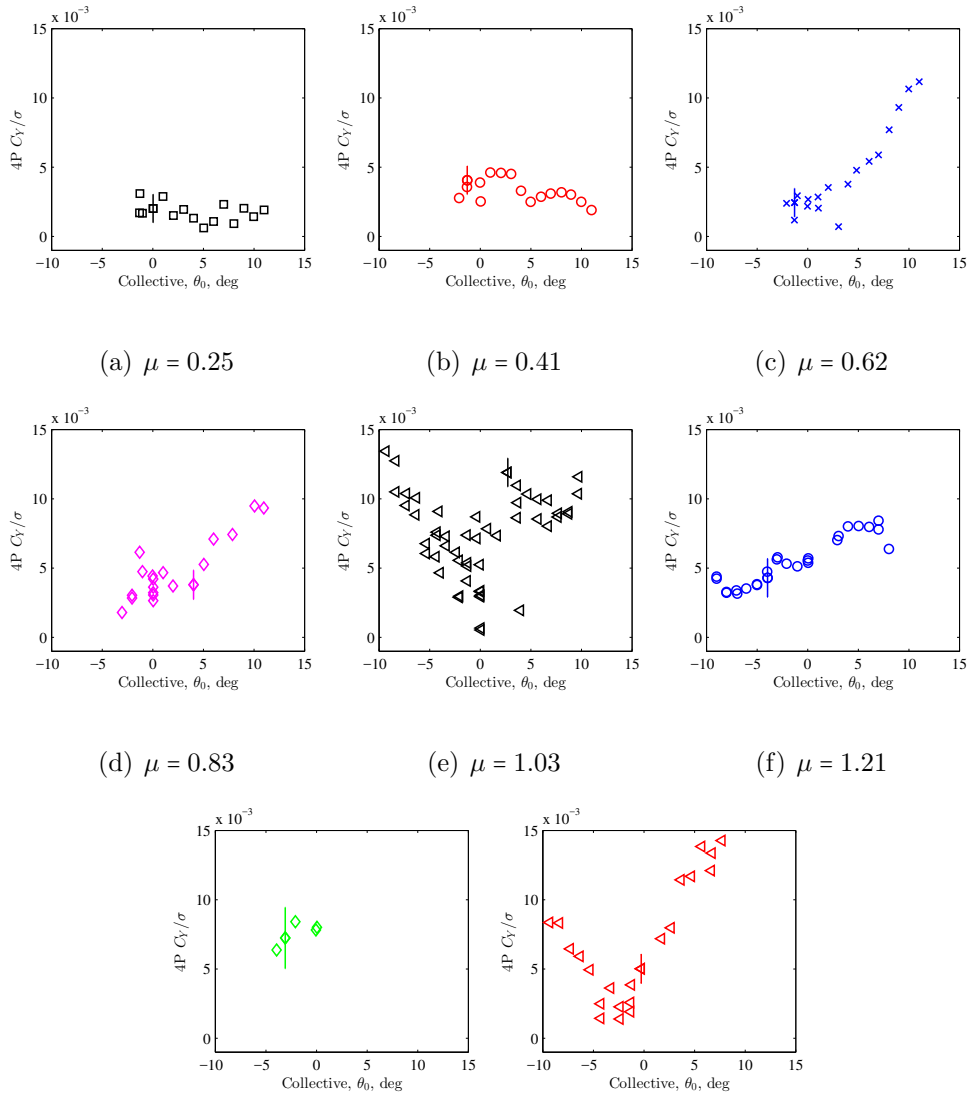

(a) $\mu = 0.25$ (b) $\mu = 0.41$ (c) $\mu = 0.62$

(d) $\mu = 0.83$ (e) $\mu = 1.03$ (f) $\mu = 1.21$

(g) $\mu = 1.51$ (h) $\mu = 1.03$, $\alpha_s = 4°$

Figure B.5: 4/rev hub side force amplitude for collective sweeps at each advance ratio. Shaft tilt $\alpha_s = 0°$ except where noted.

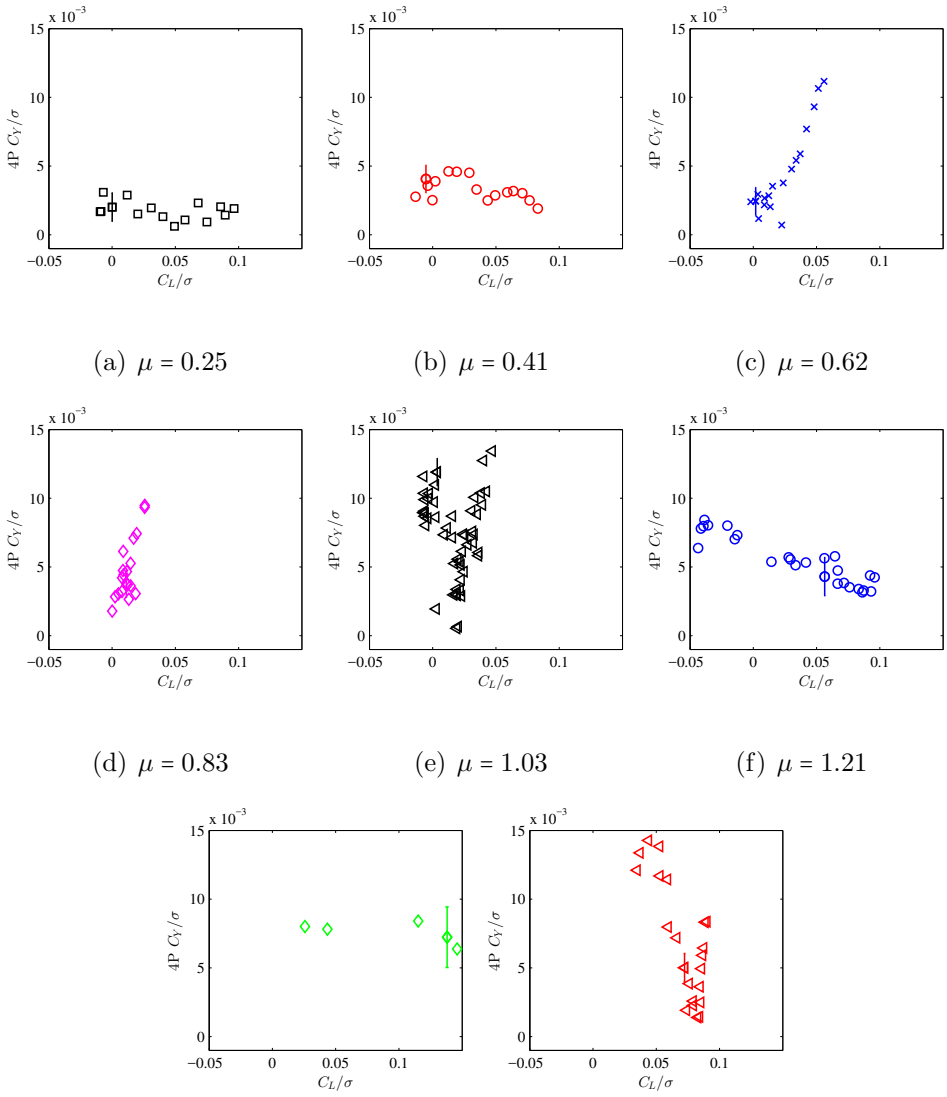

(a) $\mu = 0.25$ (b) $\mu = 0.41$ (c) $\mu = 0.62$

(d) $\mu = 0.83$ (e) $\mu = 1.03$ (f) $\mu = 1.21$

(g) $\mu = 1.51$ (h) $\mu = 1.03$, $\alpha_s = 4°$

Figure B.6: 4/rev hub side force amplitude versus rotor lift coefficient at each advance ratio. Shaft tilt $\alpha_s = 0°$ except where noted.

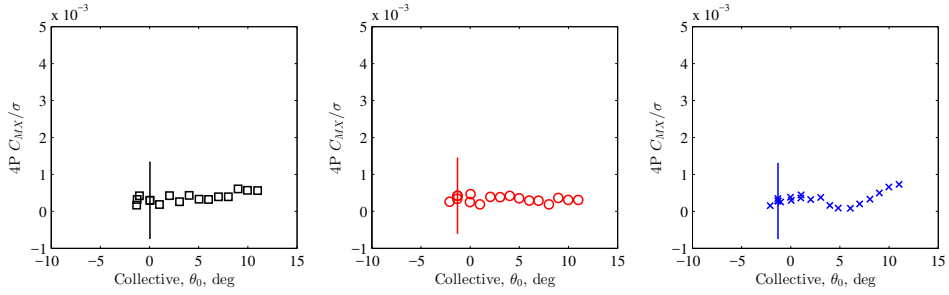

(a) $\mu = 0.25$ (b) $\mu = 0.41$ (c) $\mu = 0.62$

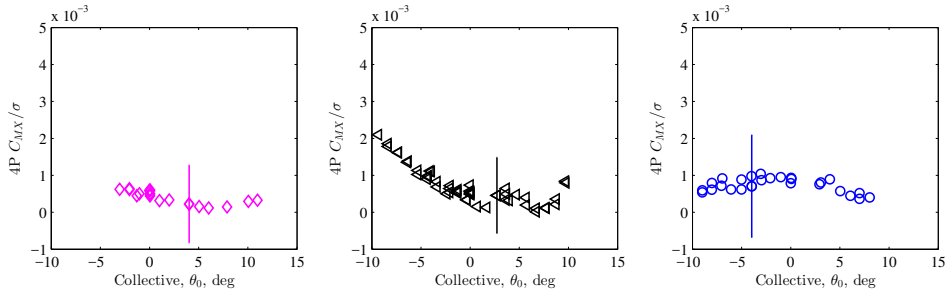

(d) $\mu = 0.83$ (e) $\mu = 1.03$ (f) $\mu = 1.21$

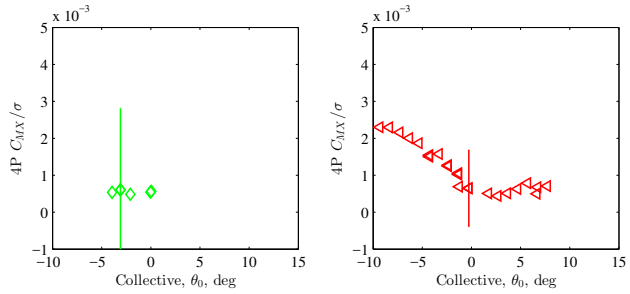

(g) $\mu = 1.51$ (h) $\mu = 1.03$, $\alpha_s = 4°$

Figure B.7: 4/rev hub roll moment amplitude for collective sweeps at each advance ratio. Shaft tilt $\alpha_s = 0°$ except where noted.

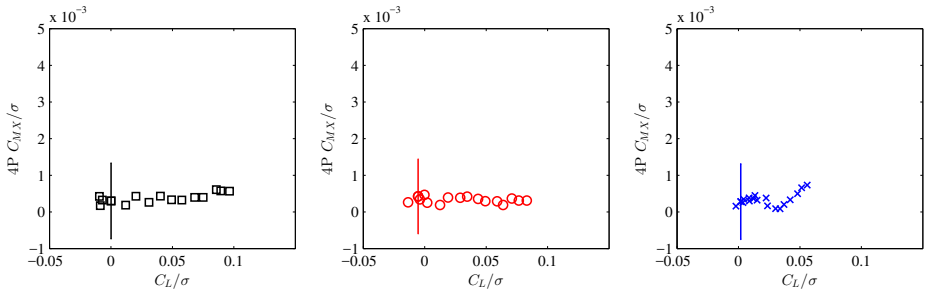

(a) $\mu = 0.25$ (b) $\mu = 0.41$ (c) $\mu = 0.62$

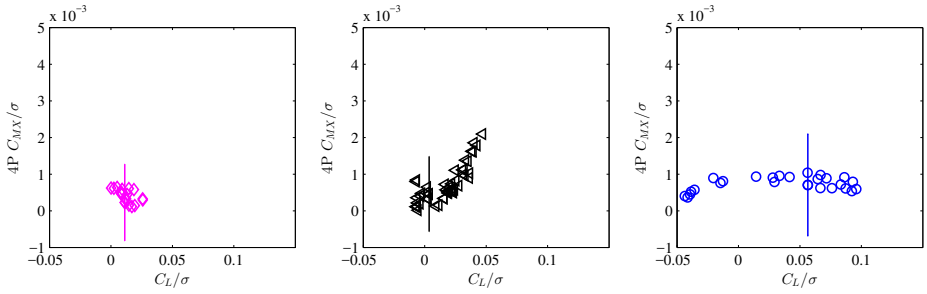

(d) $\mu = 0.83$ (e) $\mu = 1.03$ (f) $\mu = 1.21$

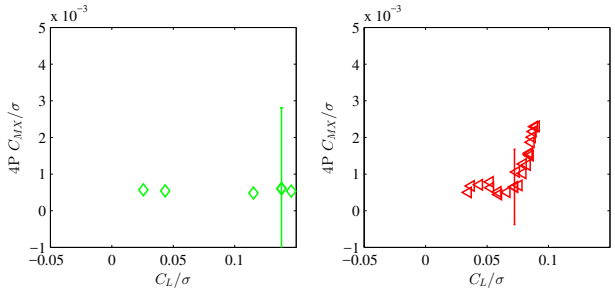

(g) $\mu = 1.51$ (h) $\mu = 1.03$, $\alpha_s = 4°$

Figure B.8: 4/rev hub roll moment amplitude versus rotor lift coefficient at each advance ratio. Shaft tilt $\alpha_s = 0°$ except where noted.

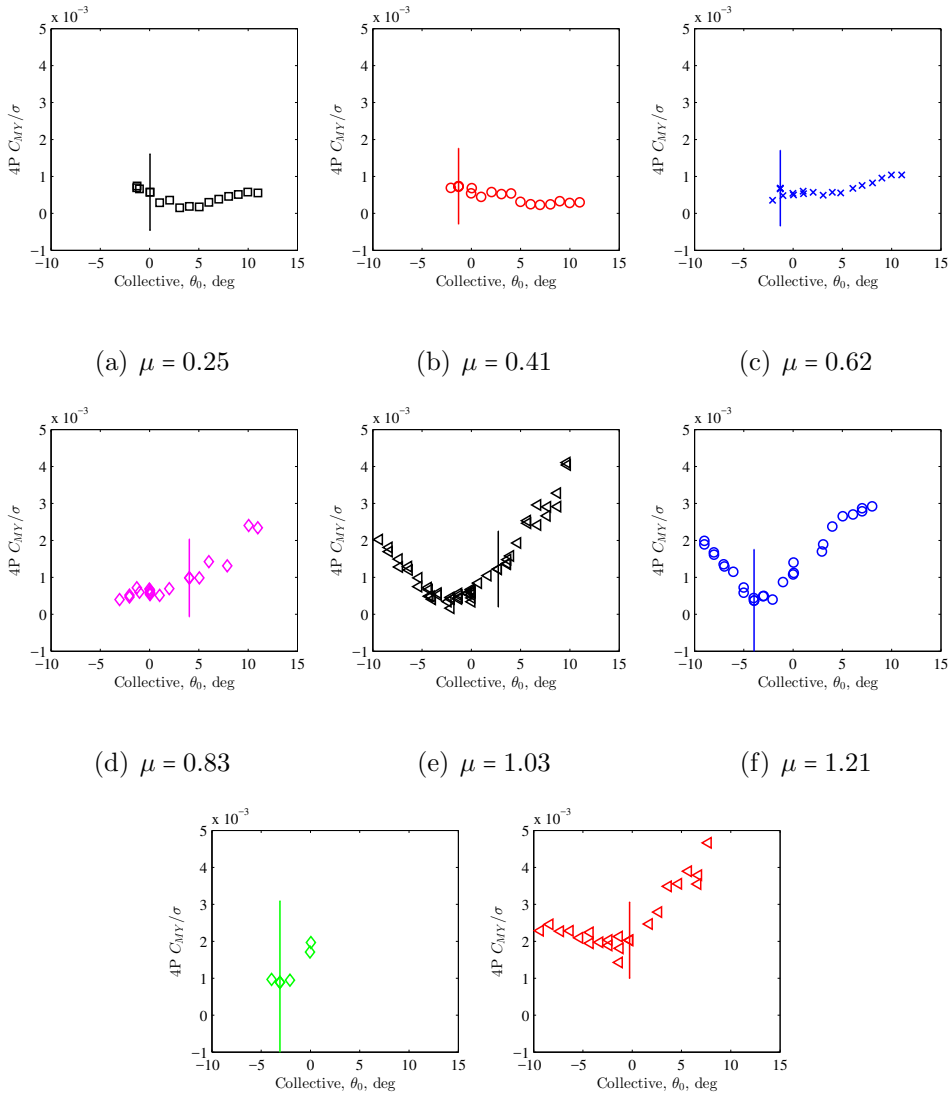

(a) $\mu = 0.25$ (b) $\mu = 0.41$ (c) $\mu = 0.62$

(d) $\mu = 0.83$ (e) $\mu = 1.03$ (f) $\mu = 1.21$

(g) $\mu = 1.51$ (h) $\mu = 1.03$, $\alpha_s = 4°$

Figure B.9: 4/rev hub pitch moment amplitude for collective sweeps at each advance ratio. Shaft tilt $\alpha_s = 0°$ except where noted.

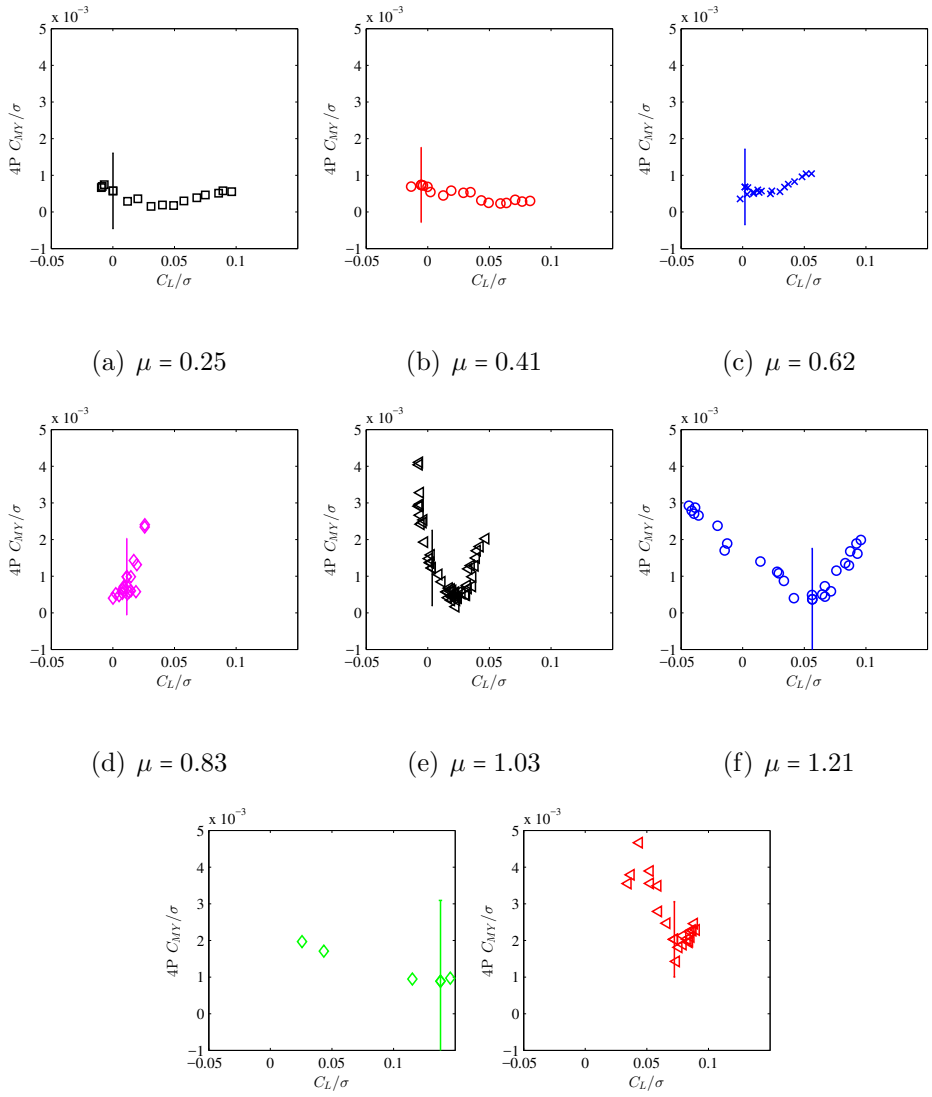

(a) $\mu = 0.25$ (b) $\mu = 0.41$ (c) $\mu = 0.62$

(d) $\mu = 0.83$ (e) $\mu = 1.03$ (f) $\mu = 1.21$

(g) $\mu = 1.51$ (h) $\mu = 1.03$, $\alpha_s = 4°$

Figure B.10: 4/rev hub pitch moment amplitude versus rotor lift coefficient at each advance ratio. Shaft tilt $\alpha_s = 0°$ except where noted.

Bibliography

[1] Ashish Bagai. Aerodynamic Design of the X2 Technology Demonstrator Main Rotor Blade. In *Proceedings of the 64th Annual Forum of the American Helicopter Society*, Montreal, Canada, April 29–May 1 2008.

[2] AirbusHelicopters. `http://press.airbushelicopters.com/en/gallery/x3-speed-record`. [Online; accessed April 3, 2016].

[3] AgustaWestland AW609. `http://www.agustawestland.com/products/aw609`, 2012. [Online; accessed September 12, 2012].

[4] Boeing. `http://www.boeing.com/defense/v-22-osprey/`. [Online; accessed April 3, 2016].

[5] Professional Pilot Magazine. `http://www.propilotmag.com/archives/2012/September12/A3_Rotor_p1.html`. [Online; accessed September 12, 2012].

[6] J Gordon Leishman. *Principles of Helicopter Aerodynamics, Second Edition*. Cambridge University Press, 2006.

[7] NAVAIR. V-22 osprey 2010 guidebook. Tech. Rep 10-28, NAVAIR, 2010. NAVAIR PMA-275.

[8] R. Blackwell and T. Millott. Dynamics Design Characteristics of the Sikorsky X2 Technology Demonstrator Aircraft. In *Proceedings of the 68th Annual Forum of the American Helicopter Society*, Montreal, Canada, April 29–May 2 2008.

[9] Douglas Nelms. Speed streak: Eurocopter's x3 high-speed hybrid helicopter combines fixed-and rotary-wing flying characteristics. *Aviation Week & Space Technology*, 174(24), 2012.

[10] Abraham E. Karem. Optimum Speed Rotor, 1999. US Patent 6,007,298.

[11] John B Wheatley and Manley J Hood. Full-scale wind-tunnel tests of a pca-2 autogiro rotor. Technical Report NACA TR 515, 1935.

[12] John R Meyer Jr, Gaetano Falabella Jr, et al. An investigation of the experimental aerodynamic loading on a model helicopter rotor blade. Technical Report NASA TN 2953, 1953.

[13] Julian L. Jenkins, Jr. Wind-tunnel Investigation of a Lifting Rotor Operating at Tip-speed Ratios from 0.65 to 1.45. Technical Report TN-D-2628, NASA, February 1965.

[14] John L. McCloud, James Biggers, and Robert H. Stroub. An Investigation of Full-Scale Helicopter Rotors at High Advance Ratios and Advancing Tip Mach Numbers. Technical Report NASA TN-D-4632, National Aeronautics and Space Administration, 1968.

[15] Bruce D Charles and Watson H Tanner. Wind tunnel investigation of semi-rigid full-scale rotors operating at high advance ratios. Technical report, DTIC Document, 1969.

[16] JR Ewans and TA Krauss. Model wind tunnel tests of a reverse velocity rotor system. Technical report, DTIC Document, 1973.

[17] Shinoda P. Peterson R.L. Norman, T.R. and A. Datta. Full-scale wind tunnel test of the uh-60a airloads rotor. In *Proceedings of the 67th Annual Forum of the American Helicopter Society*, Virginia Beach, VA, May 2011.

[18] Anubhav Datta, Hyeonsoo Yeo, and Tom R. Norman. Experimental Investigation and Fundamental Understanding of a Full-Scale Slowed Rotor at High Advance Ratios. *Journal of the American Helicopter Society*, 58(2):1–17, 2013.

[19] Todd R Quackenbush, Daniel A Wachspress, R McKillip Jr, and M Sibilia. Aerodynamic studies of high advance ratio rotor systems. In *Proceedings of the 67th Annual Forum of the American Helicopter Society,(Virginia Beach, VA)*, 2011.

[20] A Gessow and AD Grim. A method for studying the transient blade-flapping behavior of lifting rotors at extreme operating characteristics. Technical Report NACA TN 3366, 1955.

[21] Franklin D. Harris. Rotor Performance at High Advance Ratio: Theory versus Test. Technical Report NASA/CR-2008-215370, 2008.

[22] Matthew W. Floros and Wayne Johnson. Performance Analysis of the Slowed-Rotor Compound Helicopter Configuration. *Journal of the American Helicopter Society*, 54(2):22002–22002, 2009.

[23] Graham Bowen-Davies and Inderjit Chopra. Performance and Loads Correlation of the UH-60 Rotor at High Advance Ratios. In *40th European Rotorcraft Forum*, Southampton, UK, September 2014.

[24] Graham Bowen-Davies. *Performance and Loads of Variable Tip Speed Rotorcraft at High Advance Ratios*. PhD thesis, The University of Maryland, Department of Aerospace Engineering, Maryland, USA, 2015.

[25] Graham M. Bowen-Davies and Inderjit Chopra. Aeromechanics of a Slowed Rotor. *Journal of the American Helicopter Society*, 60(3):1–13, 2015.

[26] Robert A. Ormiston. Induced Power of the Helicopter Rotor. In *Proceedings of the 60th Annual Forum of the American Helicopter Society*, Baltimore, MD, June 2004.

[27] Robert A. Ormiston. A New Formulation for Lifting Rotor Performance Including Comparison with Full-Scale Data. In *Proceedings of the 64th Annual Forum of the American Helicopter Society*, Montreal, Quebec, Canada, April 2008.

[28] Robert A. Ormiston. Rotor Aerodynamic Characteristics at High Advance Ratio Relevant to Compound Rotorcraft. In *Future Vertical Lift Aircraft Design Conference*, San Francisco, CA, January 2012.

[29] J de Montaudouin, N Reveles, and MJ Smith. Computational Aeroelastic Analysis of Slowed Rotors at High Advance Ratios. *The Aeronautical Journal*, 118(1201):297–313, 2014.

[30] Mark Potsdam, Hyeonsoo Yeo, and Robert A. Ormiston. Performance and Loads Predictions of a Slowed UH-60A Rotor at High Advance Ratios. In *39th European Rotorcraft Forum*, Moscow, Russia, September 2013.

[31] Mark Potsdam, Anubhav Datta, and Buvanna Jayaraman. Computational Investigation and Fundamental Understanding of a Slowed UH-60A Rotor at High Advance Ratios. In *Proceedings of the 68th Annual Forum of the American Helicopter Society*, Fort Worth, TX, May 2012.

[32] Ben Berry and Inderjit Chopra. Wind Tunnel Testing for Performance and Vibratory Loads of a Variable-Speed Mach-Scale Rotor. In *Proceedings of the 67th Annual Forum of the American Helicopter Society*, Virginia Beach, VA, May 2011.

[33] Ben Berry and Inderjit Chopra. Performance and Vibratory Load Measurements of a Slowed-Rotor at High Advance Ratios. In *Proceedings of the 68th Annual Forum of the American Helicopter Society*, Fort Worth, TX, May 2012.

[34] Ben Berry and Inderjit Chopra. High-Advance Ratio Wind Tunnel Testing of Two Mach-Scale Rotor Geometries. In *Proceedings of the 69th Annual Forum of the American Helicopter Society*, Phoenix, AZ, May 2013.

[35] Ben Berry and Inderjit Chopra. High-Advance Ratio Wind Tunnel Testing of a Model Rotor with Pressure Measurements. In *Fifth Decennial AHS Aeromechanics Specialists Conference*, San Francisco, CA, January 2014.

[36] Ben Berry and Inderjit Chopra. Slowed Rotor Wind Tunnel Testing of an Instrumented Rotor at High Advance Ratio. In *40th European Rotorcraft Forum*, Southampton, UK, September 2014.

[37] AIAA/GTTC Internal Balance Technology Working Group et al. Recommended practice, calibration and use of internal strain–gage balances with application to wind tunnel testing. Technical report, AIAA R–091–2003, American Institute of Aeronautics and Astronautics, Reston, Virginia, 2003.

[38] Randall L Peterson and Johannes M vanAken. Dynamic calibration of the nasa ames rotor test apparatus steady/dynamic rotor balance. Technical Report NASA TN 110393, April 1996.

[39] Khanh Nguyen and Benton Lau. Dynamics of the mcdonnell-douglas large scale dynamic rig and dynamic calibration of the rotor balance. Technical Report NASA TM 108855, October 1994.

[40] Johannes van Aken, Randall L Peterson, and CJ Freedman. Calibration results of the nasa ames rotor test apparatus steady/dynamic rotor balance. In *American Helicopter Society Aeromechanics Specialists Conference, San Francisco, CA*, 1994.

[41] Stephen A Whitmore, William T Lindsey, Robert E Curry, and Glenn B Gilyard. Experimental characterization of the effects of pneumatic tubing on unsteady pressure measurements. Technical Report NASA TM 4171, March 1990.

[42] Robert Gagnon. Sub-Miniature Pressure Sensor Installation for UH-60A Main Rotor Blade Air Loads Flight Test Program. In *Proceedings of the International Telemetry Conference*, San Diego, CA, 1989.

[43] AD Gardner, K Richter, H Mai, ARM Altmikus, A Klein, and C-H Rohardt. Experimental investigation of dynamic stall performance for the edi-m109 and edi-m112 airfoils. *Journal of the American Helicopter Society*, 58(1):1–13, 2013.

[44] MJ Riley and P Brotherhood. Comparative performance measurements of two helicopter blade profiles in hovering flight. Technical report, Aeronautical Research Council, 1977.

[45] Henning Mainz, Berend G van der Wall, Philippe Leconte, Frederic Ternoy, and H Mercier des Rochettes. Abc rotor blades: design, manufacturing and testing. *Florence, Italy, September*, 2005.

[46] Kulite Semiconductor Products Inc. "sensor description". `http://kulite.com/technology.asp?p=2-1`. [Online; accessed April 13, 2016].

[47] Kulite Semiconductor Products Inc. "lq/le-062 datasheet". `http://www.kulite.com/docs/products/LQ.LE-062.pdf`. [Online; accessed April 13, 2016].

[48] Kulite Semiconductor Products Inc. "transducer handbook, section 2: Kulite sensing technology". http://kulite.com/docs/transducer_handbook/section2.pdf. [Online; accessed November 27, 2016].

[49] Kulite Semiconductor Products Inc. "transducer handbook, section 5: Application information". http://kulite.com/docs/transducer_handbook/section5.pdf. [Online; accessed April 13, 2016].

[50] Omega Engineering Inc. "positioning strain gages". http://www.omega.com/toc_asp/frameset.html?book=Pressure&file=strain-gage-position_REF. [Online; accessed April 13, 2016].

[51] Glenn L. Martin Wind Tunnel. "facilities and specifications". http://windvane.umd.edu/research/facilities.html. [Online; accessed April 16, 2016].

[52] Anand Saxena. *Primary Control of a Mach Scale Swashplateless Rotor Using Brushless DC Motor Actuated Trailing Edge Flaps*. PhD thesis, The University of Maryland, Department of Aerospace Engineering, Maryland, USA, 2015.

[53] William G. Bousman. A Qualitative Examination of Dynamic Stall from Flight Test Data. *Journal of the American Helicopter Society*, 43(4):279–295, 1998.

[54] Anubhav Datta. *Fundamental Understanding, Prediction and Validation of Rotor Vibratory Loads in Steady Level Flight*. PhD thesis, The University of Maryland, Department of Aerospace Engineering, Maryland, USA, 2004.

[55] Wayne Johnson. *Rotorcraft Aeromechanics*. Cambridge University Press, 2013.

[56] Hyeonsoo Yeo. Investigation of UH-60A Rotor Performance and Loads at High Advance Ratios. *Journal of Aircraft*, 50(2):576–589, 2013.

[57] Chris C Critzos, Harry H Heyson, and Robert W Boswinkle Jr. Aerodynamic characteristics of naca 0012 airfoil section at angles of attack from 0 degrees to 180 degrees. (NACA TN 3361), 1955.

[58] Robert E Sheldahl and Paul C Klimas. Aerodynamic characteristics of seven symmetrical airfoil sections through 180-degree angle of attack for use in aerodynamic analysis of vertical axis wind turbines. Technical report, Sandia National Labs., Albuquerque, NM (USA), 1981.

[59] Andrew H Lind, Jonathan N Lefebvre, and Anya R Jones. Experimental investigation of reverse flow over sharp and blunt trailing edge airfoils. In *31st AIAA Applied Aerodynamics Conference*, page 3036, 2013.

[60] Andrew H Lind, Jonathan N Lefebvre, and Anya R Jones. Time-averaged aerodynamics of sharp and blunt trailing-edge static airfoils in reverse flow. *AIAA Journal*, 52(12):2751–2764, 2014.

[61] Andrew H Lind and Anya R Jones. Vortex shedding from airfoils in reverse flow. *AIAA Journal*, 53(9):2621–2633, 2015.

[62] Andrew H Lind, Luke R Smith, Joseph I Milluzzo, and Anya R Jones. Reynolds number effects on rotor blade sections in reverse flow. *Journal of Aircraft*, pages 1–13, 2016.

[63] Andrew Hume Lind. *An Experimental Study of Static and Oscillating Rotor Blade Sections in Reverse Flow*. PhD thesis, The University of Maryland, Department of Aerospace Engineering, Maryland, USA, 2015.

[64] M.S. Selig, J.J. Gugliemo, A.P. Broeren, and P. Giguere. *Summary of Low-Speed Airfoil Data, Vol. 1*. SoarTech Publ., Virginia Beach, VA, 1995.

[65] G.A. Williamson, B.D. McGranahan, B.A. Broughton, R.W. Deters, J.B. Brandt, and M.S. Selig. *Summary of Low-Speed Airfoil Data, Vol. 5*. University of Illinois, Champaign, IL, 2012.

[66] John B. Wheatley. An aerodynamic analysis of the autogiro rotor with a comparison between calculated and experimental results. Technical Report NACA TR 487, 1934.

[67] G. Bir, I. Chopra, and K. Nguyen. Development of UMARC (University of Maryland Advanced Rotorcraft Code. In *Proceedings of the 46th Annual Forum of the American Helicopter Society*, Washington, D.C., May 1990.

[68] Franklin D. Harris. Preliminary Study of Radial Flow Effects on Rotor Blades. Technical report, 1966.

[69] W. J. McCroskey and Richard K. Fisher Jr. Detailed aerodynamic measurements on a model rotor in the blade stall regime. *Journal of the American Helicopter Society*, 17(1):20–30, 1972.

[70] W. J. McCroskey. The Phenomenon of Dynamic Stall. Technical Report NASA TM 81264, National Aeronautics and Space Administration, 1981.

[71] Patrick Bowles. *Performance and Loads of Variable Tip Speed Rotorcraft at High Advance Ratios*. PhD thesis, University of Notre Dame, Indiana, USA, 2012.

[72] Carr L.W. McAlister, K.W. and McCroskey W.J. Dynamic Stall Experiments on the NACA 0012 Airfoil. Technical Report NASA TP-1100, National Aeronautics and Space Administration, 1978.

[73] A. Lind and A. Jones. Unsteady aerodynamics of reverse flow dynamic stall on an oscillating blade section. *Physics of Fluids*, 28(7):1–22, 2016.

[74] Graham Bowen-Davies and Inderjit Chopra. Investigation of the Unsteady Reverse Flow Airloads at High Advance Ratios. In *41st European Rotorcraft Forum*, Munich, Germany, September 2015.

[75] H. Himmelskamp. Profiluntersuchungen an einem umlaufenden Propeller. Technical Report Mitt. Max-Planck-Inst. 2, 1950.

[76] Herrmann Schlichting. *Boundary-Layer Theory 7th Edition*. McGraw Hill, 1979.

[77] John J. Corrigan. Empirical Model for Stall Delay Due to Rotation. In *Proceedings of the American Helicopter Society Aeromechanics Specialists Conference*, San Francisco, CA, January 1994.

[78] Zhaohui Du and Michael S. Selig. A 3-D Stall-Delay Model for Horizontal Axis Wind Turbine Performance Prediction. *AIAA Journal*.

[79] W.H.H. Banks and G.E. Gadd. Delaying Effect of Rotation on Laminar Separation. *AIAA Journal*, 1(4):941–942, 1963.

[80] Zhaohui Du and M.S. Selig. The Effect of Rotation on the Boundary Layer of a Wind Turbine Blade. *Renewable Energy*, 20.

[81] Hua Ouyang Hu, Danmei and Zhaohui Du. A Study on Stall-Delay for Horizontal Axis Wind Turbine. *Renewable Energy*, 31.

[82] Tarzanin Frank J. Jr. Harris, Franklin D. and Jr. Fisher, Richard K. Experimental investigation of dynamic stall performance for the edi-m109 and edi-m112 airfoils. *Journal of the American Helicopter Society*, 15(3):35–44, 1970.

[83] Hsiao Mun Lee and Yan-Hua Wu. Experimental study of rotational effect on stalling. *Chinese Physics Letters*, 30(6):064703 1–4, 2013.

[84] Lind A.H. Jacobson K.E. Smith M.J. Jones A.R. Smith, L.R. Experimental and Computational Investigation of a Linearly Pitching NACA 0012 in Reverse Flow. In *Proceedings of the 72nd Annual Forum of the American Helicopter Society*, West Palm Beach, FL, May 2016.

[85] William G. Bousman. Evaluation of Airfoil Dynamic Stall Characteristics for Maneuverability. *Journal of the American Helicopter Society*, 46(4):239–250, 2001.

[86] N.D. Ham and M.S. Garelick. Dynamic stall considerations in helicopter rotors. *Journal of the American Helicopter Society*, 13(2):49–55, 1968.

[87] K. W. McAlister L. W. Carr McCroskey, W. J. and S. L. Pucci. An Experimental Study of Dynamic Stall on Advanced Airfoil Sections, Vol. 1-3. Technical Report NASA TM 84245, National Aeronautics and Space Administration, 1982.

[88] Robinson M.C. Hand M.M. Schreck, S.J. and D.A. Simms. Blade dynamic stall vortex kinematics for a horizontal axis wind turbine in yawed conditions. *Journal of Solar Energy Engineering*, 123(4):272–281, 2001.

[89] Graham M. Bowen-Davies and Inderjit Chopra. Aeromechanics of a Slowed Rotor. In *56th AIAA/ASCE/AHS/ASC Structures, Structural Dynamics, and Materials Conference, AIAA SciTech Forum*, pages 1–23, Kissimmee, FL, January 2015.